Enhanced rock weathering with crops in agricultural soils:

Quantifying basalt weathering rates, CO_2 capture and agronomic co-benefits

Michael Edward Kelland

A thesis submitted in partial fulfilment of the requirements for the degree of Doctor of Philosophy

The University of Sheffield
Faculty of Science
School of Biosciences

April 2023

Abstract

The impending breach of the 1.5 ºC global warming threshold has catalysed significant recent interest in engineering solutions to climate change. Carbon Dioxide Removal (CDR) technologies are favoured, as they tackle the root cause of climate change, and from within this subset of geoengineering approaches, Enhanced Rock Weathering (ERW) stands out as a potentially scalable, technically-feasible, low-cost and potent strategy. Deployed at scale, ERW aims to increase the rate of global silicate weathering – which in nature acts as a long-term sink for atmospheric carbon dioxide (CO_2) – by spreading pulverised volcanic rocks on agricultural land. Basalt may be the most suitable rock for ERW, due to its ubiquity and low content of potentially toxic trace elements. But whilst basalt does have a long history of use as a supplementary fertiliser – in the developing world and, more recently, the organic agriculture sector – there exists limited evidence for its CO_2 sequestration potential in agricultural soils.

The overarching aim of this thesis was to quantify basalt weathering and CO_2 capture rates in agricultural soils under crop cultivation, and to measure the associated impacts on key soil and plant performance characteristics. This was achieved through a series of mesocosm-scale controlled-environment experiments of increasing complexity and scale, using a variety of soil types and crops. The findings in this thesis offer support for the use of basalt fines for carbon capture in acidic agricultural soils, with reported CO_2 capture estimates in the tonnes-per-hectare range for a single rock application. The use of basalt as a supplementary fertiliser is also justified by the results, as each experiment demonstrated higher yields in rock-amended acidic soils, with additional co-benefits for crop production. However, basalt had no discernible effect in the only alkaline soil included in the trials, leaving open the question of their suitability for ERW.

Acknowledgements

This PhD thesis could not have been completed without the guidance, investment and motivation I received from a long list of friends, family, colleagues and organisations. They believed in me and kindly gifted their support, resources and advice. For that I will forever be grateful.

To my primary supervisor, Professor David J. Beerling FRS, I extend my deepest and sincerest thanks. Dependable and ever available, David is a knowledgeable and considerate supervisor with an unwavering passion for scientific discovery. I am most grateful to David for the life-changing research opportunity at the Leverhulme Centre for Climate Change Mitigation (LC3M) and for connecting me to so many brilliant academics at the University of Sheffield and partner institutions worldwide. Moreover, I am grateful for the time, patience and thought he put into the thousands of hours of discussion, correspondence, management and training that I so greatly benefitted from, and which improved every aspect of my research.

Immeasurable thanks are offered to Professor Jonathan R. Leake for his polymathic insight and expert supervision. Jonathan provided essential input into the experimental designs, laboratory methods and analytical approach for all three mesocosm-scale trials reported in this thesis, and assisted greatly in the interpretation of major results. I am extremely grateful to Jonathan for his support of my work, and for the many kind words of encouragement he gave to me over the years.

Additional supervisory support was provided by Professor Steven A. Banwart, particularly with the interpretation of geochemical data and the utilisation of primary datasets for PHREEQC model development. I am privileged and delighted to have worked with Steven on the project, and I thank him for his vital efforts. I am similarly indebted to Professor Mark E. Hodson for his supervision during my studies. Mark made important contributions to the experimental approach, notably towards the mass balance technique used to quantify weathering. He also taught me a great deal about rocks and how to measure them, for which I am most grateful.

I would like to extend huge thanks to my project supporter, Professor Gareth K. Phoenix, and to Professor Colin P. Osbourne, too, for sage advice and critical feedback on my academic progress during the PhD programme. I am also extremely grateful to

Professor Dylan Z. Childs and Drs Venelina G. Koleva and Kai S. Erdmann for their guidance and understanding, and for enabling me to give this project my all.

Special thanks are due to Dr Lyla L. Taylor for her endless support and collaboration over the years. Lyla always showed a keen interest in my project and I am grateful for the countless hours of weathering-related discussion we engaged in. Lyla has developed the most phenomenal PHREEQC models, and I thank her for the time she spent integrating into those simulations data from my experiments.

Massive thanks go to Dr Peter W. Wade for his legendary PHREEQC skills, deep knowledge of weathering and endless supply of astonishing anecdotes from an extraordinary life. Peter and I turned coffee into ideas on many an occasion, working out design improvements with our mutual obsession for high-quality data collection. He was the main developer of the 1-D reactive transport model that hugely added value to our 2020 paper, and I am indebted to him for raising the profile of that research.

I was similarly blessed to work alongside Dr Amy L. Lewis for much of my PhD, both for the camaraderie we enjoyed as students and the expertise she brought to the team. My research benefitted greatly from her rock characterisation work, notably the basalt mineralogy data she obtained through collaboration with Mr Simon J. Kemp at the British Geological Survey. I am immensely grateful for the academic, technical and moral support that Amy selflessly dedicated to my project.

Special thanks go to Dr Binoy Sarkar for his early insight on the importance of soil cation exchange processes in determining the fate of weathering products. I learned so much from Binoy about sampling, preparing and measuring soils and rocks, to a high degree of scientific rigour, and I am most grateful for his input on the experimental designs, analytical methods, data interpretation and advice on improving my writing.

Huge thanks go to Professor Sue E. Hartley OBE for her collaboration and insight into weathering-related plant silicon uptake, and for kindly arranging access to her X-ray florescence instrument for plant tissue analysis. I am indebted to Drs Emma McLarnon and Sarah J. Thorne, and to Miss Emma Bailey, too, for their expert technical assistance in determining *Sorghum* tissue silicon concentrations.

Special thanks are due to Professor Rachel H. James and Drs M. Grace Andrews, Christopher R. Pearce, T. E. Anne Cotton and Mark Lomas for their guidance and

contributions towards our 2020 paper, specifically on the strontium isotope dilution method, fungal DNA analysis and basalt surface area calculations.

I would also like to thank Professor Noah J. Planavsky, Mr Tom Reershemius and Dr Chris Reinhard for their collaboration on the upcoming paper on the titanium-cation quantification method. Noah generously arranged TiCAT analysis for hundreds of my soil samples, and I am indebted to Miss Isabelle R. Davis, Mr Rocco D'Ascanio, Miss Ayesha A. Ahmed, and everyone else who assisted with that work.

I am most grateful to Professor Ute M. Skiba and Dr Julia Drewer for their valued collaboration and analytical work towards determining soil-atmosphere greenhouse gas fluxes in the biochar co-deployment trial. Credit is due to Mr Daniel Evans for handling the collection of vital gaseous samples for this work, and indeed, for assisting me with the preparations for and execution of that experiment. Huge thanks also to Mr Derek S. Bell for his valuable assistance in setting up and breaking down that study.

Colossal thanks are due to Mrs. Irene Johnson, from whom I learned so much about how to safely, accurately and considerately conduct research in academia. She trained and personally assisted me in so many practical tasks over the years, and I am immensely grateful for the time she spent looking after the various laboratories.

I am enormously grateful for the hours of technical support provided by Dr David Johnson, particularly in the testing of samples gathered from the *Sorghum* trials. I thank David for his assistance with the day-to-day running of the second experiment, and with the wide range of geochemical analyses we undertook together.

To Dr Karen J. Bailey, I offer my deepest appreciation for her diligent technical support on the project. Karen assisted in so many ways, with all varieties of soil, rock, plant, gaseous and aqueous sample preparation and analysis. She often ventured far from her comfort zone to advance my research, and I am most grateful for her dedication and unwavering professionalism.

Abundant support was also provided by LC3M's Debbie Hill and Victoria Giordano-Bibby, and Drs Euripdes P. Kantzas, Dimitar Z. Epihov, Chandra Bellasio, Joe Quirk, and Rachel M. S. Thorley, and Professor Claire L. Corkhill. Thanks to Mr Owen Hayman, too, for help with soil collection, and to Mr Ibrahim George at the University of Huddersfield, for providing access to the spinning riffler used for basalt preparation.

Respect is duly owed to Mr Matthew Smith at the School of Biosciences' workshop, for his crucial efforts towards fabricating the mesocosms for my experiments. Big thanks also go to Drs Scott Young, Saul Vazquez Reina and Nik Reeves-McLaren, along with Fiona Keay, Robert Ashurst, Neil Bramall, Chris Hill and Andrew Fairburn, for the myriad datapoints they measured on their respective instruments.

Huge thanks are due to Messrs. Timo Blake, Ben Palmer, Steve Turner and Greg Nicholson, for keeping the lights on at the Sir David Read Controlled Environment Facility, and to Professor Sir David J. Read FRS himself for his valued critical feedback on my research. Hailing from the West Country, as I do, Sir David often compelled me to revisit my roots, and I thank him for highlighting the importance of these organs.

I am hugely grateful to the numerous organisations and individuals who kindly donated materials to my project, including Cascade Minerals, Oakbank Game and Conservation, Flitcham Farm, Moss End Farm, Hope Farm and the Allerton Project. I also thank the Natural Environment Research Council, for funding my studentship *via* the ACCE Doctoral Training Programme, and the Leverhulme Trust, for vital additional research funding through LC3M *via* a Leverhulme Research Centre Award.

Lastly, I wish to thank my family and friends for their unconditional support. To my dear wife, Emily, I offer my sincerest gratitude for her utter devotion to our wonderful children, Molly, James and Luke, and her endless support for me and my research. We relocated from Cardiff so that I could attend the PhD programme, venturing far from our support group for a new life in Sheffield, with new schools, new friends and new challenges. For this I asked so much of Emily, the kids and our close relatives. I asked them to begin a new chapter for me, to reorganise their lives around me, and to work harder, drive further and wait longer, so that I could stay the course. Thank you all so much for enduring what you did, and for trusting in me and joining me on this epic adventure. Words cannot describe the love and gratitude I have for each of you.

To my mother, Wendy, father, Ted, step-father, Keith, and my parents-in-law, Sam and Chris, I extend my deepest gratitude for the priceless support they have provided to me, Emily and our children over the years. Gargantuan thanks are due to my sister, Gaby, too, for her lifelong advocacy, and to my sister-in-law, Sarah, along with both of their respective tribes. Huge thanks also to the good friends we made in our new life, and to anyone else who helped along the way.

Author contributions

Chapter 1

M.E. Kelland researched and wrote the chapter.

Chapter 2

M.E. Kelland, P.W Wade, B. Sarkar, M.E. Hodson, J.R Leake and D.J Beerling designed the study. M.E. Kelland undertook the experiments, soil and plant measurements and data analysis. P.W Wade, L.L. Taylor and M.E. Kelland undertook the reactive transport modelling. A.L. Lewis and S.J Kemp undertook basalt geochemistry analyses with B. Sarkar. M.G. Andrews undertook and interpreted strontium (Sr) isotope geochemistry. R.H. James, C.R. Pearce and S.A Banwart contributed geochemical interpretation. S.E Hartley contributed to silicon analyses and interpretation. T.E.A. Cotton undertook molecular identification and analyses of mycorrhizal fungi. D.J. Beerling, S.A. Banwart and M.E. Kelland undertook the writing up with specific contributions and suggestions for references from all other authors.

Thanks to I. Johnson for technical support, N. Bramall and S. Young for chemical analyses, C. Hill for assisting with SEM measurements, F. Keay for undertaking the BET measurements, G. Turner and J. Rushton for assistance with the SEM-EDX analyses and interpretation, and I. Mounteney for assistance with the XRD sample preparation. Oakbank Game and Conservation kindly provided Sorghum seeds. Further thanks to A. Leake for kindly granting permission to obtain soil from the Game and Wildlife Conservation Trust, Allerton Project farm. M.E. Kelland and A.L. Lewis were supported by NERC ACCE DTP studentships. S.J Kemp publishes with the permission of the Executive Director, British Geological Survey (UKRI). Funding of this research by the Leverhulme Trust through a Leverhulme Research Centre Award (RC-2015-029) is gratefully acknowledged.

Chapter 3

M.E. Kelland, P.W Wade, B. Sarkar, M.E. Hodson, J.R. Leake and D.J. Beerling designed the study. M.E. Kelland assembled and conducted the experiment (with technical support from D.A. Johnson), carried out the leachate, porewater, soil and plant measurements, built and programmed the soil moisture data loggers, compiled all

experimental data and performed the statistical analyses. M.E. Kelland, I. Johnson and K.J. Bailey harvested and preserved the soils, cleaned and dried the root materials, and powdered the *Sorghum* tissues. M.E. Kelland and K.J Bailey performed the wet chemistry analyses. A.L. Lewis and S.J Kemp characterised the basalt. S.J. Thorne measured the plant Si. M.E. Kelland led the writing, with contributions and suggestions for references from D.J. Beerling, M.E. Hodson and A.L. Lewis.

Thanks are due to I. Johnson, K.J. Bailey, A.L Lewis and D.A. Johnson for technical support, A.L Lewis and S.J Kemp for basalt characterisation data, and S.J. Thorne for *Sorghum* tissue Si analysis. *Sorghum* seeds were donated by Oakbank Game and Conservation. Thanks also to A. Leake and the Game and Wildlife Conservation Trust for granting access to the field site and soil. M.E. Kelland and A.L. Lewis were funded by NERC ACCE DTP studentships. Additional funding from the Leverhulme Trust is gratefully acknowledged.

Chapter 4

M.E. Kelland, D. Evans, J. Drewer, U. Skiba, J.R. Leake and D.J. Beerling determined the final form of the experimental design in late-2020. Significant groundwork on the design (notably the development of key hypotheses and experimental methods) was completed in February 2019 by B. Sarkar, M.E Kelland, D.J. Beerling., J.R. Leake, A.L Lewis and M.E Hodson. D. Evans and M.E. Kelland expanded the original plan into a 3-factorial design, with particular accommodation for the measurement of soil GHG fluxes. M.E. Kelland and D. Evans collected and processed the soils for the study, and assembled and maintained the experiment with technical support from K.J. Bailey, A.L Lewis, D. Bell and I. Johnson. M.E. Kelland built and tested the drip feed irrigation system, with assistance from K.J. Bailey. M.E. Kelland managed the aqueous sample analysis pipelines, with support from A.L Lewis and K.J. Bailey. M.E. Kelland, K.J. Bailey, A.L Lewis and D. Bell excavated the post-experiment soils and dismantled the study. M.E. Kelland, D. Evans and K.J. Bailey harvested the biomass. M.E. Kelland and K.J Bailey performed the wet chemistry analyses. M.E. Kelland compiled all experimental data and performed the statistical analyses presented in this thesis. M.E. Kelland and K.J. Bailey harvested and preserved the soils and ryegrass tissues. A.L. Lewis characterised the basalt, and also prepared the ultra-fine material with assistance from D. Bell. M.E. Kelland led the writing, with essential input from D.J. Beerling.

Special thanks are due to D. Evans for considerable assistance with the set up and maintenance of this experiment, and to K.J. Bailey, A.L Lewis, I. Johnson, and D. Bell for technical support, A.L Lewis for basalt characterisation data, and U. Skiba, J. Drewer, D. Evans and K.J. Bailey for their assistance in gathering soil-atmosphere GHG flux measurements during this trial, which unfortunately could not be integrated into this thesis in time. Thanks also to the proprietors of Flitcham Farm and Moss End Farm for permitting access to their respective fields for soil collection. B. Sarkar obtained the biochar for this study from the UK Biochar Research Centre, University of Edinburgh. A.L. Lewis sourced the basalt from Hill House Quarry in Troon. D.E Evans obtained the ryegrass seeds and NPKS fertiliser. M.E. Kelland, D. Evans, A.L. Lewis and D. Bell were funded by NERC ACCE DTP studentships. Additional funding from the Leverhulme Trust is gratefully acknowledged.

Chapter 5

M.E. Kelland wrote the chapter.

Declaration

I, Michael Edward Kelland, confirm that the Thesis is my own work.

I am aware of the University's Guidance on the Use of Unfair Means (www.sheffield.ac.uk/ssid/unfair-means).

This work has not been previously presented for an award at this, or any other, university.

Where data were collected through the actions or support of others, their contributions are fully acknowledged in the text.

Section 1.2.6 of this thesis contains results from a survey of a large global rock database (Max Planck Institute for Chemistry, 2015) that was carried out in 2015 in preparation for this thesis. Some of these results – relating to potentially useful basic elements and potentially harmful trace metals in igneous rocks – appear in the following publication:

> Beerling, D.J. *et al*. (2018), 'Farming with crops and rocks to address global climate, food and soil security'. *Nature Plants*, 4(3), pp. 138–147. DOI: 10.1038/s41477-018-0108-y.

Chapter 2 of this thesis has been published under the same title and can be accessed *via* the following full reference:

> Kelland, M.E. *et al*. (2020) 'Increased yield and CO_2 sequestration potential with the C_4 cereal Sorghum bicolor cultivated in basaltic rock dust-amended agricultural soil', *Global Change Biology*, 26(6), pp. 3658–3676. DOI: 10.1111/gcb.15089.

Minor edits have been made to the original manuscript to maintain a consistent format and voice throughout this thesis.

Some of the text in Section 3.2 of this thesis is reproduced in a related (pre-publication) manuscript on the titanium isotope dilution (TiCAT) method for quantifying rock weathering, for which I am a co-first author. I anticipate that this paper will soon be published under the title:

> 'Initial validation of a soil-based mass-balance approach for empirical monitoring of enhanced rock weathering rates'
>
> Reershemius, T. and Kelland, M.E. *et al*. (no date)

However, Section 3.2 of this thesis contains additional details relating to methods and materials that were not included in that paper.

Michael Edward Kelland

Abbreviations and terms

Abiotic	Without living organisms
Afforestation	The establishment of new forest; for CDR, ecosystems services
Al_2O_3	Corundum
Al^{3+}	Aluminium cation
AMF	Arbuscular mycorrhizal fungi
Anthropogenic climate change	Rapid 21st century climate change principally driven by human-induced GHG emissions
AP	Angular projections
AR1	The First Assessment Report of the IPCC
AR6	The Sixth Assessment Report of the IPCC
Arrhenius rate equation	Equation relating SA, temperature, saturation state and pH to the dissolution rate of a particular mineral
Asbestiform minerals	Natural, asbestos-bearing minerals that are hazardous to health when inhaled
Back radiation	IR energy reradiated down to the planet's surface by GHGs
Basaltic glass	Amorphous mineral content in some basaltic rocks
BECCS	Bioenergy with carbon capture and storage; a CDR strategy
BET	Brunauer–Emmett–Teller technique for SA measurement
BGS	British Geological Survey
Biochar	Pyrolysed organic material that can be added to soils; a CDR strategy
Biological comminution	The comminution (breaking apart) of rock particles by plants and soil microorganisms
C	Carbon
C_2H_6O	Ethanol
Ca^{2+}	Calcium cation
Calcite	Calcium carbonate mineral with chemical formula $CaCO_{3(s)}$
Carbonate rocks/minerals	Rocks and minerals containing high concentrations of CO_3
Carbonate-silicate cycle	Long-term weathering cycle that has moderated atmospheric CO_2 over geological timescales
Carcinogenic	Cancer-inducing
Cd	Cadmium
CDR	Carbon dioxide removal; the extraction of CO_2 from the atmosphere
CEC	Cation exchange capacity
CH_3COOH	Acetic acid
Cl	Chlorine
Clay minerals	Fine constituents of soil; clay particles are <0.002 mm in diameter
Climate intervention	Engineering approaches to modify Earth's radiative energy budget
CN	Carbon-nitrogen
CO_2	Carbon dioxide; a common GHG
CO_3^{2-}	Carbonate anion
Coccolitho-phores	Marine organisms that incorporate calcite into their skeletal tissues

Committed warming	Unavoidable future warming linked to historic GHG emissions
Cr	Chromium
Cretaceous Thermal Maximum	A period of peak global surface temperatures 90 million years ago
DAC	Direct air capture; a CDR strategy
Diatoms, siliceous	Marine organisms that incorporate silica into their skeletal tissues
DIC	Dissolved inorganic carbon
Dipole	A pair of oppositely charged poles, separated in space
Divalent cations	Positively charged atoms with a valency of 2+
DNA	Deoxyribonucleic acid
DOC	Dissolved organic carbon
Dunite	An ultramafic igneous rock
EDX	Energy dispersive X-ray analysis
EMF	Ecto-mycorrhizal fungi
ERW	Enhanced rock weathering; a CDR removal strategy that accelerates natural silicate weathering processes
Fe	Iron
GHG	Greenhouse gas (a gas able to absorb/reradiate IR light)
Greenhouse effect	Atmospheric warming caused by GHGs
H^+	Positively charged H^+ ion; proton
H_2CO_3	Carbonic acid
H_2O_2	Hydrogen peroxide
H_2SO_4	Sulphuric acid
Harzburgite	A fast-weathering magnesium-rich silicate mineral
HCl	Hydrochloric acid
HCO_3^-	Bicarbonate anion
HF	Hydrofluoric acid
HNO_3	Nitric acid
Hyphal networks	Extended network of fungal hyphae, able to extract nutrients and water from a large soil SA
ICP-AES	Inductively coupled plasma atomic emission spectrometry
ICP-MS	Inductively coupled plasma mass spectrometry
ICP-OES	Inductively coupled plasma optical emission spectrometry
In situ carbonation	Sequestering C in silicate mineral formations by reaction with a high-concentration supply of CO_2
IPCC	Intergovernmental Panel on Climate Change
IR	Infrared (electromagnetic radiation)
K	Potassium
Land-use conflicts	Competition for land between food, energy production, CDR etc.
LC3M	Leverhulme Centre for Climate Change Mitigation
Lherzolite	An ultramafic igneous rock
Ligand	Neutral molecules, bonded to a metal atom
LIP	Large igneous province; vast igneous rock formations; associated with flood basalts

Lolium perenne	Perennial ryegrass; common grassland species
Longwave radiation	Generally refers to IR electromagnetic radiation
Ma	Million years ago
Macronutrients	Nutrients needed in larger quantities for plant growth
Mafic rock	Magnesium- and iron-rich silicate rock
Mg^{2+}	Magnesium cation
Micronutrients	Nutrients not essential for plant growth, but nonetheless potentially beneficial for crop performance
Mid-Pliocene	A period of Earth's prehistory around 3 million years ago
Mn	Manganese
Mycelium	Extended network of fungal hyphae, able to extract nutrients and water from a large soil SA
Mycorrhizal fungi	Fungal symbionts of higher plants; generally mutualistic
N_2	Molecular nitrogen
Near-infrared	Electromagnetic radiation with wavelengths 780–2500 nm
Near-ultraviolet	Electromagnetic radiation with wavelengths 180–400 nm
Negative feedback	A system mechanism that tends to lower fluctuations in the output
$NH_4CH_3CO_2$	Ammonium acetate
NH_4Cl	Ammonium chloride
Ni	Nickel
Non-carbonic acids	Other acidic agents that will dissolve primary minerals but will not directly lead to CDR
NPK	Nitrogen-phosphorous-potassium
O	Oxygen
O_2	Molecular oxygen
Olivine	Magnesium-rich silicate minerals; iron-bearing
OM	Organic matter
Opal	Silica mineral with chemical formula $SiO_{2(s)}$
Organic acids	Carbon-based acidic agents; often chemically complex
P	Phosphorus
Paleo-atmospheres	Past atmospheres in Earth’s geological history
Paris Accord	International treaty ratified in 2016, intended to limit anthropogenic climate change
Pb	Lead
pCO_2	Partial pressure of carbon dioxide
Peridotite	Coarse-grained silicate rock containing high concentrations of olivine and pyroxene
PETM	Paleocene-Eocene Thermal Maximum; 55.5 million years ago
pH	A measurement scale for acidity
Plagioclase feldspar	Aluminium-rich silicate minerals containing Ca and Na
Positive feedback	A system mechanism that tends to raise fluctuations in the output

Pre-industrial average	Baseline atmospheric CO_2 concentration before industrialisation
Proton	Positively charged H^+ ion
PSD	Particle size distribution; the range and relative abundance of different constituent particle diameters
PTEs	Potentially toxic trace elements; potentially harmful to life in high concentrations; e.g. Cr, Ni, Pb, Cd
Pyroxene	Aluminium-rich silicate minerals containing a range of cations (Ca, Mg, Na)
Radiative energy budget	The energy balance between incoming and outgoing radiation
^{85}Rb	Rubidium-85 isotope
Re	Rhenium
Reforestation	The return of forest to a historically-forested site; for CDR and/or ecosystems services
RF	Radiative forcing
Rock loading	The mass of rock material added per unit land area
Rock phosphate	The major feedstock for commercial P-fertiliser production
RSA	Reactive surface area
RTM	Reactive transport model; a geochemical simulation
SA	Surface area
SD	Standard deviation in the mean
Se	Selenium
SE	Standard error of the mean
Secondary minerals	Minerals formed through precipitation of solid phases out of solution
SEM	Scanning electron microscope/microscopy
Shortwave radiation	This generally refers to near-IR, visible and near-UV electromagnetic radiation
Si	Silicon
Silicate rocks/minerals	Rocks and minerals containing high concentrations of SiO_2
SiO_2	Silica
Soil respiration	The release of CO_2 by roots and microorganisms in the soil
SOM	Soil organic matter
Sorghum bicolor	Sorghum, a C_4 arable crop, similar to maize and millet
Stoke's Law	A physical law relating terminal velocity to the diameter of suspended particles in a fluid under gravity
$TaCl_5$	Tantalum chloride
TC	Total carbon
Teratonne	1 trillion tonnes (1.5×10^{15} kg)
TIMS	Thermal Ionization Mass Spectrometer
Troposphere	The lowest layer of Earth's atmosphere
Turgor pressure	Hydrostatic pressure driven by osmotic processes
Ultramafic rocks	Fast-weathering silicate rocks with high Mg content
UV	Ultraviolet (electromagnetic radiation)

Contents

List of figures

List of tables

List of equations

1

Introduction

Contents

Over three centuries of increasing industrialisation and land-use change, humans have released around 1½ teratonnes (1.5×10^{15} kg) of CO_2 into the air (Friedlingstein *et al.*, 2022). Driven across the air-sea interface by rising CO_2 partial pressures (pCO_2), about ⅓ of this total inventory has been absorbed by the surface ocean (Gruber *et al.*, 2019), and subsequently participates in a range of marine biogeochemical processes (Canadell *et al.*, 2021). Similar quantities of CO_2 were sequestered by terrestrial carbon (C) sinks (Keenan and Williams, 2018), through erosion or the formation of soil organic matter (SOM) and, notably, by uptake into photosynthesising organisms. Yet, despite this natural resilience within the Earth system, much of the remaining pollution now persists in the atmosphere, with present-day CO_2 concentrations (≈420 ppm; NOAA, 2023) around 50% higher than the 'pre-industrial average' (280 ppm) and, possibly, the highest for around 14 million years (Zhang *et al.*, 2013). Well mixed in the air, this surplus CO_2 interferes with the exchange of electromagnetic radiation between Earth and space and, therefore, imbalances the planetary energy budget (Figure 1.1; Le Treut *et al*. 2007).

Sunlight is the Earth system's principal energy source and is remarkably stable over long timescales, with power fluctuations of no more than 0.1% throughout much of human history (Lean, 2018). Of the sunlight reaching Earth, ≈30% is promptly reflected

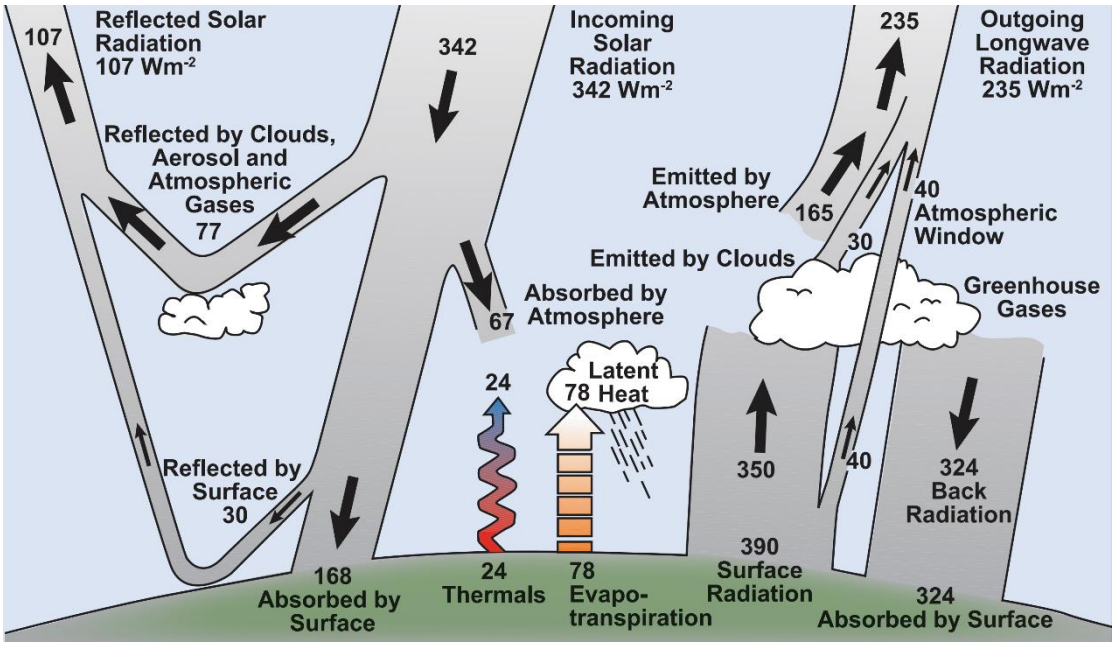

Figure 1.1 – Annual estimates for Earth's radiative energy budget. From Le Treut *et al*. (2007), after Kiehl and Trenberth (1997).

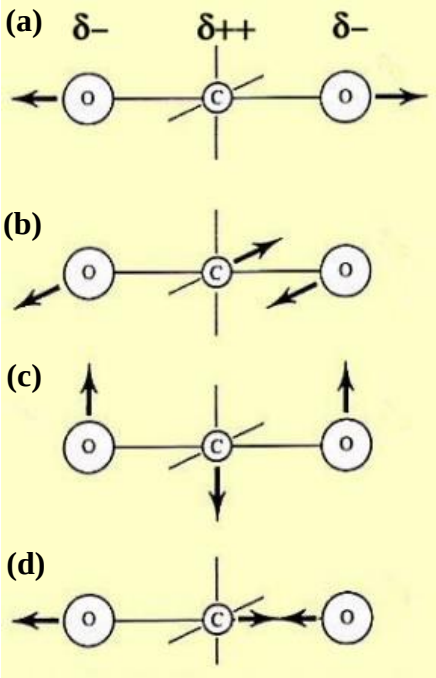

Figure 1.2 – Diagram of the four modes of vibration for a CO_2 molecule. (a) Stretching has no effect on symmetry, so IR energy is not absorbed. Molecular bending (b–c) and asymmetric stretching (d) do change dipole moment and symmetry, and can be initiated by IR-photon absorption. Adapted from a figure in (Lienhard, 2000).

back into space by the land, sea and air (Figure 1.1). Whilst the major atmospheric gases (N_2, O_2) are largely transparent to short-wave frequencies within sunlight – near-infrared (near-IR), visible and near-ultraviolet light – around 20% of incident solar energy is captured by the atmosphere (Figure 1.1) because some trace gases (and suspended liquids and particles) can absorb light energy at specific frequencies. Certain molecular gases (e.g. CO_2) can interact with IR photons – which represent ½ of the total energy in sunlight (Fondriest, 2014) – so long as parity exists between the photon frequencies and the vibrational frequencies of the gases' covalent bonds. Where the frequencies do match, and where the bond lengthening associated with energy capture would result in a dipole moment (Figure 1.2), incident IR radiation can be absorbed by the gas and then reemitted in all directions. For their ability to trap and redistribute thermal radiation, these gases are referred to as 'greenhouse gases' (GHGs).

For long-term climate stability, the constant energy input to the Earth system from sunlight must be counterbalanced by an equivalent energy output to space, as longwave radiation (mostly in the IR spectral range). Most of the incident solar energy reaching Earth is absorbed by the land and sea (Figure 1.1), which manifests as heat in surface matter that is subsequently reradiated in the IR. Hence, to balance the planetary energy budget and maintain a stable climate, much of this IR radiation must transit the atmosphere to space. However, GHGs – chiefly in the lower atmosphere (troposphere) – resist this rebalancing by absorbing IR energy at their characteristic frequencies, and reradiating some captured energy back down to the planet ('Back Radiation'; Figure 1.1). Through this additional radiative forcing (RF), global mean annual temperatures at Earth's surface (16 ºC) are far higher than they would otherwise be without GHGs (–19 ºC; Le Treut *et al*., 2007). This warming phenomenon is the 'greenhouse effect'.

1.1 Climate change

1.1.1 Anthropogenic climate change

Over ½ of all anthropogenic CO_2 emissions were released after 1990 (Friedlingstein *et al.*, 2022): A landmark year for climate science, distinguished by the first major, internationally-coordinated report on the dangers of CO_2 pollution (AR1; IPCC, 1990). At that time, it was well understood that CO_2 is a GHG, and that human-induced CO_2 emissions – from fossil fuel use, cement manufacture and global land-use changes – would likely warm the planet through artificial enhancement of the greenhouse effect (IPCC, 1990). Also, in the years leading up to the millennium, new isotopic evidence firmly linked high-CO_2 paleoatmospheres with some of the warmest periods in Earth's history – e.g. the Cretaceous (90 million years ago (Ma)) and Paleocene-Eocene (55.5 Ma) thermal maxima (Kennett and Stott, 1991; Koch, Zachos and Gingerich, 1992; Clarke and Jenkyns, 1999). What was not well known at the time, however, was the magnitude, scope and timing of the possible future impacts of a new, 21st century climate shift, and the extent to which humans were responsible for it (IPCC, 1990).

The last assessment report (AR6) from the Intergovernmental Panel on Climate Change (IPCC) strikes a very different tone to the original: Here, there is no longer any doubt that human activities are warming the planet (IPCC, 2021). Contemporary records already evidence more-extreme weather events – e.g. droughts, high-precipitation and tropical storms (IPCC, 2021) – alongside measurable, adverse impacts on global ecosystems, people and property (IPCC, 2022). Generally, the hazards to society and the environment will intensify with rising surface temperatures (IPCC, 2022), and further such rises are imminent and unstoppable due to inertia in the climate system, which has hitherto delayed the full effect of historic emissions (IPCC, 2021). Notably, the current magnitude of this 'committed warming' was recently estimated at 2.3 ºC above the pre-industrial average (Zhou *et al.*, 2021), which implies that at least a temporary breach of the Paris Accord's 2 ºC target (UNFCCC, 2015) is now inevitable. Deep and sustained cuts in anthropogenic GHG emissions are therefore urgently required, to reduce further pressures on the climate system, and to improve the odds of avoiding lasting, catastrophic environmental changes this century (IPCC, 2022).

1.1.2 Engineering the Earth system

As the main contributor to anthropogenic RF, CO_2 is the dominant driver of 21st century climate change (Myhre *et al.*, 2013). The gas is long lived in the atmosphere, and this is chiefly because the natural processes regulating long-term atmospheric CO_2 levels (see Section 1.1.3) function at an extremely slow pace (Colbourn, Ridgwell and Lenton, 2015). CO_2 emitted today can be expected to remain in the air for up to 10^5 years (Archer, 2005) and it is this effective permanence of CO_2 in the atmosphere, and not just its RF potential, that highlights the problem. Current emissions are in line with a 3 ºC increase in global surface temperatures (Hausfather and Peters, 2020), consistent with increasingly severe climate risks to natural and anthropogenic systems (IPCC, 2022). Warming of this magnitude has probably not occurred since the mid-Pliocene (*circa* 3 Ma; IPCC, 2007), so there is no historical precedence for the survival of human civilisations under similar climatic conditions. This is a strong incentive to redress the planetary energy budget, but with no natural pathways that could feasibly do so on human timescales, thoughts turn to engineering solutions for the climate problem.

A variety of climate intervention strategies have been proposed to initiate significant changes in the radiative energy budget (Figure 1.3). These can be categorised according to the mode of operation they exploit to induce negative RF (global cooling), namely:

a) Reflecting more incoming (shortwave) radiation back into space; or,

b) Increasing the outgoing flux of longwave radiation – i.e. generally, through atmospheric carbon dioxide removal (CDR).

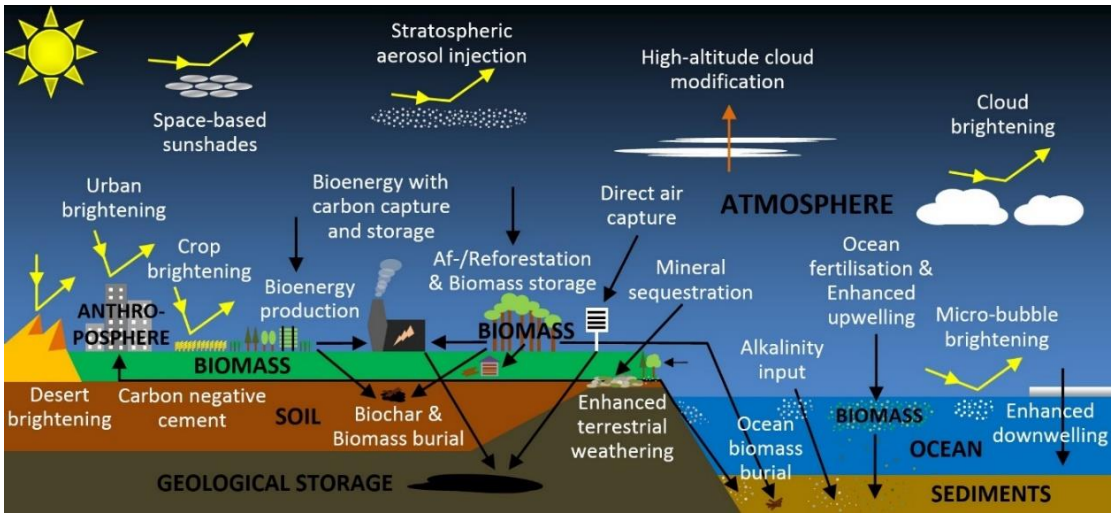

Figure 1.3 – Diagram of proposed geoengineering strategies. Yellow arrows indicate reflected shortwave radiation, black arrows show carbon transport between major reservoirs (black font) and orange arrow indicate increased outgoing longwave radiation. From Kelland (2015), adapted from Lenton and Vaughan (2009).

Strategies in category '**a**' are largely undesirable, and this is principally because they do not address the root cause of climate change: Anthropogenic CO_2 (Shepherd *et al.*, 2009). So whilst Earth can technically be cooled by changing the planetary albedo (Lenton and Vaughan, 2009), such approaches do little for the secondary effects of increased atmospheric CO_2, such as ocean acidification (Jin, Cao and Zhang, 2022). Hence, category '**b**' approaches (CDR) are favoured, as they offer genuine remediation of CO_2 pollution; however, no single CDR approach is sufficiently potent to fix the climate problem, and each are beset to varying degrees by land-use conflicts and issues of efficacy, cost, safety, scalability and technological readiness (Shepherd *et al.*, 2009; NRC, 2015). Of these approaches, Enhanced Rock Weathering (ERW; Section 1.2) stands out as a potentially low-cost, highly-scalable and low-technology CDR strategy, and therefore warrants further consideration (Taylor *et al.*, 2016; Beerling *et al.*, 2018).

1.1.3 Rock weathering in nature

Absent any future human intervention in the climate system, anthropogenic CO_2 will ultimately[*] be removed from the atmosphere *via* the carbonate-silicate geochemical cycle (Colbourn, Ridgwell and Lenton, 2015). This natural process results in modest but steady atmospheric CO_2 removal over geological timescales – currently ≈0.9 $GtCO_2$ $year^{-1}$ (Hartmann *et al.*, 2009). The respective CDR rate is dependent on surface temperature, and so silicate weathering provides vital negative feedback on long-term atmospheric CO_2 concentrations (Berner, Lasaga and Garrels, 1983). The process is initiated by carbonic acid (H_2CO_3; Equation 1.1), formed *via* absorption of atmospheric (and soil-respired) CO_2 in rain- and ground-water, which dissolves continental silicate minerals and releases their constituent base cations – notably, the divalent cations, calcium (Ca^{2+}) and magnesium (Mg^{2+}) – and silica, $SiO_{2(aq)}$, into groundwater (Equation 1.2).

$$\underset{\text{carbon dioxide}}{CO_{2(g)}} + \underset{\text{water}}{H_2O_{(aq)}} \rightleftharpoons \underset{\text{carbonic acid}}{H_2CO_{3(aq)}} \rightleftharpoons \underset{\text{hydrogen cation}}{H^+_{(aq)}} + \underset{\text{bicarbonate anion}}{HCO_3^-{}_{(aq)}} \rightleftharpoons \underset{\text{hydrogen cations}}{2H^+_{(aq)}} + \underset{\text{carbonate anion}}{CO_3^{2-}{}_{(aq)}}$$

Equation 1.1 – A simplified chemical equation for the dissolution of CO_2 and dissociation of carbonic acid in water. Adapted from Mitchell *et al.* (2010).

[*] In 10^5 years, ≈93% of fossil fuel carbon may be removed from the atmosphere (Archer, 2005).

These soluble, positively-charged weathering products and the atmospheric C – mainly in the form of dissolved bicarbonate anions (HCO_3^-); see Equation 1.2 – are fixed in solution by their mutual charge balance and subsequently transported to the oceans by watercourses, where much of the carbon will be secure for millennia (Hartmann *et al.*, 2013; Renforth and Henderson, 2017).

$$CaSiO_{3(s)} + 2H_2CO_{3(aq)} \rightarrow Ca^{2+}_{(aq)} + 2HCO_3^-{}_{(aq)} + SiO_{2(aq)} + H_2O_{(l)}$$
$$MgSiO_{3(s)} + 2H_2CO_{3(aq)} \rightarrow Mg^{2+}_{(aq)} + 2HCO_3^-{}_{(aq)} + SiO_{2(aq)} + H_2O_{(l)}$$

Equation 1.2 – Simplified chemical equations for silicate mineral dissolution by carbonic acid. Adapted from Kelly (2003).

The stoichiometry of the reactions in Equation 1.2 indicates that two moles of H_2CO_3 (and, hence, two moles of atmospheric CO_2) are consumed per mole of Ca or Mg released during silicate mineral dissolution – in practice, however, CO_2 capture is less efficient due to the effect of carbonate buffering (Renforth and Henderson, 2017). Notably, this is twice as efficient as comparable weathering of Ca- and Mg-carbonate minerals (Equation 1.3). Nonetheless, cations released through carbonic acid dissolution of carbonate minerals are free to participate in charge-balanced CDR, just as their counterpart silicate weathering products are. For this reason, carbonate mineral weathering may have some utility for generating short-term negative RF (i.e. on timescales relevant to anthropogenic climate change; Thorley *et al*., 2015). In any case, silicate rocks fairly typically contain trace amounts of carbonate minerals, so their presence and effect on weathering fluxes must always be considered. Where the difference in CDR efficiency per mole of carbonate *vs* silicate mineral does become important, however, occurs at the end of silicate-carbonate cycle, and relates to the long term fate of weathering products in the oceans.

$$CaCO_{3(s)} + H_2CO_{3(aq)} \rightarrow Ca^{2+}_{(aq)} + 2HCO_3^-{}_{(aq)}$$
$$MgCO_{3(s)} + H_2CO_{3(aq)} \rightarrow Mg^{2+}_{(aq)} + 2HCO_3^-{}_{(aq)}$$

Equation 1.3 – Simplified chemical equations for carbonate mineral dissolution by carbonic acid. Adapted from Thorley *et al*. (2015).

Most of the dissolved inorganic carbon (DIC) added to the oceans *via* ERW will remain stable for *circa* 10^5 years (Drever, 1997; Kelly, 2003). However, due to changes in pH, temperature, salinity and pCO_2, some captured C will be returned to the air when

riverine waters mix with the ocean, because the chemical equilibrium of dissolved C species (Equation 1.1) shifts to favour increased carbonate anions (CO_3^{2-}; Renforth and Henderson, 2017). This reduces C storage efficiency in seawater and results in the loss of around 17% of the total captured C to the atmosphere (Renforth and Henderson, 2017). Nonetheless, the overall CDR efficiency is maximal where weathering products reach the ocean, compared to the formation of secondary (e.g. pedogenic, benthic) carbonate minerals (Equation 1.4).

Over geological timescales, the oceans counterbalance riverine alkalinity inputs *via* the deposition of secondary minerals in seafloor sediments (Equation 1.4; Penman *et al*., 2020), notably as calcium carbonate and opal – respectively, $CaCO_{3(s)}$ (calcite) and $SiO_{2(s)}$. Although precipitates can form spontaneously (i.e. abiotically), secondary deposition processes in the oceans are predominantly biologically-mediated (Kelly, 2003) and driven by the incorporation of weathering products into the skeletal tissues of marine organisms – e.g., coccolithophores ($CaCO_3$) and diatoms (SiO_2). At the end of their lifecycles, the remains of these organisms may descend through the water column and accumulate in seafloor sediments, such that much of the calcite and silica re-enters the lithosphere through tectonic subduction (Drever, 1997; Kelly, 2003). Importantly, during calcite formation (Equation 1.4; 1st equation), one mole of CO_2 is liberated for each mole of divalent cation (e.g. Ca^{2+}). So, over geological timescales, carbonic acid weathering of silicate minerals results in one mole of CO_2 captured per mole of Ca^{2+}, whereas carbonic acid weathering of carbonate minerals is carbon-neutral (Thorley *et al*., 2015).

$$Ca^{2+}_{(aq)} + 2HCO_3^-{}_{(aq)} \rightarrow CaCO_{3(s)} + CO_{2(g)} + H_2O_{(l)}$$

$$H_4SiO_{4(aq)} \rightarrow SiO_{2(s)} + 2H_2O_{(l)}$$

Equation 1.4 – Simplified chemical equations for calcite and opal precipitation. Adapted from Penman *et al*., (2020).

As a final note on the essential chemical equations of rock weathering, it is important to highlight that other acids commonly found in nature – e.g. sulphuric (H_2SO_4) and nitric (HNO_3) acid – can substitute for carbonic acid (H_2CO_3) in silicate and carbonate reactions (Equations 1.2–3), resulting in mineral dissolution with no associated CO_2 capture. So, where groundwaters are sufficiently acidic to implicate non-carbonic acids (pH < 6.3), overall CDR estimates must be appropriately corrected (Dietzen and Rosing, 2023).

1.2 Enhanced rock weathering

ERW is a CDR strategy that operates by artificially accelerating the carbonate-silicate cycle (Section 1.1.3) through the large-scale distribution of crushed silicate rocks on land (Köhler, Hartmann and Wolf-Gladrow, 2010; Moosdorf, Renforth and Hartmann, 2014). The approach is therefore distinct from weathering strategies that directly input alkalinity into the oceans (Harvey, 2008; Schuiling and De Boer, 2011), or bring concentrated, high-purity CO_2 into contact with silicate mineral formations (i.e. '*in situ* carbonation'; Kelemen and Matter, 2008; Sanna *et al.*, 2014). ERW is a relatively recent climate engineering proposal – originally outlined in Schuiling and Krijgsman's (2006) paper – and so few studies have been conducted to quantify weathering and CDR rates, or related impacts on plant and soil characteristics (see summary in Section 1.3). Still, general predictions about the effect of key variables on weathering rates can be inferred from the fundamental rate equation for mineral weathering (Equation 1.5).

1.2.1 Silicate mineral dissolution rates

As a CDR strategy, ERW's main objective is to maximise the rate of CO_2 drawdown, and so overcoming the relatively slow reaction kinetics of silicate mineral weathering is the foremost challenge (Shepherd *et al.*, 2009). Laboratory dissolution experiments reveal that chemical weathering rates are determined by several key variables (Box 1.1), many of which may be optimised to improve weathering and CDR efficiency.

Box 1.1 – Arrhenius rate equation for chemical weathering

Where a particular mineral is dissolved by an acid-catalysed weathering mechanism, the weathering rate is governed by the general equation*:

$$W = SA \cdot k e^{\frac{-E_a}{RT}} \cdot a_{H^+}^{n}(1 - \Omega) \quad \textbf{Equation 1.5}$$

where W is the weathering rate (mol s^{-1}), SA is the total mineral surface area (m^2), k is the dissolution rate constant (mol m^{-2} s^{-1}), E_a is the apparent activation energy of the overall weathering reaction (J mol^{-1}), R is the molar gas constant (8.314 J K^{-1} mol^{-1}), T is the temperature (K), a_{H^+} is the hydrogen ion activity (mol L^{-1}), n is the order of the reaction and Ω is the mineral saturation state.

* Adapted from Renforth *et al.* (2015) and Palandri and Kharaka (2004).

The mineral weathering rate is directly proportional to the total mineral surface area (SA ; Equation 1.5), calculated as the product of the total mass of added mineral × SA per unit mass of mineral. To maximise weathering rates, ERW proposals usually prescribe that rock materials are pulverised into smaller grains (Schuiling and Tickell, 2010; Hartmann *et al.*, 2013); but, as reviewed in Section 1.2.5, the energy requirements (and associated GHG emissions and costs) for grinding exponentially increase with decreasing grain size. With respect to total SA, ERW researchers and practitioners have several points of control to manage: rock loading (i.e. t rock ha^{-1}), material selection (e.g. for rock porosity/hardness) and particle size distribution (PSD). Experimentally, rock PSDs can be manipulated by milling, sieving or exploiting differences in terminal velocities of different-sized rock particles suspended in gases (e.g. vortex separation) or liquids (i.e. using Stoke's Law; Dey, Zeeshan Ali and Padhi, 2019).

The form of Equation 1.5 indicates that the weathering rate will increase non-linearly with temperature. It can be shown (Appendix A) that an increase in temperature from T_0 to T_1 results in enhancement of the weathering rate by a factor of $\frac{W_1}{W_0}$, where:

$$\frac{W_1}{W_0} = e^{\left[\frac{E_a}{R}\left(\frac{1}{T_0}-\frac{1}{T_1}\right)\right]} \quad \textbf{Equation 1.6}$$

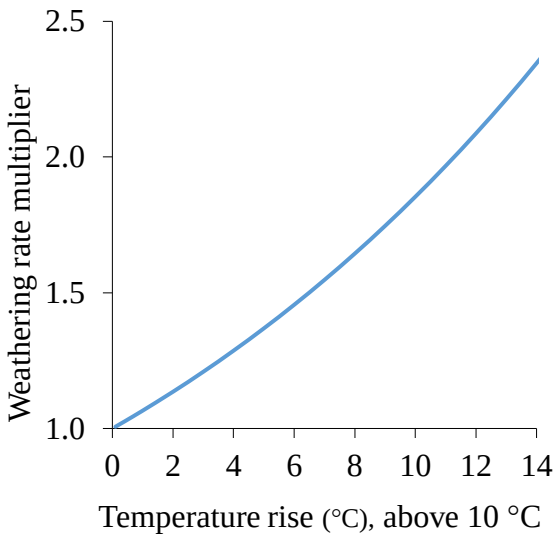

Figure 1.4 – Temperature dependence of forsterite dissolution. Calculated using Equation 1.6, taking E_a = 42.6 kJ mol^{-1} for forsterite dissolution at pH 6 (Giammar, Bruant and Peters, 2005).

Figure 1.4 illustrates that a 10 °C increase in temperature will nearly double the dissolution rate of forsterite – the Mg-rich end member of the fast-weathering olivine series. Many other common silicate minerals have higher activation energies, and may therefore be even more sensitive to changes in temperature. Soil respiration rates should also increase exponentially with temperature, and this is likely to improve weathering rates (see below). Soil respiration is optimal near field capacity (about 60% water-filled pore space; Davidson and Janssens, 2006).

As stipulated in Equation 1.5, mineral weathering rates will decrease as porewater solutions near saturation with respect to the particular primary mineral phase. In controlled ERW experiments, accelerated weathering rates may therefore be achieved by increasing the flux of irrigation water to the mineral weathering site. Saturation states may also be beneficially modified through removal of dissolution products by soil exchange processes (e.g. sorption by clay minerals), or by interaction with specific organic compounds (e.g., Al^{3+} complexation by organic acids; Kaiser and Zech, 2000).

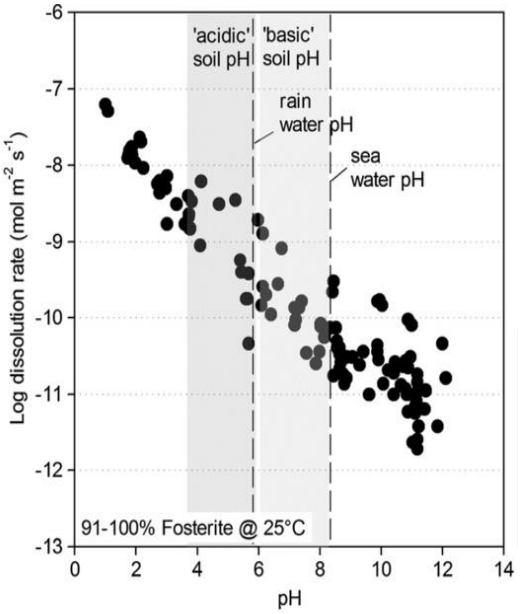

Figure 1.5 – The relationship between pH and the forsterite dissolution rate. (Hartmann *et al*., 2013).

The pH of the weathering environment exerts strong control over dissolution rates, as suggested by the proportionality between W and a_{H^+} in Equation 1.5, and Figure 1.5. Faster weathering would thus be expected in more acidic soils, and could be further enhanced by biological activity – e.g. soil respiration (meaning increased soil pCO_2), N-cycling and secretion of organic acids by mycorrhizal fungi (Bolan, Hedley and White, 1991; Hoffland *et al.*, 2004; Leake *et al.*, 2008; Banwart, Berg and Beerling, 2009). Expanding on the latter, the role of mycorrhiza in weathering is now reviewed.

1.2.2 Weathering by plants and mycorrhizal fungi

Mycorrhizal fungi are a taxonomically diverse and ubiquitous fungal group that associate with the roots of over 90% of vascular plants (Bonfante and Genre, 2010). By interfacing with plant roots, mycorrhizal fungi facilitate a generally mutualistic symbiotic relationship, whereby the fungus supplies water and nutrients to the host in exchange for chemical energy in the form of photosynthate (Smith and Read, 2008). The two most prolific groups, arbuscular mycorrhizal fungi (AMF) and ecto-mycorrhizal fungi (EMF), connect with plants *via* different mechanisms, with the former penetrating the root cells and the latter forming a hyphal sheath around the root tips (Zabinski and Bunn, 2014).

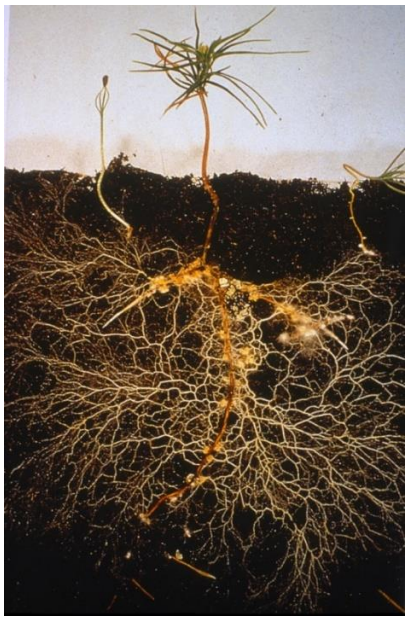

Figure 1.6 – Scott's pine (*Pinus sylvestris*) seedlings inoculated with EMF. (Wundernest, 2012).

EMF almost exclusively associate with woody plants, e.g. spruce (*Pinus sylvestris*) and oak (*Quercus spp.*), whereas AMF form assemblages with a much wider variety of woody and herbaceous plants (Theimer and Gehring, 2007; Kleczewski, Lewandowski and Bonello, 2008). To maintain their often vast hyphal networks (Figure 1.6), mycorrhizal fungi can draw substantial amounts of photosynthate from their host plants (≈10% of net primary production for AMF and up to 30% for EMF; Högberg and Högberg, 2002; Leake *et al*., 2004). This thread-like network (or mycelium) acts as an extension of the roots and improves water uptake by the plant, in part due to the greatly increased surface area (Augé, 2001).

Host plants can trade photosynthate energy with the fungus in exchange for essential nutrients that might otherwise be unavailable to them, e.g. phosphorus (P) and potassium (K), which can be procured by the fungus through active weathering of soil minerals (Berner, Berner and Moulton, 2003; Smits *et al.*, 2012). Recent research (Rosling, Lindahl and Finlay, 2004; Leake *et al.*, 2008; Quirk *et al.*, 2012) suggests that mycorrhizal fungi can seek out minerals in soil, and may target individual grains offering the highest SA. Once in contact with the rock, fungal hyphae can detect and respond to surface irregularities – e.g. ridges, channels and pits – to exploit physical weaknesses and expedite the weathering process (Landeweert *et al.*, 2001). Physical weathering may then be enhanced through turgor pressure, generated by specialised infection cells (appressoria), and more significantly *via* trenching and penetration of the rock surface by hyphae (Hoffland *et al.*, 2004). Capitalising on physical footholds, mycorrhizal fungi also exude a range of ligand- and proton-based weathering agents, which further accelerate mineral dissolution (Leake *et al.*, 2008).

Of particular relevance for ERW are laboratory and field observations of preferential colonisation of P-rich minerals by both AM and EM fungi (Leake *et al.*, 2008; Quirk *et al.*, 2012) and the increase in plant uptake of rock-derived P under low-P conditions (Leake *et al*., 2008). These results indicate that if P-rich silicates are deployed in P-limited soils, mycorrhizal partnerships may respond by diverting additional energy for

P-procurement from the introduced minerals. Hence, mycorrhiza may enhance silicate weathering rates, whilst enhancing plant growth through increased P availability.

Although enhanced weathering by mycorrhiza is anticipated in some ERW studies (Schuiling and Tickell, 2010; Moosdorf, Renforth and Hartmann, 2014), the extent to which nutrient stress will drive biological weathering is presently unclear (Hartmann *et al.*, 2013). Specifically, no controlled experiments have yet been attempted to quantify changes in plant growth and weathering rates resulting from a mycorrhizal response to bulk soil additions of P-rich silicate minerals. It is proposed that such experiments are now needed to better predict the impact of ERW deployment on natural ecosystems.

1.2.3 Possible applications for ERW

Early modelling studies investigated deployment of ERW in tropical forests (Köhler, Hartmann and Wolf-Gladrow, 2010; Taylor *et al.*, 2016) and indicated considerable potential to capture atmospheric C and counteract ocean acidification. But this approach is disadvantaged by the challenge of distributing substantial amounts of rock over vast and inaccessible areas, necessitating expensive and carbon-intensive aerial application of minerals. Managed agricultural land is better-suited to ERW, not least because much of the requisite infrastructure and soil management expertise will be present in the target area (Schuiling and Krijgsman, 2006; ten Berge *et al.*, 2012; Beerling *et al.*, 2018). Notably, the introduction of alkaline rocks into managed soils may help to relieve soil acidity, which is a common agricultural problem (Figure 1.7).

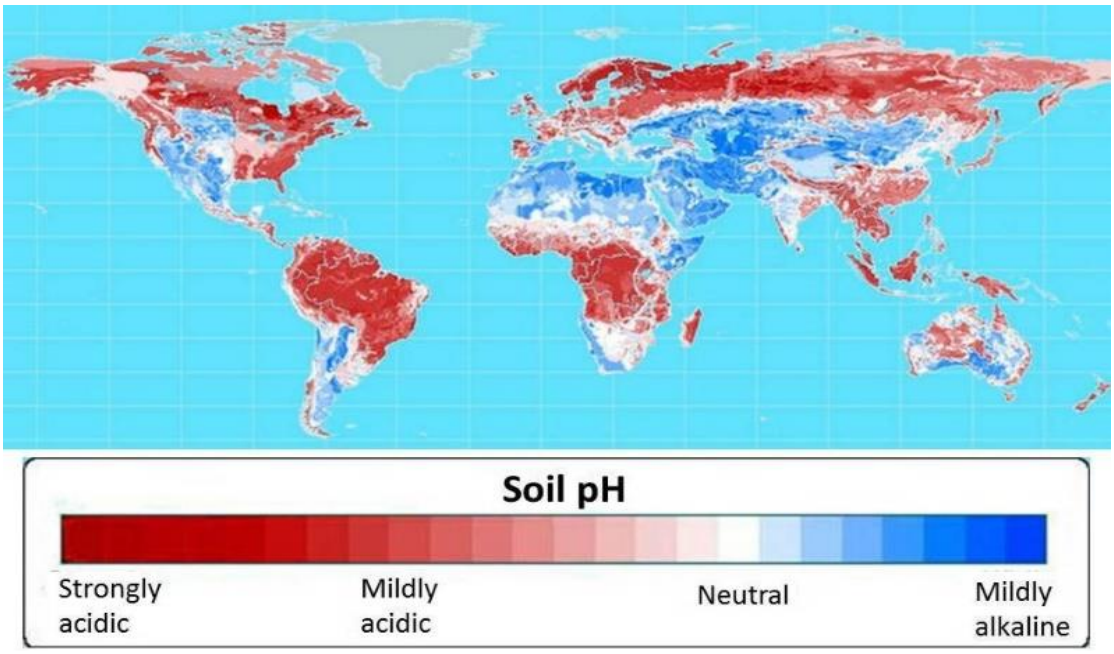

Figure 1.7 – Map illustrating the global variance in soil pH. (Kochian, 2014).

Excess soil acidity is generally deleterious for plant growth and is routinely managed by introducing carbonate minerals (e.g. lime) into soils (FAO, 2015a). The practice of agricultural liming is probably only slightly carbon-positive (Schuiling and Krijgsman, 2006). However, by substituting carbonates for silicates (which will likely modify pH at a much slower rate), the same process of pH control could be carbon-negative. Selected accordingly, silicate minerals might also represent a cost-effective fertiliser, given the potential to supply micronutrients, e.g. selenium (Se), and macronutrients (e.g. Mg, Ca) that are often absent from mass-produced agrochemicals (van Straaten, 2006). Moreover, long-term production of soluble chemical fertilisers is threatened by diminishing reserves of high-grade rock phosphate (Cordell, Drangert and White, 2009), so the P content of silicate minerals may have agronomic value. Additional benefits (e.g. improved crop resilience through increased plant-available Si) may be realised by ERW, but further research is needed to confirm this, and the other potential advantages outlined above (Moosdorf, Renforth and Hartmann, 2014). It is also noted that ERW could present significant hazards to ecosystems and human health – e.g. transient pH effects in soil/aquatic systems, or the release of airborne particulates and potentially toxic and/or carcinogenic material from silicate rocks (Hartmann *et al*., 2013). Further research is required to assess these risks.

1.2.4 Target crops for ERW

Table 1.1 – Top six global crops by cultivated area. (FAO, 2015b).

Crop	Cultivated area (ha)
Wheat	218,460,701
Maize	184,192,053
Rice (paddy)	164,721,663
Soybeans	11,269,782
Barley	49,781,046
Sorghum	4,210,446

Approximately 38% of Earth's land surface is arable or under permanent crops and pastures, which exceeds global forest cover (31%; World Bank, 2015). An area larger than the Amazon basin (≈8 million km^2 or 6% of the entire land surface) is dedicated to the production of just six crops (Table 1.1; FAO, 2015b), and the CDR potential in these soils alone could be substantial.

Of these extensively grown annual crops, maize, soybean and sorghum are known to associate well with AMF (Hata, Kobae and Banba, 2010), and may therefore be suitable subjects for controlled experiments of mycorrhiza-driven ERW. Common cultivars of wheat, rice and barley may not be ideal, however, given their typically poor response to AMF inoculation (Hata, Kobae and Banba, 2010).

Maize, soybean and sorghum are thus identified as prevalent (and potentially important) food/bioenergy crops that are known to be mycorrhizal, and could accordingly be used to test the mycorrhizal response to ERW. Of these crops, only soybean is unable to exploit the C_4 photosynthetic pathway, which should enable comparatively high rates of photosynthesis under optimal lighting/warmth. The more vigorous growth of C_4 plants may thus result in higher P demands, and could in turn incentivise the allocation of photosynthate to enhance mineral weathering. On this basis, C_4 plants may be expected to weather P-rich silicate minerals at a faster rate than C_3 plants (e.g. soybean).

1.2.5 Energy requirements and costs

Feasibility studies of ERW on agricultural land indicate that the transport and comminution of silicate rocks will be the most energy-intensive and expensive aspects of the strategy (Renforth, 2012; Moosdorf, Renforth and Hartmann, 2014). Whilst transport emissions and costs may be minimised by exploiting silicate resources near to the application site (Schuiling and Krijgsman, 2006), local rocks will not necessarily be suitable and bulk haulage is likely to be required. The cost and energy needed may ultimately be dictated by the choice of source rock, which in turn dictates the payload and transit-distance penalties (Renforth, 2012).

The energy required for comminution will be principally influenced by the desired grain size distribution (PSD), but may also be affected by the hardness and consistency of the rock (Schuiling and Tickell, 2010). Figure 1.8 suggests that exponentially greater inputs of energy are needed to create larger mineral SAs, and so this key engineering control on the weathering rate may be limited by financial and efficiency constraints.

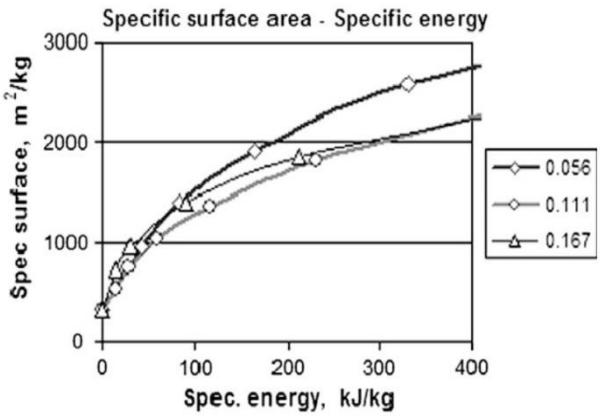

Figure 1.8 – Relationship between grinding energy input and mineral surface area at three different feed in rates. (Stamboliadis, Pantelaki and Petrakis, 2009).

Given the limitations, the capacity for mycorrhizal fungi to use photosynthate energy for mineral comminution could permit the use of larger grains and, hence, improve the affordability and CDR efficiency of ERW (Moosdorf, Renforth and Hartmann, 2014). Preliminary cost estimates for ERW deployment on agricultural land are in the region

of \$25–\$600 tCO_2^{-1}, depending on the choice of source rock (Renforth, 2012); however, these figures do not account for any agronomic value of the added silicate materials, or any potentially beneficial biologically-mediated effects on silicate mineral weathering. Experiments examining the mycorrhizal response to difference grain sizes could help to elucidate the energy savings and financial value of 'biological comminution', and would thus make an important contribution to ERW research.

1.2.6 Silicate rocks for enhanced weathering

Although silicates are the most abundant minerals on Earth – constituting >95% of the lithosphere (Hancock and Skinner, 2000) – not all silicate minerals will be suitable for ERW. Given the overall aim to maximise the weathering rate, proposals have typically advocated the use of ultramafic rocks (e.g. harzburgite or dunite; Schuiling and Krijgsman, 2006; Köhler, Hartmann and Wolf-Gladrow, 2010) due to their high content of olivine – the most easily weathered silicate mineral (Figure 1.9).

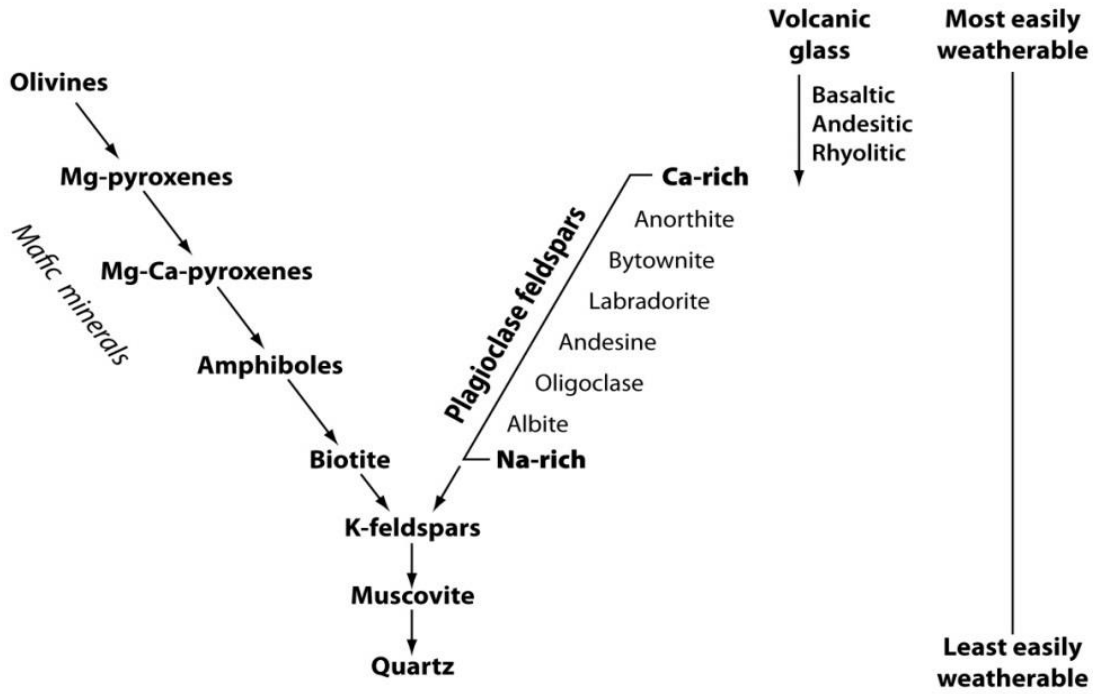

Figure 1.9 – Weathering stability series for silicate minerals. (Churchman and Lowe, 2012).

Global reserves of ultramafic rocks are believed to be substantial – perhaps >90 trillion tonnes within 100 metres depth (Bide, Styles and Naden, 2014) – but inadequate reserves of dunite (the peridotite with the highest olivine content) could limit its potential for long-term ERW (Taylor *et al.*, 2016). Much larger continental reserves of

less olivine-rich peridotites (e.g. harzburgite) exist near the surface, notably in the Samail ophiolite of Oman. Remarkably, this massive reserve alone contains sufficient peridotite to sequester the entire atmospheric CO_2 inventory several dozen times over (Kelemen and Matter, 2008).

As an alternative to ultramafic rocks, the mafic rock basalt has also been suggested for ERW (Schuiling and Krijgsman, 2006; Taylor *et al.*, 2016). Whilst basalt tends to weather more slowly, owing to the lower olivine and higher pyroxene/plagioclase feldspar content (ICL, 2015), enormous resources exist in large igneous provinces (LIPs) worldwide (Figure 1.10). It can therefore be concluded that the carbon sequestration potential of ERW is unlikely to be limited by global rocks reserves.

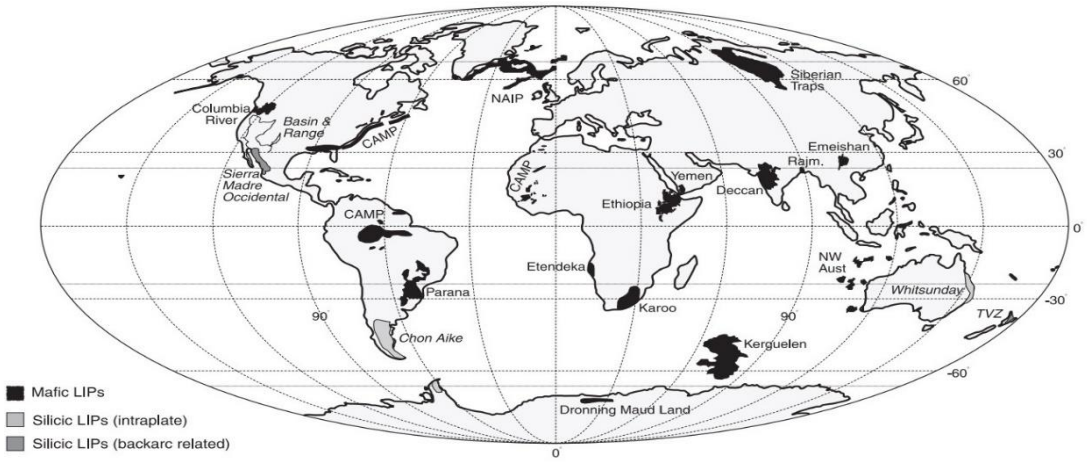

Figure 1.10 – Global distribution of Large Igneous Provinces. (Bryan *et al*., 2002).

There is presently no consensus on the most suitable rock type for ERW, and indeed, the selection may even be site-specific (Schuiling and Tickell, 2010). Other factors besides mineral abundance and reactivity will be important in choosing an appropriate source rock – e.g. cost, mineralogy (including asbestiform minerals) and overall cation content. Renforth's (2019) work indicates that the rocks most suitable for carbon sequestration will be both reactive and cation-rich, with their maximum ERW potential, E_{pot} (in units of tonnes of CO_2 sequestered per tonne of rock material), being:

$$E_{\mathrm{pot}} = \frac{M_{\mathrm{CO2}}}{100}\left(\alpha\frac{\mathrm{CaO}}{M_{\mathrm{CaO}}} + \beta\frac{\mathrm{MgO}}{M_{\mathrm{MgO}}} + \varepsilon\frac{\mathrm{Na_2O}}{M_{\mathrm{Na_2O}}} + \theta\frac{\mathrm{K_2O}}{M_{\mathrm{K_2O}}} + \gamma\frac{\mathrm{SO_3}}{M_{\mathrm{SO_3}}} + \delta\frac{\mathrm{P_2O_5}}{M_{\mathrm{P_2O_5}}}\right)\eta \quad \textbf{Equation 1.7}$$

Where M denotes molecular mass; oxide values are input as wt.%; α, β, γ, δ, ε, and θ are constants accounting for the oxides' relative contributions to carbon sequestration

(assumed to be 1, 1, –1, –2, 1 and 1 in this thesis); and, η (assumed to be 1.662 in this thesis) accounts for CO_2 lost to the atmosphere due to carbonate buffering in the oceans.

Following Equation 1.7, MgO will have a greater CO_2 capture potential than CaO owing to its equivalent valency but lower molecular mass. So, high-Mg peridotites such as harzburgite, lherzolite, dunite and wehrlite would appear to be ideal rocks for ERW. Figure 1.11 suggests that peridotites will sequester more than twice as much CO_2 as an equivalent mass of basalt. However, an examination of the trace element content of peridotites (overleaf) reveals that these may be unsuitable feedstocks for ERW.

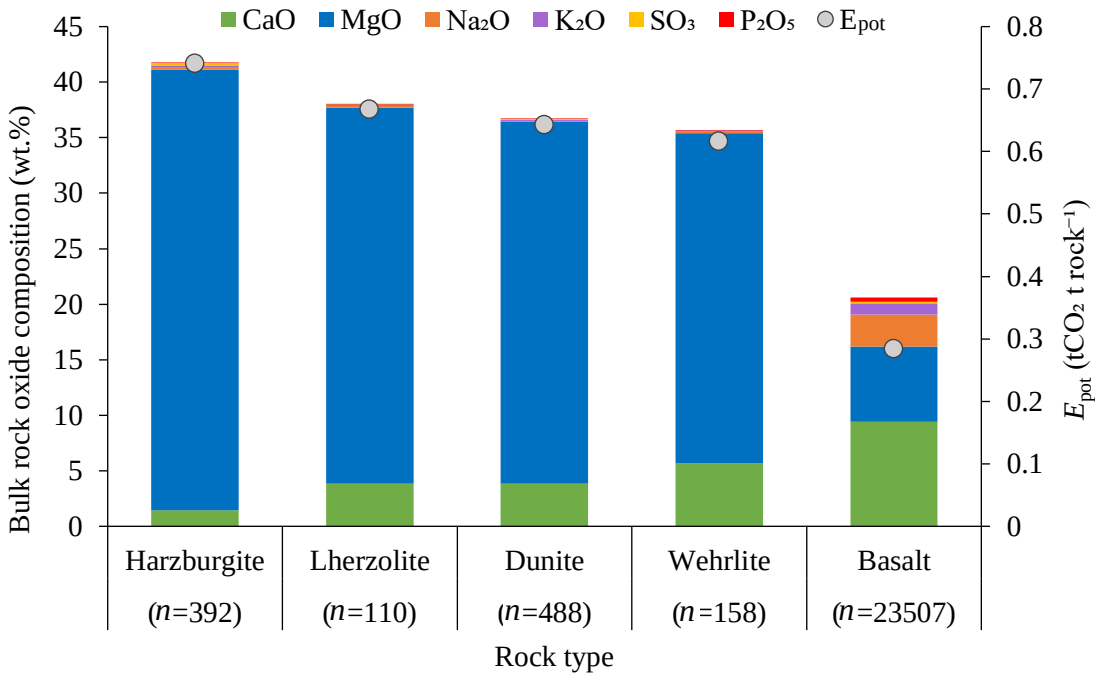

Figure 1.11 – Major oxide content and maximum ERW potential (E_{pot}) for four peridotites and basalt. Raw data obtained from the Max Planck Institute for Chemistry (2015). E_{pot} was calculated using Equation 1.7, adapted from Renforth (2019).

Foreseen by some researchers (Schuiling and Krijgsman, 2006; Hartmann *et al.*, 2013; Taylor *et al.*, 2016) is the potential for release of potentially toxic elements (PTEs) into the soil as silicate rocks dissolve. Figure 1.12 indicates high levels of chromium (Cr) and nickel (Ni) in peridotite, which could present risks to both plants and animals, given their known toxicities (Shanker *et al.*, 2005; Cempel and Nikel, 2006; Yu, 2008). In contrast, basalt contains comparatively low levels of these metals; when weighted according to their respective CDR potentials (Figure 1.12), basalt contains at least 4½ times less Cr and 7 times less Ni than peridotite per unit CO_2 sequestered. Moreover,

globally-average data suggest that basalt typically contains 8 times more P and 9 times more K than any of the peridotites examined in this review (Figure 1.13).

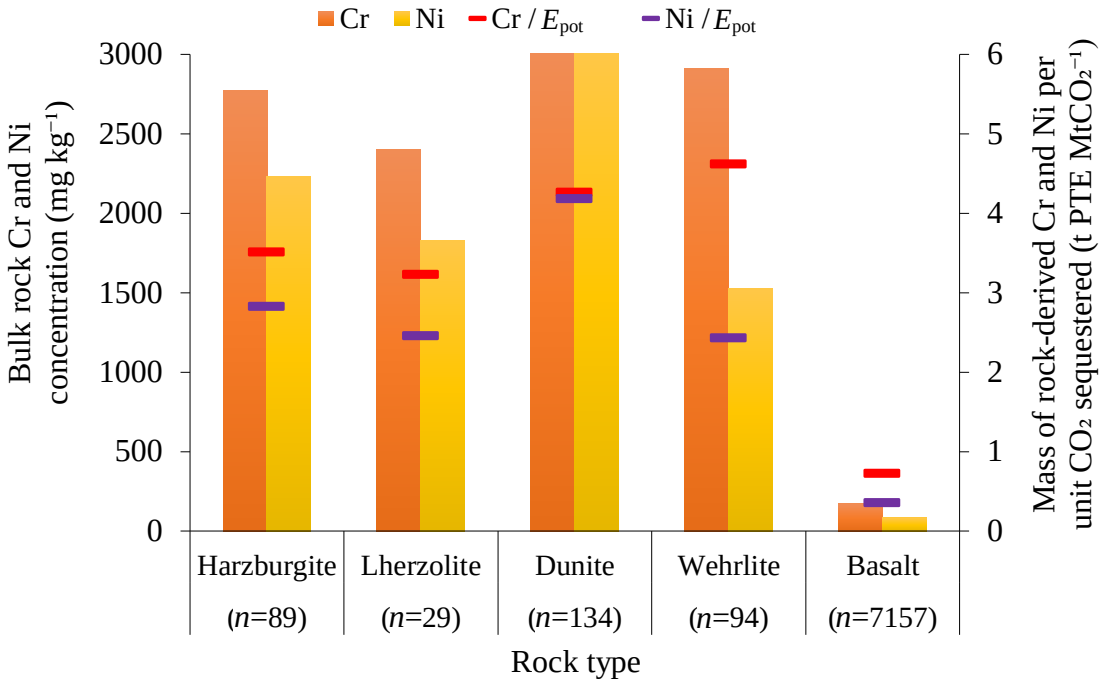

Figure 1.12 – Graph of Cr and Ni content for four peridotites and basalt. Raw data obtained from the Max Planck Institute for Chemistry (2015).

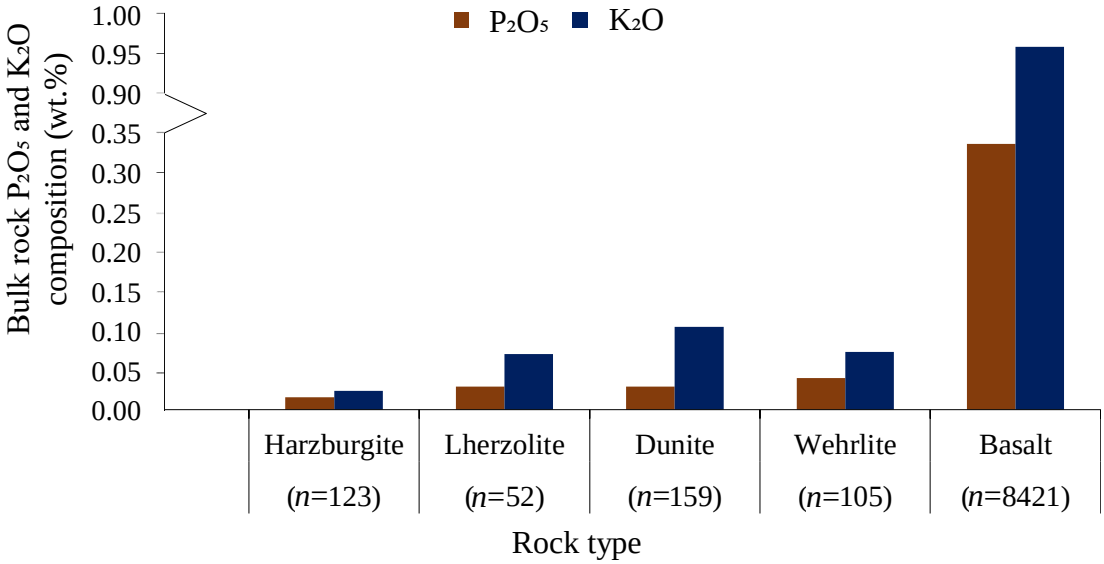

Figure 1.13 – Graph of P_2O_5 and K_2O composition for four peridotites and basalt. Raw data obtained from the Max Planck Institute for Chemistry (2015).

In light of these high levels of macronutrients and comparatively low levels of Cr and Ni, basalt may be a more-suitable source rock for ERW. Research is needed to further assess the risks associated with bulk soil additions of basalt and other silicate rocks.

1.3 Literature review summary

A critical evaluation of the literature highlighted ERW as a promising CDR strategy for near-term deployment. The fundamental science of rock weathering is well understood, and there are no known technological barriers to large-scale roll-out (Shepherd *et al*., 2009). In essence, the strategy would work by accelerating one of Earth's existing feedback mechanisms, and so does not make compulsory any significant scientific breakthrough or development of a novel synthetic carbon sink. There is also potential for repurposing significant global inventories of mining by-products, and perhaps even for modest reductions in agrochemical and lime usage, if yields can be bolstered by amending soils with basalt.

A major advantage for ERW over alternative CDR options – e.g. bioenergy with carbon capture and storage (BECCS), direct air capture (DAC) and biochar – is the C storage aspect of the strategy. Most CDR approaches demand active management of the captured C, either as a purified compressed gas (BECCS, DAC) or in solid form (e.g. standing stock, timber, pyrolysed materials etc.). For *these* strategies to generate globally-significant CDR, their respective CO_2 storage infrastructures would need to be comparable in scale to that of the global infrastructure producing CO_2 – that is, all of the world's tankers, drilling platforms, pipelines, powers stations, combustion engines, cement plants, land clearance projects *et cetera*. Even this does not do justice to the sheer magnitude of the engineering projects such strategies would have to complete to enact meaningful CDR in the 21st century. Add to that the obligation for protracted ongoing monitoring of storage locations (to ensure captured C is not leaking back into the air) and the true scale of the challenge is summarised. ERW neatly sidesteps this complexity, cost and risk by outsourcing responsibility to the oceans. And where deployed silicate minerals are weathered by carbonic acid, such that their constituent cations are demonstrated to have reached the surface ocean, zero-maintenance multi-million-year C storage is *practically* assured. The key challenge, then, is to evidence that such weathering has occurred, and this is very much the Achilles heel of ERW. Silicate weathering in nature is often an extremely slow process, sometimes resulting in very small changes in geochemistry that are difficult to measure over short timescales. Accurate methods are therefore needed to quantity the extent to which added silicate minerals have weathered in soils, and in this regard, there is scope for improvement.

1.3.1 Outstanding research questions

In this introductory chapter, a number of knowledge gaps were identified that could lead to future research. Notably, every parameter in the standard Arrhenius equation (Equation 1.5) may be scrutinised to quantify its relative influence on weathering rates.

Mineral SA is a key aspect of experimental control that mesocosm-scale studies can and should exploit. As only a few kilograms of rock are required for small-scale experiments, variation in the masses and PSDs of rock materials added to mesocosms can be minimised using high-precision balances and accurate sample subdivision techniques (e.g. spinning riffling), which are impractical for larger plot- and field-trials. Hence, this advantage should be levered to compensate for the loss of realism that inevitably occurs when soils are extracted from the field and brought into the laboratory. For ERW experiments, mineral reactive surface area (RSA) is the 'dose' variable, akin to the drug in a pharmaceutical trial, so careful handling of pulverised material is required to control variance in the RSA. The effect of particle size on weathering rates in the context of ERW is poorly understood, and thus offers an immediate opportunity for research. There will be energy, financial and environmental costs associated with engineering high-potency, high-RSA basalt powders for ERW (through grinding, milling or sieving), which implies that an optimum particle size could be empirically identified.

The effect of temperature on weathering is possibly less interesting with regards to controlled-environment studies, because only limited action can be taken to encourage higher soil temperatures in the field. As an aside, basalt's generally dark hue implies that it will absorb comparatively more incident solar energy than typical soils will, which could raise soil temperatures and initiate a variety of secondary effects – e.g. changes in soil respiration, pCO_2, soil-atmosphere GHG fluxes, as well as planting and harvest schedules. Where rock material is top-dressed, the albedo effect may be more important, but this has not yet been investigated in a controlled experiment.

The existing evidence for soil pH modification by ERW is somewhat more substantial, and indeed, goes some way to explaining the fertilisation effect observed in previous trials. However, the speed and magnitude with which crushed basalt can alter the pH of different soils is largely unknown. Where rock weathering proceeds *via* and acid-catalysed mechanism, mineral dissolution should occur faster in soils of lower pH; however, such soils may also contain higher concentrations of non-carbonic acids,

which frustrates the accurate estimation of CDR. Whether or not mineral weathering will be faster in acidic or alkaline soils of similar textural class is currently unknown.

Mineral saturation state is a potentially important parameter for ERW in agricultural soils, given that much of the world's agricultural land is rain-fed. Where water is limited, associated increases in mineral saturation states could retard further weathering of primary minerals and facilitate the precipitation of secondary mineral phases in the soil column. Moreover, the addition of certain soil additives (e.g. manure, compost, biochar etc.) should increase the cation exchange capacity (CEC) such that pore water saturation states are lowered, which may encourage accelerated dissolution of primary minerals. This latter concept is untested, but may represent a fruitful area of research, and could have direct implications for another touted advantage for ERW: the potential for co-deployment with other land-based CDR options. ERW is not expected to induce land-use conflicts with any of the key global agriculture sectors (food, fibre, fodder and fuel), and indeed, should be investigated for possible use in conjunction with soil-based strategies such as af-/re-forestation, biochar and BECCS.

The effect of mineralogy on weathering rates is also poorly understood, as prior ERW studies naturally selected ultramafic minerals for the speed of reaction, and thus largely overlooked the wide range of mafic rocks available. Recent work in this field (Lewis *et al*., 2021) has since elucidated much about the varying CDR and plant fertilisation potentials of different basalt mineral assemblages, but further research is required.

Other notable gaps in the literature include possible adverse environmental impacts of basalt weathering on managed soils and downstream watersheds, potential trace metal contamination of food products and soils, and possible inhalation risks related to airborne silicate particulates that are known to be hazardous to human health.

Lastly, previous weathering studies at the mesocosm-scale suggest the existence of a plant-mediated positive feedback on weathering, driven by belowground photosynthate allocation to mycorrhizal symbionts that can extract nutrients from primary minerals and, in turn, drive higher primary production (the 'carbon-energy flux' hypothesis; Quirk *et al*., 2014). A range of experiments could be conceived of to test this hypothesis in the context of ERW, perhaps, with different crops and inoculants, but perhaps with consideration of the background level of essential plant nutrients (N, P and K), which could affect the extent of mycorrhizal association. Under favourable conditions, this effect could effectively divert some of the 'free' energy from sunlight into mineral comminution at the grain-scale, and therefore warrants investigation.

1.4 Thesis aims and chapter outline

This thesis is set out in five chapters, starting with a general introduction that draws together the essential background science. Three consecutive experimental chapters are then presented, followed by a final chapter including discussion, reflection and concluding remarks.

Based on the research gaps identified in Section 1.3.1, this thesis aimed to investigate the following questions:

1. Can basalt weathering and CDR rates be determined empirically in a mesocosm-scale experiment with agricultural soil under crop cultivation?
2. Does ERW of basalt confer any co-benefits for crop performance – e.g. yield?
3. Does the addition of basalt modify key soil performance characteristics – e.g. soil pH and plant-available Si concentrations?
4. Does the amendment of soil with basalt result in the accumulation of PTEs in the effluent water, plant tissues or soils?
5. How are mineral weathering and CDR rates affected by co-deployment of basalt with other soil-based CDR approaches (e.g. biochar) or organic-rich fertiliser?

Synopses for each chapter are set out below, along with a brief supporting rationale:

Chapter 2 relates to the pilot experiment, which was designed (in late-2015) at a time when very few small-scale ERW experiments had been published, and fewer still related to CDR in agricultural soils. Notably, ten Berge *et al*. (2012) had shown that Mg released by olivine weathering was readily assimilated by ryegrass and – through competitive adsorption onto soil exchange surfaces – liberated plant-available K from the native soil. However, the experiment was not designed to produce effluent, and since the increase in effluent alkalinity export is both a key prediction and the *modus operandi* of ERW, it was reasoned that more could be done to better simulate field conditions. For this reason, greater inspiration was taken from Renforth *et al*.'s (2015) study, which took the format of a flow-through column experiment, where olivine was added to an intact soil core that was continually irrigated to encourage mineral weathering. Here, carbon capture in the leachate was inferred from measurements of cation fluxes, proving the concept of a mesocosm-scale ERW trial in which much of the complexity of the natural soil environment can be simulated. However, considerable

quantities of water were supplied to the columns to achieve this result, and no particular consideration was given towards the cultivation of a large cover crop, which might be expected to strongly influence soil hydrology and geochemistry. Hence, Renforth *et al*.'s (2015) approach was modified for this pilot experiment, and for both subsequent experiments in this thesis, through the use of highly-homogenised agricultural soils, intermittent irrigation regimes, and the inclusion of a cover crop (along with the necessary replication needed to account for the extra biological variation). The results from this experiment were published (Kelland *et al*., 2020), and the PHREEQC-based model developed from the primary data collected in this trial was subsequently used to probe research questions in other peer-reviewed publications (Lewis *et al.*, 2021; Vienne *et al.*, 2022).

Building on the pilot experiment, Chapter 3 covers the successor trial and showcases considerable advances in temporal and spatial resolution of weathering signals (e.g. pH, alkalinity and cation export), as well as basalt-related impacts on soil and plant characteristics. New technologies and advanced methods were developed, and CDR potential was estimated with greater certainty, under profoundly contrasting soil and nutrient conditions that are relevant both to developed and developing world agricultural practices. Direct measurements of effluent and pore water DIC and DOC are reported here as an experimental first, along with more precise measurements of soil moisture conditions. Doubtless due to its striking visual appearance, the experiment garnered the attention of the BBC's former science editor, David Shukman, and subsequently appeared in both national and regional TV news broadcasts in the weeks leading up to the 24th Conference of the Parties to the United Nations Framework Convention on Climate Change. Many of the marginal results from the pilot experiment achieved statistical significance in this later study, and this is testament to the overall reduction in experimental error achieved in the larger, two-factorial trial.

As the final soil and plant samples from the second *Sorghum* trial were being processed and preserved for analysis (March 2020), progress was arrested by the rapidly unfolding global pandemic caused by the novel coronavirus, SARS-CoV-2. This *significantly* delayed analysis of the solid-phase samples from that experiment, and set back plans to run a third trial investigating the effect of different soil types. After a 12-month research hiatus, a larger, more-ambitious three-factorial trial was underway; however, time was running short, and the project's scope was necessarily limited by these events.

Chapter 4 is therefore a mostly-complete analysis of data collected from the third experiment, which investigated the co-deployment of basalt with biochar in both acidic and alkaline sandy, grassland soils. Considerable variation in plant performance effects was measured between treatments, and the partial mass balance calculated with the available data indicate extreme differences in CDR potential of the different substrates.

In Chapter 5, the headline results from each experiment are combined in a meta-analysis, where evidence of trends within the datasets address each of the thesis's stated research aims. Space is dedicated for reflection on the scope and relevance of the research findings, as well as the likely limitations and imperfections within the various experimental designs. Finally, further improvements and possible future research avenues are suggested, and conclusions are draw on the overall utility of ERW with basalt, both as a low-tech CDR strategy and a low-cost, soil enhancer.

2

Increased yield and CO_2 sequestration potential with the C_4 cereal *Sorghum bicolor* cultivated in basaltic rock dust-amended agricultural soil

Contents

2.1 Introduction

Deployment of large-scale CDR strategies are required together with drastic phase-down of CO_2 emissions from fossil fuels to meet internationally agreed climate targets (UNEP, 2018). Research is therefore urgently required to determine efficacy, co-benefits, environmental risks, scalability and costs of such CDR strategies (NRC, 2015; EASAC, 2018; UNEP, 2018). ERW is a land-based CDR strategy addressing multiple UN Sustainable Development Goals (Smith *et al.*, 2019) which involves amending agricultural soils with crushed abundant silicate rocks (e.g. basalt) to accelerate carbon capture. Implemented on croplands it has potential to increase production, protect against pests and diseases and assist in restoring acidified nutrient-depleted soils (Hartmann *et al.*, 2013; Kantola *et al.*, 2017; Beerling *et al.*, 2018; Zhang *et al.*, 2018). The applied silicate minerals undergo reactions with CO_2 in the soil, releasing base cations (e.g., Ca^{2+}, Mg^{2+}) and alkalinity. Depending on soil chemistry, this can result in either the formation pedogenic carbonates or bicarbonate being delivered to the oceans *via* run-off; both routes store carbon with an estimated lifetime of tens of millennia (Hartmann *et al.*, 2013; Renforth and Henderson, 2017). Minimising adverse effects of ERW from mining, including associated impacts on biodiversity (Edwards *et al.*, 2017) is contingent on exploiting existing silicate rock waste streams, for example, from quarries and legacy reserves, and artificial silicates (Manning *et al.*, 2013; Beerling *et al.*, 2018; Das *et al.*, 2019). Undertaken at large scale, ERW is a CDR strategy that may have potential to support food and soil security and help avert ocean acidification (Köhler, Hartmann and Dieter A Wolf-Gladrow, 2010; Hartmann *et al.*, 2013; Taylor *et al.*, 2016).

Numerical modelling investigations (Köhler, Hartmann and Dieter A Wolf-Gladrow, 2010; Taylor *et al.*, 2016) have assessed the CDR potential of ERW largely in the context of tropical forests, but the focus is now turning towards croplands and soils on which deployment with existing land-spreading technology should be feasible (Kantola *et al.*, 2017; Beerling *et al.*, 2018; Strefler *et al.*, 2018). Experimental and field trial programmes are thus underway examining CO_2 removal rates and feedbacks on crop performance and soil health. Such trials have reported rates of CO_2 removal following amendment of different agricultural soils across a range of application rates with the fast-weathering Mg-silicate, olivine (ten Berge *et al.*, 2012; Renforth, Pogge von Strandmann and Henderson, 2015; Dietzen, Harrison and Michelsen-Correa, 2018;

Amann *et al.*, 2020). However, CO_2 removal by weathering of olivine-dominant dunite is often accompanied by increases in potentially toxic Ni and Cr concentrations that may be problematic for agricultural applications. Basalt rock is a proposed alternative silicate, containing at least six plant-essential nutrients – K, P, Ca, Mg, Fe and manganese (Mn) – and very low concentrations of Cr and Ni (Hartmann *et al.*, 2013; Kantola *et al.*, 2017; Beerling *et al.*, 2018). Although Si is regarded as a non-essential element for plants, cereals, the most important crops globally, accumulate Si in their straw and stover, with benefits for crop yield and resistance to abiotic and biotic stress (Guntzer, Keller and Meunier, 2012; Debona, Rodrigues and Datnoff, 2017). When crop residues are not returned to the land, this depletes the plant-available Si pools and can constrain yields (Haynes, 2017). Amending highly weathered soils of tropical agricultural regions with basalt increased yields of crops, and improved soil health (e.g. increased soil pH and CEC; (van Straaten, 2006; Hartmann *et al.*, 2013; Edwards *et al.*, 2017; Beerling *et al.*, 2018). Additionally, soils produced from basaltic quarry fines have inorganic carbon sequestration potential *via* in situ carbonate formation, especially when mixed with organic matter (Manning *et al.*, 2013). However, the amendment of soils with crushed basalt on crop production outside the tropics, possibly substituting in part for expensive rock-derived P- and K-fertilisers (Beerling *et al.*, 2018; Amann and Hartmann, 2019), and its CDR potential remain to be assessed.

This study investigated ERW carbon removal and co-benefits with the C_4 crop *Sorghum bicolor* grown at bench-scale in mildly acidic clay-loam agricultural soil amended with basaltic rock dust. *Sorghum* is one of the most widely cultivated cereal crops in the world and the fifth most important crop for food and animal feed, with the United States being the leading producer (Turhollow, Webb and Downing, 2010). It also provides a representative functional type similar to the C_4 crop maize suitable for cultivation at the mesocosm scale under controlled environment conditions. *Sorghum* and maize are often grown in slightly acidic clay-loam soils that are important agricultural soils of western Europe and the United States. Depending on fertiliser treatment *Sorghum* can form symbiotic associations with AMF (Hindumathi and Reddy, 2011) that are important biotic agents of mineral dissolution (Quirk *et al.*, 2012). This study's experimental approach, therefore, is a first step towards understanding the potential applicability of ERW with basalt in a temperate-zone agricultural context which will be important for understanding suitability for large-scale deployment of this CDR strategy (Beerling *et al.*, 2018; Zhang *et al.*, 2018; Haque *et al.*, 2019). Basaltic mineral

dissolution and carbon sequestration potential were assessed with elemental budgets (plants–soil–leachate pools). Over longer multiyear time horizons, dissolution trajectories and resulting CDR were assessed using a 1-dimensional (1-D) reactive transport soil profile geochemical model calibrated to the experimental results, measured basalt mineralogy and PSD.

2.1.1 Experimental design

This pilot experiment adopted a balanced one-factor design to enable straightforward statistical analysis *via* a one-way analysis of variance (ANOVA) approach. Replicates included in this study were planted with a single specimen of *Sorghum bicolor*, with six soil columns amended with crushed basalt and six left unamended as controls.

2.1.2 Hypotheses

Based on the previous research outlined in Section 2.1, it was anticipated that the amendment of a mildly-acidic UK agricultural soil with crushed basalt would result in increased CDR, improved crop yields and higher soil pH. Accordingly, the following hypotheses were formulated and tested in this study:

($H1_0$) *Sorghum* grown in basalt-amended soil will not produce higher seed yields, compared with plants grown in unamended (control) soil.
($H1_1$) *Sorghum* grown in basalt-amended soil will produce higher seed yields, compared with plants grown in unamended (control) soil.

($H2_0$) Soil pH will not increase following amendment with basalt.
($H2_1$) Soil pH will increase following amendment with basalt.

($H3_0$) The application of basalt to the soil will not result in increased CDR.
($H3_1$) The application of basalt to the soil will result in increased CDR.

2.2 Materials and methods

2.2.1 Weathering rector design

Experiments were conducted with replicated mesocosms housed within the Sir David Read Controlled Environment Facility at the University of Sheffield. Weathering reactors were constructed from two lengths of 160 mm external diameter (152 mm internal diameter) polyvinyl chloride pipe, coupled by a polyurethane-sealed joint, where a 600 mm long upper-section contained the soil and a 400 mm long base-section housed the leachate collection assembly (Figure 2.1a). A 20 mm diameter nylon nozzle was set into the bottom of the soil-containing upper-section, to direct leachate into a1 L amber glass Winchester bottle *via* a polytetrafluoroethylene funnel. A 50 mm deep drainage layer located at the base of the columns was used to prevent migration of soil particles into leachate nozzles, and comprised 5 mm diameter polyethylene beads placed on a high-density polyethylene screen (2 mm mesh size). Algal growth in the

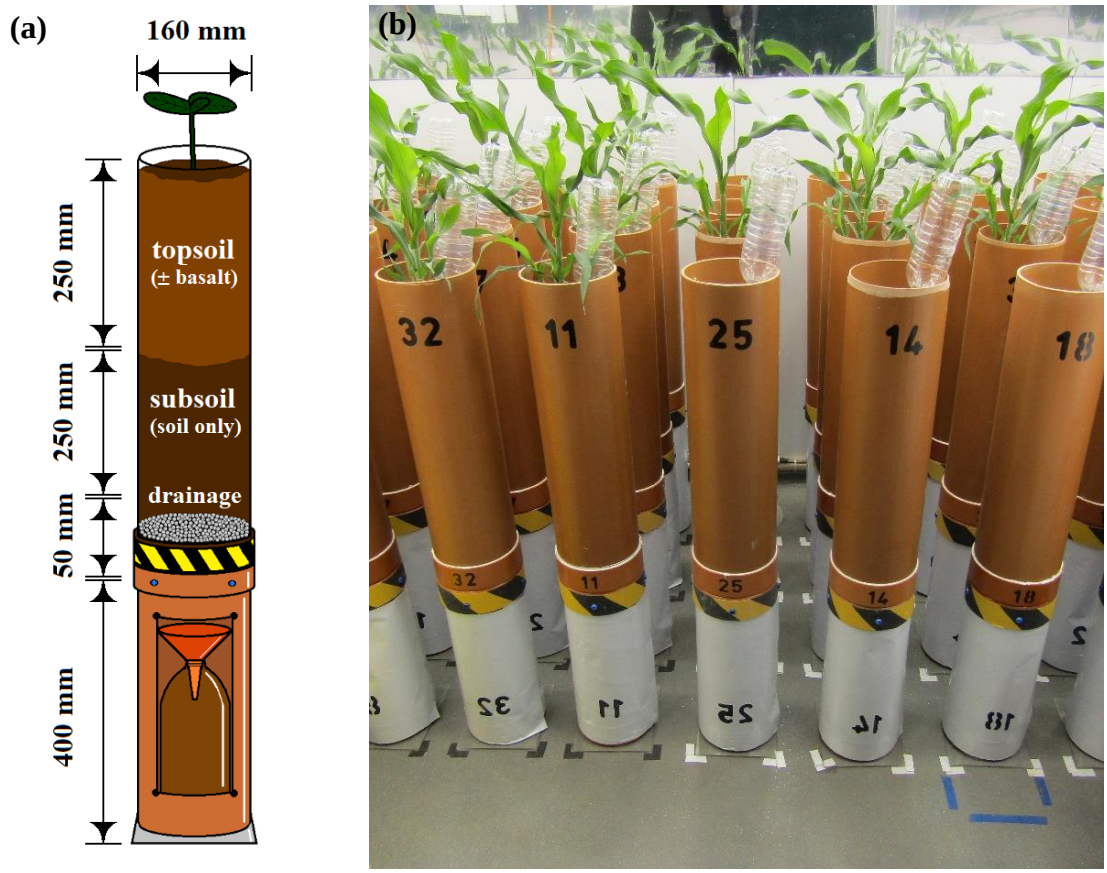

Figure 2.1 – Weathering reactors. (a) Schematic diagram of a reactor column and (b) photograph of assembled reactors with young *Sorghum* plants in the controlled environment growth chamber.

Winchester collection bottles was minimised by enclosing them in detachable opaque plastic membranes (Figure 2.1b). A 50 mm deep layer of polyethylene beads was placed on the surface of the soil columns to act as a physical barrier between the soil and air. This was implemented to maintain field-relevant soil moisture conditions by reducing evaporation and to minimise moss growth by shading the underlying soil.

2.2.2 Soil characterisation and preparation

Mildly acidic soil (pH = 6.6; measurement protocol in Section 2.2.5) with a clay-loam texture – 31.8%, 35.4% and 32.8% by mass of clay (<2 µm), silt (2–60 µm) and sand (60–2,000 µm), respectively – was collected from an agricultural field of *Brassica napus* (oil seed rape) at the Game and Wildlife Conservation Trust, Allerton Project, Leicestershire, United Kingdom (latitude 52.604328°N, longitude 0.825659°W). The initial soil had a CEC (determined by an ammonium acetate extraction; Section 2.2.5) was 25.4 cmol (p+) kg^{-1}, with >99% base saturation, and a low total organic carbon (TOC) content of 1.2% (wt%). Prior to filling the mesocosms, soil was processed by removing large stones (with diameters >20 mm) and invertebrates, and then passed through a rotary soil sieve (20 mm mesh size; model: CRS400, Clarke Power Products).

A sub- and topsoil arrangement was engineered in the upper-section of the weathering reactor to simulate a tillage regime (Figure 2.1a), composed of 4.3 and 5.0 kg of soil, and compacted to a bulk density of ≈1.05 and ≈1.2 kg L^{-1} respectively. The effective soil column depth was 500 mm. Well-characterised crushed basalt (see Section 2.2.6; total mass of 181.5 ± 0.5 g per column; equivalent to 10 kg m^{-2}) from a typical volcanic arc mountain in the Cascade Range (near Madras, Oregon, United States), was mixed with soil in the upper 250 mm of the treated columns (n = 6) to simulate plough layer mixing depth. This application rate, equivalent to 100 t ha^{-1}, is lower than that used in a recent modelling study (150 t ha^{-1} or 15 kg m^{-2}; Strefler *et al.*, 2018). Into this layer, commercial AMF inoculum was mixed (25 g per column) to promote establishment of symbiosis (PlantWorks UK Ltd).

Planted weathering reactors containing only soil and mycorrhizal inoculum (without the basalt amendment) were maintained as the control treatment (n = 6). Basalt-filled nylon mesh (35 µm diameter) bags (50 × 50 mm) were also buried in the top 250 mm depth of the basalt-amended soil columns (2 per column) filled with 3 g of sieved and washed basalt grains (50–150 µm size fraction). The mesh was chosen to exclude roots

but permit access to fungal hyphae from mycorrhiza. These bags were recovered at the end of the experiment to determine changes in surface chemistry and analysis of the microorganisms colonising the rock grains.

2.2.3 Plant materials

Dwarf hybrid *Sorghum bicolor* (Pennsylvania 115; Oakbank Game and Conservation) was cultivated in the weathering reactors. To minimise experimental variability, *Sorghum* seedlings were selected (based on total leaf length and developmental stage) from specimens grown in a controlled environment outside of the weathering reactors. Approximately 300 seeds were pregerminated on filter paper (Whatman #1), moistened with distilled water, placed in zip-lock plastic bags and incubated at 25°C in darkness for 24 hours. About 100 seeds with roughly equal radicle length (*ca.* 5 mm) were selected for planting in seed-trays containing the experimental soil, transferred to the growth room, and maintained at 60%–70% relative humidity, with an 18-hour day length at 25/17°C day/night temperatures. After 24 hours, 30 seedlings emerged from the soil, of which the 12 largest plants were grown for a further 14 days, before being randomly assigned for transplantation to weathering reactors in the growth room maintained under the same controlled environment conditions. Plants were grown under artificial light with a spectral intensity range of 400–700 nm and a photosynthetic photon flux density of 800 μmol photons m^{-2} s^{-1}, and for the first 60 days (from emergence to boot stage). *Sorghum* is a short-day plant, so to ensure that all specimens flowered at a similar time, the day length was set to 18 hours during the vegetative growth stage (days 0–60) and then shortened to 10 hours to induce the reproductive stage (days 61–harvest). Plants were harvested at physiological maturity, segregated into root, shoot and seed tissues, and dried in a forced-air oven at 60°C for 24 hours.

2.2.4 Irrigation regime and effluent collection

Reactors were irrigated on a 5-day rotation basis using reverse osmosis water delivered *via* a bespoke drip-feed irrigation system at 12.5 ml min^{-1} (Figure 2.2; total irrigation amount of 13.9 L over 120 days). The flow rate of each adjustable drip-feeder was calibrated gravimetrically. The amount of irrigation water added manually during the experiment was also measured gravimetrically. Urea was dissolved in irrigation water (total 0.71 g prilled urea per reactor during the 120-day experiment) and supplied periodically to each reactor with the total addition rate representative of high yielding

croplands worldwide (Potter *et al.*, 2010). No P- or K-fertiliser was added during the experiment to incentivise mycorrhizal association and colonisation of the added basalt, which contained P- and K-bearing minerals. Irrigation water supply was adjusted to produce about 150 ml of leachate in about 24 hours after each irrigation event (Figure 2.2). Mean infiltration rate during the experiment was 2.1 mm day^{-1}. A 5% subsample of collected leachate was filtered through a Minisart 0.22 μm cellulose nitrate filter (Sartorius UK Ltd), and refrigerated at 4°C prior to chemical analyses.

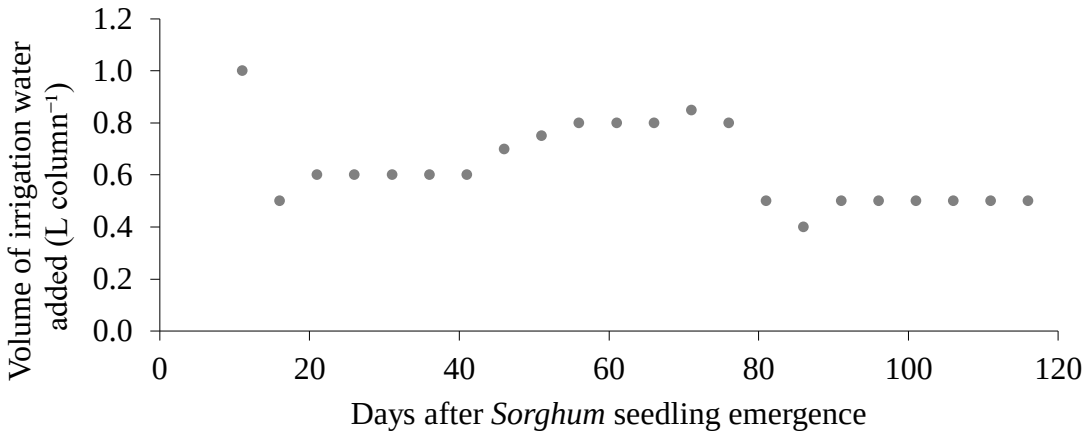

Figure 2.2 – *Sorghum* irrigation regime. Plants with and without basalt amendment to soils were irrigated with the same quantity of water, according to the above 5-day irrigation schedule.

2.2.5 Leachate, soil, plant and rock analysis

Leachate and soil pH were measured with a Jenway 3540 Bench Combined Conductivity/pH Meter (Jenway, Stone, UK). Measurements were standardised using a 3-point calibration on the hydrogen ion molar activity scale (pH = −log{H+}) using standard solutions at pH 4.00, 7.00 and 14.00. Leachate pH was measured from a 30 ml aliquot taken immediately after collection. For soil pH measurements, 15 g of air-dried soil was weighed into a 100 ml glass beaker and gradually mixed with 30 ml of deionised water (1:2 mass ratio of soil:water) using a glass stirrer, for 3 min. The solution was left to equilibrate with the atmosphere for 30 min before recording the measured pH of the slurry to 0.01 pH units. Dissolved cation concentrations in the leachate were quantified by Inductively Coupled Plasma Atomic Emission Spectrometry (ICP-AES; Spectro-Ciros-Vision, Spectro Analytical Instruments GmbH; detection limit for Mg/Ca/Sr = 0.001 mg L^{-1}; calibrated with multi-element

standards from certified stock solutions). Soil exchangeable cations were isolated by leaching soil with 1 M ammonium acetate ($NH_4CH_3CO_2$; pH 7; Chapman, 1965), and subsequent elemental analysis of the extracts was conducted by ICP-AES. Soil and basalt total inorganic carbon (TIC) and TOC measurements were made using a CN analyser (Vario EL Cube; Elementar) on samples before and after treatment with 6 M HCl; soil: acid ratio of 90 mg to 0.5 ml (n = 6 homogenised samples per depth at four depths, 12.5, 25, 37.5 and 50 cm).

Sorghum root, shoot and seed masses were powdered separately using a grinding mill (Model: A10 S2; IKA-Werke GmbH & CO. KG). Cation concentrations were determined by digesting plant materials in 6 ml nitric acid and 2 ml perchloric acid mixture on a hot block (200°C) for 20 min and analysing the extracts by ICP-AES. Silicon concentrations in plant materials were measured following standard protocols (Reidinger, Ramsey and Hartley, 2012) on pelletised powdered samples by X-ray fluorescence spectroscopy (XRF; Spectros Niton XL3t900 GOLDD; Thermo Scientific) calibrated using Si-spiked synthetic methyl cellulose, and validated using Certified Reference Material NCS DC73349 ‘Bush branches and leaves’ from the China National Analysis Center for Iron and Steel.

Basalt grains recovered from nylon bags were split into subsamples with one subjected to XRF spectroscopy measurements (Model: Zetium; Malvern Panalytical Ltd) to determine changes in surface chemical element composition and the others used for deoxyribonucleic acid (DNA) extraction and subsequent molecular analysis to characterise the identity of microorganisms colonising particles. Fungal colonisation was examined by imaging the grains under a scanning electron microscope (SEM; Model: VEGA3, TESCAN) at the Biomedical Sciences Electron Microscope Unit, University of Sheffield. Images were acquired using a secondary electron detector at an accelerating voltage of 20 kV under high vacuum conditions ($<1 \times 10^{-4}$ Torr).

DNA was extracted from basalt in the mesh bags using a DNeasy PowerSoil Kit (Qiagen Ltd). Amplification of partial 5.8S, ITS2 and partial 28S fungal sequences was performed by PCR with MyTaq™ Polymerase (Bioline) and primers gITS7 (Ihrmark *et al.*, 2012) and ITS4 (White *et al.*, 1990), modified to include the Illumina overhang adapter sequences (Pétriacq *et al.*, 2017). Triplicate PCRs were carried out on 1 µl of template DNA extract in the presence of the manufacturer's buffer (including dNTPs)

and 0.4 µM of each primer in 20 µl reactions (PCR conditions: 94°C for 2 min; 35 cycles at 94°C for 30 s, 53°C for 30 s and 72°C for 30 s; and 72°C for 1 min). Products of the three PCR reactions were then pooled per sample and purified using AMPure XP beads (Beckman Coulter Inc., USA). Dual indexes were added using the Nextera XT Index Kit (Illumina Inc. UK) following the manufacturer's instructions. Amplicons were then purified again using AMPure XP beads, quantified and pooled. Sequencing was performed using 250 bp sequencing on a MiSeq sequencer (Illumina Inc., at The Earlham Institute, Norwich, UK).

De-multiplexed FastQ files were filtered using USEARCH 9.1 (Edgar, 2010) with a maxEE value of 1. Only forward reads were analysed due to length variability in the ITS2 region producing potential biases for paired data. Primer sequences were removed and UCHIME was used to detect chimeras (Edgar *et al.*, 2011). Comparisons were made to the QIIME/UNITE reference ITS database (Nilsson *et al.*, 2019) and sequences were clustered at 97% using QIIME (Caporaso *et al.*, 2010). Singletons were removed from the data as these are often sequencing errors (Majaneva *et al.*, 2015). Sequences have been deposited in the European Nucleotide Archive under accession number PRJEB28082.

2.2.6 Basaltic rock characterisation

Pulverised basalt was sourced from the Cascade Mountain Range, Oregon (Central Oregon Basalt Products LLC). The rock is middle Miocene in age and belongs to the 'Prineville Chemical Type Unit' of the Columbia River Basalt (Smith and Hayman, 1987); with a chemical index of alteration of 38%, as calculated from the oxide data (Table B.1; Nesbitt and Young, 1982), it is considered relatively unaltered. The mineralogy of the Oregon basalt (Table B.2) was determined using X-ray diffraction (XRD) analysis at the British Geological Survey (BGS) Keyworth laboratories. Samples were spiked by 10% (wt%) with corundum (Al_2O_3) to aid quantitative analysis and spray-dried from an ethanol (C_2H_6O) suspension at 80°C to ensure random orientation of mineral phases.

XRD data were collected using a PANalytical X'Pert-pro diffractometer (Malvern Panalytical Ltd) using CoKα radiation (λ = 1.78896 Å) from 4.5–85° 2θ run at 45 kV and 40 mA conditions. Crystalline mineral phases were identified using PANalytical HighScore Plus software coupled to the International Centre for Diffraction Data

(ICDD) PDF-4+database. Crystalline mineral and amorphous material quantification was completed using the Rietveld refinement technique within the same HighScore Plus software package and using crystallographic information from the Inorganic Crystal Structure Database (Hellenbrandt, 2004) following the methodology in (Kemp *et al.*, 2016).

XRD indicated that the Central Oregon basalt contained a high percentage of amorphous material interpreted to be basaltic glass (≈25%; Tables B.2 and B.3). The elemental composition of the basaltic glass was determined with scanning electron microscopy-energy dispersive X-ray spectroscopy (SEM-EDX) to better constrain the reactive transport model (RTM) calculations (Figures B.1–3). Samples were C coated to approximately 25 nm thickness in an Agar AGB7367A automatic SEM C evaporation coater. Analysis was performed using a FEI QUANTA 600 SEM, operating at an accelerating voltage of 20 kV, spot size 5 and under high vacuum conditions (<1 × 10^{-4} Torr) also at the BGS laboratories. Energy dispersive X-ray analysis (EDX) was conducted using Oxford Instruments X-MAX large area (50 mm^2) silicon drift detector, running with Oxford Instruments INCA (v4) software. The EDX system was used to identify the point-elemental compositions from samples and is capable of detecting elements from atomic number 4 (B) to atomic number 92 (U) with a detection limit of the order of 0.2–0.5 weight % for most elements. Areas of the amorphous glassy phase were identified from backscattered electron images and relevant spectra and concentration determined from point analyses.

Bulk pulverised basalt was split into representative samples using a spinning riffler (Microscal Ltd), and the particle size distribution (Figures B.4 and B.5a) was established using a laser diffraction particle size distribution analyser (Model: LA-950; Horiba UK Ltd). The P_{80} value (80% of the particles have a diameter less than or equal) of the soil-applied pulverised basalt was ≈1,250 µm (Figure B.4c).

Specific surface area measurements were made using the Brunauer–Emmett–Teller (BET) N_2-adsorption (Brunauer, Emmett and Teller, 1938) method using a Micromeritics Gemini VII 2390a instrument (Micromeritics Instrument Corporation; Figure B.5b; Table B.4).

2.2.7 Sr isotope analyses

Radiogenic Sr isotope ($^{87}Sr/^{86}Sr$) analyses were conducted in clean laboratory facilities at the University of Southampton. Leachate samples analysed for radiogenic Sr isotopes were acidified to pH < 2 using concentrated HNO_3. *Sorghum* shoot samples for radiogenic Sr isotope measurements were digested with 5 ml of concentrated nitric acid in a microwave digestion system, dried, reacted with 30% hydrogen peroxide (H_2O_2) to ensure complete oxidisation of organic compounds, dried, redissolved in 3% HNO_3, and finally passed through 0.45 µm polypropylene syringe filters (Whatman Puradisc). To isolate exchangeable soil cations for radiogenic Sr isotope measurements, 1.0 g soil subsamples were reacted with 1 M NH_4Cl (adjusted to pH = 8) for 24 hours and then centrifuged. The supernatants were passed through 0.45 µm polypropylene syringe filters (Whatman Puradisc), dried and redissolved in 3% HNO_3. A 10 g subsample of the basalt rock was powdered in a ring and puck mill. The carbonate and silicate fractions of the powdered rock were isolated using a sequential leaching and digestion procedure. To isolate the carbonate fraction, subsamples of the powder (≈1.0 g) were reacted with 4 M acetic acid (CH_3COOH) for 24 hours. The mixtures were centrifuged, and the supernatants were passed through 0.45 µm polypropylene syringe filters (Whatman Puradisc) and collected in Teflon beakers. Filtered supernatants were dried and redissolved in 3% HNO_3. The remaining residues, assumed to represent the silicate fraction, were oven dried, and 0.1 g subsamples were reacted in a 5:3 mixture of concentrated hydrofluoric acid (HF) and HNO_3 at 140°C, dried, refluxed in concentrated HNO_3, dried, refluxed in 6 N HCl, dried and finally, redissolved in 3% HNO_3. Sr concentrations of all samples (water, plant, soil and rock) were measured on a Thermo-Fisher iCAP 6500 Inductively Coupled Optical Emission Spectrometer (ICP-OES) at the National Oceanography Centre Southampton. Sr measurements were within ±5% of reported values for standards analysed throughout the analyses.

Radiogenic Sr isotope measurements were conducted using a Thermo-Scientific Triton Thermal Ionization Mass Spectrometer (TIMS) following methods presented in Andrews *et al*. (2016). Briefly, sample aliquots containing 200 ng of Sr were dried, redissolved in 8 M HNO_3, and eluted through inverted pipette tips packed with Sr-Spec resin. The purified Sr fractions were dried, redissolved in 2 µl of 8 N HNO_3, and loaded onto single, outgassed rhenium (Re) filaments with 1 µl of a tantalum chloride ($TaCl_5$) solution. Ion beams were collected in multidynamic mode. To correct for instrumental

mass fractionation, the $^{86}Sr/^{88}Sr$ ratio was normalised to 0.1194 using an exponential law. During analysis of $^{87}Sr/^{86}Sr$ ratios, the rubidium-85 (^{85}Rb) ion beam was monitored to ensure that ^{85}Rb did not isobarically interfere with ^{87}Sr. No interferences were observed. For the period of study, repeated analyses of NBS 987 standard yielded a mean $^{87}Sr/^{86}Sr$ ratio of 0.710250 ± 0.000008 (±2σSD, n = 6). The current long-term, mean $^{87}Sr/^{86}Sr$ ratio is 0.710251 ± 0.000010 (±2σSD, n = 32).

For treatment samples, a two-component isotope mixing equation was used to determine the mole fraction of Sr in cation reservoirs derived from basalt weathering (f_x), as opposed to soil weathering:

$$f_x = \frac{\delta_x - \delta_{soil}}{\delta_{basalt} - \delta_{soil}} \quad \textbf{Equation 2.1}$$

where δ denotes the $^{87}Sr/^{86}Sr$ ratio of the treatment cation reservoir (x = plant, exchangeable soil, or leachate), the corresponding control cation reservoir ('soil') and the basalt silicate digest or basalt carbonate leachate ('basalt').

2.2.8 Reactive transport model

Column reactors were conceptualised as a 250 mm deep soil column constituting five 50 mm deep cells, and a 50 mm deep well-mixed fluid reservoir in contact with the atmosphere at the base of the column. The RTM was constructed with the PHREEQC platform (Parkhurst and Appelo, 2013) using the T&H.dat geochemical reaction database (Appelo and Postma, 2005), which includes surface complexation constants for particulate organic matter based on the WHAM model (Tipping and Hurley, 1992; Tipping, 1998). Speciation of oxidised and reduced forms of nitrogen was explicitly decoupled to allow for irreversible kinetic transformations of excess urea fertiliser to nitrate, as observed empirically. Flow of irrigation water through the column was simulated by a time series of irrigation events at the top of the soil that resulted in 1-D vertical flow of pore solution and advection of solutes through the layers producing the overall mass of leachate from the columns (4.58 L in 120 days). The model incorporated chemical dissolution of source minerals having the measured stoichiometries of basaltic mineral phases, and their relative mass concentrations, as identified by the XRD results (Table B.2). Reactive surface area for each mineral was apportioned according to the mineral weight percent of the basalt grains.

Chemical dissolution rate laws and coefficients for basaltic glass were sourced from (Flaathen, Gislason and Oelkers, 2010) and those for other minerals from the US Geological Survey (Palandri and Kharaka, 2004). Solubility constants of the basaltic minerals were taken from the THERMODDEM database (Blanc *et al.*, 2012) and for the basaltic glass from (Aradóttir, Sonnenthal and Jónsson, 2012). Changes in reacting particle sizes due to element mass transfer to solution during dissolution were simulated using the shrinking particle model (Rimstidt, 2014). Background weathering of soil minerals was represented by a porewater solution chemically identical to leachate from the basalt-free systems. Figures C.1 and C.2 provide schematic and systems diagrams defining the processes and interactions of the RTM.

Modelled geochemical processes included equilibrium of dissolved inorganic carbon species with atmospheric CO_2, and a profile of partial pressures of CO_2 in the soil profile representing autotrophic and heterotrophic respiration (Nan *et al.*, 2016). Apparent reactive surface area (RSA) and CEC were optimised within MATLAB (version 2019a; The MathWorks, Inc.) using the 'fmincon' function. Separate optimisations were performed on individual treated columns with several candidate sinks for Al and Fe (amorphous $Al(OH)_3$ and $Fe(OH)_3$, gibbsite, kaolinite, and goethite). Based on the smallest root-mean-square errors between model and observed leachate Al (Figures C.3 and C.4) and 18 leachate and extractable elements (Figures C.5 and C.6), the solid equilibrium phases are determined to be amorphous $Al(OH)_3$ and $Fe(OH)_3$, along with calcite, amorphous silica and pyrophyllite (MnO_2). These phases react reversibly on the relatively short residence times of the soil fluids. Apparent CEC was optimised because measured CEC will include the charge separately represented by the WHAM model, and because the single extraction method used could have resulted in dissolution of existing phases, such as calcite. These optimisations suggest less than 10 cmolc kg^{-1} soil of the total observed charge is unaccounted for in the model (Figure C.7).

Cation exchange on clay surfaces was modelled using PHREEQC's default exchange convention. Exchange site composition was initially determined by equilibration with the measured ionic composition of soil pore waters in the basalt-free control experiments with optimised CEC. The total number of sorption sites attributable to OM was derived from the concentration of extractable OM, as measured experimentally. Following the protocol described in Example 19 of the PHREEQC documentation (Parkhurst and Appelo, 2013), these sites were apportioned to the 20 WHAM surface species using WHAM constant charges of −1.42 meq g^{-1} humic acid for four

monoprotic phenolic sites, −2.84 meq g^{-1} humic acid for all diprotic or carboxylic sites and total charge −7.1 meq g^{-1} humic acid. CO_2 capture was calculated as the sum of $HCO^{-3}_{(aq)}$ exported in the leachate plus CO_2 incorporated into pedogenic carbonate minerals minus half of the $HCO^{-3}_{(aq)}$ originating from weathering of the carbonate mineral component of the basalt (Table B.2).

In the model, growth of *Sorghum* influences the geochemistry of the system by removing Ca, Mg and Si from the soil with concomitant release of hydrogen ions to the soil. Using an average leachate chemistry from the control columns as the influent, implicitly accounts for both dissolution of existing soil minerals and 'background' plant growth unrelated to the treatment. *Sorghum* growth due to the treatment is therefore the difference between growth in the individual treated column and the average growth in control columns. *Sorghum* growth was modelled as a linear function which removed ions at a constant rate up to the maximum plant growth at 120 days, when harvesting of the plant was simulated by switching off the growth function for the rest of the annual cycle. In the 5-year modelling scenarios, a new growth cycle was modelled, as described above, for the first 120 days of each year, followed by a fallow period until the beginning of the next year.

2.3 Results and discussion

2.3.1 *Sorghum* yield response

After 120 days, yield of mature *Sorghum*, measured as seed dry mass per plant, increased significantly by 21 ± 9.4% (*SE*) in response to the basalt treatment compared to control plants ($p < 0.05$, one-way ANOVA) with no significant changes in shoot or root biomass (Figure 2.3). This evidence for increased seed yield following basalt application supports rejection of the respective null hypothesis (*H*1: 0) in favour of the alternative (*H*1: 1). Yield improvements occurred without significantly ($p > 0.05$) increased seed concentrations of potentially toxic trace elements from basalt (Figure 2.4). The yield increase in *Sorghum* occurred without addition of P and K fertiliser and is comparable to that reported for the C_4 crop sugarcane in field trials with crushed basalt applications of 1–10 kg m^{-2}, in combination with standard NPK fertiliser treatments, on the highly weathered soils of Mauritius (D'Hotman and de Villiers, 1961). Over five successive harvests in that study, sugarcane yields increased by up to 30% compared with plots receiving fertiliser and no basalt addition (D'Hotman and de Villiers, 1961).

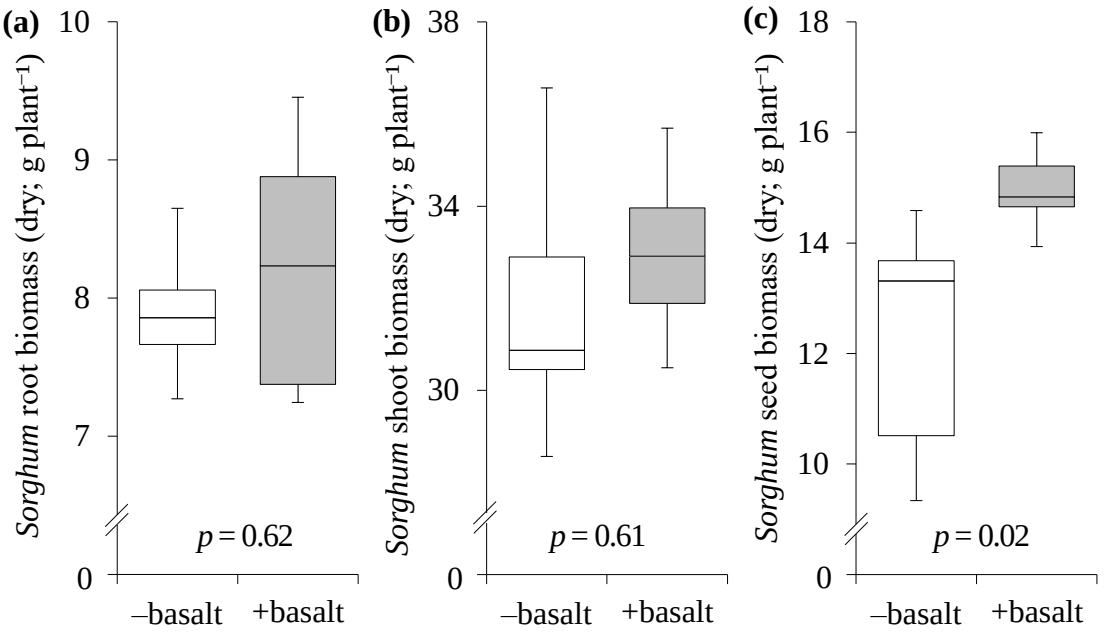

Figure 2.3 – Effect of basalt-amended soil on *Sorghum* biomass. (a) root, (b) shoot, and (c) seed dry mass. Stated *p* values were determined in R *via* a one-way ANOVA. $n = 6$.

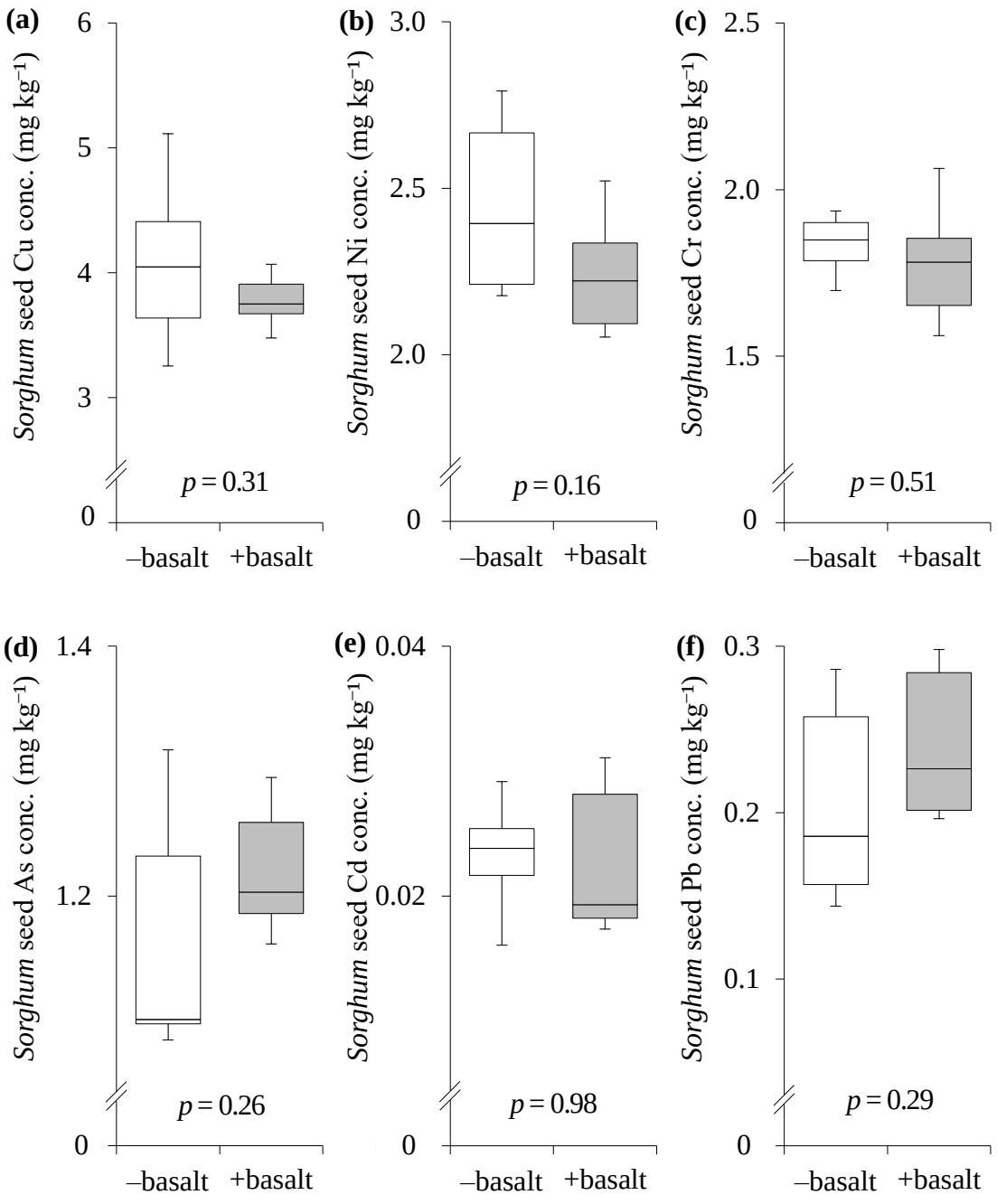

Figure 2.4 – Potentially toxic trace elements in *Sorghum* seeds. (a) copper, (b) nickel, (c) chromium, (d) arsenic, (e) cadmium, and (f) lead. Stated *p* values were determined in R *via* a one-way ANOVA. $n = 6$.

2.3.2 Elemental budgets of *Sorghum* plants

Whole plant elemental budgets showed significant increases in Si ($p < 0.05$; Figure 2.5a), Ca and Sr pools ($p < 0.01$; Figures 2.5b and 2.5f), with overall Mg, K and P budgets remaining unchanged, but seed K increasing significantly ($p < 0.05$; Figure 2.5c). Crushed basalt was the only supplemental source of Si, Ca, K and Sr, and uptake and accumulation of these elements in *Sorghum* shoots, allied to soil pH increases (see below), indicates mass transfer from the source rock on the experimental timescale. Increased shoot Si can enhance the resilience of plants to abiotic stresses, including drought, salinity, heat (Burghelea *et al.*, 2015; Korchagin, Caner and Bortoluzzi, 2019) and resistance to lodging due to wind or rain (Artyszak, 2018) as well as to biotic attack (van Bockhaven, de Vleesschauwer and Höfte, 2013; Meharg and Meharg, 2015). Shoot Si increases following soil silicate treatments, for example, provided direct protection from pests and diseases for major C_3 (soybean, wheat and rice) and C_4 crops (sugarcane and maize) and indirect protection *via* changes in the release of herbivore-induced plant volatiles enhancing parasitoid attraction (Liu *et al.*, 2017).

Significantly increased total shoot Si mass (26 ± 5.4%, *SE*) following basalt treatment in this study mirrors increased concentrations of Si in rye grass biomass following addition of olivine (Si, 50–180% increase) (ten Berge *et al.*, 2012). However, in those experiments (ten Berge *et al.*, 2012), olivine significantly increased Mg and reduced plant Ca uptake by 7–58% compared to results with basalt in this study: increases of 11 ± 3.1% (*SE*) in Ca and 11 ± 2.5% (*SE*) in its geochemically similar tracer Sr, but no change in plant Mg uptake (Figures 2.5b, 2.5e and 2.5f).

2.3.3 Leachate and soil biogeochemistry

Significantly increased leachate pH (Figure 2.6a) is consistent with basalt weathering; calcium–silicate mineral dissolution consumes hydrogen ions and produces alkalinity. Similar pH increases followed basalt amendment of acidic weathered tropical soils and reduced Al toxicity, a factor limiting plant growth on acidic soils (Gillman, 1980; Anda, Shamshuddin and Fauziah, 2013, 2015). Mitigation of soil acidification by basaltic rock dust weathering indicates its potential to substitute for the practice of liming. This could avert CO_2 emissions during production and application of lime to soils; in the United States alone this has been estimated to contribute 2% of agricultural GHG emissions

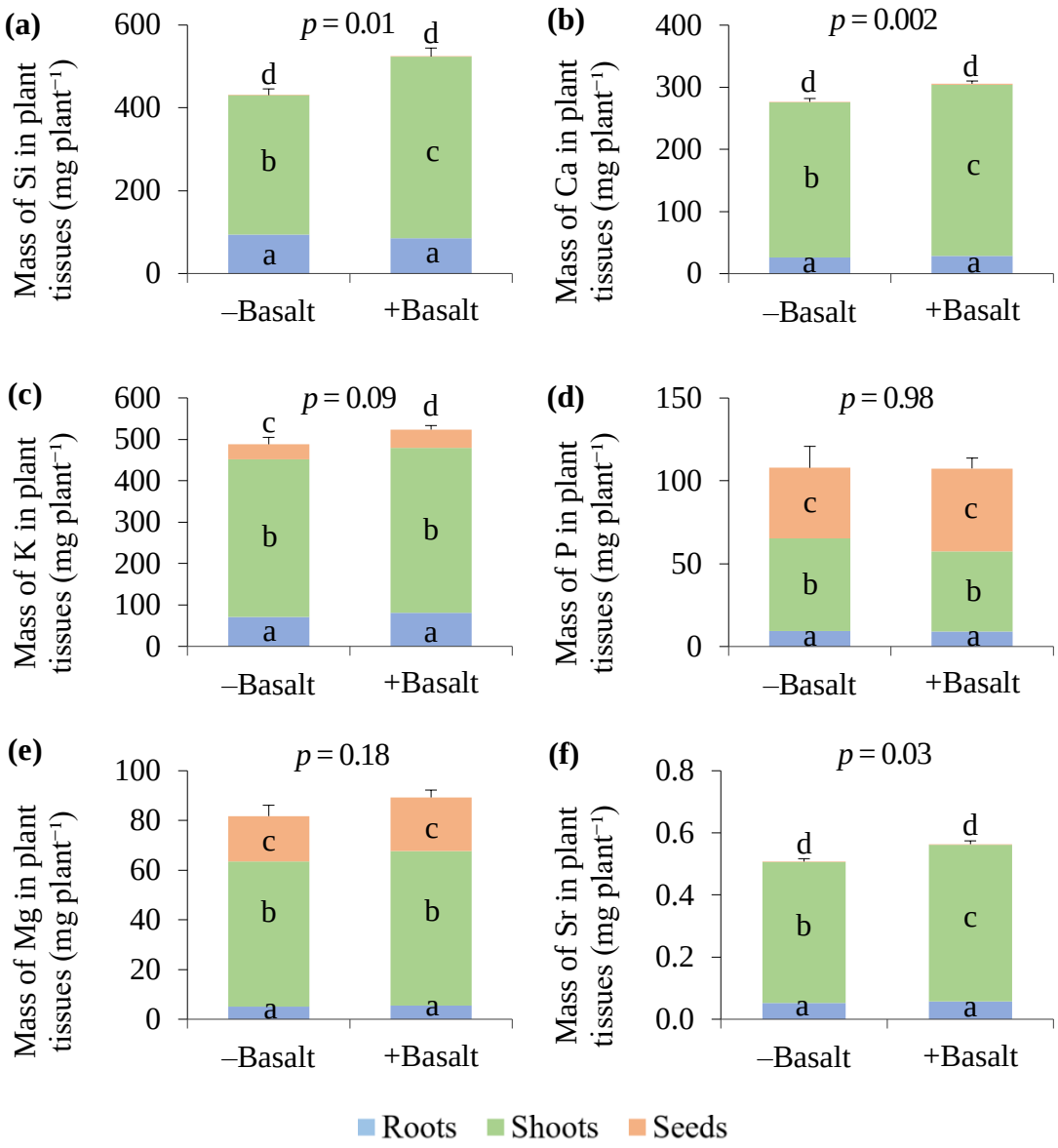

Figure 2.5 – Effect of basalt-amended soil on total *Sorghum* tissue elemental budgets in Chapter 2. (a) silicon, (b) calcium, (c) potassium, (d) phosphorus, (e) magnesium and (f) strontium. Error bars represent *SE* in the mean for total analyte mass. Bars sharing the same letter are not statistically different ($p > 0.05$). Stated p values relate to total analyte mass and were determined in R *via* a one-way ANOVA. $n = 6$.

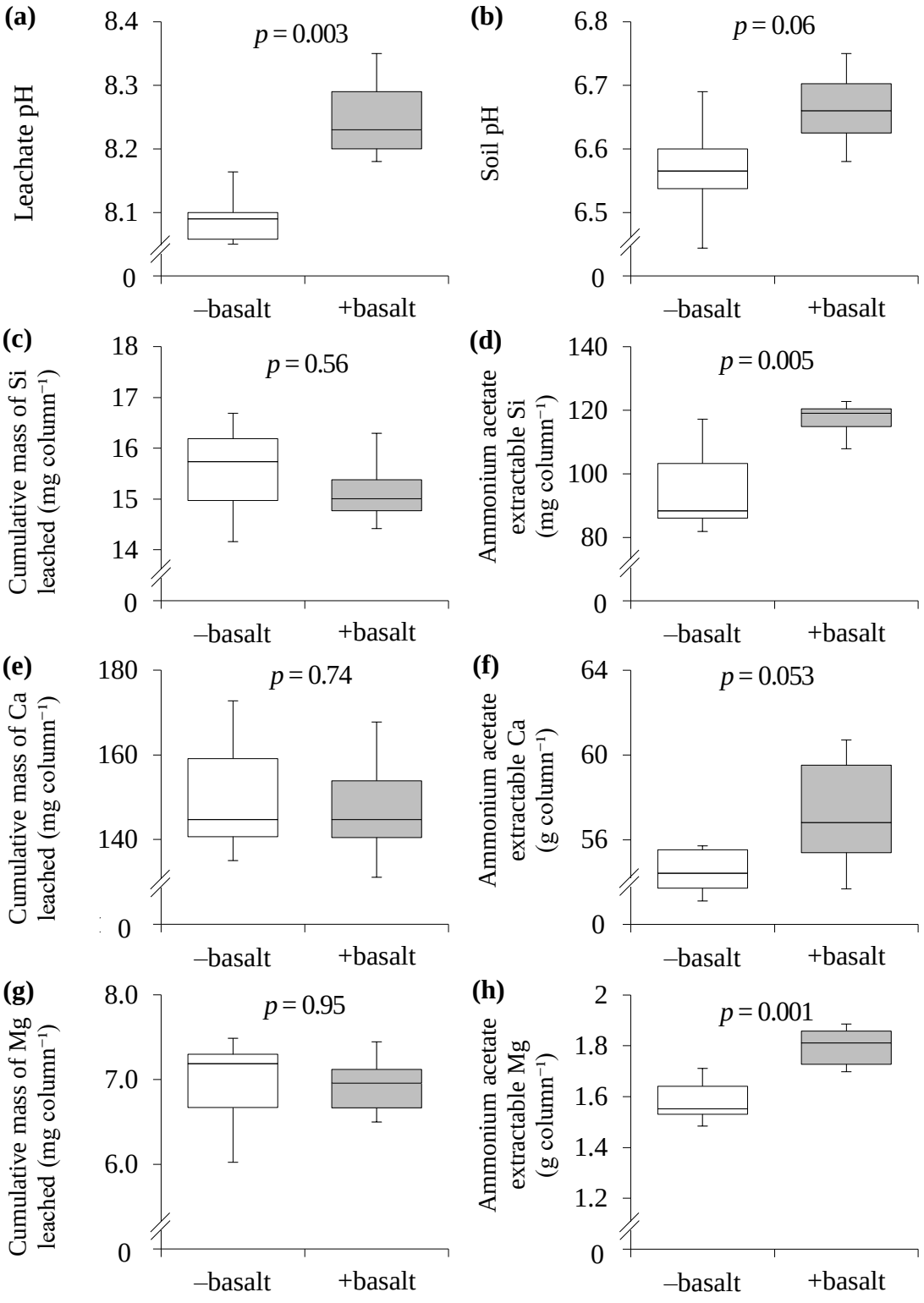

Figure 2.6 – Effect of basalt-amended soil on leachate and soil chemistry. (a) leachate pH, (b) soil pH, (c) leachate silica, (d) soil exchangeable silica, (e) leachate calcium, (f) soil exchangeable calcium, (g) leachate magnesium, and (h) soil exchangeable magnesium. Stated *p* values were determined in R *via* a one-way ANOVA. $n = 6$.

(West and McBride, 2005). For comparison, application of 20.4 kg m^{-2} of olivine to an acidic sandy soil increased the pH from 4.8 to 6.0 after 224 days, but also increased the uptake of Ni originating from the olivine in ryegrass (ten Berge *et al.*, 2012). The marginal (not statistically significant) increase in soil pH observed in this study (Figure 2.6b) offers insufficient support for rejection of the respective null hypothesis (*H*2: 0).

Ammonium acetate extractable soil Si, and the exchangeable pool of soil Mg increased significantly ($p < 0.01$, one-way ANOVA; Figures 2.6d, and 2.6h) in response to the basalt treatment, although there was no significant effect on exchangeable Ca (Figure 2.6f). Marked increases in soil exchangeable pools of Mg (200%–700%) occurred in planted olivine mesocosm weathering trials (ten Berge *et al.*, 2012; Amann *et al.*, 2020). Replenishment of depleted soluble Si pools by basalt weathering as seen in the present work represents a substantial co-benefit of ERW because repeated biomass harvesting of silica accumulating crops by intensive cultivation depletes plant-available Si in soils (Haynes, 2017). Crop production and harvesting in the United States, for example, removes an estimated 19 million tonnes of silica annually and negatively affects yields, especially of sugarcane and rice (Tubana, Babu and Datnoff, 2016). Adoption of Si-fertilisation practices, such as dressing soils with natural and artificial silicates to maintain crop yields, could help redress the problem in Europe, North America (Crooks and Prentice, 2017; Artyszak, 2018) and the tropics (Ma, 2004; Ma and Yamaji, 2006; Meena *et al.*, 2014). In east Asia, this approach has been practiced for the past decade to improve crop production (Cuong *et al.*, 2017; Li *et al.*, 2018).

No significant changes in leachate Si, Mg or Ca were detected following the basalt treatment, after 120 days (Figures 2.6c, 2.6e and 2.6g), suggesting elements released by weathering were retained in the plant–soil system in this study. Lack of leachate chemistry response has also been observed following a very high olivine application (220 t ha^{-1}) to loamy soils (pH = 7.8) supporting the growth of wheat and barley (Amann *et al.*, 2020). Moreover, no statistically significant difference ($p > 0.05$) in alkalinity between treatments was determined *via* a charge balance calculation (1,148 ± 245 μeq L^{-1}; 1 *SD*, $n = 6$, without basalt vs. 1,100 ± 147 μeq L^{-1}; 1 *SD*, $n = 6$, with basalt); these values are within the range of agricultural sites (350–3,800 μeq L^{-1}) (Fortner *et al.*, 2012).

2.3.4 Element release from basalt weathering

Comparison of the total measured amount of Ca, Mg and Si in the plant tissues (dry biomass (Figure 2.3; Table D.2) × analyte concentration (Table D.2)), column leachate (leachate volume × analyte conc. (Table E.1)) and exchangeable soil cations (dry soil mass × extract analyte conc. (Table F.1)), and provides a minimum estimate of mass transfer of these elements from basalt weathering into the plant–soil system (Table 2.1). Additional mass transfer resulting in secondary mineral formation is unaccounted for in the sampling protocol, but may be inferred from geochemical modelling. Measured major cations released by basaltic grain weathering were generally retained in the soil exchange pool (Table 2.1; see Section 2.3.5). The ultimate fate of these accumulated base cations is important for carbon capture but uncertain. If flushed from the soil profile into run-off over time, they constitute a weathering flux per m² of land area, as typically measured by dissolved element fluxes of base cations ($2Ca^{2+} + 2Mg^{2+} + Na^{+} + K^{+}$, eq m^{-2} land $time^{-1}$) in streamwater draining from watersheds that plays a key role in CO_2 removal.

Calculated element mass transfer rates (mol m^{-2} s^{-1}) from dissolving basalt grains on a per unit physical surface area of rock (based on BET surface area; 7.35 m^2 g^{-1}), using elemental budgets in the plant, soil and leachate pools, yields dissolution rates that can be compared with literature values. Dissolution rates were also calculated based on measured Mg released. Mg is present in the most reactive components of our basalt (olivine and diopside; Table B.2) and is less affected by plant uptake (Figure 2.5e) and secondary mineral precipitation than Ca. This is consistent with significant ($p < 0.05$) Mg depletion on the grain surfaces, as determined by XRF (Figure 2.7). Dissolved Si was not used as a tracer for mineral dissolution due to potential retention as amorphous silicate coatings that have not been quantified, for example, on soil and basalt particles (Daval *et al.*, 2011). Rates for Mg release normalised to the BET surface area of our milled basalt rock (10^{-13} mol m^{-2} s^{-1}; Table 2.1) are a similar order of magnitude to those observed for dissolving Mg-rich olivine mineral grains in planted mesocosm experiments ($10^{-13.1}$–$10^{-13.7}$ mol m^{-2} s^{-1}) (Amann *et al.*, 2020) ($10^{-11.8}$–$10^{-12.7}$ mol m^{-2} s^{-1}) (Renforth, Pogge von Strandmann and Henderson, 2015). The mineralogy of the basalt (Table B.2) suggests that if Mg were being released primarily from the olivine exposed at the surfaces of the grains, the release rate normalised to olivine surface area would give a calculated rate approximately 100-fold higher. This assumes

Table 2.1 – Changes in whole-system elemental budgets and transfer rates resulting from basalt amendment (100 t basalt ha^{-1}) of a mildly acidic clay-loam soil (pH 6.6; 250 kg N ha^{-1}) planted with *Sorghum bicolor*, after 120 days. Values are mean differences (±*SE*) between basalt-amended (n = 6) and unamended (control) planted reactor columns (n = 6). Positive values indicate increased element concentrations due to basalt amendment. Soil extraction results are depth-integrated averages (±*SE*) for subsamples taken from six equidistant depths. Surface areas are expressed as SA_L for land surface area, and SA_R for rock surface area.

Element	Effect of basalt treatment on rate of elemental release					Measured elemental release from basalt†	Rate of elemental release (BET SSA = 7.35 m^{-2} g^{-1} basalt) ‡
	Leachate	Plant (µmol m^{-2} SA_L d^{-1})			Soil extraction* (mmol m^{-2} SA_L d^{-1})		
		Roots	Shoots	Seeds		(mmol m^{-2} SA_L d^{-1})	(mol m^{-2} SA_R s^{-1})
Ca	–31 ± 91	26 ± 22	300 ± 84	1.9 ± 2.7	17 ± 14	18 ± 14	2.8×10^{-12} ± 2.2×10^{-12}
Mg	–0.35 ± 5.1	5.5 ± 7.4	72 ± 79	63 ± 40	4.0 ± 0.91	4.2 ± 0.93	6.6×10^{-13} ± 1.5×10^{-13}
K	30 ± 17	110 ± 96	210 ± 210	96 ± 44	0.68 ± 1.3	1.1 ± 1.4	1.8×10^{-13} ± 2.3×10^{-13}
Na	–0.63 ± 11	0.52 ± 3.7	4.2 ± 5.0	0.3 ± 1.3	0.33 ± 0.53	0.33 ± 0.53	5.2×10^{-14} ± 8.4×10^{-14}
Si	–5.2 ± 8.5	–140 ± 90	1600 ± 390	1.7 ± 1.5	0.36 ± 0.10	1.9 ± 0.4	2.9×10^{-13} ± 6.9×10^{-14}

*Derived from ammonium acetate extraction on soil samples representative of the whole column.

†Measured moles released from basalt, Q, is calculated:

$$Q = \mathrm{A}_{Bas} + \mathrm{B}_{Bas} + \mathrm{C}_{Bas} + \mathrm{D}_{Bas} + \mathrm{E}_{Bas} - (\mathrm{A}_{Con} + \mathrm{B}_{Con} + \mathrm{C}_{Con} + \mathrm{D}_{Con} + \mathrm{E}_{Con})$$

Where A, B, C, D and E are the measured moles of the element in the leachate, roots, shoots, seeds and soil extraction, and the subscripts *Bas* and *Con* relate to the basalt treatment and control.

The overall uncertainty, δQ, is calculated by summing the errors for each system component in quadrature, using the following equation (Kirchner, 2001),

$$\delta\mathrm{Q} = \sqrt{\delta\mathrm{A}_{Bas}{}^2 + \delta\mathrm{B}_{Bas}{}^2 + \delta\mathrm{C}_{Bas}{}^2 + \delta\mathrm{D}_{Bas}{}^2 + \delta\mathrm{E}_{Bas}{}^2 + \delta\mathrm{A}_{Con}{}^2 + \delta\mathrm{B}_{Con}{}^2 + \delta\mathrm{C}_{Con}{}^2 + \delta\mathrm{D}_{Con}{}^2 + \delta\mathrm{E}_{Con}{}^2} \quad \textbf{Equation 2.2}$$

‡Calculated by dividing the measured moles released from basalt by BET-determined rock surface area (SSA = 7.35 m^{-2} g^{-1} basalt).

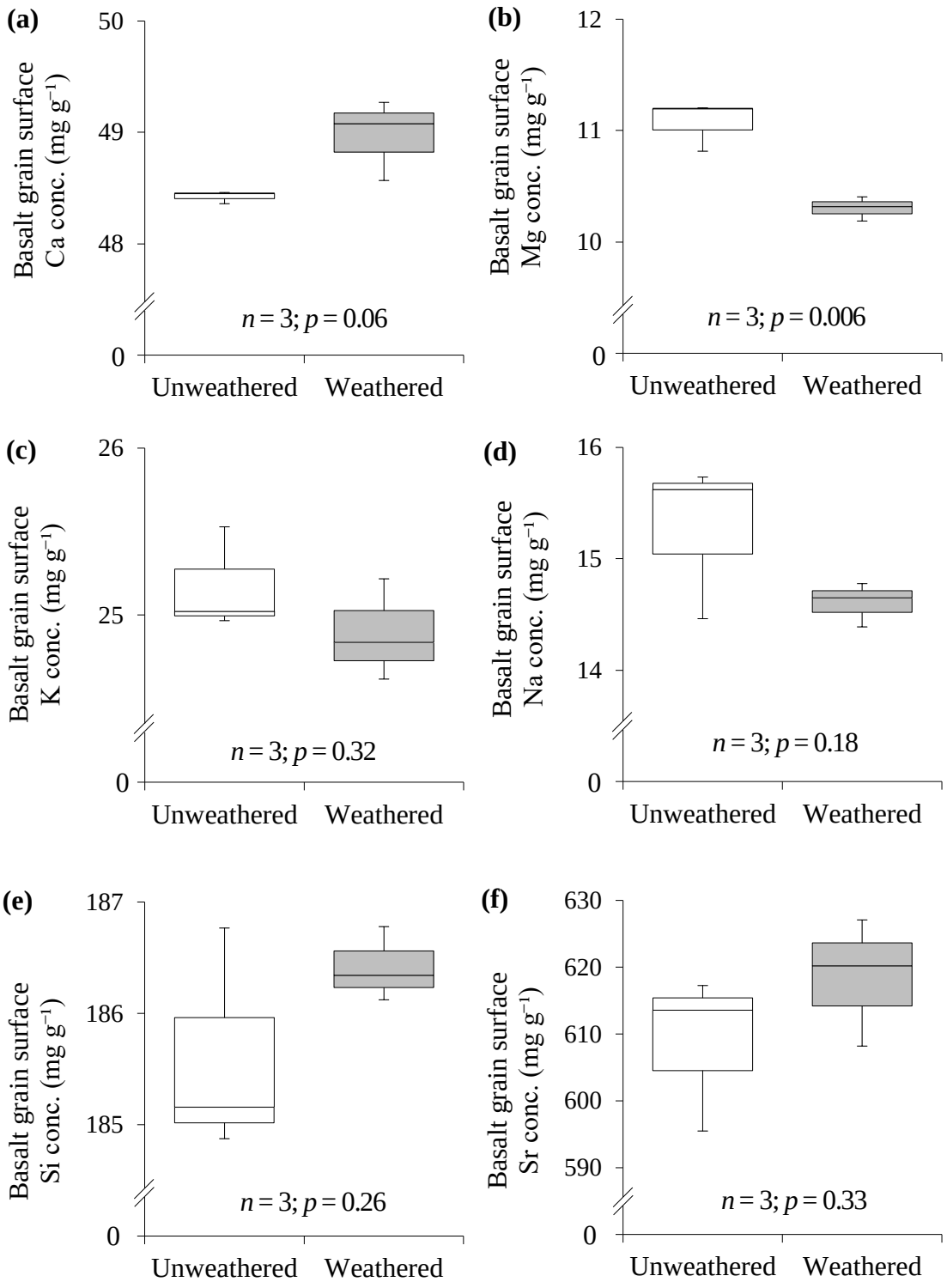

Figure 2.7 – Unweathered and weathered surface elemental concentrations for basalt grains retrieved from in-growth bags, as determined by X-Ray Fluorescence. Stated *p* values were determined in R *via* a one-way ANOVA.

that olivine surface area as a fraction of measured surface area scales with wt% olivine in the basalt. These much higher Mg mass transfer rates are similar to those reported in the literature for olivine dissolution in laboratory weathering experiments. Rates reported by (Amann *et al.*, 2020) in planted mesocosms were based on dissolved Mg flux in leachate only and did not account for accumulation on soil ion exchange surfaces, such as clay minerals. In this study, the exchangeable pool accumulated a 100-fold excess or more of released cations compared to the plant and leachate pools of released Mg (Table 2.1).

The BET method is postulated to overestimate RSA of dissolving minerals, partly due to measuring internal pore surface area that is inaccessible to reacting pore fluids (Brantley and Mellott, 2000) leading to underestimation of surface area-normalised weathering rates. Apparent RSA was calculated using the RTM, constrained by the elemental budgets (Table 2.1). The RSA value was obtained by optimisation (Section 2.2.8) where the RTM input files were updated with new RSA values. Model goodness-of-fit was evaluated using the root-mean-square difference between Mg release by basalt dissolution and the experimentally determined Mg mass transfer into the plant, leachate and soil exchange pools in samples collected after 120 days (Table 2.1). Based on this approach, apparent RSA in the RTM was 7.35 $m^2\ g^{-1}$, essentially the same as the BET SA. The RTM does not capture repeated evapotranspiration-driven wetting and drying cycles experienced in the soil columns, the formation of preferential flow paths or possible precipitation of secondary minerals occluding dissolving surfaces, as seen in other mesocosm ERW experiments (Zhang *et al.*, 2018; Amann *et al.*, 2020). With constant moisture and drainage, the RTM is comparable to batch reactor experiments where particle surfaces are fully wetted and exposed continually to the fluid. Nevertheless, modelled leachate Si flux is slightly underestimated compared to observations, and Si release rates (10^{-13} mol $m^{-2}\ s^{-1}$; Table 2.1) are lower than those reported for fluid batch reactors with milled basalt particles in the absence of soil and plants (1.38×10^{-11} mol Si $m^{-2}\ s^{-1}$ to 7.0×10^{-10} mol Si $m^{-2}\ s^{-1}$; at 25°C; Navarre-Sitchler and Brantley, 2007).

2.3.5 Strontium isotope evidence for basalt dissolution

Radiogenic Sr isotopes help determine the relative contribution of Sr from cation sources (soil and basalt) to soil column cation reservoirs (plant, soil exchangeable cation sites and leachate). The initial (pre-treatment) exchangeable soil $^{87}Sr/^{86}Sr$ ratio was the highest of the sample set (0.71180) while the basalt silicate digest and carbonate leachate $^{87}Sr/^{86}Sr$ ratios were the lowest of the sample set (0.70428 and 0.70541, respectively). Irrigation water had a Sr concentration below the detection limit of the ICP-OES and so is assumed to have negligibly contributed to the Sr isotope budget of the soil columns. Urea (CH_4N_2O) is assumed to have a negligible Sr component. Control plant, exchangeable soil and leachate $^{87}Sr/^{86}Sr$ ratios were lower than the initial (pre-treatment) exchangeable soil $^{87}Sr/^{86}Sr$ ratio, suggesting preferential weathering of soil minerals with relatively lower $^{87}Sr/^{86}Sr$ ratios throughout the experiment (Figure 2.8; Tables D2, E2 and F2).

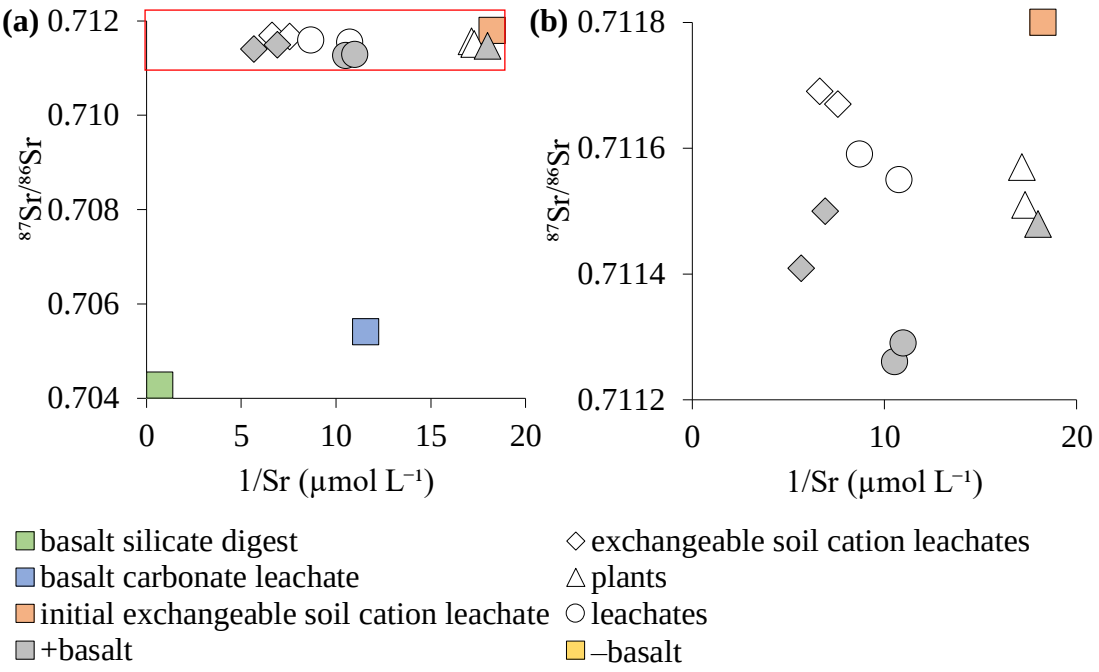

Figure 2.8 – Shifts in the strontium isotope composition of the major pools in the mesocosms. (a) the $^{87}Sr/^{86}Sr$ ratios *versus* 1/Sr ratios for Sr sources as well as cation reservoirs (i.e., leachate, exchangeable soil and *Sorghum* shoots) in treatment (+basalt) and control (−basalt) soil columns. Red box indicates the area expanded in (b). It is unlikely that 1/Sr ratios in plant, leachate, and soil exchangeable reservoirs conservatively trace source mixing in the column due to *Sorghum* Sr uptake.

Treatment (+basalt) plant, exchangeable soil, and leachate $^{87}Sr/^{86}Sr$ ratios were lower than the $^{87}Sr/^{86}Sr$ ratios of the corresponding reservoirs in the control (−basalt) soil columns and closer to the basalt source (Figure 2.8). This provides clear evidence for basalt dissolution and its contribution to the cation reservoirs in treated soil columns.

Based on the two-component isotope-mixing model (Equation 2.1), it is calculated that approximately 4.1%, 3.0% and 0.9% of Sr in plants, exchangeable soil and leachate, respectively, originate from basalt weathering. These values represent lower limits and marginally increase (4.9%, 3.6% and 1.1%, respectively) if the basalt-derived Sr is assumed to originate from carbonate weathering, and the basalt carbonate leachate $^{87}Sr/^{86}Sr$ ratio is implemented in the calculation instead of the basalt silicate digest ratio. These results suggest that dissolved Ca is predominantly retained in the soil column or transferred to plants, with little Ca mobilised into leachate. It is noted, however, that the transfer of basalt-derived Sr into pedogenic carbonate was not examined, but this is likely to be small given no statistically significant change in TIC between the control and treatment columns (Section 2.3.7).

2.3.6 Mycorrhizal fungal grain interactions

Root-associating mycorrhizal fungi are implicated in field trials (Quirk *et al.*, 2012) and experiments (Quirk *et al.*, 2014) in accelerating physical and chemical rates of mineral grain dissolution processes. Hence, interactions between fungi and basalt grains in the root-excluding nylon mesh bags filled with basalt particles in the *Sorghum* root zone (top 15 cm) were examined. Retrieval of rock grains after 120 days indicated extensive colonisation by fungi (2.0 ± 0.1 m hyphae g^{-1} rock) similar to that reported for crushed basalt-filled mesh-bags buried in soils beneath established (10–30 m high) trees with mycorrhizal fungal partners (Quirk *et al.*, 2012). Fungal hyphae proliferated throughout grains in the basalt bags, often connecting multiple grains (Figure 2.9). Hyphae were unpigmented, lacked septa and possessed angular projections (Figure 2.10), typical characteristics of AMF which supply plant roots with nutrients and contribute to bioweathering (Quirk *et al.*, 2012, 2014; Burghelea *et al.*, 2015, 2018).

DNA extracted from mesh-bags on harvesting the plants revealed that up to 45% of the fungal sequences were Glomeromycotina, the phylum-forming AMF (Figure 2.11). This substantial contribution of AMF to total fungal DNA likely under-represents their hyphal biomass because not all AM fungal hyphal fragments contain nuclei and they

produce fewer spores than other fungal groups identified in the bags and so have a lower DNA:biomass ratio. Under scanning electron microscopy, weathered grains retrieved from the mesh bags colonised by AMF (i.e. post-experiment) had rough, disrupted, surface structures and attached hyphae (Figure 2.12), whereas unweathered grains (i.e. pre-treatment) were characterised by smooth planar surfaces, with sharper angular geometries, suggesting crystal cleavage surfaces (Figure 2.13).

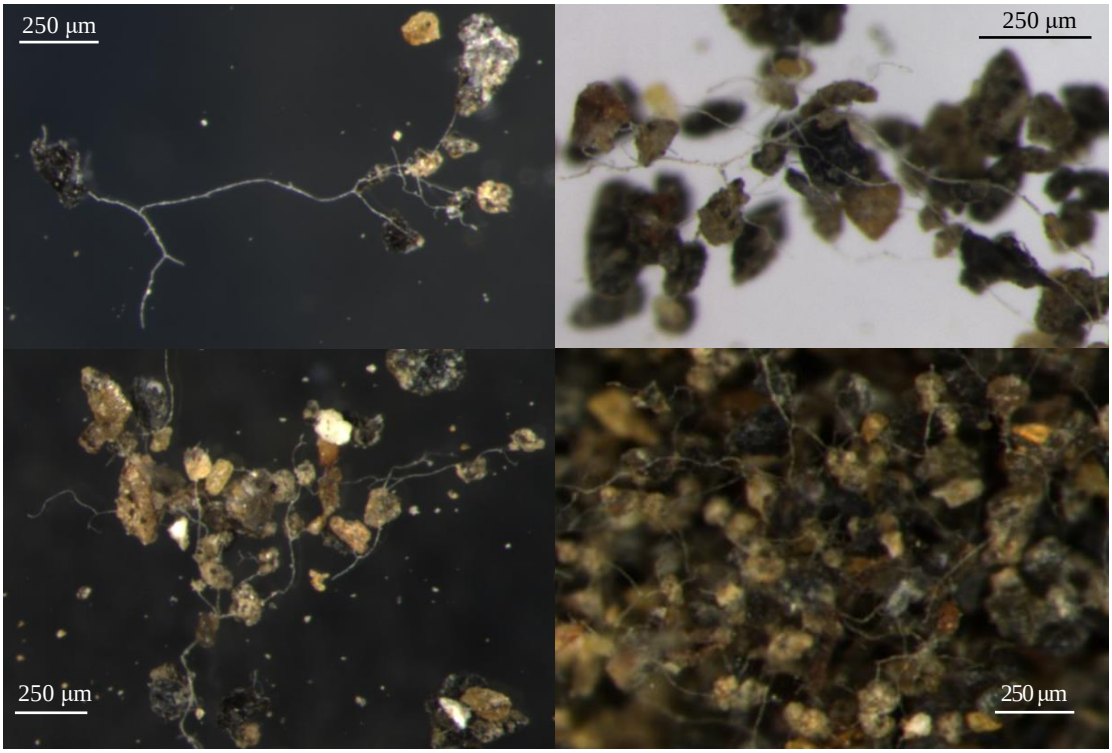

Figure 2.9 – Microscope images of basalt grains recovered from buried root-excluding mesh bags. Images illustrate extensive basalt grain-fungal interactions, with fungal hyphae contacting weathered grains, often linking multiple grains together.

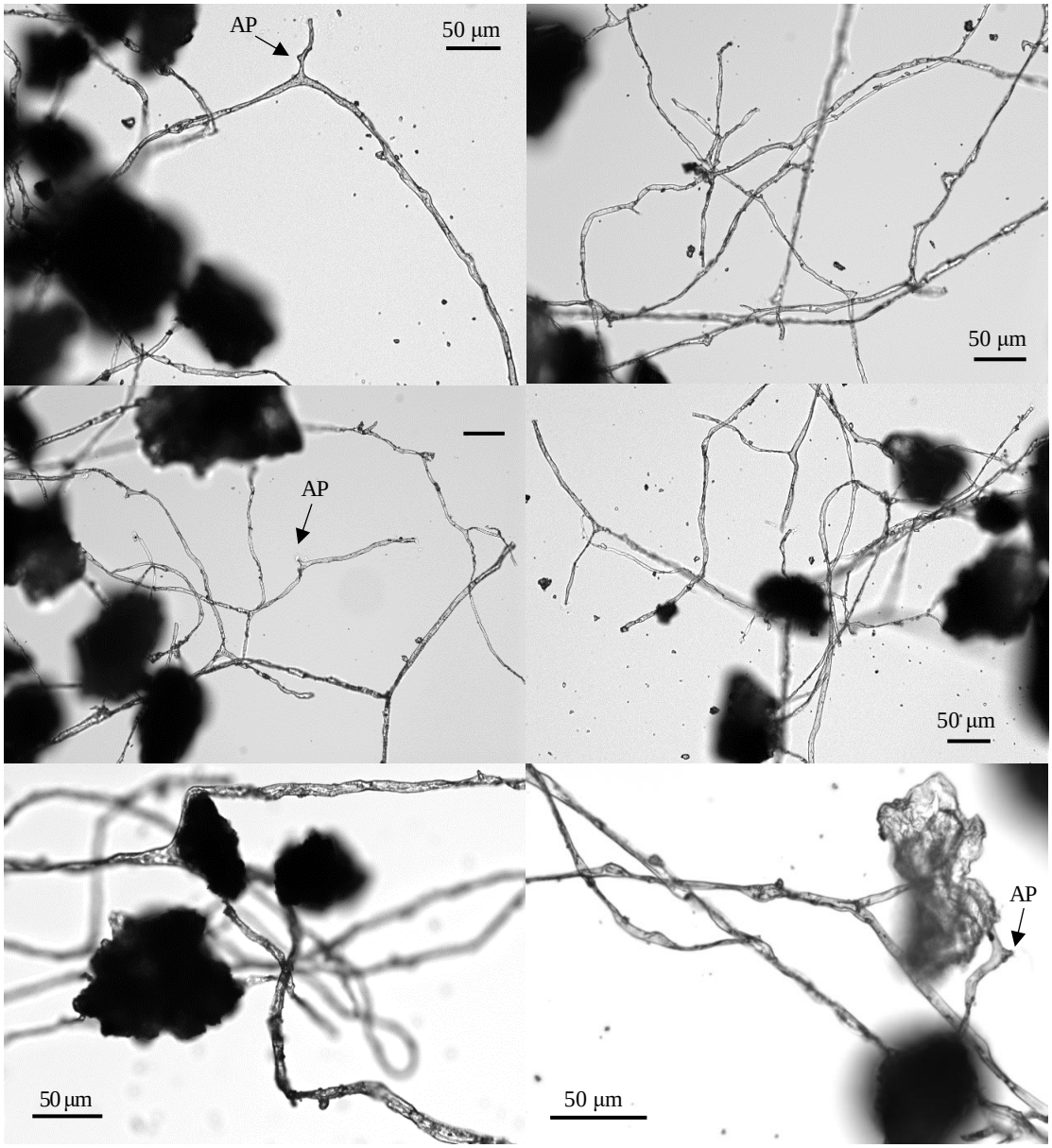

Figure 2.10 – Compound microscope images of hyphae in mesh bag-buried basalt grains. Note the hyphae are unpigmented with angular projections (AP) and generally lack septa, which are typical features of arbuscular mycorrhizal fungi.

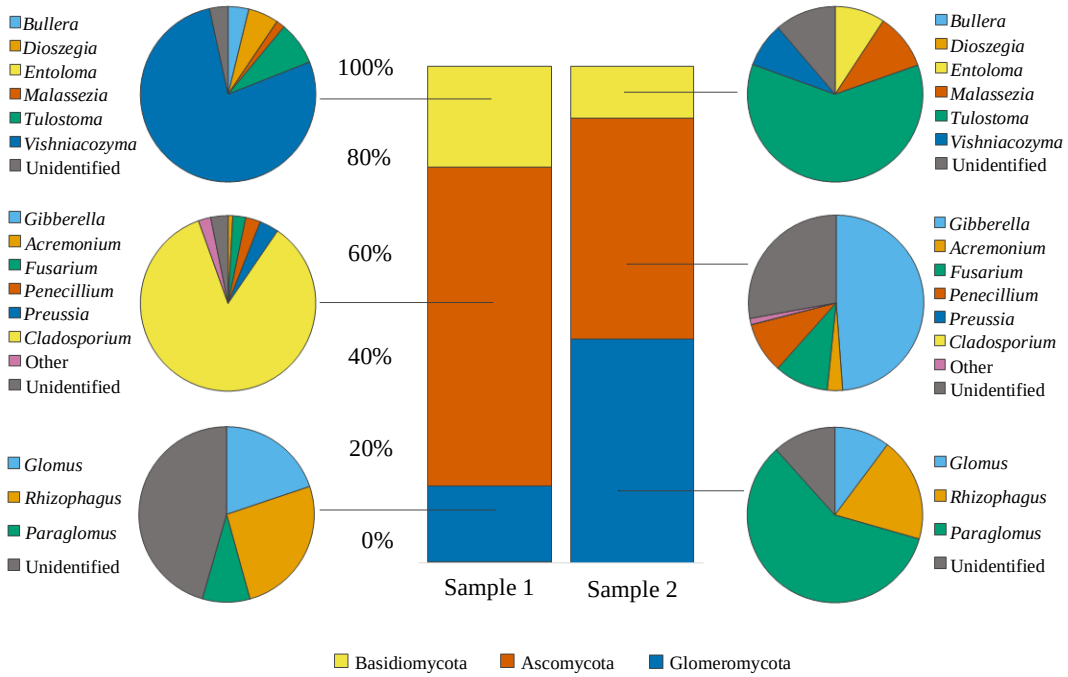

Figure 2.11 – Fungal DNA sequences identified in weathered basalt bags. DNA sequence analysis was undertaken on a matched pair (same grain size, rooting depth, different columns) of weathered (i.e. post experiment) basalt samples. Central bars show the proportion of fungal sequences identified at the phylum level. Pie charts indicate the relative abundance of fungal genera within the major phyla. The dataset consisted of 327,964 sequences after quality control and chimera and singleton removal, representing 801 operational taxonomic units (OTUs). Of these, 306,949 sequences (589 OTUs) were identified as fungal. Up to 45% of fungal sequences in each sample were Glomeromycota and the most abundant operational taxonomic unit (OTU) in one sample was Paraglomus laccatum, an AMF. However, it is likely that this substantial contribution of AMF to total fungal DNA under-represents their contribution to hyphal biomass as the basalt samples were taken at the end of the plant growth life-cycle. At that time, shoots were no longer photosynthesising and roots had senesced so were no longer actively supporting the obligately biotrophic mycorrhizal fungi and fresh root litter is likely to have increased the abundance of fast-growing saprotrophic genera (e.g. Cladosporium, Penicillium and Fusarium). Furthermore, not all AMF hyphal fragments contain nuclei whereas many other fungi detected do not form hyphae (e.g. the yeasts Vishniacozyma, Bullera and Dioszegia) or are taxa which produce numerous spores (e.g. Cladosporium, Acremonium and Penicillium), that better preserve DNA than AMF hyphae.

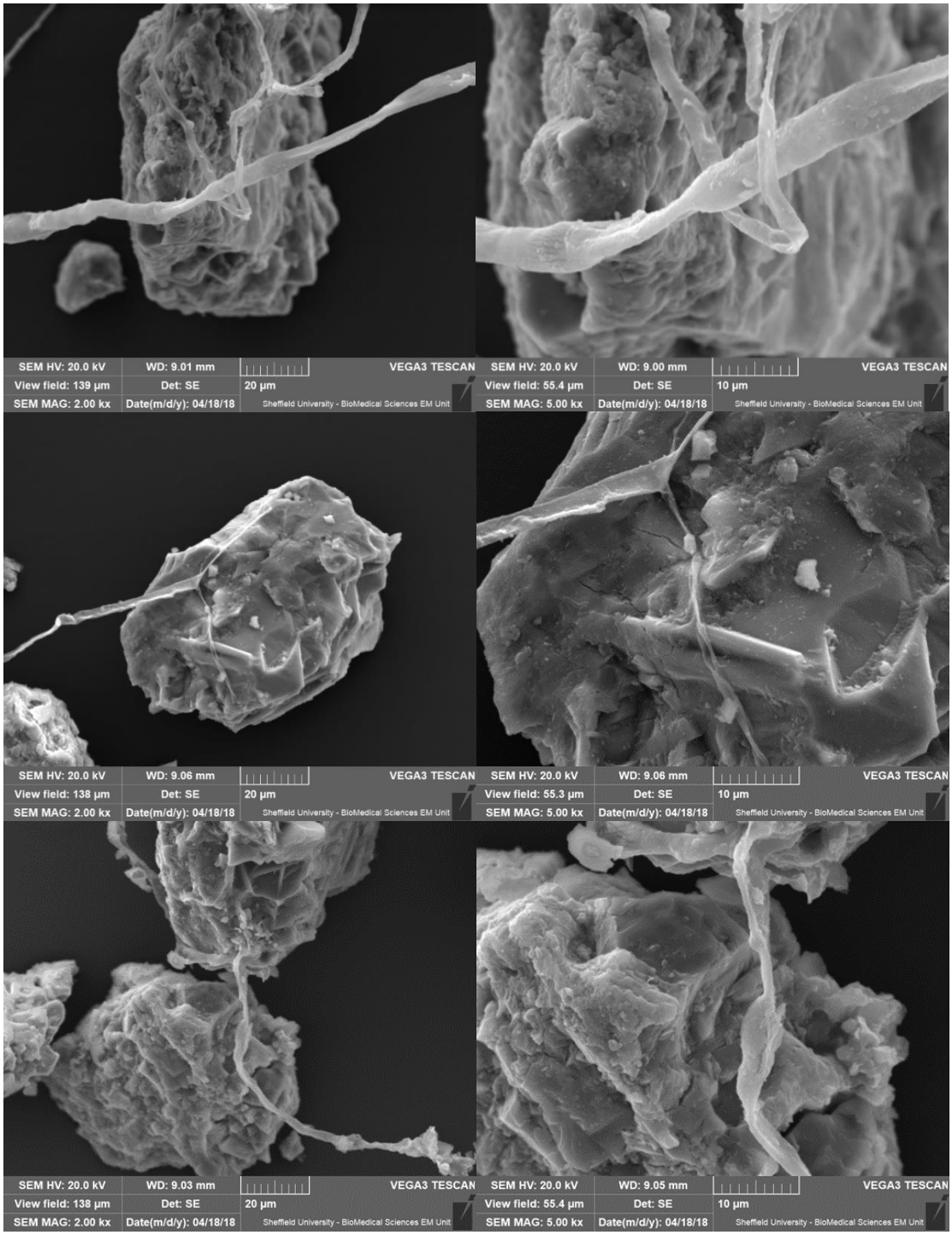

Figure 2.12 – Scanning electron microscope images of weathered basalt grains. Left-hand images are low magnification and right-hand images are high magnification, evidencing intimate basalt grain-fungal interactions.

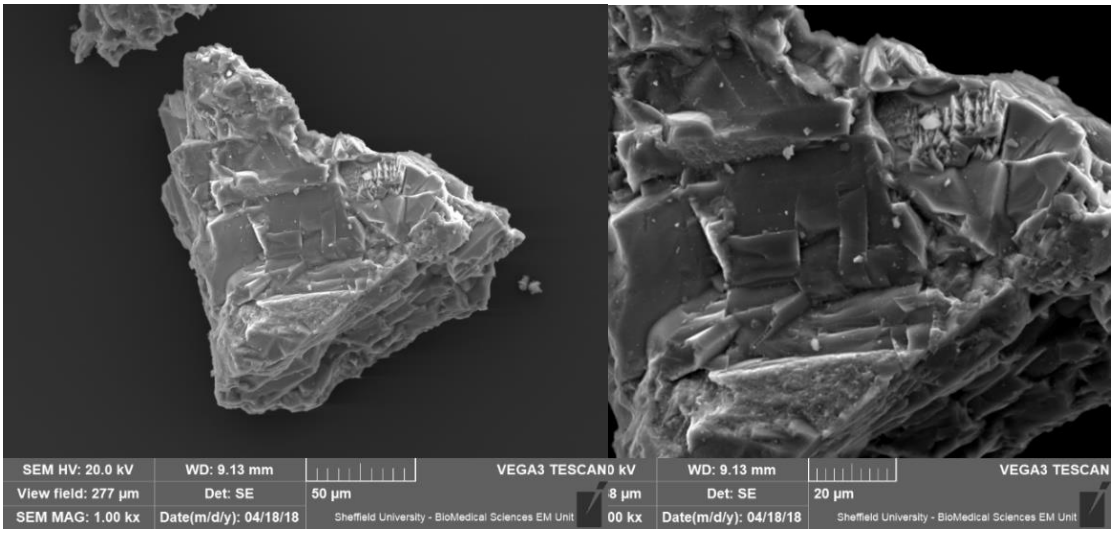

Figure 2.13 – Scanning electron microscope images of unweathered basalt grains. Left-hand image is low magnification and the right-hand image is high magnification. Both images illustrate smooth angular geometries of surface structures.

2.3.7 Modelled basalt dissolution and CO_2 sequestration

Reactive transport model simulations, constrained by observations after 120 days were run forward in time for 5 years to assess mineral dissolution and carbon capture dynamics beyond the timescale of the experimental trials. Model results suggest that the olivine and diopside basaltic minerals undergo rapid dissolution relative to the other components (Figure 2.14a). Simulated basalt dissolution leads to the formation of secondary minerals including calcite (calcium carbonate) and the amorphous phases, $Al(OH)_3$ and $Fe(OH)_3$ over time, which act as sinks for the weathered Ca, Al and Fe ions respectively (Figure 2.14b).

Cumulative total CO_2 sequestration by coarse-grained basalt weathering is simulated to reach ≈3 tCO_2 ha^{-1} within 2 years (Figure 2.14c), and continues to rise towards a maximum of ≈4 tCO_2 ha^{-1} after 5 years. Initially, pedogenic carbonate (calcite) formation dominates CO_2 sequestration as the fast-reacting minerals (olivine and diopside) undergo dissolution releasing rapidly divalent cations.

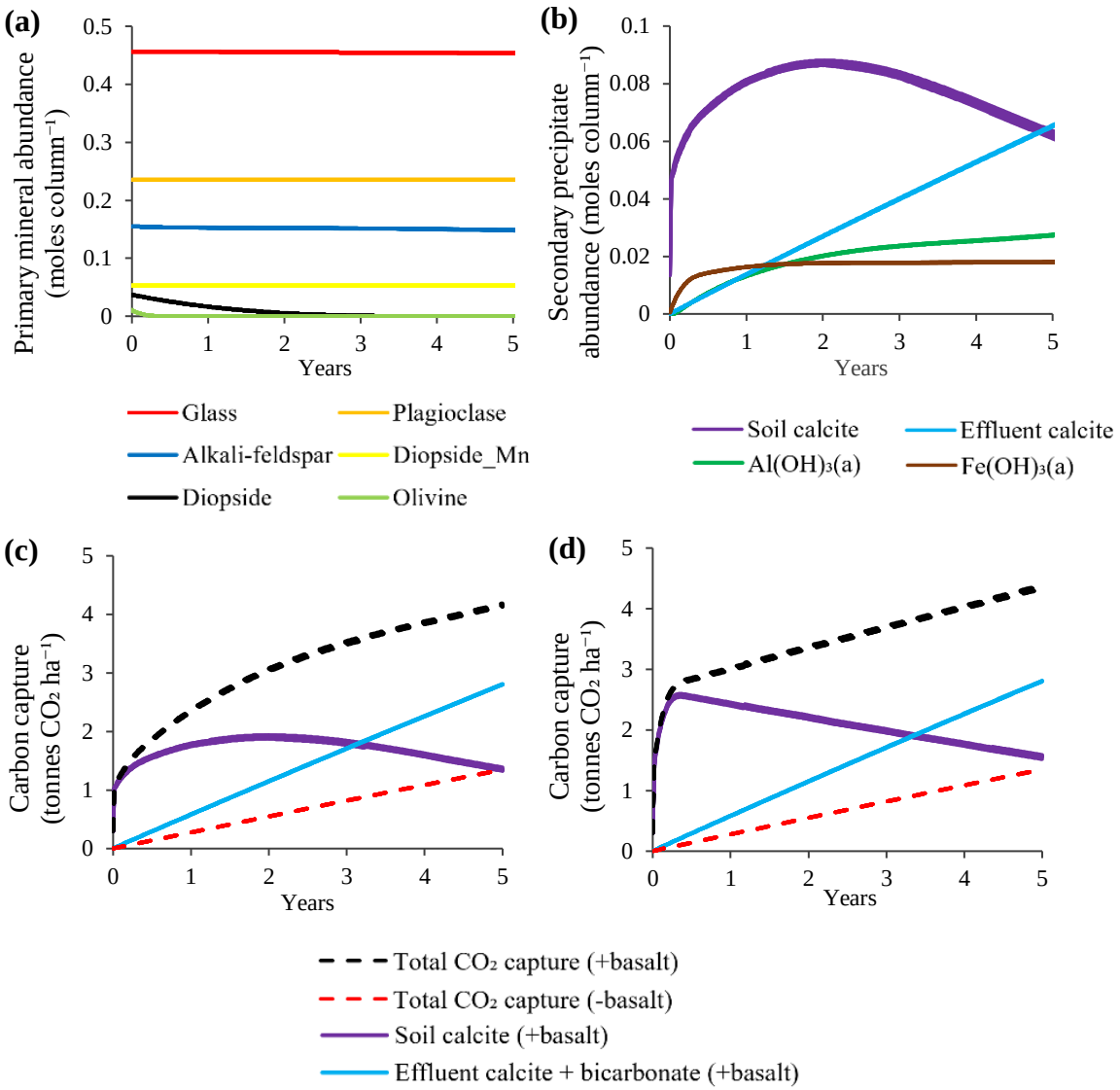

Figure 2.14 – Reactive transport modelling of basalt mineral dissolution and carbon capture. Simulated changes in (a) dissolution of individual basaltic minerals (as moles column^{-1}), (b) secondary mineral or precipitate formation, (c) cumulative CO_2 sequestration with coarse-grained basalt (P_{80} ≈1,250 µm, i.e. 80% of particles ≤ this diameter) and (d) cumulative CO_2 sequestration with a 10-fold finer-grained basalt (P_{80} ≈125 µm).

Diopside is exhausted after approximately 2 years, and soil-formed calcite begins to dissolve, exiting the systems in the effluent as bicarbonate and reprecipitated calcium carbonate, a storage reservoir that linearly rises over the 5 years of the simulations (Figure 2.14c). Simulations with a 10-fold smaller particle size distribution result in a faster dissolution of olivine and diopside leading to more rapid CO_2 sequestration via pedogenic carbonate formation (Figure 2.14d), but with similar cumulative sequestration after 5 years (4.2 tCO_2 ha^{-1} for the coarse-grained basalt vs. 4.4 tCO_2 ha^{-1}

for the 10-fold smaller particles). Amplification of carbon sequestration resulting from the basalt treatment, relative to the 'control columns' was 3.1- and 3.2-fold after 5 years for the two sets of simulations (experiment and small particles respectively). This evidence for increased CDR following the basalt treatment strongly supports rejection of the respective null hypothesis (*H*3: 0), in favour of the alternative (*H*3: 1).

Estimated CO_2 sequestration rates via basalt weathering in our planted mesocosms are comparable with those of prior mesocosm ERW studies in which soils were amended with milled silicates (Table 2.2). Application rates, types of silicate, irrigation regimes and duration of experiment contribute differences in estimated CO_2 sequestration rates, but lowest rates correspond to studies in which pedogenic carbonate formation has not been estimated (Table 2.2).

Table 2.2 – CO_2 sequestration rates from mesocosm-scale ERW studies

Study	Rock material	Rock loading (t rock ha^{-1})	Sequest-ration period (years)	CO_2 sequestered (tCO_2 ha^{-1})	CO_2 efficiency (tCO_2 t $rock^{-1}$)	RCO_2 theoretical maximum[a]
ten Berge *et al.* (2012)	Olivine	1.63	0.62	0.29[b]	17.8%	0.91
	Olivine	204	0.62	2.69[b]	1.3%	0.91
Dietzen *et al.* (2018)	Olivine	10	0.25	3.13[c]	31.3%	0.69
	Olivine	50	0.25	4.16[c]	8.3%	0.69
Haque *et al.* (2019)	Wollas-tonite	221	0.15	39.3[d]	17.8%	0.51
Amann *et al.* (2020)	Dunite	220	1	0.023[e]	0.01%	0.84
	Dunite	220	1	0.049[e]	0.02%	0.84
This study	Basalt	100	1	2.36[f]	2.4%	0.14
	Basalt	100	1	3.01[g]	3.0%	0.14

[a]Using reported MgO and CaO values and the R_{CO2} equation (2) in Renforth (2012)
[b]Calculated from mass of Mg in plant and soil exchangeable pools
[c]Calculated from mass of Mg in soil exchangeable pool
[d]Calculated from soil inorganic carbon, alkalinity and thermogravimetric analysis
[e]Calculated from mass of Mg in leachate
[f]Modelled with particle $P_{80} \approx 1280$ µm
[g]Modelled with particle $P_{80} \approx 128$ µm

Both sets of RTM simulations support the application of larger particle sizes for Oregon basalt for carbon removal than are typically adopted in ERW numerical studies – e.g., 10–20 µm diameter (Köhler, Hartmann and Dieter A Wolf-Gladrow, 2010; Moosdorf, Renforth and Hartmann, 2014; Taylor et al., 2016; Strefler et al., 2018). This reduces

energy costs for milling and the associated carbon emissions penalty from fossil fuels (Moosdorf, Renforth and Hartmann, 2014; Lefebvre et al., 2019). In practical terms, carbon removal rates may be lowered by 10%–30% after accounting for emissions from logistical operations (mining, grinding, distributing, spreading) (Moosdorf, Renforth and Hartmann, 2014; Lefebvre et al., 2019). Nevertheless, this study's results support ERW as an effective climate change mitigation tool comparable to widely advocated agriculture-based greenhouse gas mitigation measures, including set-aside, grazing land and cropland management options (Paustian *et al.*, 2016).

A TIC budget based on the experimental observations indicates no significant ($p > 0.05$) change in pedogenic carbonate mineral formation across all depths (Figure 2.15a) over the 120-day experiment. Statistical comparison of slopes of the fitted regression and 1:1 line indicated no significant difference ($p > 0.05$; MANOVA). The modelled change in soil TIC in the post-experiment basalt treated columns is small compared to background levels in the control columns (Figure 2.15c). Simulation results (Figure 2.14c) indicate the duration of our experiment was likely too short to detect a substantial increase soil TIC with basalt treatment (Figure 2.15). Precipitation of inorganic carbon through pedogenic carbonate formation (Figures 2.14 and 2.15) has nevertheless been reported for pot-based trials with wollastonite-amended agricultural soil supporting maize and beans (Haque *et al.*, 2019), and a long-term (7-year) field study (Manning *et al.*, 2013). However, the fate of pedogenic carbonate will depend on seasonal rainfall patterns and land management. Its fate requires assessment in field scale trials under different climatic conditions and farming practices (Zamanian, Pustovoytov and Kuzyakov, 2016). It is recognised that CO_2 may have been lost from the experimental basalt-treated columns *via* soil organic matter mineralisation, and CO_2 release by respiration in response to increased pH (Malik *et al.*, 2018). However, the agricultural soil in the columns was low in organic matter (≈1%), in common with most agricultural soils, and the control and treated soil organic carbon concentrations matched each other after 120 days (Figure 2.15b). Soil respiration measurements following low (10 t ha^{-1}) and high (50 t ha^{-1}) applications of finely powdered olivine to an acidic organic-rich podzol soil (pH = 4.9) support this view, with no significant increases in cumulative CO_2 fluxes relative to unamended controls (Dietzen, Harrison and Michelsen-Correa, 2018) fertiliser.

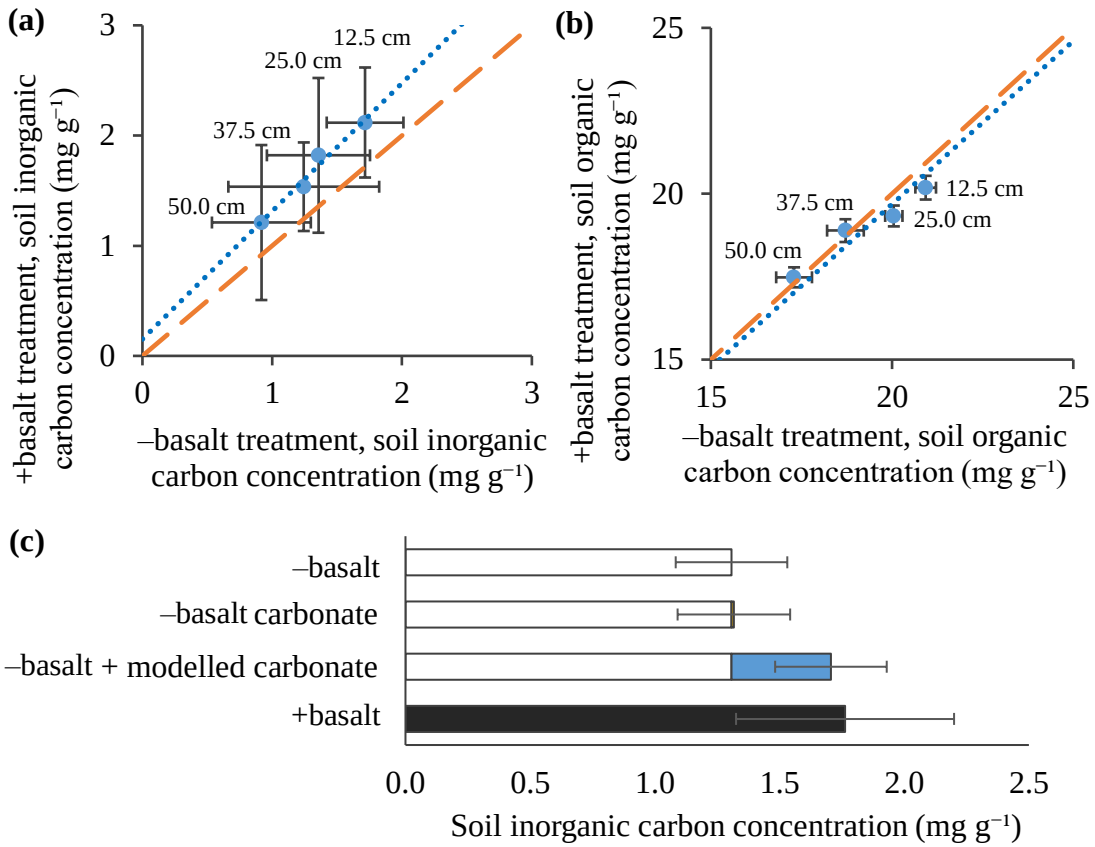

Figure 2.15 – Measured and modelled soil carbon changes in response to basalt treatment. (a) comparison of measured total inorganic carbon (TIC) in soils with and without basalt at four depths, normalised to TIC starting concentrations, after 120 days (one-way MANOVA, $p > 0.05$). Dashed orange line is the 1:1 line. (b) Comparison of observed soil TIC in the postexperimental control (−basalt bar) and basalt-treated (+basalt bar) columns (mean ± SE for all depths). Also shown is the reactive transport model predicted TIC increase due to result of basalt weathering (−basalt + modelled carbonate stacked bar), which compares favourably with observations (i.e. solid bar), and the very small increase accounted for by native basalt-carbonate dissolution and reprecipitation (−basalt + basalt carbonate). (c) Comparison of measured total soil organic carbon in soils with and without basalt at four depths, normalised to starting concentrations, after 120 days (one-way MANOVA, $p > 0.05$). Dashed orange line is the 1:1 line. Error bars represent *SE*.

2.4 Conclusions

This study demonstrates that amending a slightly acidic clay-loam soil with a high loading of coarse-grained basaltic rock dust substantially increases *Sorghum* yield without P and K usage or adverse trace element uptake into the seed, under experimental conditions. Elemental mass budgets indicate that products of basalt dissolution (alkalinity and cations) will not be immediately transported directly to the marine environment *via* surface waters because of uptake of elements into plant biomass and temporary sequestration onto soil exchangeable sites (e.g. clay and organic matter). Geochemical reactive transport modelling indicates that a single application of basalt might achieve carbon sequestration rates of 2–4 $tCO_2\ ha^{-1}$ over 1–5 years. The fates of the newly formed soil carbonates and weathered elements taken up into biomass will depend on land management practices. The long-term fate of these weathering products requires assessment through field trials. Currently, primarily crop grain biomass is removed from fields and the shredded fast-decomposing stover normally returned back to the soils, whereby the cations within unharvested biomass become available to participate in carbon capture.

This study with a clay-loam soil represents a first step towards supporting the applicability of ERW to European and North American agriculture in which cereals with high silica demand are the most important crops. However, further investigations are warranted at lower rates of basaltic rock dust application to optimise cost effectiveness. If yield improvements follow under field conditions, associated economic gains could offset costs of ERW deployment. Furthermore, volcanic rock dust is a recognised fertiliser in organic agriculture (van Straaten, 2006) which, by avoiding superphosphate fertilisers, supports diverse active mycorrhizal fungal networks (Verbruggen *et al.*, 2010) to facilitate mineral dissolution and subsequent CDR (Quirk *et al.*, 2012, 2014; Burghelea *et al.*, 2015, 2018). With organic agriculture land area increasing fourfold in 10 years to occupy 57.8 million hectares (in 2018) across 178 countries, our findings highlight new opportunities for upscaling ERW practices in this rapidly expanding sector (Organics International, 2018). Furthermore, it raises the prospect that conventionally managed agricultural land suffering depletion of available Si pools as a result of intensive cropping, with cereals and straw and stover removal for biofuels and other uses (Haynes, 2017), may also be suitable for ERW.

3

Higher CO_2 capture, basalt weathering rates and associated *Sorghum* yield bonus in agricultural soil amended with NPK fertiliser, compared to a bovine manure fertiliser regime with equivalent total N

Contents

3.1 Introduction

Several prior mesocosm-scale ERW experiments have demonstrated promising CDR potential and/or related agronomic co-benefits following the amendment of soils with crushed silicate minerals (ten Berge *et al.*, 2012; Renforth, Pogge von Strandmann and Henderson, 2015; Amann *et al.*, 2020; Kelland *et al.*, 2020; Vienne *et al.*, 2022). A general introduction on the use of silicate rocks in agriculture is set out in Chapters 1 and 2, but is expanded upon here with further consideration on the suitability of ERW in different agricultural settings. Scalability is proposed as a key advantage for ERW (Renforth, 2012; Taylor *et al.*, 2021), because to generate globally-meaningful CDR, many of the land-based alternatives (e.g. DAC, BECCS, biochar (Section 1.1)) demand massive capital investment (Shackley *et al.*, 2011; Fajardy *et al.*, 2021; McQueen *et al.*, 2021; IEA, 2022) to build supporting infrastructure that is necessarily comparable in scale to the global infrastructure emitting GHGs. However, implicit to this notion of superior scalability is the assumption that ERW will be largely compatible with the wide range of soil types, agricultural practices and environmental conditions that exist within the global land area under management – about 38% of the terrestrial surface area (FAO, 2020) – for which there is little empirical evidence.

Broadly, global agricultural production can be segregated into two main categories: conventional farming, which employs fertilisers, and organic farming, where synthetic agrochemicals may be prohibited and essential plant nutrients (N, P and K) are principally supplied by carbon-rich sources, e.g. manure and compost (Azarbad, 2022). Organic fertilisers are commonly used in the developing world, as agrochemicals are often prohibitively expensive, and this is particularly relevant given that many of the world's poorest nations are located in the warm, wet tropics – optimal conditions for ERW. Nonetheless, most of the world's food is grown with 'conventional', petrochemical-based fertilisers, because it is currently more economical for farmers to do so in the developed world (Panhwar *et al.*, 2019). A considerable body of evidence points to the adverse environmental impacts of this 'conventional' farming approach, such as soil and groundwater pollution (Mylonas *et al.*, 2020), eutrophication of water courses (Withers *et al.*, 2014), higher energy usage and increased GHG emissions compared with organic farming (Poux and Aubert, 2018). Organic agriculture produces relatively lower yields (Seufert, Ramankutty and Foley, 2012), but is considered to be more sustainable (Muller *et al.*, 2017), and this is partly due to the finite global reserves of high-grade mineral feedstocks used in the synthesis of P and (to a lesser constraint)

K chemical fertilisers, which are predominantly owned and exploited by a small number of countries (Maggio *et al.*, 2012). Driven by necessity, or concerns about sustainability and environmental impacts, but also nutritional quality (Montgomery and Biklé, 2021), the organic sector has seen rapid expansion in recent years. Currently, about 1.6% of the global land area under cultivation (arable and pasture) is considered organic, and recent estimates for the 2020–2021 cycle indicate an annualised sector growth rate of around 1.7% (Willer, Schlatter and Trávníček, 2023). With crushed basalt approved for use as a soil amendment under European Union (EU) organic farming regulations (834/2007, 889/2008 and 1235/2008) (Soil Association, 2021), and commercial interests already rolling out large-scale ERW projects internationally (Lithos, 2023; UNDO, 2023) it is likely that basalt will soon be routinely applied to agricultural soils modified with carbon-rich fertilisers. Research is therefore needed to assess and compare the performance of ERW under 'non-conventional' fertilisation regimes.

In this mesocosm-scale controlled environment experiment, the effect of synthetic and manure fertilisers on basalt weathering rates, CDR and associated agronomic co-benefits was investigated. Building on experience gained from the pilot experiment (Chapter 2), several important method advancements and design improvements were established for this trial, including increased replication, higher resolution depth-wise analysis of soil characteristics and time-series measurements of leachate and pore water geochemistry (Section 3.1.1). Weathering rates were determined by a conventional mass balance approach, and the values derived from this study are herein compared against estimates independently-determined *via* a new weathering quantification approach that relates the concentration of relatively immobile titanium (Ti) to the concentration of major cations (CAT), known as TiCAT (Reershemius and Kelland *et al.*, 2023). As in Chapter 2, pulverised basalt was applied to a clay-loam agricultural soil in which a dwarf variety of the globally-important C_4 cereal *Sorghum bicolor* was grown to physiological maturity. After harvesting of the aboveground biomass, this successor trial introduced an additional simulated 'fallow' period, where the controlled environment was adjusted to more closely approximate the Western European winter (Section 3.2.4). Extra time was therefore allowed for the continuation of weathering processes after removal of the cover crop and, potentially, the evolution of a stronger weathering 'signal'. By this method, the present study was positioned to acquire far more data than the previous, and to examine, for the first time, the effect of contrasting fertilisation techniques on ERW efficacy in a circumneutral pH soil, under middle-latitude climate conditions.

3.1.1 Reflections on the pilot experiment

Through a critical evaluation of the pilot experiment's performance (Chapter 2), several deficiencies in the design were identified. Notably, the plants in that study were grown under very low P and K conditions, and this was principally to encourage symbiosis between *Sorghum* and the AMF added as inoculum, because the available evidence (van Schöll *et al.*, 2008; Quirk *et al.*, 2012, 2014; Koele *et al.*, 2014) indicated that such partnerships can lead to accelerated mineral weathering. Strong evidence for fungal-grain interactions in the pilot experiment is presented in Section 2.3.6, but it is unlikely that the partnership or effect on weathering rates was fully realised in that trial. Laboratory weathering experiments with rocks and AMF/EMF (Smits *et al.*, 2012; Quirk *et al.*, 2014) indicate that colonisation of soil mineral resources by mycorrhizal fungi may be driven by the search for nutrients and water, and powered by an associated increase in belowground photosynthate allocation by the plant. In the pilot study, several individual plant specimens showed occasional symptoms of K deficiency (Figure 3.1), which in *Sorghum* presents as irregular necrotic bands along the leaf margins of older leaves (Chen *et al.*, 2016). This, and the modest yields in that trial, indicates that all plants were likely K-deprived, and may therefore suggest that there was little surplus photosynthate available to divert to the fungus. Hence, conditions were probably sub-optimal for the establishment of a strong plant-mediated positive feedback on weathering rates (Quirk *et al.*, 2014), and this was naturally addressed in this later study through the addition of K (and P) fertiliser in both regimes.

Figure 3.1 – Evidence of K deficiency in an 8-week old *Sorghum* specimen grown in the pilot experiment (Chapter 2)**.**

No plants in the pilot experiment displayed symptoms of drought stress beyond a slight curling of the leaf margins of younger leaves at what was likely the period of maximum photosynthesis – between boot (≈day 60) and soft dough stage (≈day 85); (Rice, 1973). On extraction of the soils (after 120 days), however, it was clear that moisture levels in the deepest layers were higher than those in the topsoil, and that around ¼ of the overall *Sorghum* root system was embedded in these deeper, wetter soils. This is an unusual

artefact and may indicate that moisture content in the top- and sub-soils poorly simulated field conditions. By extracting soils from the field – as whole-intact cores (Renforth, Pogge von Strandmann and Henderson, 2015; Buckingham *et al.*, 2022) or as bulk soil, like in this study – researchers are necessarily cutting off that substrate from substantial water reservoirs that, in nature, can act to replenish soil moisture in three dimensions. In column-based studies such as this, the surface area available for water influx into the system is limited to the upper soil surface only, whereas the surface area available for efflux (*via* the effluent outlet, topsoil and leaf surface areas) may be considerably greater, especially if large plants are cultivated. There is then an inherent bias in the water balance that, on reflection, should be monitored more carefully and adjusted for, if necessary, to avoid creating unrealistically low soil moisture conditions. Such effects on hydrology are implicated (West *et al.*, 2023) in the interpretation of low CDR rates for this particular rock type (Buckingham *et al.*, 2022), and are likely to have moderated CDR potential in the pilot experiment also. This inadvertent suppression of soil moisture content may be related to the development of undesirable preferential flow paths in previous mesocosm-scale experiments (Kelland *et al.*, 2020; Buckingham *et al.*, 2022), which were naturally disadvantaged by the smooth hydrophobic internal surface area of the pipe products chosen (being intentionally designed to encourage water flow). In the pilot experiment, soil column edges began to separate from the pipes' internal surfaces under the driest conditions, which – because upper soil surfaces were obscured by polyethylene beads – was the first direct evidence that soil moisture levels were very low. To better manage water availability in the present study, depth-integrated soil moisture was gravimetrically determined at regular 3-day intervals. Further data were also generated through the depth-wise deployment of bespoke, resistance-type soil moisture probes interfaced with low-cost, Arduino-based data-loggers capable of recording soil moisture reading every minute.

3.1.2 Experimental design

The overarching aim of the experiment was to measure and compare basaltic mineral weathering rates and associated CDR estimates under petrochemically-derived ('chemical' herein) and organic fertiliser regimes. In particular, the existence of a statistically significant interaction effect between basalt application rate and fertiliser type would be tested, to objectively determine which fertiliser treatment resulted in the largest CDR potential, and which provided the most significant ancillary benefits to plants and soils.

To ensure adequate control treatments for each of the fertiliser regimes in this study, a balanced two-factorial design was used (Table 3.1). This facilitated straightforward statistical analysis *via* an ordinary two-way ANOVA (or two-way repeated measures ANOVA, for time- and depth-series data), with related conventional *post hoc* testing.

Table 3.1 – The balanced, two-factorial experimental design used in Chapter 3

	chemical fertiliser (NPK)	organic fertiliser (bovine manure)
–basalt	×7 replicates	×7 replicates
+basalt	×7 replicates	×7 replicates

Adopting standard experimental protocols, sampling bias and pseudoreplication were mitigated through a fully-randomised complete block design, with random-isation of growth room locations, as well as in the orders of sampling and measurement.

Soil and plant sampling errors were reduced by processing all of the material from each system component into a single homogenised batch prior to subdivision. Instrument error was mitigated through appropriate standard calibration procedures.

3.1.3 Hypotheses

The co-application of manure with ultra-fine basaltic powder has no experimental precedent, so predictions for the likely outcome of the experiment were largely based on fundamental principles. It is reasonable, for example, to assume that plants cultivated in soil amended with chemical fertiliser will grow larger and faster than their counterparts in the organic regime, because agrochemicals are often designed to rapidly release nutrients. This may have secondary impacts on rhizospheric acidification, soil respiration and moisture, that could each feasibly affect weathering rates during the trial. Manure was also expected to affect topsoil hydrology, given its high water holding capacity (Vengadaramana, Jashothan and Thairiyanathan, 2019) which may increase weathering through higher mineral wetted SA (Section 1.4), but was also predicted to

introduce new geochemical properties into the soil, such as increased CEC (Hao and Chang, 2002). In this study, it was proposed that the removal of cations from pore waters, by adsorption onto OM, could lower mineral saturation states and, hence, encourage accelerated weathering rates (Section 1.4). The addition of new microbial communities (from within the manure material) was also theorised to be possibly beneficial for mineral weathering, if the resulting effect leads to increased soil respiration rates and, therefore, lower soil pH.

Based on the above considerations, the following hypotheses were tested:

(*H*4: 0) The basalt-related crop yield increase will be highest in the NPK regime.
(*H*4: 1) The basalt-related crop yield increase will be highest in the manure treatment.

(*H*5: 0) The rise in shoot Si after basalt is added will be highest in the NPK regime.
(*H*5: 1) The rise in shoot Si after basalt is added will be highest in the manure regime.

(*H*6: 0) The edible tissues of plants grown in basalt-treated soil will contain lower or statistically similar total masses of PTEs, compared with mineral-free controls.
(*H*6: 1) The edible tissues of plants grown in basalt-treated soil will contain significantly higher total masses of PTEs, compared with mineral-free controls.

(*H*7: 0) Leachate and pore water will contain lower or statistically similar DIC concentrations after basalt is applied.
(*H*7: 1) Leachate or pore water will contain significantly higher DIC concentrations after basalt is applied.

(*H*8: 0) Significant basalt-related soil pH rises will be highest in the NPK regime.
(*H*8: 1) Significant basalt-related soil pH rises will be highest in the manure regime.

(*H*9: 0) Cations weathered from the added basalt will not preferentially accumulate in the soil cation exchange pool, and will principally register in the plant and leachate.
(*H*9: 1) Cations weathered from the added basalt will preferentially accumulate in the soil cation exchange pool, rather than the plant and leachate.

(*H*10: 0) Basalt weathering and CDR rates will be highest in the NPK treatment.
(*H*10: 1) Basalt weathering and CDR rates will be highest in the manure treatment.

3.2 Materials and methods

3.2.1 Weathering reactor design and construction

Replicated mesocosms (n = 7; Figure 3.2) for the four soil treatments in this study (NPK *vs* manure; ±basalt) were constructed from two sections of PVC pipe, joined by a pair of PVC endcaps fixed in a back-to-back arrangement (152 mm internal diameter pipe, 160 mm internal diameter endcaps; Brett Martin, Newtownabbey, UK).

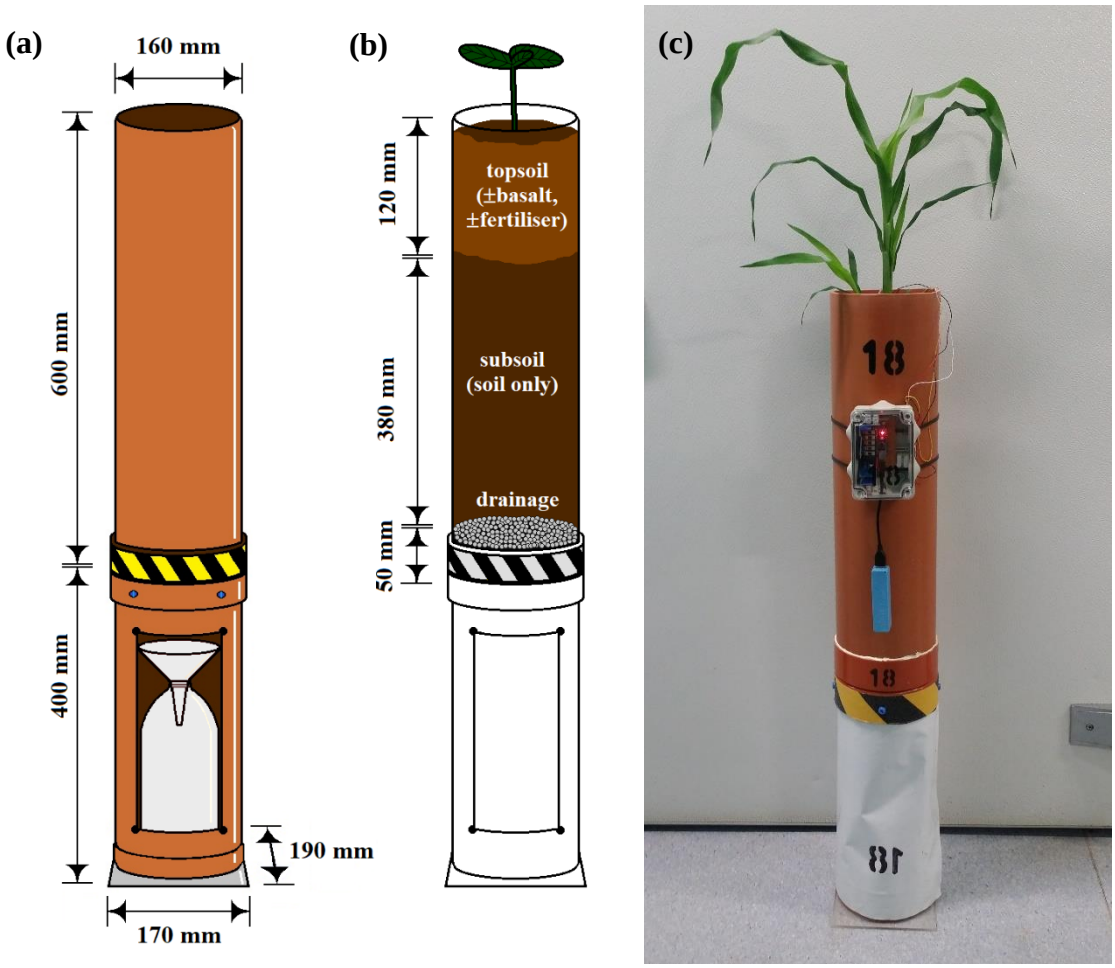

Figure 3.2 – Weathering reactor design. (a) Schematic diagram of mesocosm exterior, (b) cutaway indicating sub- and top-soil arrangement simulating a tillage regime, and (c) photograph of a weathering reactor, with 4-week-old *Sorghum* and custom-built soil moisture datalogger.

The freestanding mesocosms were stabilised with a 170 mm × 190 mm acrylic baseplate fixed to a further 160 mm internal diameter endcap that was attached to the lower pipe section. Weight-bearing external joints were secured with PVC weld cement (Tangit ABS; Henkel, Düsseldorf, Germany) and internal seals were formed from high-strength polyurethane sealant (PU18; Bond It Ltd, Elland, UK), to avoid Si contamination from Si-based sealants.

Substrate was loaded into the 600 mm-long upper section and leachate collection apparatus were housed in the 400 mm-long lower section (Figure 3.2a). The joint attaching these pipe sections was fitted with a 20 mm internal diameter nylon nozzle to direct leachate into a high-density polyethylene bottle *via* a polypropylene funnel (1 L narrow-neck polyethylene bottle, 150 mm lightweight polypropylene filter funnel; Azlon Ltd, Stoke-on-Trent, UK). Soil particle migration into the leachate nozzle was reduced by emplacing a 60 mm-deep drainage layer in the base of the substrate-holding top section, comprised of 20 mm diameter polyoxymethylene balls (Bearing Warehouse Ltd, Sheffield, UK), due to the high compressive strength and chemical stability of this material. A detachable 3-ply opaque mylar membrane (Reflex Total Blackout; GroWell Horticulture Ltd, Sheffield, UK) was fitted to the lower section to reduce algal growth in the leachate collection apparatus.

3.2.2 Substrate characterisation and preparation

Mildly acidic (pH 6.45) agricultural soil of clay-loam texture – 29.0, 34.3 and 36.7% by mass of clay (<2 µm), silt (2-60 µm) and sand (60-2,000 µm), respectively – was collected from farmland under *Brassica napus* (oil seed rape) cultivation at the Game and Wildlife Conservation Trust, Allerton Project, Leicestershire, UK (latitude 52.611286 ºN, longitude 0.831559 ºW). The soil had a CEC of 22.0 cmol (p+) kg^{-1} (based on concentrations of exchangeable Ca^{2+}, Mg^{2+}, K^{+}, Na^{+} and inferred H^{+}), with base saturation of 70.0%, calcium saturation of 63.4% and had a gravimetric water content (GWC) at field capacity of 0.68 g g^{-1}. The soil total carbon concentration was 2.3% (wt%) and the soil organic carbon concentration was 1.1% (wt%).

Soil clods were manually teased apart at 18 °C and stored in partially sealed poly-propylene bags to reduce moisture loss. Large stones (with diameters >20 mm) and invertebrates were removed before the soil was passed through a woven stainless-steel sieve (2 mm mesh size). After separation and sieving, the soil had a GWC of 0.28 g g^{-1}.

Organic fertiliser for the experiment was derived from bovine manure collected from Hope Farm, Hassop, UK. The manure was air dried for 30 days, then manually comminuted at 18 °C by passing it through a stainless-steel sieve (2 mm mesh size).

Mesocosms were filled with substrate in a sub- and top-soil arrangement to simulate a tillage regime (3:1 mass ratio of sub- to top-soil; Figure 3.2b). The total dry mass of soil in each mesocosm was 8.252 kg, which – being compacted to a column height of 500 mm – had an average bulk density of 0.91 kg L^{-1}. After subsoils were added and lightly compacted, columns were introduced into the controlled environment (see Section 3.2.4 for initial settings) and irrigated with 500 ml of water (purified by reverse osmosis) on four occasions between day –14 and day –1. This pre-conditioning was conducted to reduce background noise in the leachate geochemistry measurements, and to ensure that the variance in leachate volumes (*SE* = ≈ 1%) was tolerable. Basalt and fertiliser were added, as required, to the topsoil only and were mixed thoroughly into the substrate immediately prior to mesocosm filling on day 0. After loading and lightly compacting the topsoils, a pore water sampler (Model: macro-rhizon; Van Walt, Haslemere, UK) was installed in each column at a depth of 6 cm. A total mass of 91 g (equivalent to 5.0 kg m^{-2}) of basalt (see below) was added to each treated mesocosm. Soils treated with chemical fertiliser received individually weighed quantities of analytical-grade compounds (0.347 g of prilled urea, 1.633 g of powdered diammonium phosphate and 1.482 g of powdered potassium chloride), which were estimated to compensate for soil nutrient losses to the crop and leachate during the experiment. Mesocosms treated with organic fertiliser received 17.7 g (equivalent to 1.0 kg m^{-2}) of air-dried cow manure, which contained 2.57, 1.23 and 3.08% total nitrogen, phosphorus pentoxide and potassium oxide, respectively. The manure application rate was calculated to approximately equal the total nitrogen application rate in the chemical fertiliser treatment, being 25 g N m^{-2} (250 kg N ha^{-1}).

Soil pH was measured using a Jenway 3540 Combined Conductivity/pH Meter (Cole-Parmer Ltd, Stone, UK) calibrated with standard solutions at pH 4.00, 7.00 and 14.00. Prior to pH determination, a 15 g oven-dried, representative soil sample was thoroughly mixed with 30 ml of deionised water in a 100 ml borosilicate glass beaker using a glass stirrer. The solution was then left for 30 min before recording the pH of the slurry to 0.001 pH units. Soil exchangeable cations were extracted from a 2 g oven-dried,

representative soil subsample by agitation with 20 ml of 1 M analytical-grade ammonium acetate ($NH_4CH_3CO_2$; pH 8.5) for 2 hours at a 50 ° incline in a rotary shaker (Model: Stuart Rotator Disk SB3; Cole-Palmer Ltd, Stone, UK). The slurry was centrifuged (Model: Heraeus Megafuge 40; Thermo Fisher Scientific, Bremen, Germany) at 4,000 g for 10 min, passed through a 0.45 µm cellulose nitrate syringe filter (MiniSart; Sartorius, Goettingen, Germany) and acidified in a matrix of 2% analytical-grade nitric acid. Cation concentrations in the extract were then determined using an iCAP Q Inductively Coupled Plasma Mass Spectrometer (ICP-MS) (Thermo Fisher Scientific, Bremen, Germany) at the School of Biosciences, University of Nottingham (Sutton Bonington Campus), UK. This instrument was calibrated using multi-element internal and external standards derived from certified solutions. The limits of detection for each analyte are reported in Appendix G. Soil carbon measurements were made using a Vario EL Cube Carbon-Nitrogen Analyzer (Elementar, Stockport, UK), with SOC content determined by comparing C concentrations before and after soil treatment with 6 M HCl (soil:acid ratio of 90 mg to 0.5 mL) for 24 hours.

3.2.3 Basaltic rock characterisation and preparation

Crushed basalt of middle Miocene age and belonging to the 'Prineville Chemical Type Unit' of the Columbia River Basalt was sourced from the Cascade Range, Oregon (Central Oregon Basalt Products LLC, Madras, OR). The rock was passed through a series of stainless-steel sieves of decreasing mesh size (250 µm, 100 µm and 50 µm mesh size), suspended in analytical-grade ethanol and sonicated for 30 minutes in a 5 L Pyrex beaker to separate submicron particles from larger grains. The suspension was then left for 24 hours (sufficient to settle particles with diameters > 1 µm) after which the supernatant was decanted and the settled basalt material was exposed to the air for 72 hours to evaporate the residual ethanol. The particle size distribution of the treated basalt was measured using an LA-950 laser diffraction particle size distribution analyser (Horiba UK Ltd, Northampton, UK), where the particle diameter range was found to be 1.5–300 µm and the P_{80} value (the size at which 80% of the particles have diameters less than or equal to) was 35 µm (Figure B.6). The basalt mineralogy (Figure B.7) was determined by Dr A. Lewis *via* XRD analysis at the British Geological Survey (BGS) Keyworth laboratories, using the protocol reported in Lewis *et al*. (2021).

3.2.4 Plant materials

A single specimen of dwarf hybrid *Sorghum bicolor* (Pennsylvania 115, Oakbank Game and Conservation, Cambridgeshire, UK) was cultivated in each reactor column (Figure 3.2c). Approximately 600 seeds were germinated on filter paper (Whatman #1; Cytiva, Sheffield, UK) moistened with distilled water, placed in grip seal polyethylene bags and incubated at 25 °C in darkness for 24 hours. 144 seeds of similar radicle length (ca. 5 mm) were selected for planting in 24-cell seed trays containing soil from the same field site. Seed trays were transferred to a growth room and maintained at 60–70% relative humidity, with an 18-hour day length and 25/17 °C day/night temperatures. After 24 hours, 87 seedlings emerged from the soil, of which the 28 largest were grown for a further 9 days and chosen at random for transplantation to mesocosms on day 0.

Figure 3.3 – *Sorghum bicolor* growing in mesocosms within a growth room at the Sir David Read Controlled Environment Facility, Sheffield, UK.

Atmospheric CO_2 concentrations in the controlled environment (Figure 3.3) were automatically maintained at 400 ppm, to offset losses due to photosynthesis. A photosynthetic photon flux density of 800 µmol photons m^{-2} s^{-1} was maintained during the 18-hour days (apart from a 1-hour lighting ramp up/down during day/night transitions) between emergence and boot stage (day ≈60). Leaf length measurements were taken approximately every 3 days during this period. From day 61 onwards the day length was reduced to 10 hours and on day 115 (at physiological maturity) *Sorghum* seeds and shoots were harvested. Materials from the main stem and tillers were divided by tissue type, with younger leaves (leaf numbers 11–17) harvested separately from older leaves (numbers 1–10), stems and seeds.

Henceforth a fallow period was simulated by reducing the day/night temperatures to 5/3 °C and maintaining relative humidity at approximately 75% until the experiment was terminated on day 235. *Sorghum* roots were harvested during post-experiment soil

collection, after which they were subjected to a sequential washing process. Root materials were first thoroughly washed with tap water to remove the bulk of the attached soil from the tissues. Small batches of roots (≈5 g; fresh weight) were then transferred into a woven stainless steel sieve (150 µm mesh-size) and thoroughly rinsed with UHP water (<18.2 MΩ.cm) until the effluent ran clear. Root materials, including fine roots, were then removed from the sieve *via* floatation of cleaned tissues in UHP water, and manual extraction with tweezers. Root tissues were then dried in a forced-air oven at 60 °C for 48 hours (see Section 3.2.6 for details on pre-analysis sample preparation).

3.2.5 Irrigation regime

Throughout the *Sorghum* lifecycle, mesocosms were weighed every 3 days using a portable laboratory balance (Navigator NVT; Ohaus, Parsippany, NJ, USA) to estimate depth-averaged soil gravimetric water content (GWC). An artificial rainwater solution (Table 3.2) was then used to approximately compensate for soil water losses *via* evapotranspiration, with equal volumes of solution being supplied to each mesocosm (Figure 3.4). Irrigation water was delivered manually to the upper surface of each soil column using a 1.5 L low-pressure portable sprayer (Model: Exo Terra Mister; Rolf C. Hagen Inc., Montreal, Canada), with amounts measured gravimetrically to the nearest 1 g. On six occasions (approximately every 12 days between day 0 and day 80), equal volumes of additional irrigation solution were supplied to all soil columns to produce leachate for geochemical analysis. During the simulated fallow period (days 115–235) mesocosms were weighed every 14 days and variably irrigated to fix soil GWC at 0.38 g g^{-1}.

Table 3.2 – Chemical composition of the 'artificial rainwater' irrigation solution used in Chapter 3

Salt	Solution concentration (mg L^{-1})
$NaNO_3$	0.000135
NaCl	0.004790
$CaCl_2.2H_2O$	0.001100
K_2SO_4	0.000450
$MgSO_4.7H_2O$	0.002050
$(NH_4)_2SO_4$	0.002270

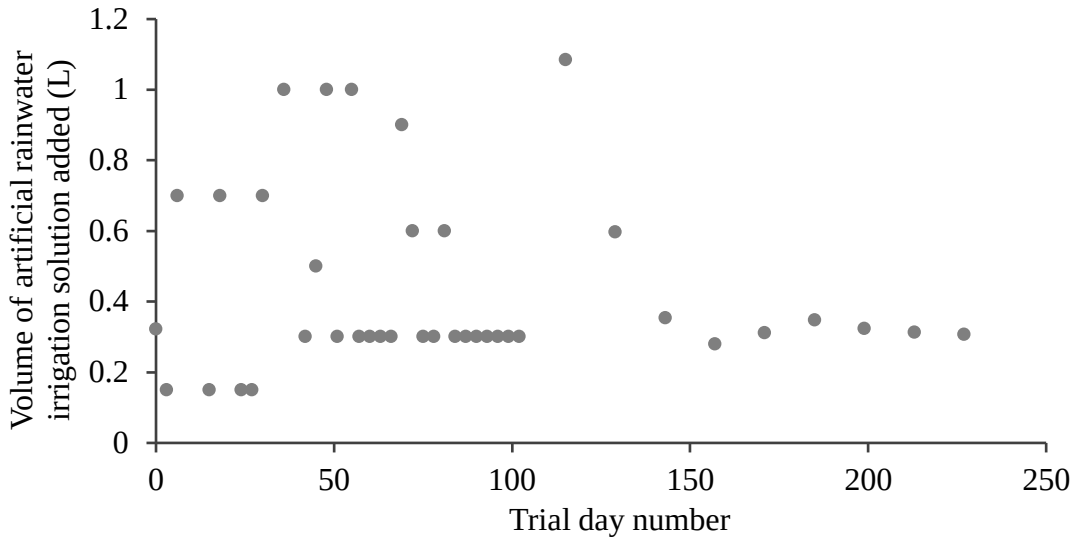

Figure 3.4 – Irrigation regime for Chapter 3. During the *Sorghum* lifecycle, plants in all treatments were irrigated with the same quantity of 'artificial rainwater', according to the above irrigation schedule. The amounts of water added were calculated to approximately compensate for soil water losses *via* evapotranspiration and leaching.

3.2.6 Leachate, soil and plant sample preparation and cation analysis

Leachate was prepared for cation analysis by filtration of subsamples through a 0.45 µm cellulose nitrate filter (Minisart: Sartorius, Goettingen, Germany) and stabilisation in a matrix of 2% (vol%) analytical-grade nitric acid. Harvested *Sorghum* root, shoot and seed tissues were dried in a forced-air oven at 60 ºC for 48 hours and comminuted separately using a laboratory grinding mill (Model: A10 S2, IKA-Werke GmbH & CO. KG, Staufen, Germany). Oven-dried, powdered tissue samples were then subjected to a 45-min microwave-assisted (Model: Multiwave; Anton Paar Ltd, St Albans, UK) nitric acid-hydrogen peroxide digest (0.2 g tissue:3 mL nitric acid:3 mL MQ water:2ml hydrogen peroxide), after which extracts were prepared for cation analysis by centrifugation and filtration of the supernatant through a 0.45 µm filter.

Substrate was excavated from the mesocosms in five layers: the topsoil/amended layer (0-12 cm depth), three intermediate subsoil layers (12-24, 24-36, 36-48 cm depth) and the bottommost subsoil layer (48-50 cm depth). Each layer was teased apart by hand into a bulk sample, homogenised, sieved (2 mm mesh size) and dried in a forced-air oven at 60 ºC for 48 hours. Soil exchangeable cations were then leached from representative soil subsamples using the ammonium acetate extraction protocol outlined in Section 3.2.2. Soil 'plant-available' Si concentrations were estimated using

an acetic acid (CH_3COOH) extraction, where 10 g of oven-dried soil was agitated with 25 ml of 0.5 N acetic acid at 25 °C for 18 hours at a 50 ° incline in a rotary shaker (Model: Stuart Rotator Disk SB3; Cole-Palmer Ltd, Stone, UK). The slurry was centrifuged (Model: Heraeus Megafuge 40; Thermo Fisher Scientific, Bremen, Germany) at 4,000 g for 10 min and passed through a 0.45 µm cellulose nitrate syringe filter (MiniSart; Sartorius, Goettingen, Germany), before Si analysis of the extract by ICP-MS (see below).

Multi-element cation analysis of all prepared leachate, plant and soil extracts was conducted at the School of Biosciences, University of Nottingham (Sutton Bonington Campus) using an iCAP Q ICP-MS (Thermo Fisher Scientific, Bremen, Germany), calibrated with multi-element internal and external standards derived from certified solutions. Instrument limits of detection for all measured analytes are reported in Table G.1. *Sorghum* tissue Si concentrations were determined by Dr. Sarah J. Thorne using the same XRF protocol and instrument specified in Section 2.2.5.

Leachate pH and alkalinity were determined using a fully-automated titrator (Model: 902 Titrando; Metrohm, Runcorn, UK) with sample carousel and robotic titro-sampler (Model: 855; Metrohm, Runcorn, UK). Destructive sampling of the relatively small (≈30 ml) pore water samples was prioritised for cation and anion analysis, rather than alkalinity measurements. Pore water pH was therefore determined using the aforementioned Jenway 3540 Combined Conductivity/pH Meter (Cole-Parmer Ltd, Stone, UK). Total dissolved C (TC) and total dissolved inorganic carbon (DIC) were measured using a total organic carbon (TOC) analyser (Model: TOC-L CPH; Shimadzu, Kyoto, Japan). Total dissolved organic carbon (DOC) levels were estimated by subtracting primary DIC measurements from TC values. Multipoint instrument calibration was achieved using manufacturer-recommended reagents prepared into at least three volumetrically-diluted standards spanning the full operational range of C concentrations.

3.2.7 Soil moisture probes and dataloggers

Custom-made dataloggers were prototyped and assembled to record soil moisture measurements from low-cost (£1), resistance-based soil moisture probes (Model: YL-69; unbranded; deployed in all 28 soil columns at four depths (6, 12, 24 and 48 cm). Datalogger functions were controlled by a programmable microprocessor (Model:

Nano; Arduino, New York, NY), interfaced with standard definition (SD) data storage and clock modules, which were housed in a water-resistant polycarbonate enclosure (Figure 3.2c). The C++ code managing the timings and storage of measurements by the was adapted from a similar bespoke system (ElectronicWings, 2017) and is presented in Appendix H.

Components were soldered together and switches to reverse the polarity of the voltage applied to the moisture probes were installed, and were periodically thrown to mitigate degradation of the stainless steel contacts in the probe unit through electrolysis. Moisture probes were hardened for the high water pressures expected in the deeper soil layers, through a series of water-proofing modifications designed to mitigate short-circuiting of the probe electronics or contacts. Metal contacts (other than the measuring surfaces) were first encased in a 5 mm-deep layer of melted bees wax, and after setting, probes were wrapped in three layers of poly-tetrafluoroethylene tape, fixed and protected by an outer layer of PVC tape. All 112 moisture probes were individually calibrated in the initial soil at five soil moisture levels, through extensive repeat testing in bulk soil samples with known gravimetrically-determined moisture content. Individual (exponential) calibration curves were then determined for each probe. Clock modules were also calibrated, due to observed variance in clock speed.

3.3 Results and discussion

3.3.1 *Sorghum bicolor* performance

All plants in this experiment received supplementary N, P and K (chemical or organic) fertiliser and grew around 2½ times more massive – trial average; mean whole-plant (dry) biomass = 130.7 ± 2.3 (*SE*) g plant^{-1} – than their counterparts in Chapter 2 (54.3 ± 1.2 (*SE*) g plant^{-1}), which received only equivalent N as urea. This fertilisation effect is implicated in several key inter-experimental differences identified in the datasets, and is well illustrated in Figure 3.5, which shows a comparison of time-series data from both trials, covering the first 60 days of the (115-day) *Sorghum* lifecycle. In this later study, relative increases in total leaf length (Figure 3.5a), a proxy measurement for leaf biomass, are coincident with increases in the cumulative water deficit (Figure 3.5b) –

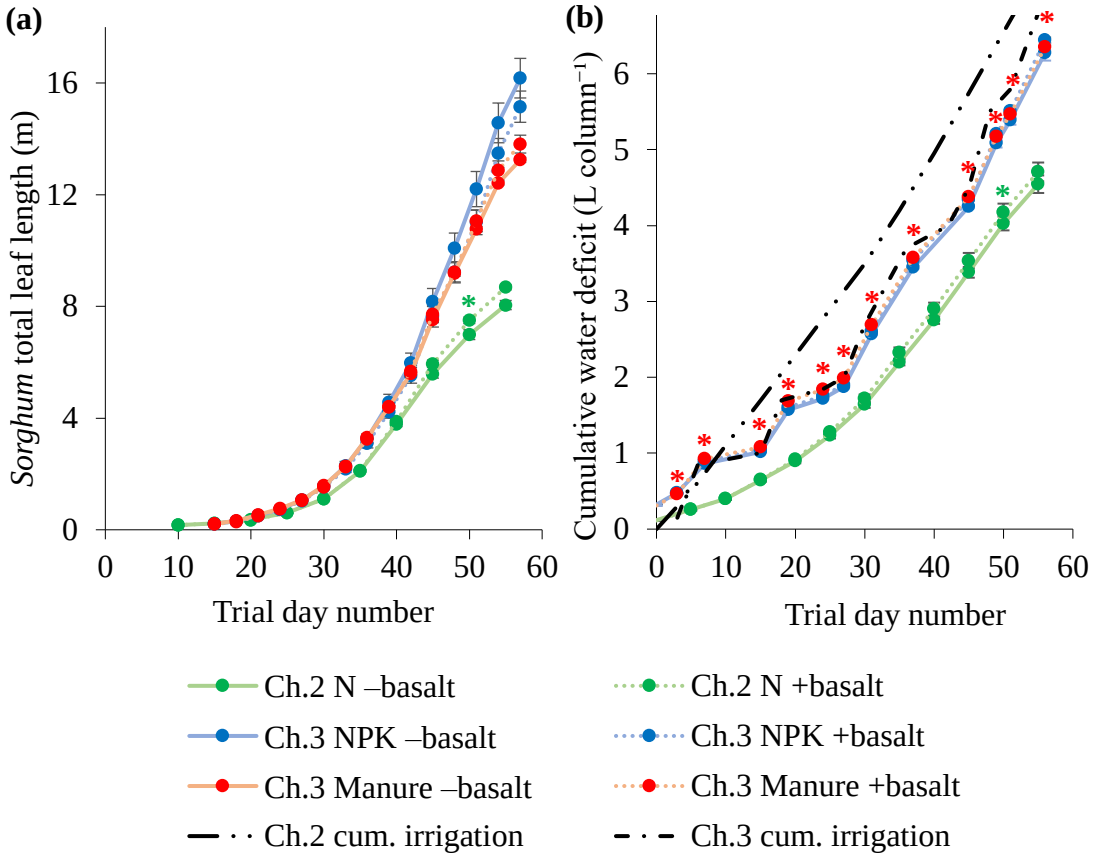

Figure 3.5 – Comparing the total length of *Sorghum* leaves, cumulative irrigation and water deficit volumes measured over the first 60 days of the experiments in Chapters 2 and 3. (a) a time-series comparison of *Sorghum* total leaf length (a proxy for leaf biomass), and (b) per column cumulative water deficit (see Equation 3.1) for both *Sorghum* trials. All statistical analyses were performed in R. Asterisks represent a statistically significant change (for the fertiliser with matching colour code) following basalt amendment to soil (Bonferroni adjusted *p*-value < 0.05; two-way repeated measures ANOVA; *n* = 6).

a measure of water loss from the system defined in Equation 3.1 as the cumulative per column difference between irrigation and leachate volumes (in units of L column^{-1}):

$$Cumulative\ water\ deficit = \sum_{i=1}^{n} I_i - L_i \qquad \textbf{Equation 3.1}$$

Where n is the total number of irrigation events, i is the order number for a particular irrigation event (i.e. for the 1st irrigation event, $i = 1$), I is the volume of irrigation water added, and L is the volume of leachate collected after the respective irrigation event.

As soil volumes were equivalent in both trials, higher cumulative water deficits in the second (Figure 3.5b) suggest that soils were relatively drier and/or evapotranspiration rates were comparatively higher. This is consistent with the longer leaf lengths measured (which imply higher water use; Figure 3.5a), and because total irrigation volumes during this timeframe were lower in the later study (Figure 3.5b), due to unintended constraints within the experimental design (see Section 3.3.3). Whilst *Sorghum* is commonly grown and well-adapted to perform in drier soils (Abreha *et al.*, 2022), the reduced availability of soil water in this experiment was probably sub-optimal for mineral weathering.

Following the application of basalt, total seed biomass per plant (Table 3.3) increased by a significant 13.8 ± 3.5% (*SE*) in the NPK fertiliser treatment of this study (one-way ANOVA; $p = 0.0008$) and rose by a significant 6.8 ± 2.7% (*SE*) in the manure regime also (one-way ANOVA; $p = 0.02506$), with no attendant increase in seed concentrations of PTEs (Section 3.3.2). Moreover, the positive effect on yield was highly significant across fertiliser type (two-way ANOVA; $p = 9\times10^{-6}$), but with no significant interaction effect between rock application and fertiliser regime.

These findings well reproduce the yield results from Chapter 2 (and research therein cited; Section 2.3.1), where a significant 21 ± 9.4% (*SE*) increase in seed biomass (one-way ANOVA; $p = 0.0214$) was achieved with a coarser grade of the same basalt material, but at twice the rock loading. The higher absolute yields in this trial are likely due to higher nutrient availability (from the added P and K fertilisers), with the biggest yields seen in the chemical fertiliser regime, doubtless due to the faster release rate of readily-available plant nutrients from the rapidly-dissolving synthetic compounds.

Table 3.3 – *Sorghum* root shoot and seed (dry) biomass after 115 days

Units: Biomass, g plant^{-1}		Chapter 3 Acidic (pH = 6.6), clay-loam soil			
		NPK fertiliser (n = 7)		Manure fertiliser (n = 7)	
	Treatment	Mean	*SE*	Mean	*SE*
Root biomass (0–12 cm depth)	–basalt	8.61	0.40	8.86	0.27
	+basalt	8.42	0.30	9.03	0.21
Root biomass (12–24 cm depth)	–basalt	1.97	0.06	1.45	0.03
	+basalt	2.00	0.11	1.80	0.03
Root biomass (24–36 cm depth)	–basalt	0.32	0.02	0.35	0.04
	+basalt	0.41	0.06	0.24	0.01
Root biomass (36–48 cm depth)	–basalt	0.20	0.03	0.16	0.01
	+basalt	0.23	0.03	0.32	0.06
Root biomass (48–50 cm depth)	–basalt	3.14	0.24	4.11	0.12
	+basalt	2.95	0.10	3.18	0.10
Total root biomass	–basalt	14.24	0.63	14.93	0.25
	+basalt	14.02	0.24	14.58	0.27
Main culm stem biomass	–basalt	36.36	0.52	37.15	0.32
	+basalt	33.90	0.30	38.24	0.69
Main culm leaf biomass	–basalt	20.29	0.43	18.39	0.15
	+basalt	18.38	0.12	18.16	0.35
Main culm seed biomass	–basalt	50.91	0.58	46.09	0.28
	+basalt	55.73	0.48	49.23	0.41
Tiller stem biomass	–basalt	5.90	0.22	2.24	0.05
	+basalt	7.13	0.37	3.09	0.06
Tiller leaf biomass	–basalt	12.20	0.20	5.19	0.07
	+basalt	11.79	0.22	6.85	0.13
Tiller seed biomass	–basalt	0.00	0.00	0.00	0.00
	+basalt	5.18*	0.38*	0.00	0.00
Total shoot biomass	–basalt	74.75	0.94	62.98	0.46
	+basalt	71.21	0.30	66.34	1.07
Total seed biomass	–basalt	**50.91**	**0.58**	**46.09**	**0.28**
	+basalt	**57.95**	**0.29**	**49.23**	**0.41**
Whole plant total biomass	–basalt	132.62	1.75	123.99	0.48
	+basalt	143.18	0.48	123.11	1.88

Values in red indicate a statistically significant effect (one-way ANOVA; $p < 0.05$) following basalt soil amendment, for the respective tissue and fertiliser. Emboldened values indicate a significant change (two-way ANOVA; $p < 0.05$) following basalt application, across both fertiliser treatments in the experiment. Blocks with peach backgrounds indicate a statistically significant interaction effect between basalt and fertiliser (two-way ANOVA; $p < 0.05$). All statistics were determined in R. Asterisks indicate that data are from the only three *Sorghum* specimens that bore seeds on their tillers.

The yield bonus following basalt amendment in the manure regime was not as large as the respective gains in the NPK treatment, which runs counter to initial predictions, as it was anticipated that the strong fertilisation effect from fast-acting chemical fertilisers would mask any contribution from the basalt towards overall nutrient demands. Yet the basalt fertilisation effect was most significant in the NPK regime, which indicates that it may have been driven by other factors – e.g. increased soil pH and the associated improvements in plant nutrient uptake efficiency (Roques *et al.*, 2013). Marginal and statistically significant increases in topsoil pH (in the NPK and manure treatments, respectively) lend support for a pH-driven basalt fertilisation effect (Section 3.3.4); however, this may have manifested differently in the two fertiliser regimes due to the high cation affinity of the OM added *via* the manure, which was in this trial very effective in suppressing pore water ion concentrations (Figures 3.11b, 3.12). Lower ionic strengths in the organic regime indicate that a proportion of the available cations – derived from the fertiliser, native soil or basaltic minerals – were sequestered from pore waters by sorption onto manure-derived OM. Manure-treated soils were, hence, subjected to a buffering influence that may have reduced the availability of weathering products in the pore waters, diminishing the basalt-related yield bonus in this regime. Accordingly, the respective null hypothesis (*H*4: 0) is not rejected, as the co-application of rock and manure did not produce a larger basalt-related yield bonus.

Crop yield data for the chemical fertiliser regime (Table 3.3) reveal a differential response to basalt soil amendment in the seed biomass produced by tillers – the side-shoots that can develop in this cultivar from the axillary buds of the 2nd, 3rd, 4th and 5th main leaves during vegetative growth. Notably, only 3 out of 28 plants in this study had tillers that produced seed, and all were in the NPK +basalt treatment (Table 3.3). Further interrogation of the leaf length data from both experiments indicates that a differential tiller response to the basalt application was measurable in the first few weeks of the *Sorghum* lifecycle, and is evidenced by differences in the total length of leaves from the main stem (Figure 3.6a) and tillers (Figure 3.6b; Table D.1). A retrospective analysis of the pilot study data from day 50 reveals that the significant 7.3 ± 1.2% (*SE*) increase in total leaf length following basalt soil amendment (Figure 3.5a; two-way repeated measures ANOVA; $p = 0.04$) is accounted for by a similarly significant 13.9 ± 2.8% (*SE*) increase in total tiller leaf length (Figure 3.6b; two-way repeated measures ANOVA; $p = 0.04$), with no significant change on the main culm (Figure 3.6a).

By day 57, plants within the manure treatment of this successor study also showed a significant (13.4 ± 5.3% (*SE*)) increase in total tiller leaf length (Figure 3.6b; two-way repeated measures ANOVA; p = 0.048), along with a significant 3.6 ± 1.2% (*SE*) decrease in total main culm leaf length (Figure 3.6a; two-way repeated measures ANOVA; p = 0.037). Due to improvements in tissue harvesting, leaf length results from this study are also supported by evidence from *Sorghum* biomass (Table 3.3; harvested after the 115-day lifecycle) which reveals a significant 31.9 ± 8.4% (*SE*) increase in tiller leaf biomass in the manure +basalt treatment, compared with rock-free controls (Figure 3.6b; one-way ANOVA; p = 0.002). Moreover, a statistically significant disordinal interaction was identified *via* multifactorial analysis (two-way ANOVA; p = 0.03), indicating that the effect of rock dust amendment on tiller biomass is dependent on the fertiliser regime.

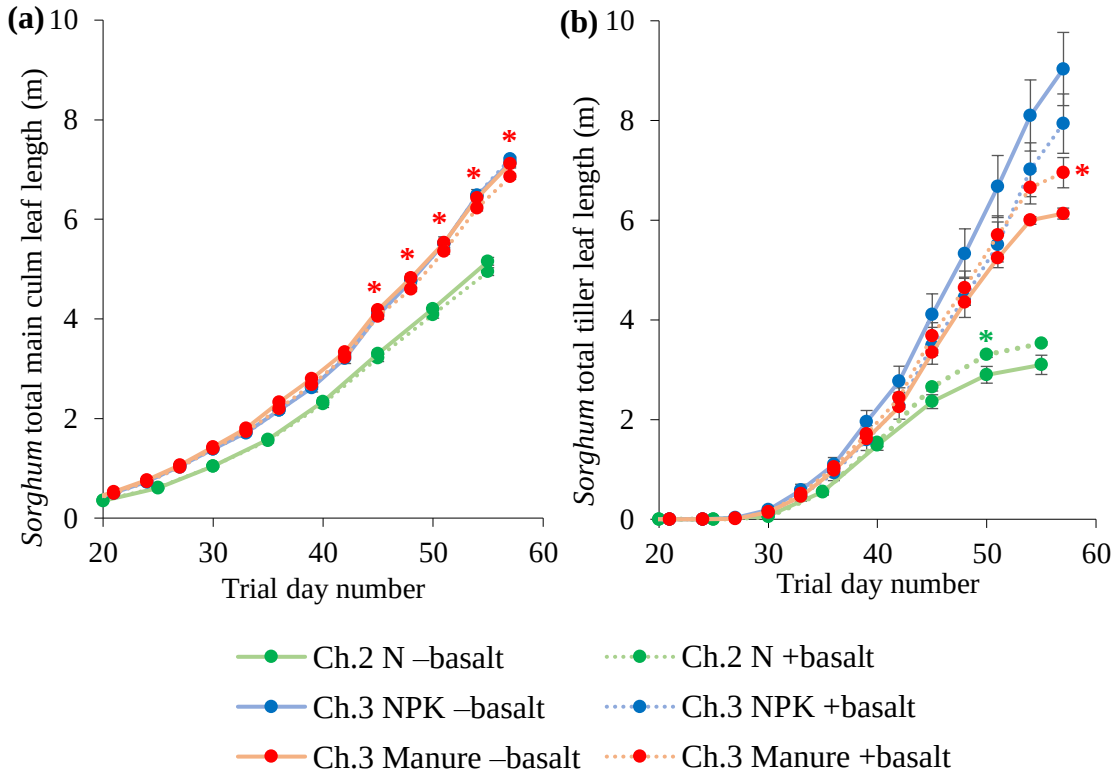

Figure 3.6 – Comparing the total length of *Sorghum* main culm and tiller leaves, measured over the first 60 days of the trials in Chapters 2 and 3. (a) a time-series comparison of the total length of *Sorghum* leaves on the main culm (a proxy for leaf biomass), and (b) the total length of *Sorghum* tiller leaves. All statistical analyses were performed in R. Asterisks indicate a statistically significant change following basalt amendment to soil (p < 0.05; two-way repeated measures ANOVA; Ch.2, n = 6; Ch.3, n = 7).

Increased tiller growth is generally advantageous for *Sorghum* performance, being associated with up to 80% of overall yields (Lafarge and Hammer, 2002). The tiller response is known to be suppressed by physical and chemical factors, such as low availability of light, assimilates, N or water (Lafarge and Hammer, 2002; Kim *et al.*, 2010). Under favourable conditions, tillers may develop independently from the main culm, with their own shoot and root systems, enabling greater flexibility for the plant to exploit available light and soil resources. Accordingly, the early suppression of a basalt-related tiller response in the chemical fertiliser regime may reflect the higher abundance of essential nutrients in the pore waters (supplied by the fast-acting N, P and K-containing synthetic compounds), such that plants were disincentivised from further colonisation of the soil to extract nutrients at this early stage of tiller development. This interpretation of the results from the NPK treatment is supported by *Sorghum* tissue data for this fertiliser type (harvested at the end of the lifecycle), which confirm no significant differences in shoot or root biomass allocation following basalt amendment (Table 3.3).

Root data from the manure treatment, reveal that the significant increase in tiller leaf biomass is accompanied by a significant 24.4 ± 9.4% (*SE*) increase (one-way ANOVA; $p = 0.01$) in root biomass within the 12–24 cm deep soil layer (the layer below the basalt-soil mixed layer), along with a corresponding and statistically significant 22.5 ± 8.7% (*SE*) decrease (one-way ANOVA; $p = 0.04$) in root biomass within the 48–50 cm deep soil layer (which sits above the drainage and is considerably wetter than other layers). These results indicate that plants in the organic fertiliser regime responded to the basalt treatment by preferentially colonising the soil layer best placed to intercept the downward flow of nutrients leached from the basalt. Moreover, the reduced allocation of root resources to the 48–50 cm deep soil layer indicates that the plants in this treatment may have prioritised nutrients over water. Further research is warranted to investigate the complex interplay between basalt soil treatments and plant growth characteristics. This could involve targeted, controlled experiments to determine the effect of basalt amendments on shoot and leaf morphology, photosynthesis rates, root colonisation responses and plant tolerances to water, nutrient and pathogen stresses. But in this study and for this cultivar of *Sorghum*, morphological divergence in response to the basalt treatment was dependent on the fertiliser regime and represented an early indicator of weathering.

3.3.2 *Sorghum* elemental budgets and tissue cation concentrations

Elemental budgets for the plants were calculated as the sum of all tissue-specific cation budgets, which are defined here as tissue analyte concentration × total tissue (dry) biomass for roots, shoots and seeds (Table D.2–3). *Sorghum* budgets made a proportionally larger contribution towards the overall mass balance in this study (Table 3.4–5), owing to the larger plants. Whole plant Si and Ca budgets were not significantly altered by the basalt treatment (Figure 3.7a–b), contrasting with results from the pilot experiment, where total plant uptake of these analytes increased significantly ($p < 0.05$).

In the present study, failure to detect any basalt-related changes in whole plant Si and Ca (or the chemically similar Sr; Figure 3.7f) could be due to the greater absolute budgets and large associated uncertainties (Table D.2–3), which likely lowered the signal-to-noise ratio of the basalt-related effects. Despite the meticulous sequential washing protocol applied to root material, these tissues were subject to a relatively higher risk of contamination from soil and additive compounds, which may explain the large associated errors (Table D.2–3). For this reason, differences in aboveground tissue concentrations are resolved with comparatively greater precision. In the manure fertiliser regime, basalt amendment was associated with a significant 11.4 ± 3.6% (*SE*) increase in total shoot Si, with respect to rock-free controls (one-way ANOVA; $p = 0.006$), so given the much weaker (and not statistically significant) effect in the NPK regime(Figure 3.7a), supports rejection of the respective null hypothesis ($H5: 0$) in favour of the alternative ($H5: 1$). These findings echo the similarly significant 30.2 ± 3.3% increase in shoot Si in the first *Sorghum* trial (Section 2.3.2). In this later study, tissue-wise analysis of *Sorghum* materials indicates that the significant increase in shoot Si is principally driven by significantly ($p < 0.05$) higher Si concentrations in younger leaves (tiller and main culm leaves 11–17) and stems, as was observed in both fertiliser regimes (Figure D.1). Importantly, this increase was achieved against high background levels of plant-available silicon in the soil (300–400 mg Si g^{-1}; Section 3.3.5), which are likely to far exceed the critical limit (Korndörfer *et al.*, 2001; Mahendran *et al.*, 2021), and contrasts with results from a field trial with rice using silica slag as the soil amendment (Paye *et al.*, 2018), where strong effects were generally observed in the most depleted soils. Increased shoot Si is associated with a range of improvements in *Sorghum* performance, such as drought tolerance (Abreha *et al.*, 2022), protection from lodging and resistance to fungal pathogens (De Lima *et al.*, 2019). Hence, the repeated results lend support for the use of crushed basalt as a supplementary Si fertiliser.

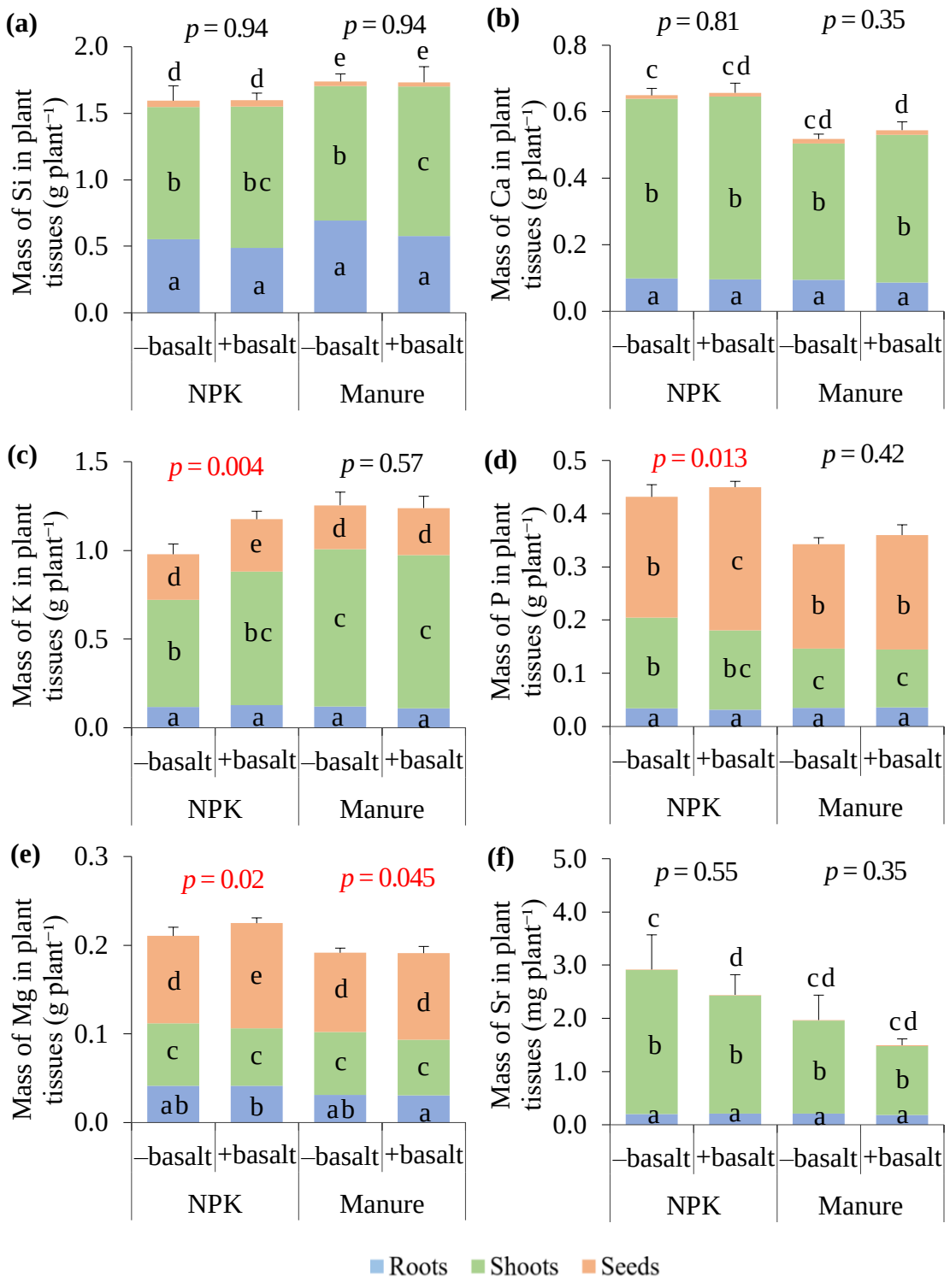

Figure 3.7 – Effect of basalt-amended soil on total *Sorghum* tissue elemental budgets in Chapter 3. (a) silicon, (b) calcium, (c) potassium, (d) phosphorus, (e) magnesium and (f) strontium. Error bars represent *SE* in the mean for total analyte mass. Bars sharing the same letter are not statistically different ($p > 0.05$; one-way ANOVA with Tukey *post hoc* test). Stated p values relate to significant differences ($p < 0.05$; one-way ANOVA) in total analyte mass following the application of basalt, for the fertiliser treatment, and were determined in R. $n = 7$.

Whole plant K in the chemical fertiliser regime increased by a significant 24.9 ± 8.1% (*SE*) (one-way ANOVA; $p = 0.004$) following basalt application, driven in part by a significant 15.0 ± 5.0% (*SE*) increase (one-way ANOVA; $p = 0.007$) in the seed K budget (Figure 3.7c). These increases are similar in magnitude to the 16.5% increase in ryegrass K concentrations measured following amendment of a K-depleted sandy soil with the silicate mineral, olivine, where no accompanying increase in P concentrations was observed (ten Berge *et al.*, 2012). In the present study, however, whole plant P did increase significantly (12.8 ± 4.8% (*SE*); one-way ANOVA; $p = 0.01$) in rock-amended NPK-fertilised soil (Figure 3.7d), dominated by significant gains (18.4 ± 7.0% (*SE*); one-way ANOVA; $p = 0.01$) in the seed P budget (Figure 3.7d). Overall plant P and K budgets in the manure treatment were not significantly affected by the addition of basalt (Figure 3.7c–d), although a significant increase in seed P concentration was detected (18.4 ± 7.0% (*SE*); one-way ANOVA; $p = 0.01$).

No significant differences in primary nutrient budgets were detected in soils treated with basalt in the previous *Sorghum* study, despite the absence of chemical P and K fertiliser in that trial, which was intended to incentivise basalt colonisation by the plant/AMF. Hence, in the NPK treatment of this later study, the increased uptake of cationic macronutrients following basalt amendment could indicate faster weathering of P and K from primary minerals, or may be explained by pH-driven improvements in nutrient uptake efficiency, which in this regime amounts to the amplification of an already high nutrient baseline. These findings, coupled with the yield results (Section 3.3.1), indicate that a significant fertilisation effect occurred after basalt amendment to soils treated with chemical and organic fertilisers, with the biggest overall rise in crop performance seen in the former.

Total plant Mg budgets (Figure 3.7e) rose significantly following basalt amendment of NPK-treated soil (14.5 ± 6.3% (*SE*); one-way ANOVA; $p = 0.024$). This, again, differs from the results in Chapter 2, where no significant effects on *Sorghum* Mg content were determined (Section 2.3.2), but is more in line with the 44 % increase in ryegrass Mg concentrations measured in a previous pot trial (ten Berge *et al.*, 2012) following a considerable dose of the fast-weathering magnesium-silicate, olivine. In the present study, and for ten Berge *et al*. (2012) also, soil background Mg levels were relatively low (Section 3.3.4), and so the measured increase in total plant Mg represents strong evidence for mass transfer from primary minerals into the plant, because the only supplementary source of Mg was the added basalt. Mg can exhibit high mobility in soils, but has a high charge affinity (Gransee and Führs, 2013), and so the evidence for

lower plant Mg content in the organic fertiliser regime lends support to the suggestion that cations weathered from the rock may have been preferentially adsorbed by OM within the manure, and were therefore less available for uptake by the plant.

Seed concentrations of PTE associated with basic rocks (Cd, Cr, Cu, Ni, Pb) were all either unchanged or significantly ($p < 0.05$) lower following basalt application in both fertiliser regimes (Table D.2–3), which aligns with similar findings in Chapter 2, and suggests the null hypothesis (*H*6: 0) should not be rejected. In the NPK fertiliser regime, seed Cr concentrations reduced by a significant 28.9 ± 8.2% (*SE*) compared with control plants (one-way ANOVA; $p = 0.01$), and Ni was also significantly reduced in the seed (28.7 ± 5.7% (*SE*); one-way ANOVA; $p = 0.002$). The effect of basalt on seed PTE concentrations may be partially explained by the increased seed yield following rock application, which can dilute tissue concentrations of assimilated metals. But it is likely also due to a reduction in mobility of these relatively high-atomic mass metals in soils, which is known to be induced by relatively minor pH increases (M. M. Sintorini *et al.*, 2021), and could well be associated with the effects of basalt weathering. Accordingly, the basalt application had no adverse effect on PTE concentrations in any plant tissues (Table D.2–3).

3.3.3 Soil moisture

In this experiment the maximum irrigation rate was constrained by design factors, such as the selection of a low-permeability clay-loam soil that is prone to flooding when close to field capacity, yet shrinks and cracks when dry. This necessitated careful maintenance of soil moisture in all replicates, which was difficult to achieve in practice, and was regularly frustrated by the need for very slow delivery of irrigation water to the soil surface to prevent flooding. The relatively small surface area available for water influx into the mesocosm – compared with the total surface area available for efflux *via* the plant, soil surface and effluent – likely limited peak soil moisture, particularly under maximum *Sorghum* canopy cover (boot stage; day ≈60). Unlike the pilot experiment, the present study was designed to generate leachate on-demand according to a 12-day aqueous sample collection and analysis schedule, with additional water supplied on a 3-day cycle to account for evapotranspirative loses only. The quantity of water added for leachate production and tri-daily maintenance was the same for all treatments, and was determined according to ground-truthed whole-column GWC values from the driest soil treatment. However, due to variable water usage between treatments, the uniform irrigation rate and inter-treatment fertilisation differences led to divergent soil moisture conditions (Figure 3.8), which may have affected weathering rates in this trial.

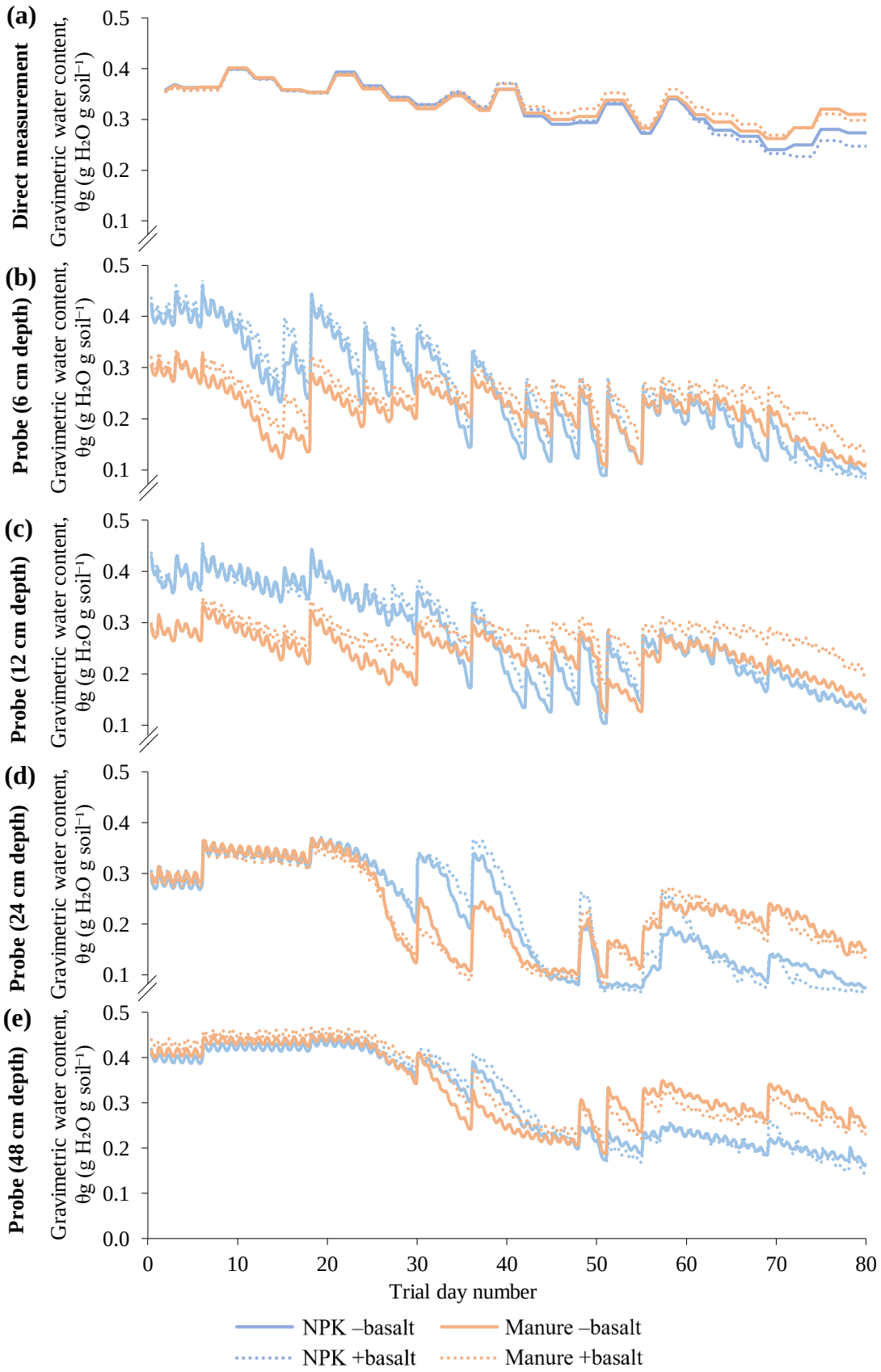

Figure 3.8 – Soil gravimetric water content over the first 80 days. Charts show (a) gravimetrically-determined soil moisture content (3-day moving averages; synchronised with the 3-day irrigation and weighing schedule), and (b–e) estimated GWC based on data from calibrated soil moisture probes from four soil depths (6, 12, 24 and 48 cm; 3-hour moving averages).

Soil moisture data obtained directly by weighing the columns (Figure 3.8a) are a simple yet reliable measure of whole-column GWC. Errors due to variations in plant biomass between treatments are likely to be small, as there were no significant differences in total root biomass at the end of this study (Table 3.3) and the largest inter-treatment difference in total shoot (fresh) biomass (on day 115) was only 0.016 ± 0.009 (*SE*) kg – i.e. an error of around 0.2 ± 0.1 %, given the minimum whole-column soil (dry) mass of 8.252 ± 0.001 (*SE*) kg. Multifactorial analysis of these direct observations (two-way repeated measures ANOVA; Figure 3.7a) indicates no statistically significant effect of basalt on GWC in either fertiliser regime ($p > 0.05$), but does suggest that significant differences in soil moisture *between* fertiliser regimes had developed by day 63 (two-way repeated measures ANOVA; $p < 0.04$). Specifically, through comparatively higher evapotranspiration rates, plants enlarged by the effects of the chemical fertiliser probably developed lower average soils moisture than their counterparts in the organic regime (Figure 3.8a).

Data from the experimental soil moisture probes (Figures 3.8b–e) well match the steady decline in GWC evidenced by direct gravimetric measurements (Figure 3.8a), albeit with much higher background noise. Resistance-based soil moisture probes such as these are prone to interference from a range of sources, such as changes in pore water EC driven by temperature (Hayashi, 2004) or the release/removal of ions into/out of solution due to weathering and cation exchange processes. The influence of temperature manifests here as a diurnal oscillation superimposed on the dataset (Figure 3.8b–e) driven by regular daily temperature swings in the growth room, and is therefore straightforward to account for. Correcting for changes in pore water ionic strength is more challenging, however, but necessary, because resistance-based probes will erroneously register an influx of weathered cations as an increase in soil moisture. Ultimately, porewater measurements were not frequent enough to accurately compensate for this effect, and so the underlying signal could not be satisfactorily decoupled. Nonetheless, probe data permit a qualitative assessment of broad hydrological changes that may have occurred during the first 80 days of the trial. Notably, the greatest extremes in soil moisture were measured in the uppermost layer (6 cm depth), consistent with it being closest to the irrigation source, heavily colonised by *Sorghum* roots (Table 3.3) and proximal to the column's main surface of evaporation. Data from the deepest probes (24 and 48 cm) also imply that GWC is largely unchanged in the subsoil until *Sorghum* roots reach this reservoir (day ≈25;

Figure 3.8e). Such insights are broadly consistent with the other datasets in this study, but more-reliable data could potentially be used for improved geochemical modelling of mesocosm-scale weathering. It is unclear, however, if moisture probes operating *via* other principles – capacitance, time domain reflectometry (TDR), frequency-domain sensors (FDS) etc. – would satisfactorily mitigate the issues faced in this experiment.

3.3.4 Leachate and pore water geochemistry

Improving on the predecessor, this study was designed to resolve small differences in leachate geochemistry between experimental treatments *via* the inclusion of additional analytes, high-precision instrumentation and increased statistical power. Further depth was also added through better monitoring of the water mass balance, which revealed significantly reduced leachate volumes in the NPK (–12.8 ± 2.1% (*SE*); $p = 0.011$) and manure regimes (–23.4 ± 1.8% (*SE*); $p = 0.0002$) during the first leaching event after basalt was added (Figure 3.8a; pair-wise comparison; two-way repeated measures ANOVA). The physical properties of milled basalt are implicated in this early divergence, rather than selection bias, because baseline effluent volume testing indicated low variance in the subsoils being conditioned (*SE* ≈ 1%). Specifically, the fine oven-dried basalt powder – which, like manure, has a non-negligible water holding capacity – is proposed to have intercepted irrigation water added to the topsoil during the first week, lowering efflux *via* the leachate. Ultimately, the sequestered water was lost through evapo-transpiration as it is does not register in the GWC record (Figure 3.8a), and whilst it is unclear if this conferred any early performance benefit to the plants, the lower flow rates evidently affected leachate elemental concentrations and mass budgets (Figure 3.9).

Basalt additions did not significantly affect leachate pH, EC or alkalinity during the study (Figure 3.9b-d), according to a time-wise analysis of the datasets (two-way repeated measures ANOVA; $p < 0.05$). In the manure regime, however, a significant 106.2 ± 28.1% (*SE*) increase in cumulative effluent DIC ($p = 0.042$) is resolved 70 days after the basalt was applied (Figure 3.9e), concomitant with reduced (but not significantly lower) DOC budgets at this timepoint (Figure 3.9f). DIC and DOC budgets were both generally higher in the NPK treatment where basalt was added, notably from day ≈35 onwards, but did not evolve significantly during the trial (two-way repeated measures ANOVA). Hence, there is only partial support for the related alternative hypothesis (*H*7: 1), as a significant increase in DIC was only seen in the manure regime.

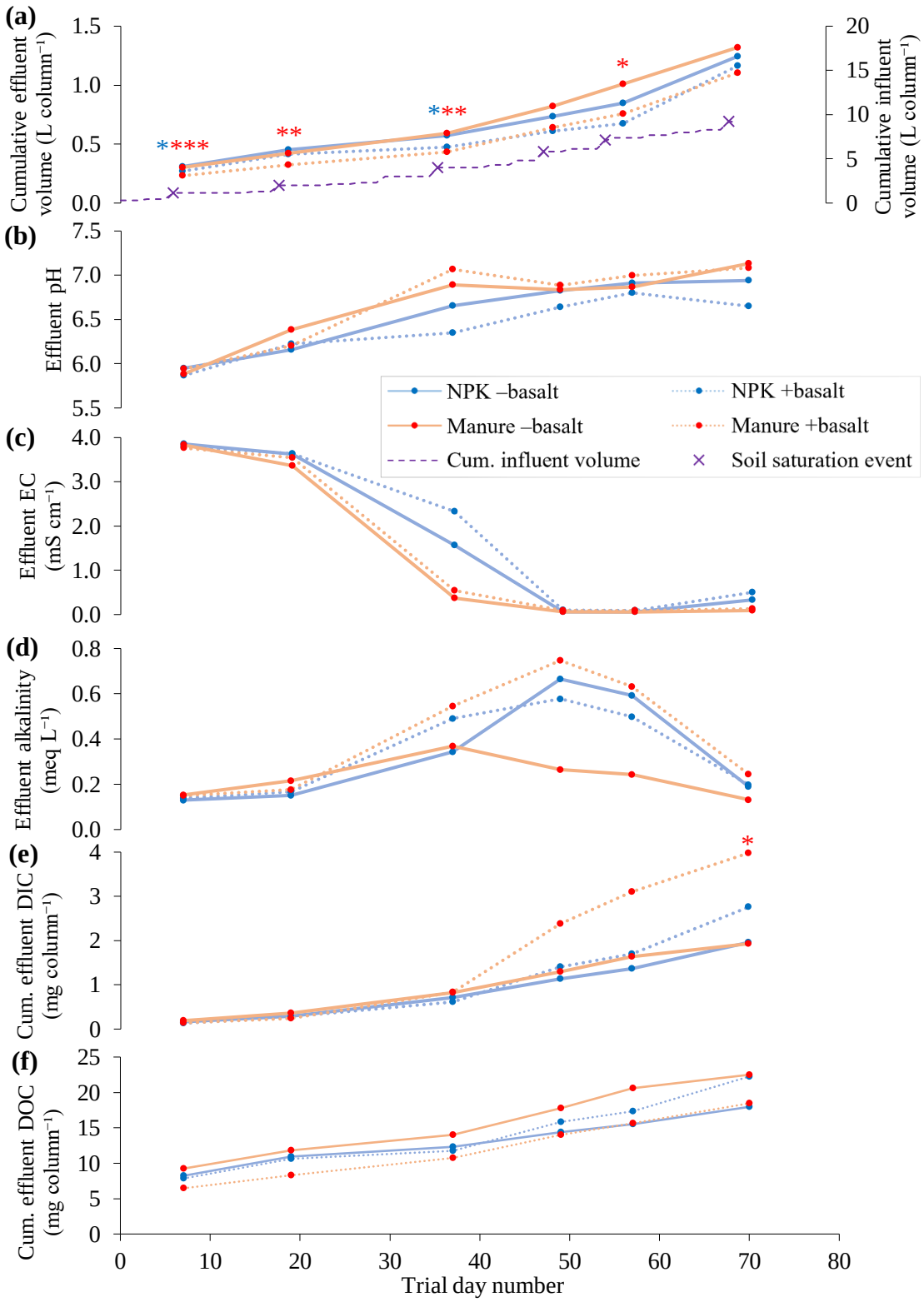

Figure 3.9 – Leachate geochemistry time-series. 70-day time-series for (a) influent and effluent volumes, and effluent (b) pH, (c) EC, (d) total alkalinity, and cumulative flux of (e) inorganic and (f) organic carbon. Soil saturation events (to force effluent production) are marked as purple crosses. Single asterisks indicate a statistically significant change following basalt amendment to soil ($p < 0.05$; two-way repeated measures ANOVA; $n = 7$). Double asterisks indicate that $p < 0.01$. Triple asterisks indicate that $p < 0.001$. Solid and dotted lines do not indicate data interpolation and are purely for ease of visual reference. Error bars are omitted for clarity. All statistical analyses were performed in R.

These large changes in dissolved C notably occur at a time of reduced soil moisture (Figure 3.8a) and low leachate volumes (Figure 3.9a), coinciding with the rapid expansion of *Sorghum* canopies between growing point differentiation (day ≈35) and boot stage (day ≈60). The higher DIC export from basalt-amended soils may therefore be linked to enhanced primary production over this timeframe, along with associated increases in soil respiration (Zak *et al.*, 2000) that should elevate soil pCO_2, and hence drive additional DIC into pore waters. The corresponding marginal decrease in effluent DOC in the Manure +basalt treatment is consistent with autotrophic respiration (which converts organic C to inorganic C), and that *increased* DOC was observed in the chemical fertiliser regime may simply reflect the larger basalt fertilisation bonus in this treatment (Section 3.3.1).

Time-wise comparisons (two-way repeated measures ANOVA) of cumulative effluent budgets for key elements of interest (Ca, Mg, K, Na, Si) indicate that rock-related effects in the NPK treatment develop significance at the first timepoint only (Figure 3.10), along with a significant reduction in leachate volume (Figure 3.10a). Budgets in the manure regime are, however, consistently and significantly ($p < 0.05$) lowered by the addition of basalt (two-way repeated measures ANOVA), with the reduced totals reflecting low efflux rates (Figure 3.9a). The drop in leachate volumes is immediate (day 7; Figure 3.9a), which implicates the enhanced water holding capacity of the co-deployed manure and rock mixture, along with related fertilisation effects from mineral weathering. Indeed, interception of irrigation water by topsoil OM and finely-milled basalt may well explain the early morphological divergence and preferential allocation of roots to shallower depths observed in this treatment (Section 3.3.1).

Mean effluent concentrations of nitrate, sulphate, PTEs (As, Cd, Co, Cr, Cu, Ni, Pb) and other metals of interest (Al, Fe, Mo, Sr, Ti) were suppressed following basalt amendment, in both fertiliser regimes (Tables E.2–4). This is partly an effect of lower leachate volumes, but for high-atomic mass metals, likely also due to pH-induced reductions in metal mobility (Sintorini *et al.*, 2021) associated with the alkalising properties of basalt.

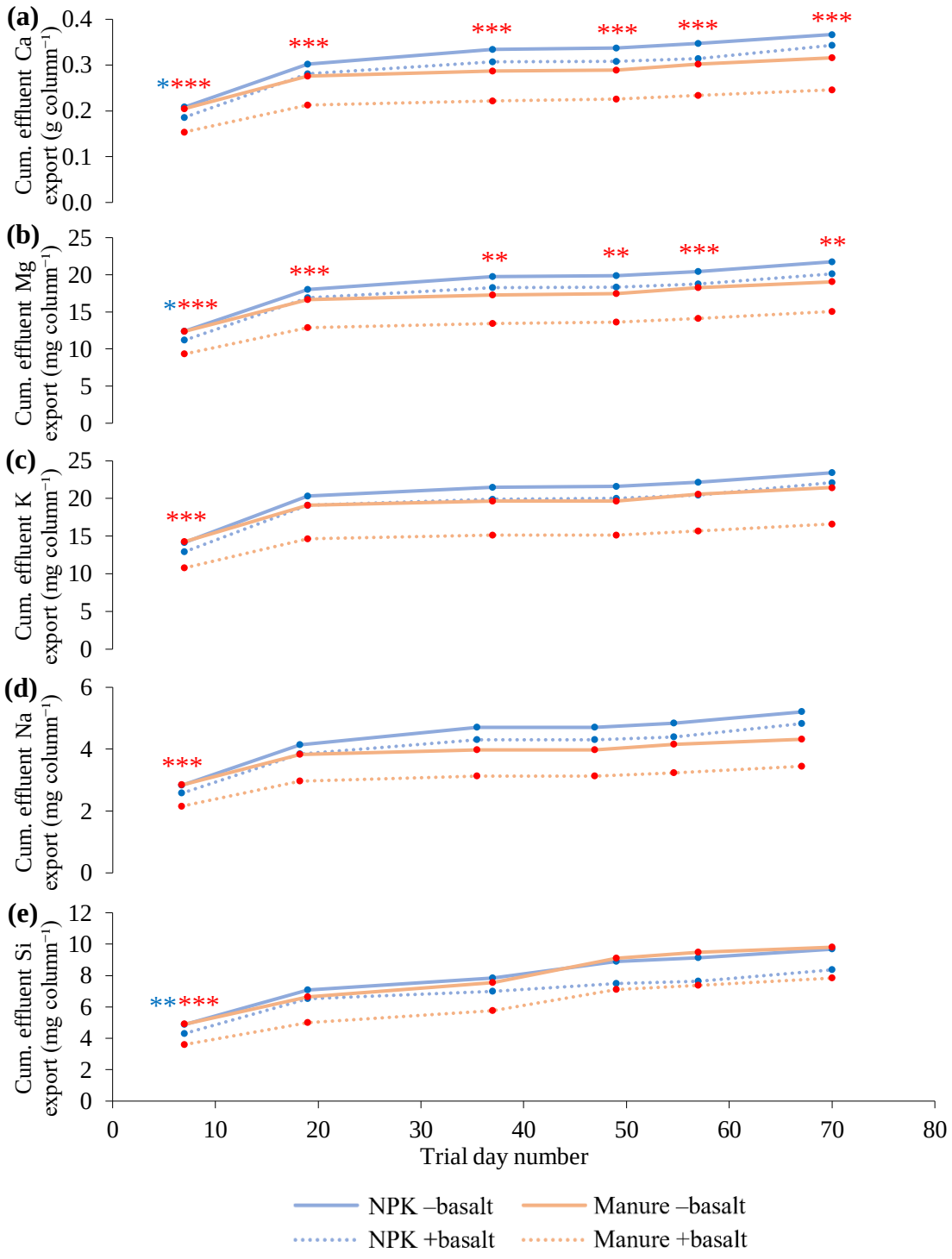

Figure 3.10 – Leachate major cation and Si budgets, time-series results. 70-day effluent time-series for elemental budgets of (a) Ca, (b) Mg, (c) K, (d) Na, and (e) Si. Single asterisks indicate a statistically significant change following basalt amendment to soil ($p < 0.05$; two-way repeated measures ANOVA; $n = 7$). Double asterisks indicate that $p < 0.01$. Triple asterisks indicate that $p < 0.001$. Solid and dotted lines do not indicate data interpolation and are purely for ease of visual reference. Error bars are omitted for clarity. All statistical analyses were performed in R.

Pore water samples – extracted in this study *via* rhizon samplers, buried 6 cm deep in the soil – offer snapshots of the geochemical processes occurring in the topsoil over time (Figure 3.11), with superior signal strength, noise reduction and sample preservation, compared to leachate. Soil solution pH did not significantly change over time (Figure 3.11a), perhaps due to the soil's considerable pH buffering capacity, or because pH changes were moderated by other biogeochemical processes. Pore water EC was significantly higher in the NPK regime, for the first leachate event only (two-way repeated measures ANOVA; $p = 0.032$), which is likely due to the release of ions from a fast-weathering component of the rock. As with the leachate (Figure 3.9e–f), pore water carbon levels are increasingly perturbed as the thriving plants transition from vegetative into reproductive growth (day ≈35–60; Figure 3.10c–d). Here, in the Manure +basalt treatment, a highly significant ($p < 0.01$) 79.8 ± 16.1% (*SE*) increase in DIC is mirrored by an equally significant ($p < 0.01$) 36.7 ± 6.6% (*SE*) reduction in DOC by day 57 (Figure 3.10c–d). Again, this trend is consistent with increased autotrophic respiration in the co-treated soil, but may also be affected by interactions between DOC and mineral surfaces or weathering products, which can have a stabilising influence and may improve soil OM retention (Kaiser and Zech, 2000). Again, due to the weaker (not significant) effect in the NPK regime, there is only partial support for the related alternative hypothesis (*H7*: 1).

Pore water concentrations of major cations are minimal (Figure 3.12) when DIC/DOC differences in the co-applied soil develop significance (day ≈57; Figure 3.11c–d), indicating that the soil water C budget was probably dominated by the effects of increasing belowground allocation of photosynthate by the cover crop. This higher implied pCO_2 in the topsoil amended with basalt and manure (Figure 3.11c) should theoretically be conducive to accelerated mineral weathering rates (Section 1.3). In NPK-treated soils, the significant increase in pore water DIC is small yet practically immediate (day 7; Figure 3.11c), consistent with the rapid dissolution of a fast-weathering mineral or small basalt particles with a relatively high SA:mass ratio. The significant reduction in DOC is equally abrupt in the organic regime (day 7; Figure 3.11d) and, given the lesser influence of the smaller plants, could be more affected by OM-mineral interactions (Jagadamma *et al.*, 2014).

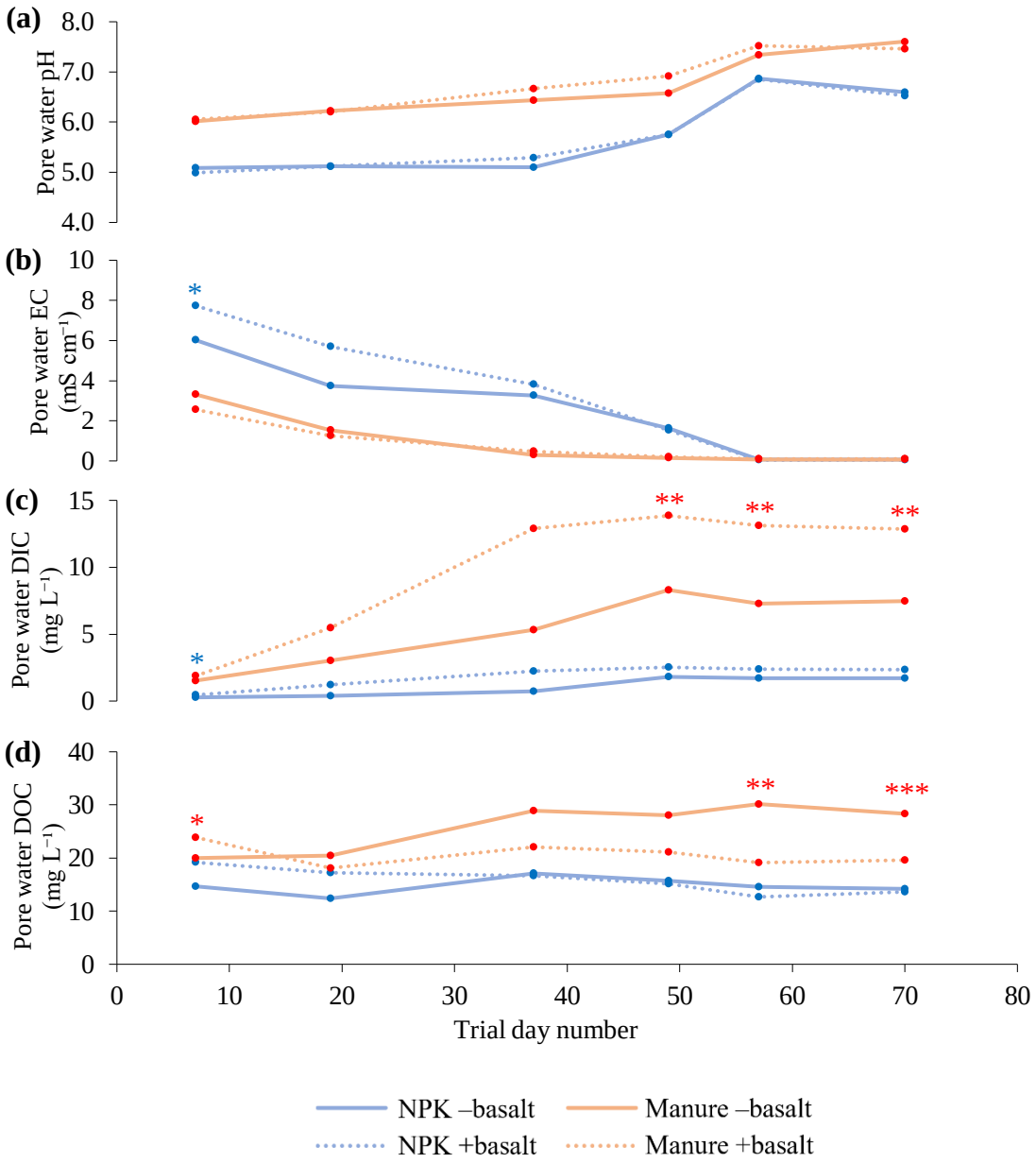

Figure 3.11 – Pore water geochemistry time-series. 70-day time-series for pore water (a) pH, (b) EC, and dissolved (c) inorganic and (d) organic carbon. Soil saturation events (to force effluent production) are marked as purple crosses. Single asterisks indicate a statistically significant change following basalt amendment to soil ($p < 0.05$; two-way repeated measures ANOVA; $n = 7$). Double asterisks indicate that $p < 0.01$. Triple asterisks indicate that $p < 0.001$. Solid and dotted lines do not indicate data interpolation and are purely for ease of visual reference. Error bars are omitted for clarity. All statistical analyses were performed in R.

Records of the evolution of pore water cation concentrations in the different treatments (Figure 3.12) provide evidence for a contrasting dynamic response to basalt soil amendments. In the NPK treatment, the response is characterised by rapid and highly significant (day 7; $p < 0.01$) increases in Ca, Mg and Na concentrations (Figure 3.12,b,d), along with less significant ($p < 0.05$) increases in K and EC in the pore waters (Figures 3.12c and 3.11b). These strong early signals of mineral weathering then lose significance as the trial proceeds, coincident with progressively reduced soil water cation concentrations as the plants grew larger, took up more water and nutrients and, hence, exerted greater control over pore water chemistry. Plant uptake of weathered cations (along with associated soil biogeochemical processes) is therefore implicated in the loss of the initial pore water weathering signal, and is consistent with significantly increased whole-plant K and Mg budgets (Figure 3.7c,e). Whilst the concentrations of all major cations (Ca, Mg, Na and K) generally reduce as the experiment proceeds (Figure 3.12), there are no clear numerical relationships between these elements.

Pore water Na concentrations, which in the NPK regime are on average 35.4 ± 21.1% (*SE*) higher in concentration after basalt is added, achieve statistical significance from the very first measurement (day 7; two-way repeated measures ANOVA; $p < 0.01$; Figures 3.12d) and present alongside a similarly significant 34.4 ± 20.7% (*SE*) increase in Cl^-. This close stoichiometric relationship is strong evidence for the rapid dissolution of common salt (NaCl; which has no direct impact on CDR), perhaps introduced into the experiment as small quantities of mineral halite (NaCl) in the rock dust, or otherwise mobilised from the soil and/or irrigation water by the basalt. Rapid influx into pore water solutions of the other major cations is, however, consistent with the weathering of primary Ca-, Mg- and K-bearing silicate minerals, although also consistent with the dissolution of Ca and Mg carbonates. The influx of divalent cations from either pathway could potentially invoke a K-driven fertilisation effect, as was observed for olivine dissolution in a nutrient-poor sandy arable soil (ten Berge *et al.*, 2012), where weathered release of Mg^{2+} from the ultramafic mineral is believed to have displaced bio-available K^+ from exchange sites within the K-depleted substrate.

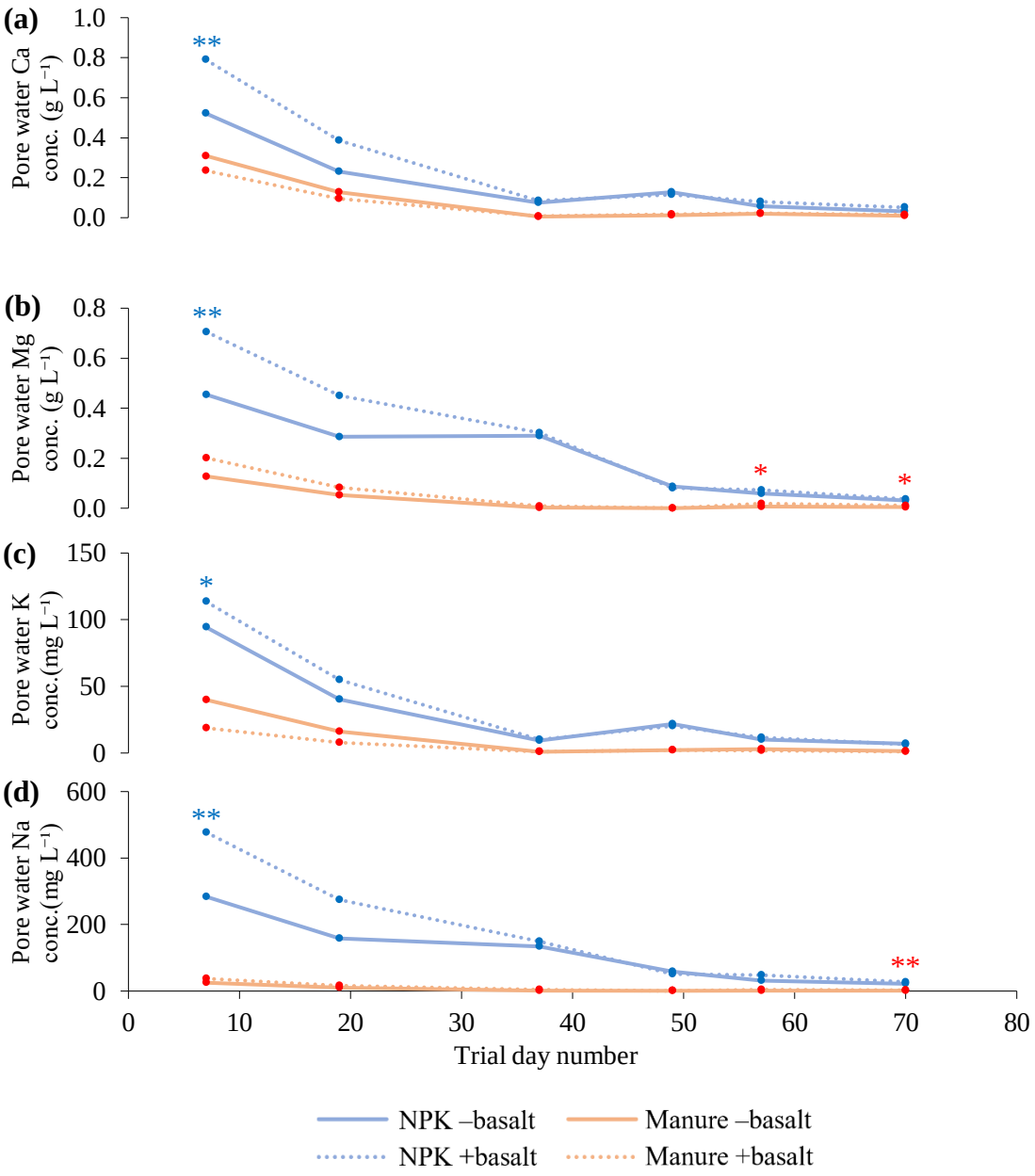

Figure 3.12 – Pore water major cation concentrations, time-series results. 70-day effluent time-series for dissolved concentrations of (a) Ca, (b) Mg, (c) K, and (d) Na. Single asterisks indicate a statistically significant change following basalt amendment to soil ($p < 0.05$; two-way repeated measures ANOVA; $n = 7$). Double asterisks indicate that $p < 0.01$. Triple asterisks indicate that $p < 0.001$. Solid and dotted lines do not indicate data interpolation and are purely for ease of visual reference. Error bars are omitted for clarity. All statistical analyses were performed in R.

The distinction between carbonate and silicate weathering matters, because only silicate mineral dissolution will achieve multi-million-year C storage, whereas carbonate weathering – which may still be useful over timescales relevant to anthropogenic climate change – is effectively carbon neutral in the long run (Thorley *et al.*, 2015). Dissolution rates for carbonate minerals are likely to be at least 4 times faster than the most reactive silicate minerals (Knapp and Tipper, 2022) – e.g., forsterite, which represents around 2.5 % (by mass) of the basalt in this study. The carbonate content of the bulk rock was determined to be 0.34 ± 0.07 % (*SE*) (Table B.2), and given the fine grade of rock powder engineered for this trial, it is possible that in this mildly acidic soil, the entire carbonate inventory might weather from the rock. This amounts to 91 ± 0.001 (*SE*) g × 0.0034 ± 0.0007 (*SE*) = 0.31 ± 0.06 (*SE*) g of carbonate material, which is assumed to be calcite for modelling purposes (Table B.2), but could conceivably also be Mg carbonate, which is a more potent source of positive change per unit mass. This amount of pure Mg carbonate, which represents the maximum positive charge added as carbonate material within the basalt, equates to 0.31 ± 0.06 (*SE*) g $MgCO_3$ × 24.305 g Mg mol^{-1} ÷ 84.314 g $MgCO_3$ mol^{-1} = 89.4 ± 0.02 (*SE*) mg of Mg^{2+}. Final weathering budgets for major divalent cations in the NPK fertiliser regime (Ca^{2+} and Mg^{2+}; Table 4.1) implicate basalt in the net delivery of ≈413 ± 106 (*SE*) mg of Mg^{2+}-equivalent cationic mass into soils, plants and leachate, leaving a comfortable margin of error to report these findings as strong evidence for silicate mineral weathering on the timescales of the experiment. Indeed, even by this most unfavourable interpretation of the results, charge supplied by basalt-related carbonate sources can account for no more than ≈21.7 ± 5.6 (*SE*) % of the accumulated charge from divalent cations in this study (compared as Mg^{2+}-equivalent quantities), or no more than ≈18.2 ± 4.7 (*SE*) % of the accumulated Ca^{2+}-equivalent charge if the calculation is repeated for calcite (which is the assumed carbonate mineral in this thesis). So, whilst an expected contribution from fast-reacting carbonates may help to explain the strong initial weathering pulse in this fertiliser regime, total elemental budgets (Section 3.3.6) imply that dissolution of Ca- and Mg-bearing silicate minerals (e.g. plagioclase, olivine) is likely to be the dominant weathering process in the NPK-treated soil.

In the organic fertiliser regime, an initial pulse of cationic influx is statistically absent from the pore water record (Figure 3.12), and this is probably due to the sorptive effect of the added manure (Figure 3.11b). By adsorbing and re-releasing weathering products

via ion exchange, OM in the manure can respond to concentration gradients and may act as an additional cation reservoir (Section 3.3.6). This buffering effect could therefore introduce a time-lag in the pore water cation signals, and indeed, this is supported by evidenced collected towards the end of the sampling period (day 57, Figure 3.12b,d), which indicates the gradual evolution of statistical significance for the same chemical signatures of mineral weathering observed in the NPK regime. Specifically, highly significant ($p < 0.01$) 161.0 ± 88.9 (*SE*) % increases in mean pore water Na^+ concentrations are, again, stoichiometrically balanced by a highly significant ($p < 0.01$) 162.6 ± 90.0 (*SE*) % increase in mean Cl^- concentrations, now firmly implicating basalt as the source of the additional NaCl. The highest pore water Cl^- concentrations recorded for an individual replicate was <0.2 mg g^{-1}, which is well below the critical range for toxicity (*circa* 4–7 mg g^{-1}) in Cl^--sensitive crops (Tavakkoli, Rengasamy and McDonald, 2010), and is thus inconsequential here.

In the manure treatment, dissolution of the entire basalt carbonate phase in manure-treated columns, would still be insufficient to explain the measured mean influx of ≈154 ± 106 (*SE*) mg of Mg^{2+}-equivalent into the soil, plants and leachate, and can account for no more than around 50 ± 5.6% (*SE*) of the net increase in the divalent cation budget (Ca^{2+} and Mg^{2+}; Table 4.2). Given the statistically significant ($p < 0.05$; two-way repeated measures ANOVA) increase in pore water Mg concentrations observed after basalt was applied (days 57 and 70; Figure 3.12b), enhanced dissolution of Mg-rich silicate minerals (i.e., olivine) is implicated as a major weathering mechanism in the basalt-amended organic fertiliser regime, also.

3.3.5 Soil pH, plant-available Si and exchangeable cation budgets

Due to its control over so many physical and biogeochemical parameters, soil pH is very much a 'master variable' for agronomists (Neina, 2019). Soil acidity can affect mineral weathering rates (Section 1.3), the solubility and cycling of nutrients (Neina, 2019), PTE mobilisation (Sintorini *et al.*, 2021), soil microbial community structures (Bartram *et al.*, 2014), soil emissions of GHGs (Hénault *et al.*, 2019), and other variables of importance to ERW (Beerling *et al.*, 2018). Upward pH adjustments are anticipated given the addition of alkaline silicate material to the soil, and hence, were a key prediction in this study. Changes in bulk soil pH following basalt application were not resolved with significance in the pilot experiment (Figure 2.6b), which is reconcilable given the small quantity of basalt added (dry; 0.181 kg) to the topsoil (dry;

4.65 kg). In this study, half the mass (dry; 0.091 kg) of a much finer grade of basalt was added to a comparatively smaller topsoil mass (1.980 kg), lowering the topsoil:rock mass ratio from around 26:1 to 22:1, and potentially amplifying the weathering signal.

Soil materials were harvested from the experiment in five layers of irregular depth (rather than the four equivalent layers originally planned) in response to visual evidence of a distinct 5 cm-deep subsoil layer at the base of the soil column (Figure 3.13). This layer was heavily colonised by roots, visually darker than the shallower layers above and speckled with rust-coloured deposits indicative of secondary deposition of iron(III) oxides (Figure 3.13). This unique soil layer was probably subjected to unusual pressure and concentration gradients, which may have altered its geochemistry in a manner inconsistent with the drier layers above. Water and gas exchange with the atmosphere (*via* the 20 mm diameter outlet) could induce more extreme chemical changes in pore waters at the lowest depths, potentially leading to precipitation of secondary mineral phases where sufficiently high saturation states are achieved (Section 2.3.7).

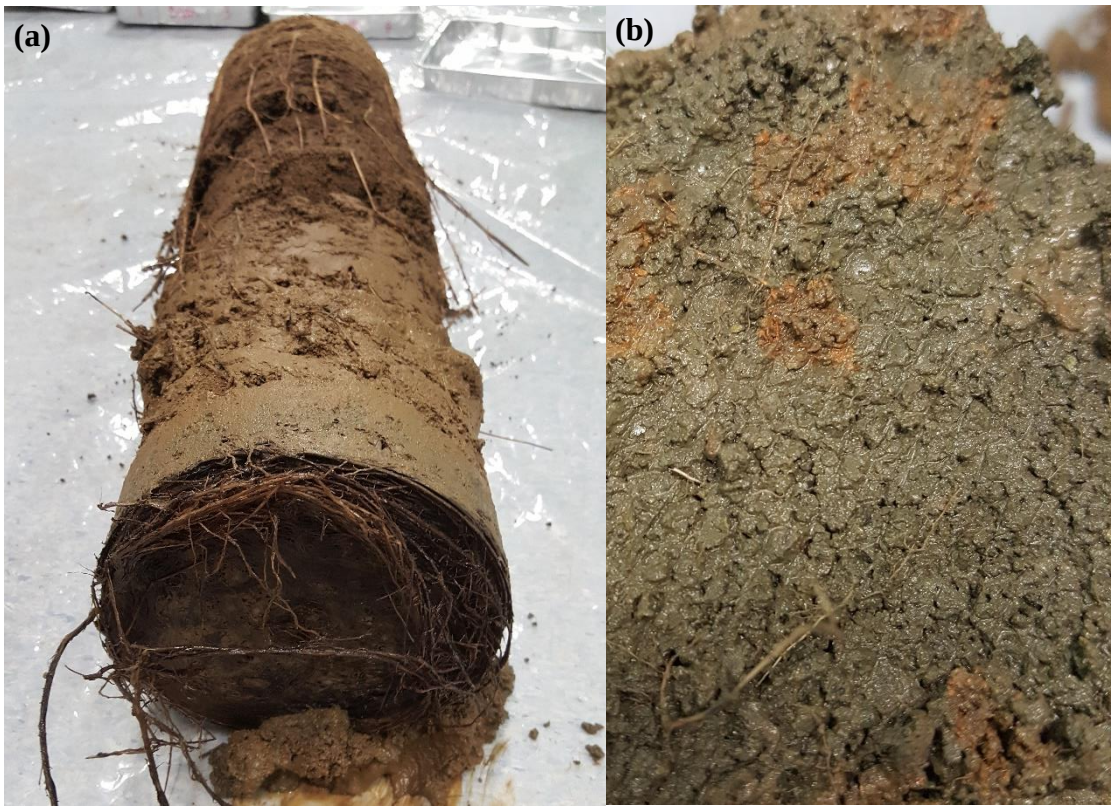

Figure 3.13 – Photographic evidence of divergent soil geochemistry in the base of the mesocosms. (a) photograph indicating preferential root colonisation of the deepest substrate layer, and (b) close-up photographic evidence of secondary mineral deposition (likely to be iron(III) oxide) in the soil layer nearest to the effluent outlet.

Following basalt application to manure-treated soil, a weak but statistically significant 0.07 ± 0.01 (*SE*) unit pH increase is identified on day 235 (one-way ANOVA; $p = 0.04$; based on untransformed [H^+] data; Figure 3.14a). Resolution of this faint signal, which is consistent with mineral weathering, was evidently only possible due to the very low pH variance in this treatment (*SE* ≈ 0.02 pH units). This implies that the treatment may have been strongly pH buffered (presumably mediated by OM within manure), and that the pH equilibrium shifted to a more alkaline state after the basalt application, due to the weathered release of base cations into the topsoil. The pH variance was higher in the chemical fertiliser treatment (*SE* ≈ 0.04 pH units), frustrating detection of a significant result despite the larger 0.12 ± 0.06 (*SE*) unit increase in topsoil pH. Hence, the respective null hypothesis is rejected (*H*8: 0) in favour of the alternative (*H*8: 1). These findings agree well with data obtained in the previous *Sorghum* trial (0.10 ± 0.02 (*SE*); Figure 2.6b), which together lend support for the use of basaltic rock powder for modest acidity regulation in this soil type.

Cations, liberated into pore waters by mineral dissolution, represent the primary weathering signal of interest in this study. Due to their relatively high charge density, Ca^{2+} and Mg^{2+} released from basalt will readily interact with ion exchange sites associated with soil OM and clay minerals, and may even induce a secondary weathering signal through the competitive displacement of native soil exchangeable cations – e.g. K (ten Berge *et al.*, 2012). Such signals may be measurable within a few weeks of basalt application, but due to the sheer size of this cation reservoir (Section 3.3.6) and the typically large associated uncertainties, minor compositional changes in the soil exchange pool can be difficult to determine with significance. For the clay-loam soil used in this study, Ca is the dominant exchangeable cation, and so the weathered release of this analyte into pore waters (from silicate and carbonate minerals) will present against especially high background levels. Accordingly, the application of basalt had no significant effect on topsoil exchangeable Ca in any treatment or depth, except in the lowest soil layer of the NPK regime, where a significant 6.0 ± 2.3 (*SE*) % increase in ammonium acetate ($C_2H_7NO_2$) extractable Ca is resolved (two-way ANOVA; $p = 0.02$).

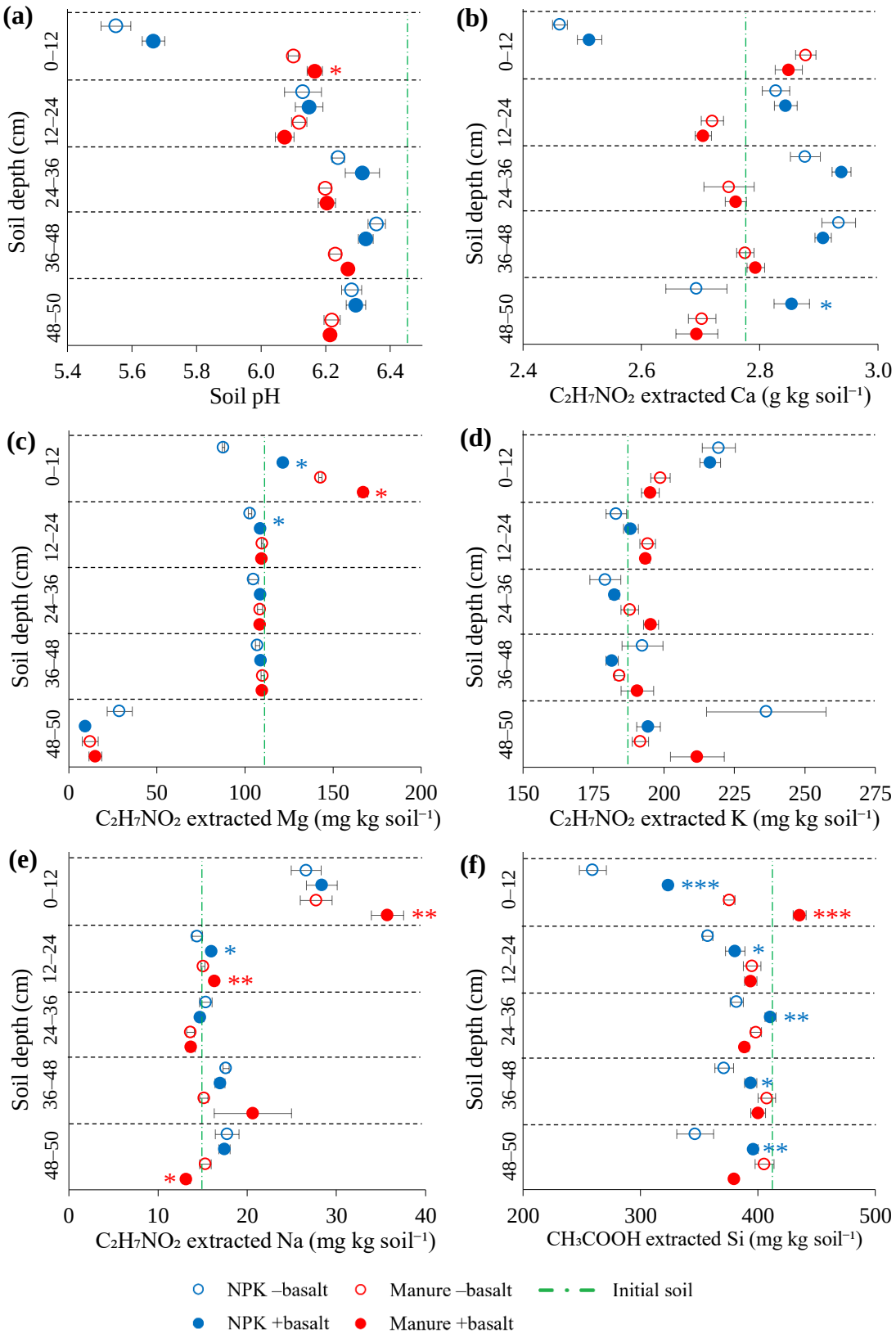

Figure 3.14 – Depth-wise analysis of post-experiment soil pH, soil exchangeable cations and plant-available Si. (a) Soil pH by depth, and the concentration per unit mass of bulk soil for exchangeable (b) Ca, (c) Mg, (d) K, (e) Na, and (f) plant-available Si. Single asterisks indicate a statistically significant change following basalt amendment to soil ($p < 0.05$; one-way ANOVA; $n = 7$). Double asterisks indicate that $p < 0.01$. Triple asterisks indicate that $p < 0.001$. Error bars represent the *SE*. All statistical analyses were performed in R.

These data suggest that ion exchange sites in soils near the drainage layer became enriched in Ca after basalt was added, however, the nature of this additional Ca is unclear. Given the fast dissolution kinetics of Ca carbonate minerals, it is possible that traces of secondary pedogenic carbonates formed in these soils would also dissolve in the $C_2H_7NO_2$ extractant, such that the results returned from this analysis could potentially overestimate the contribution from secondary solid phases. Either way, this increase in Ca indicates cationic mass transfer into the subsoil (Figure 3.14b), with primary mineral weathering posited as the source.

Mg^{2+} has a higher charge density than Ca^{2+}, due to its smaller atomic radius, meaning that it can outcompete Ca^{2+} for access to ion exchange sites. This would serve to restrict Mg^{2+} mobility, concentrating it in the topsoil cation exchange pool, and potentially also displacing stoichiometrically-balanced quantities of other cations into the pore water. Low baseline Mg levels in this soil type facilitate far greater measurement precision for this analyte of interest, which is found to significantly increase in concentration within topsoils after basalt amendment in both the NPK- (38.4 ± 1.4 (*SE*) %; one-way ANOVA; $p = 7.5 \times 10^{-13}$) and manure-treated (17.1 ± 2.0 (*SE*) %; one-way ANOVA; $p = 1.1 \times 10^{-6}$) columns (Figure 3.14c). The fast-weathering silicate mineral, olivine, is implicated as the source of the supplementary Mg, although a minor contribution from Mg carbonate is possible (Section 3.3.4). Exchangeable Mg is also elevated in the substrate directly underneath the topsoil (12–24 cm depth; Figure 3.14c), with a significant ($p < 0.05$) 5.6 ± 1.9 (*SE*) % increase that is particularly noteworthy, because no rock amendment was applied to this layer. These data evidence the extent of the downward propagation of the Mg weathering signal at this point in time (day 235), and are a reminder that the subjects in this experiment are dynamic, interconnected systems far from equilibrium. Here, a statistically significant Mg signal breakthrough occurred in the 12–24 cm depth layer after around 33½ weeks, but with more time, weathering, and perhaps, repeat applications of basalt, this signal should ultimately breakthrough into the leachate. The further release of cations from primary mineral weathering in the topsoil should then begin to register in the effluent, progressively shifting the solution chemistry to a new equilibrium and effecting C sequestration *via* the charge-balanced export of bicarbonate. This result implies that soil core analysis could be used to predict weathering signal breakthrough for ERW field trials and commercial-scale deployment, and enable a direct assessment of the magnitude and timescales for long-term CDR.

No significant changes in soil exchangeable K were detected in this study (Figure 3.14d). Na was significantly higher for both fertiliser types at the 12–24 cm depth (one-way ANOVA; $p < 0.05$; Figure 3.14e) and also significant in the topsoil and deepest layer. This is probably inconsequential for CDR and related to the dissolution of NaCl, likely added *via* the basalt (see Section 3.3.4). Overall, Na concentrations in this soil are fairly low (Tavakkoli, Rengasamy and McDonald, 2010) and thus, the small increase in Na is unlikely to affect crop performance.

Increases in plant-available Si following basalt application are large and highly significant (two-way ANOVA; $p < 0.001$) in both the NPK- (24.7 ± 5.6 % *SE*) and manure-treated topsoil (15.9 ± 2.1 % *SE*; Figure 3.14f). In the chemical fertiliser treatment, a clear Si weathering signal propagates through all five soil layers, with sufficient potency to achieve statistical significance at each depth (Figure 3.14f), suggesting a possible impending breakthrough of the Si signal into the effluent. In this regime, plants in the control (NPK –basalt) treatment are implicated in the significant depletion of soil Si, with respect to initial levels (Figure 3.14f). Here, the addition of 50 t ha^{-1} of basalt curbed this depletion to around ½ of the magnitude (Figure 3.14f), providing strong support for the use of basalt fines as a supplementary Si source.

Overall, no clear numerical relationships were identified between the concentration of soil-exchangeable major cations, acetic acid-extractable Si and soil pH in this study.

3.3.6 Basalt weathering and CDR rate estimates

Elemental budgets for key indicators of silicate mineral weathering (Ca, Mg, K, Na and Si) were calculated in accordance with the method in Section 2.3.4. Where time-wise, tissue-wise or depth-wise sampling was undertaken, individual elemental budgets for each sampling point were calculated, and then mathematically combined at full accuracy in the required proportions to produce a single representative value, along with appropriately propagated uncertainties.

Mirroring the pilot experiment, final mass balance tables for this study (Tables 3.3–4) suggest that divalent cations (Ca^{2+} + Mg^{2+}) dominate the weathering budget on a mass basis, with the soil exchange reservoir representing the largest component. Hence, the respective null hypothesis (*H*9: 0) – which states that rock-derived cations will not preferentially accumulate in the soil – is rejected in favour of the alternative (*H*9: 1).

Net leachate budgets were negative, as seen in the previous trial (Table 2.1), and probably linked in this study to comparatively reduced leachate volumes following

basalt application (Section 3.3.4). Weathering rates for almost every indicator measured were higher in the chemical fertiliser regime than they were in the organic treatment (Table 3.3), and this may be due to a combination of factors in the NPK regime that were ultimately conducive to enhanced weathering – e.g., lower soil pH and CEC, and increased primary production (despite any associated adverse impacts on hydrology). The manure – and to some extent, the basalt, also (Section 3.3.3) – evidently intercepted irrigation water in the topsoil, which was for this study hypothesised to enhance chemical weathering rates by increasing the total wetted mineral SA (Section 3.1.3). The higher CEC and lower background nutrient load of the manure-treated substrate also meant that the topsoil more-effectively supressed cation concentrations in the pore waters – including plant nutrients, e.g. K – and this possibly dampened any plant-mediated positive feedback on basalt weathering rates. *Sorghum* growth in the NPK treatment was not nutrient-limited to the extent that it was in the organic treatment. Here, instead, it is posited that a less-buffered, more-intense initial release of mineral weathering products from the rock (against an already high background nutrient load; Figure 3.12c) led to a stronger, basalt-related fertilisation effect in *Sorghum* (Table 3.3), which – through the implied increases in primary production and soil respiration rates – may have comparatively supressed pH in the rhizosphere and, hence, induced the accelerated release of further basalt weathering products.

To facilitate statistical comparisons between treatments, molar quantities of Ca^{2+}, Mg^{2+} and K^{+} (in the leachate, plant and soil exchange reservoirs) were converted into equivalents – i.e. moles of positive charge – by applying the required valency factor (2× multiplier for Ca^{2+} and Mg^{2+}; 1× multiplier for K^{+}). These figures were then combined into a single value for each column, representing the total equivalents accumulated in the leachate, plant and soil exchange pools (Figure 3.15). Na was excluded from this analysis as it is associated with the dissolution of common salt (NaCl) in the present study (Section 3.3.4), which does not affect CDR. Total mean equivalents in the NPK +basalt treatment (1.40 ± 0.01 *SE* equivalents column^{-1}) were a significant 3.0 ± 0.7 (*SE*) % higher than the respective controls (1.35 ± 0.01 *SE* equivalents column^{-1}; one-way ANOVA, p = 0.001; Figure 3.14). In the manure regime, however, total equivalents rose 1.0 ± 0.7 (*SE*) % following basalt amendment, which was not statistically significant, and hence, the rock had no significant effect on C capture (Figure 3.14). The related null hypothesis (*H*10: 0) is therefore not rejected.

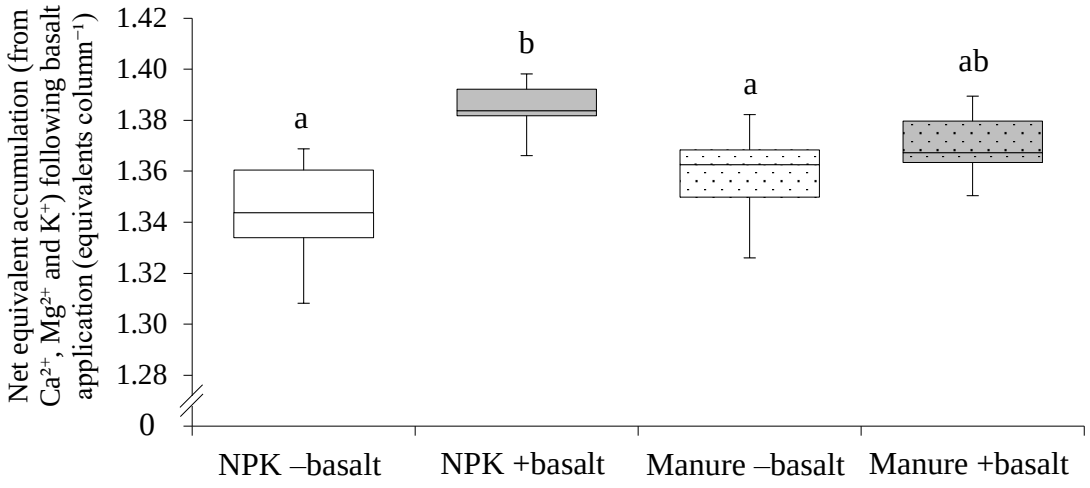

Figure 3.15 – Box plot comparing the accumulation of equivalents in the leachate, plant and soil exchange pools of the different soil treatments in Chapter 3. Values represent the equivalents related to molar quantities of Ca^{2+}, Mg^{2+} and K^{+} measured in the leachate, plant tissues and soil exchange pool. Treatments sharing the same letter are not statistically different ($p > 0.05$; one-way ANOVA with Tukey *post hoc* test). All statistics were determined in R.

Estimates of 'potential' CDR for the different fertiliser systems were derived from the equivalent budgets, on the basis that the difference in total equivalents between control and basalt-treated columns represents the maximum charge available for CDR. These net accumulated equivalents are considered here to be only 'potential' CDR, because at the end of the experiment (day 235), most of the cations included in the charge budget were engaged at ion exchange sites in the soil (Tables 3.4–5). It is reasonable to assume that – given sufficient time and leaching – much of this excess charge will eventually be exported from the mesocosms in the effluent. But at the field- and catchment-scale, the biogeochemical mechanisms governing real-world analogues for this process are complex, and may be further confounded by changes in climate or through human interference in agricultural systems (e.g. *via* land management practices, fertiliser and OM applications, acid rain etc.). Such considerations are beyond the scope of this thesis, where for simplicity it is presumed that the entire net charge inventory will ultimately reach the oceans. Conversion of net equivalents into initial CO_2 capture is straightforward, since each mole of positive charge exported in the effluent will have sequestered one mole of bicarbonate (HCO_3^-), and thus one mole of atmospheric CO_2. However, the chemical equilibrium between dissolved C species ($CO_{2(aq)}$, carbonic

Table 3.4 – Changes in whole-system elemental budgets and transfer rates resulting from basalt amendment (50 t basalt ha^{-1}) of a mildly acidic clay-loam soil (pH 6.45; NPK fertiliser; 250 kg N ha^{-1}; 414 kg P_2O_5 ha^{-1}; 490 kg K_2O ha^{-1}) planted with *Sorghum bicolor*, after 235 days. Values are mean differences (±*SE*) between basalt-amended (n = 7) and unamended (control) planted mesocosms (n = 7). Positive values indicate increased element concentrations due to basalt amendment. Soil extraction results are mass-weighted, depth-integrated averages (±*SE*) for the entire column. SA are expressed as SA_L for land surface area, and SA_R for rock SA.

Element	Effect of basalt treatment on rate of elemental release					Measured elemental release from basalt†	Rate of elemental release (BET SSA = 14.54 m^{-2} g^{-1} basalt) ‡
	Leachate	Plant (µmol m^{-2} SA_L d^{-1})			Soil extraction* (mmol m^{-2} SA_L d^{-1})		
		Roots	Shoots	Seeds		(mmol m^{-2} SA_L d^{-1})	(mol m^{-2} SA_R s^{-1})
Ca	–138 ± 107	–13.1 ± 64.8	51.8 ± 199	15.5 ± 11	2.82 ± 0.96	2.74 ± 1.02	$1.1\times10^{-12} \pm 3.9\times10^{-13}$
Mg	–15.7 ± 11.1	2.10 ± 47.9	–53.3 ± 70.7	326 ± 151	0.98 ± 0.08	1.24 ± 0.12	$4.8\times10^{-13} \pm 4.6\times10^{-14}$
K	–7.78 ± 4.93	52.8 ± 61.1	901 ± 428	450 ± 229	–0.03 ± 0.23	1.37 ± 0.43	$5.3\times10^{-13} \pm 1.7\times10^{-13}$
Na	–3.86 ± 3.22	–0.05 ± 0.13	14.1 ± 27.0	0.72 ± 0.7	0.07 ± 0.06	0.08 ± 0.07	$2.9\times10^{-14} \pm 2.9\times10^{-14}$
Si	–10.97 ± 1.57	–559 ± 1008	568 ± 259	75.7 ± 66	2.68 ± 0.38	2.75 ± 1.20	$1.1\times10^{-12} \pm 4.6\times10^{-13}$

*Si data are from an acetic acid extraction (to estimate of plant-available Si) and cation data were derived from an ammonium acetate leach. Both extractions were conducted on representative soil samples from five layers (0–12, 12–24, 24–36, 36–48, 48–50 cm depths).

†Measured moles released from basalt and associated uncertainties were calculated following the method in Table 2.1.

‡Calculated by dividing the measured moles released from basalt by BET-determined rock surface area (SSA = 14.54 m^{-2} g^{-1} basalt).

Table 3.5 – Changes in whole-system elemental budgets and transfer rates resulting from basalt amendment (50 t basalt ha^{-1}) of a mildly acidic clay-loam soil (pH 6.45; manure fertiliser; 250 kg N ha^{-1}; 120 kg P_2O_5 ha^{-1}; 300 kg K_2O ha^{-1}) planted with *Sorghum bicolor*, after 235 days. Values are mean differences (±*SE*) between basalt-amended (n = 7) and unamended (control) planted mesocosms (n = 7). Positive values indicate increased element concentrations due to basalt amendment. Soil extraction results are mass-weighted, depth-integrated averages (±*SE*) for the entire column. SA are expressed as SA_L for land surface area, and SA_R for rock SA.

Element	Effect of basalt treatment on rate of elemental release					Measured elemental release from basalt†	Rate of elemental release (BET SSA = 14.54 m^{-2} g^{-1} basalt) ‡
	Leachate	Plant (µmol m^{-2} SA_L d^{-1})			Soil extraction* (mmol m^{-2} SA_L d^{-1})		
		Roots	Shoots	Seeds		(mmol m^{-2} SA_L d^{-1})	(mol m^{-2} SA_R s^{-1})
Ca	–409 ± 43.7	–47.5 ± 45.5	202 ± 164	–7.3 ± 12	1.33 ± 0.95	1.06 ± 0.92	$4.1\times10^{-13} \pm 3.5\times10^{-13}$
Mg	–38.5 ± 4.78	–5.05 ± 27.6	–75.8 ± 76.7	–58 ± 138	0.60 ± 0.08	0.43 ± 0.18	$1.6\times10^{-13} \pm 7.1\times10^{-14}$
K	–29.0 ± 4.11	–58.79 ± 52.41	–147 ± 591	–116 ± 233	0.26 ± 0.14	–0.09 ± 0.55	$-3.5\times10^{-14} \pm 2.1\times10^{-13}$
Na	–8.90 ± 0.89	–0.07 ± 0.10	31.9 ± 17.7	–0.4 ± 1.1	0.33 ± 0.11	0.35 ± 1.09	$1.4\times10^{-13} \pm 4.2\times10^{-14}$
Si	–16.4 ± 2.90	–998 ± 1056	960 ± 290	–46 ± 44	0.96 ± 0.22	0.86 ± 1.15	$3.3\times10^{-13} \pm 4.4\times10^{-13}$

*Si data are from an acetic acid extraction (to estimate of plant-available Si) and cation data were derived from an ammonium acetate leach. Both extractions were conducted on representative soil samples from five layers (0–12, 12–24, 24–36, 36–48, 48–50 cm depths).

†Measured moles released from basalt and associated uncertainties were calculated following the method in Table 2.1.

‡Calculated by dividing the measured moles released from basalt by BET-determined rock surface area (SSA = 14.54 m^{-2} g^{-1} basalt).

acid, carbonate and bicarbonate anions) is expected to shift as weathering products enter the oceans – due to changes in pH, salinity, temperature and pCO_2 – such that around 17% of the initially captured carbon will return to the atmosphere (Renforth and Henderson, 2017). To account for these predicted losses, a factor of 0.831 was applied to the CDR values prior to reporting.

Final estimates for CDR potential are presented in Figure 3.16, which includes results for the NPK and manure fertiliser treatments, along with a retrospective analysis of data from Chapter 2 (N fertiliser). Whilst reported here alongside considerable uncertainty, CDR results for the pilot experiment (2.0 ± 1.2 tCO_2 ha^{-1}) are broadly in line with modelling predictions (Section 2.3.7), which is unsurprising as the model was tuned with this dataset. Smaller uncertainties in this later trial facilitate the identification of a statistically significant 0.80 ± 0.18 tCO_2 ha^{-1} increase in (potential) CDR in the NPK regime where basalt was applied ($p < 0.05$; two-way ANOVA). In the manure regime, a much reduced 0.26 ± 0.16 tCO_2 ha^{-1} is resolved, without significance, indicating less-favourable conditions for mineral weathering in the manure-treated soil (Figure 3.16).

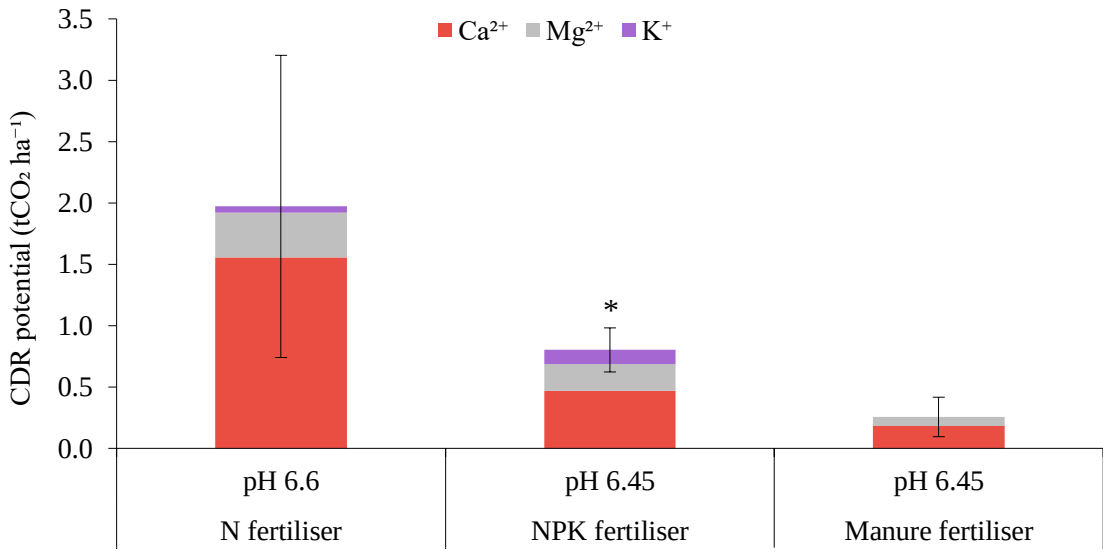

Figure 3.16 – Estimates of potential CDR for the experimental basalt treatments in Chapters 2 and 3. The relative contributions of Ca^{2+}, Mg^{2+} and K^+ towards total surplus charge are shown as different colours within the stacked bar chart. CDR estimates are derived from measurements of additional cationic mass accumulated in the leachate, plant and soil exchange pools following basalt application. Molar quantities of additional Ca^{2+}, Mg^{2+} and K^+ in the pools were converted into equivalents and combined into a single value. Equivalents were then converted to CDR potential according to the 1:1 molar ratio of charge:CO_2 captured. Values are corrected for carbonate buffering (Renforth and Henderson, 2017). Asterisk indicates a statistically significant change following basalt amendment to soil ($p < 0.05$; two-way ANOVA; $n = 7$).

3.3.7 Comparison with alternative CDR quantification method: TiCAT

Soils from this experiment were subjected to testing *via* a new mass balance method for quantifying mineral weathering, which relates titanium (Ti) concentrations to the concentration of major cations (CAT) in the sample (TiCAT). Full details of the analytical approach are set out in the related publication (Reershemius and Kelland *et al.*, 2023), but briefly, the amount of basalt originally added to each soil sample can be back-calculated by measuring the concentration of Ti, which is an immobile element that will remain in the solid phase after the more mobile major cations (Ca, Mg, Na, K) have been released from the rock. The elemental composition of the initial rock material is known (Table B.1), so the initial quantity of major cations in the sample can be estimated. The differences between initial and post-experiment cation concentrations can then be used to calculate the cation loss from the sample (i.e. the weathering rate).

In Reershemius and Kelland *et al.* (2023) the same mass balance data from this study were reworked to more appropriately suit the new method's mode of operation, resulting in higher potential CDR estimates than those reported in Section 3.3.6. These higher figures reflect a change in the assumed baseline for background weathering of native soil minerals, and is justified in the paper (Reershemius and Kelland *et al.*, 2023).

Estimates recalculated using a conventional mass balance approach – given the assumptions in Reershemius and Kelland *et al.* (2023) – indicate potential CDR in the NPK regime to be 1.68 ± 0.28 $tCO_2eq\ ha^{-1}$, compared with 1.05 ± 0.39 $tCO_2eq\ ha^{-1}$ in manure-treated soils. TiCAT estimates for the same samples suggest potential CDR of 2.73 ± 1.11 $tCO_2eq\ ha^{-1}$ in the chemical fertiliser treatment, *versus* 1.74 ± 1.41 $tCO_2eq\ ha^{-1}$ in the organic regime, which in both cases is within error (Reershemius and Kelland *et al.*, 2023). It is worth noting that conventional mass-balance estimates are composite figures, calculated from thousands of individual measurements of soil, plant and leachate characteristics, which each attracted costs and took many hours of laboratory work to determine. By comparison, TiCAT is a potentially high-throughput and relatively less-expensive approach, that nonetheless yields remarkably similar results. Accordingly, this new weathering rate quantification method has considerable potential for monitoring, reporting and verification of CDR in ERW trials.

3.4 Conclusions

In this study, the application of finely-milled basalt to a mildly acidic, clay-loam agricultural soil resulted in improved *Sorghum* yields in the prescribed chemical and organic fertiliser regimes. The magnitude and timing of the basalt-related effects on crop performance, mineral weathering and CDR, were different in the two fertiliser regimes, with the strongest effects mostly seen in the NPK chemical fertiliser treatment. In this regime, the application of basalt generated statistically significant (potential) CDR (0.80 ± 0.18 tCO_2 ha^{-1}), based on a conservative mass balance approach. Under the organic regime, however, CDR was determined to be only 0.26 ± 0.16 tCO_2 ha^{-1}. To explain this discrepancy, it is suggested that the added manure markedly increased soil pH, and thus probably inhibited chemical weathering in accordance with the established Arrhenius equation (Equation 1.5). Moreover, it is proposed that basalt-related improvements in crop performance were tempered by OM in the manure, *via* its propensity to adsorb weathering products onto ion exchange surfaces. This may have considerably reduced the availability of supplementary plant nutrients released into pore waters from the rock, with adverse impacts on primary production. In short, the manure may have arrested plant-mediated positive feedback on weathering rates.

Echoing the results from the previous experiment, cations liberated from basalt predominantly accumulated in the soil cation exchange pool (and to a lesser extent, the plants), reinforcing the notion that mineral dissolution and CDR are not necessarily synchronous. Evidence for breakthrough of weathering signals into deeper soil layers (notably, Si and Mg accumulation) raises the question of whether the system was still evolving when the experiment was terminated, and indeed, how long it might take for appreciable quantities of weathering products to register in the leachate. Given that ERW relies on this mode of C sequestration, research into time-lags in the CDR signal is required to improve temporal estimates for carbon capture. The rapid onset of basalt-related effects on pore water and plant chemistry may be indicative of carbonate mineral dissolution, which is chemically fairly similar to agricultural lime and is, likewise, approximately carbon neutral over long timescales. However, the low carbonate content of the basalt used in this trial is insufficient to account for the full weathering budget, which – by elimination – represents strong evidence that silicate mineral weathering was the dominant cation release pathway.

The agricultural use of basalt for soil pH control and as a Si fertiliser is well-supported by the findings in this, and the previous (Chapter 2), study. A modest (<0.01 unit) but significant rise in pH was detected 235 days after basalt was added to manure-treated soils, and considerable increases in shoot and (plant-available) soil Si are reported for both fertiliser regimes, with high confidence. Increased soil Si availability is known to have a wide range of beneficial effects on higher plants, and so this promising agronomic co-benefit may well translate into real-world yield improvements, and thus could have tangible economic value. Further research at the laboratory- and field-scale is needed to quantify the crop protection benefits associated with basalt applications. Notably, no evidence of adverse effects from the added basalt was found during the course of this study. As in the predecessor, PTEs did not accumulate in *Sorghum* edible tissues, and probably had reduced mobility in the soil due to the alkalising effect of the basalt. So whilst the manure fertiliser appears to be less conducive to mineral weathering and CDR, the agronomic benefits alone may justify deployment of ERW in an organic agricultural setting.

In this study, which used a single soil type, the differing physical and chemical properties of the fertilisers chosen resulted in considerable divergence in the system response to basalt. Other soils and land management practices may also induce divergent results, and if ERW is shown to be incompatible with a particular type or practice, this could limit the land area available for deployment, and thus, the scalability of the strategy. Given the small associated literature base, research is urgently required to determine the effects of different soil types, CECs, OM content and commonly used soil additives on mineral weathering rates and CDR.

4

Basalt weathering, CDR and rock dust-related *Lolium perenne* fertilisation not improved by amending a sandy acidic soil with biochar, and not effective in a sandy alkaline soil

Contents

4.1 Introduction

The previous chapter began by questioning the assumption that ERW is highly scalable, by considering its applicability in different 'real-world' agricultural settings. Building on this theme, the present chapter involves strongly-contrasting soil types, explores novel interactions with another CDR strategy, and introduces a different model plant, perennial ryegrass (*Lolium perenne*), to simulate pasture in a controlled environment. In short, this study focused on two highly-relevant factors that could potentially affect weathering rates and, hence, constrain the land area available to ERW: soil pH and the interaction of basalt with co-applied biochar.

Humanity is deeply reliant on the world's diverse and complex soils, which are currently required for around 95% of global food production (FAO, 2022). The huge assortment of soils – which may each have their own characteristic ecosystems (USDA-NRCS, 1999) – can be taxonomically reduced to twelve soil 'orders' (Figure 4.1), based on measurable soil properties such as CEC, water and OM content, base saturation, texture, depth *et cetera*. The effects of these fundamental soil parameters on weathering

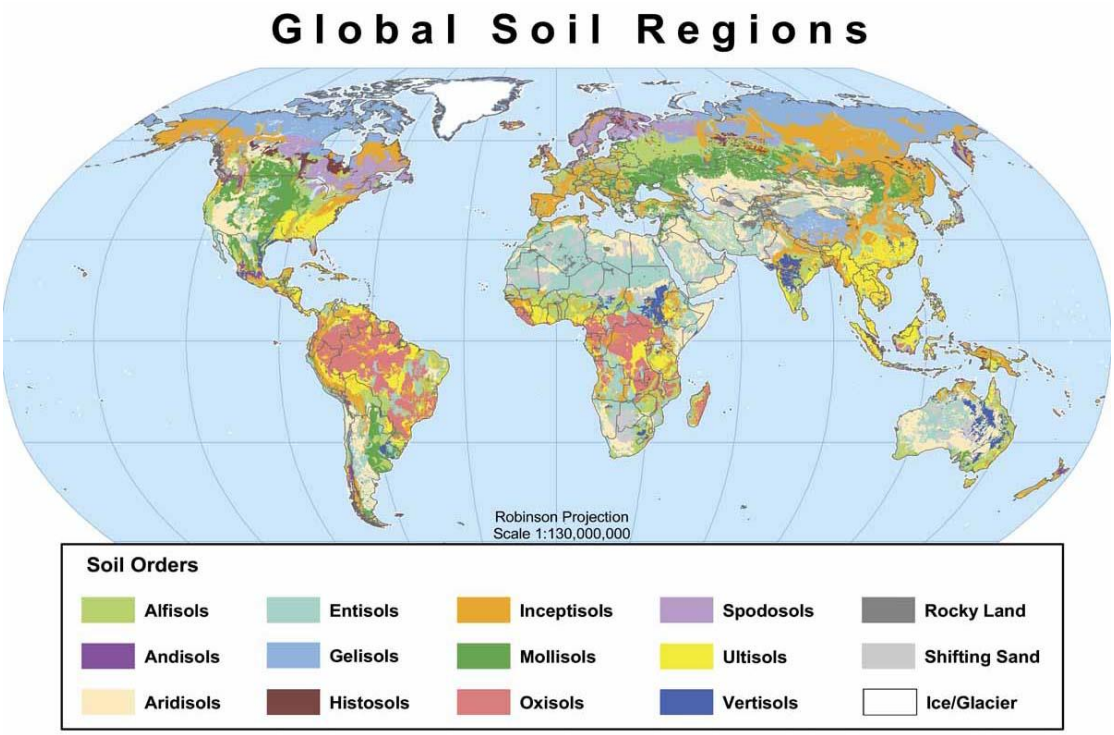

Figure 4.1 – The global distribution of the twelve soil orders. (USDA-NRCS, 1999).

rates can, in some cases, be confidently predicted *a priori*, with reference to the established laws of mineral dissolution. Soil pH is a prime and relevant example of this, since it is known to vary greatly in the world (Figure 1.7), and explicitly appears in the Arrhenius equation for mineral weathering (Equation 1.5). Indeed, the formula receives untransformed hydrogen ion concentration, $[H^+]$, as the input variable for acidity, which spans such a wide range in nature that the logarithmic pH scale is necessary. Hence, according to the Arrhenius equation, mineral dissolution rates associated with the circumneutral (pH 6.6) soil in Chapter 2 could be increased by an order of magnitude by selecting a soil with a pH of 5.6*, as was done for this study. A sandy, calcareous agricultural soil – typical of the highly productive East Anglian lowlands – was chosen as the alkaline counterpart to this less-productive, sandy acidic soil – formed on the Millstone Grit that underlies much of the Peak District's landscape.

No singular CDR option is anticipated to be potent enough to offset all anthropogenic emissions (Shepherd *et al*., 2009; NRC, 2015), and so a package of measures will likely be required. However, some of the terrestrial CDR options (Figure 1.3) can be expected to encounter land-use conflicts – for example, land that might otherwise be used for food production may be turned over to biofuel crops (for BECCS) or forestry (af-/re-forestation). But there is no obvious reason why ERW and biochar (which are soil-amendment strategies) could not both be deployed in the above scenarios, perhaps even as a single combined soil amendment, to stack multiple layers of CDR on the same footprint. Accordingly, to examine the effects of this combination on weathering rates and related agronomic co-benefits, basalt-biochar co-deployment was simulated in this study, in both the acidic and alkaline sandy soils.

Contemporary thinking on ERW principally focusses on managed arable land, to exploit synergies with mechanised agriculture and, hence, reduce the cost of rapid deployment. Whilst this is a sensible strategy, arable agriculture represents only around 30% of the world's agricultural land by area, with permanent grassland (3.4 billion ha globally) dominating the mix (O'Mara, 2012). Much of the UK's arable production is concentrated in the dry eastern counties (Figure 4.2a). But grasslands spread over the

*In practice, it is not quite as simple as this, because the influence of non-carbonic acids (which do not lead to CDR) is likely to be greater in this pH range (Dietzen and Rosing, 2023).

wetter western counties of England and Scotland, and also Wales and Northern Ireland, and are co-located with some of the most acidic soils in the Union (Figure 4.2b). Given the previous argument in favour of ERW deployment in low-pH soils, UK grasslands would appear to be an under-researched deployment area. Accordingly, this study introduced *Lolium perenne* as the model crop – the dominant species in most UK pastures – and simulated environmental conditions characteristic of the British climate.

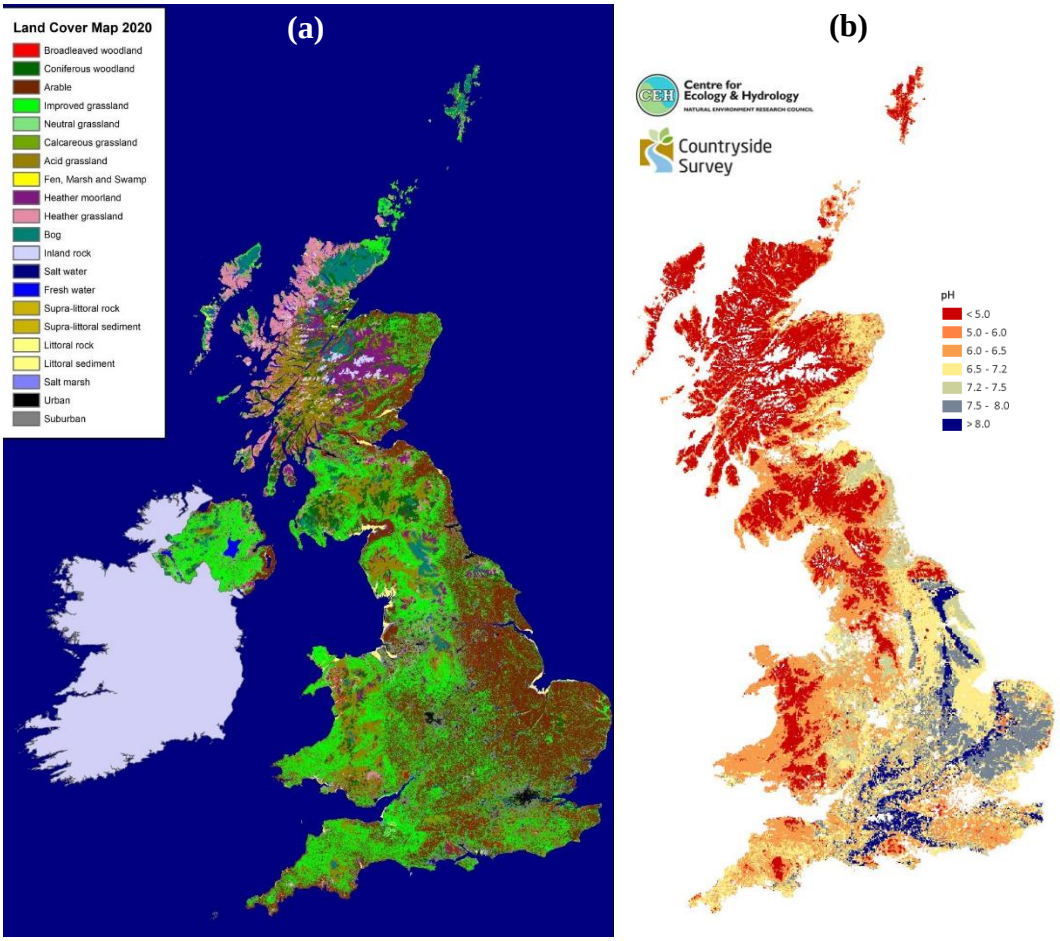

Figure 4.2 – UK land cover and soil pH maps. (a) UK land cover map, and (b) UK topsoil pH map (UKSO, 2007; UKCEH, 2021).

In this unprecedently large, multi-factorial mesocosm-scale trial, the effect of soil type and co-applied biochar on basalt weathering rates, CDR and related agronomic co-benefits was investigated. Weathering budgets were built using the methods refined in Chapters 2 and 3, and the opportunity to repeatedly harvest the cover crop was exploited to better understand the dynamics of the basalt-related fertilisation effect. In this way, the relative importance of these weathering factors was examined for the first time.

4.1.1 Reflections on the *Sorghum* trials

Both *Sorghum* experiments had been successful in determining CDR estimates and identifying (or, indeed, reconfirming) basalt-related benefits for the crop and soil. However, soil moisture data collated in Chapter 3 strongly indicate that hydrological artefacts were introduced by the related experiments' designs, and that in both cases this could have unrealistically supressed basalt weathering rates. Accordingly, a new, fully-automated drip-feed irrigation system was constructed for this trial, to ensure adequate soil moisture in the highly permeable sandy soils. Moreover, the *Sorghum* trials suggest that most of the weathered cations will register in the soil exchange pool, and so a far more streamlined approach was taken in this study, to arrive directly at CDR estimates (by largely ignoring the minor contributions from plants and effluent). In so doing, several relevant and previously unexamined factors were tested using the same sample analysis pipelines and workloads.

4.1.2 Experimental design

Replication was reduced down to six in this new trial, as confidence grew in the methods. A balanced 3-factorial design was utilised for the study (Figure 4.3; acidic *vs* alkaline, ±biochar, ±basalt), enabling cross-comparison of all three factors:

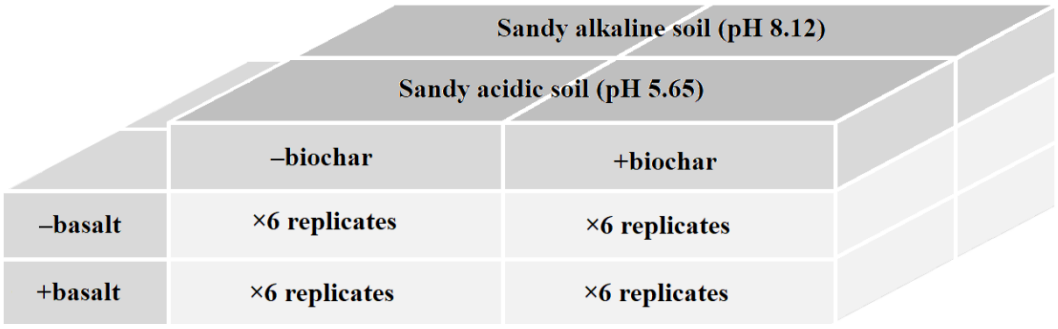

Figure 4.3 – 3-D representation of the 3-factorial experimental design in Chapter 4

4.1.3 Hypotheses

Equipped with results from the two previous ERW experiments, predictions for the outcome of this trial are clearer.

In Chapter 3, the addition of alkaline soil amendments (basalt and manure) led to increased pore water pH, which likely improved nutrient uptake efficiency in the mildly

acidic (pH 6.45) clay-loam soil. Here, however, the more-acidic (pH 5.65) Moss End Farm soil treatments can be expected to benefit even more significantly from pH-related improvement in NPKS uptake (following basalt and/or biochar amendment), whereas the alkaline (pH 8.12) soils should become less-productive as a result, because their pH environments will shift further away from the optimal circumneutral range. Moreover, the magnitude of the soil pH increase following basalt application is expected to be lower in the Flitcham Farm soil, because mineral dissolution should be slower under alkaline conditions and, hence, fewer cations will be liberated to influence pH.

Biochar is reasoned to behave in a similar way to manure, in that it will readily adsorb cations from the porewaters, but may not necessarily increase weathering rates as implied by the standard Arrhenius equation (i.e. by lowering mineral saturation states in the pore waters; Equation 1.5). It is unclear why this occurred in Chapter 3, but may be related to a synchronous suppression of plant-mediated feedback on weathering rates, or perhaps some other biological influence. Hence, in this study, the basalt-related fertilisation effected is not expected to be enhanced by biochar, nor are the weathering and CDR rates. CDR is firmly predicted to be highest in the acidic soil.

In the *Sorghum* trials, the heavy-clay soil likely dominated the chemistry of the pore water at depth, such that leachate weathering signals were extremely faint. Whilst some improvement can be expected this trial – as both sandy soils have lower CECs and higher water permeability – it is nonetheless anticipated that the primary weathering signal will preferentially accumulate in the soil, and not the effluent.

Based on the above considerations, the following hypotheses were tested:

(*H*11: 0) The basalt-related crop yield bonus will be highest in the alkaline soil.
(*H*11: 1) The basalt-related crop yield bonus will be highest in the acidic soil.

(*H*12: 0) The basalt-related crop yield bonus will be enhanced by biochar.
(*H*12: 1) The basalt-related crop yield bonus will not be enhanced by biochar.

(*H*13: 0) Significant differences in leachate geochemistry will be detected in at least one soil type or biochar treatments, following basalt application.
(*H*13: 1) No significant differences in leachate geochemistry will be detected in any of the soils or biochar treatments, following basalt application.

(*H*14: 0) The basalt-related soil pH increase will be highest in the alkaline soil.

(*H*14: 1) The basalt-related soil pH increase will be highest in the acidic soil.

(*H*15: 0) Cations weathered from the added basalt will preferentially accumulate in the leachate, rather than the soil cation exchange pool.

(*H*15: 1) Cations weathered from the added basalt will preferentially accumulate in the soil cation exchange pool, rather than the leachate.

(*H*16: 0) Basalt weathering and CDR rates will be highest in the alkaline soil.

(*H*16: 1) Basalt weathering and CDR rates will be highest in the acidic soil.

(*H*17: 0) Basalt weathering and CDR rates will be enhanced by biochar.

(*H*17: 1) Basalt weathering and CDR rates will not be enhanced by biochar.

4.2 Materials and methods

4.2.1 Weathering reactor design and construction

Replicated mesocosms (n = 6) for the eight soil treatments in this study (acidic *vs* alkaline, ±biochar, ±basalt) were built using the same basic design and materials in Chapter 2, but with a shortened top- and bottom-section (Figure 4.4). As before, substrate was added into the upper section and leachate collection apparatus were housed in the lower, with basalt and biochar additives mixed into the topsoil only (Figure 4.4a). Mesocosms were fitted with collars (Figure 4.4b) to enable an airtight fit with custom-built static chambers, designed to measure soil-atmosphere GHG fluxes*.

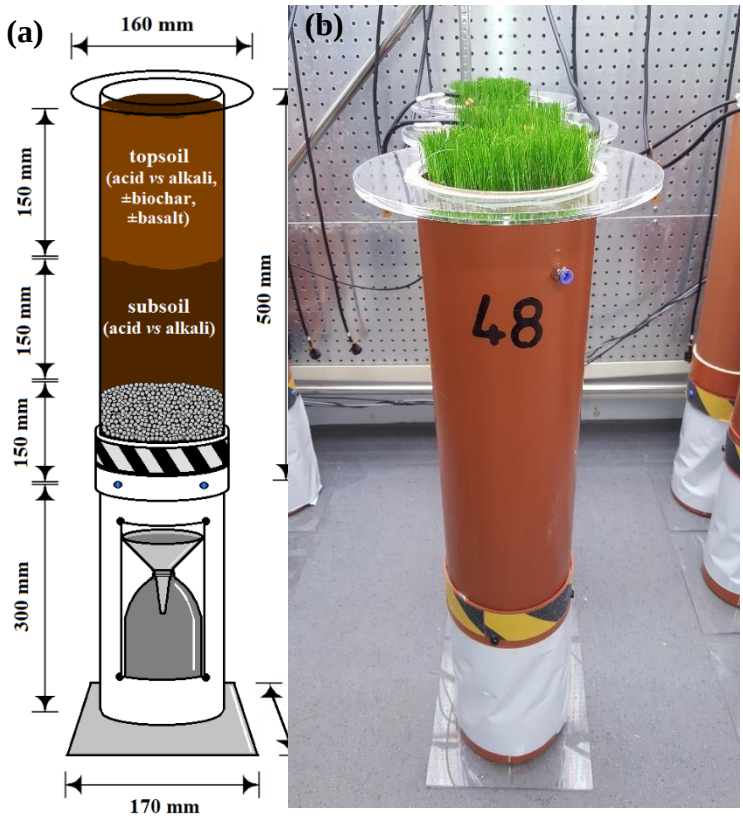

Figure 4.4 – Weathering reactor design. (a) Cutaway diagram of a mesocosm, showing sub- and top-soil arrangement simulating a tillage regime, and (b) photograph of a weathering reactor, with *Lolium perenne* and bespoke drip-feed irrigation. The acrylic plate attached to the top of the column was designed to interface with a static chamber for the measurement of soil-air GHG fluxes.

*Unfortunately, results relating to CH_4, N_2O and CO_2 fluxes could not be prepared in time for this thesis

4.2.2 Substrate characterisation and preparation

The sandy acidic (pH 5.65) soil for this experiment was collected from grassland at Moss End Farm in Derbyshire, UK (latitude 52.8061787 ºN, longitude 0.5853904 ºW). The soil had a (dry) bulk density of 0.98 kg L^{-1} and a gravimetric water content (GWC) at field capacity of 0.35 g g^{-1}. On collection, the soil had an initial GWC of 70.22 g g^{-1}. The CEC of this soil was measured to be very low, at just 5.7 cmol (p+) kg^{-1}, based on concentrations of exchangeable Ca^{2+}, Mg^{2+}, K^{+}, Na^{+} only.

The sandy alkaline (pH 8.12) soil for this experiment was collected from the margins of an arable field under *Beta vulgaris* cultivation at Flitcham Farm in Norfolk, UK (latitude 53.1802098 ºN, longitude 1.9914990 ºE). The soil had a (dry) bulk density of 1.09 kg L^{-1} and a GWC at field capacity of 0.30 g g^{-1}. On collection, the soil had an initial GWC of 0.21 g g^{-1}. The CEC of this soil was measured to be 23.4 cmol (p+) kg^{-1}, based on concentrations of exchangeable Ca^{2+}, Mg^{2+}, K^{+}, Na^{+} only. This is similar to the CEC of the mildly acidic clay-loam soil used in Chapters 2 and 3 (Section 3.2.2)

Soils were teased apart by hand at 18 °C and stored in partially-sealed polypropylene bags to reduce moisture loss. Large stones (with diameters >20 mm) and invertebrates were removed before the soil was passed through a rotary soil sieve (20 mm mesh size; model: CRS400, Clarke Power Products). A sub- and topsoil arrangement was engineered in the upper-section of the mesocosm to simulate a tillage regime (Figure 4.4a), each composed of 2.896 kg of soil, compacted to a bulk density of ≈1.1 kg L^{-1}. The total soil column depth was 500 mm. Well-characterised, basaltic rock powder (see Section 4.2.3; total mass of 728 ± 0.05 g per column; equivalent to 4 kg m^{-2} or 40 t basalt ha^{-1}) and softwood biochar pellets (see Section 4.2.3) were well mixed into the soil in the upper 150 mm of treated columns (n = 6), to simulate a tillage regime. Initial soil characterisation was carried out following the same protocols and equipment as in Section 3.2.2.

4.2.3 Basaltic rock and biochar characterisation and preparation

An intrusive analcime gabbro (Lewis *et al.*, 2021) used in this study was sourced from Hill House Quarry near Troon, Scotland, UK, and was chosen for its low amorphous mineral content and high weathering potential. To produce an ultra-fine powder, the rock was subjected to the same refinement protocol detailed in Section 3.2.3, which produced a similar particle diameter range of 1.5–300 µm, with a the P_{80} value of ≈45

µm. The rock mineralogy and BET SA measurements were determined by Dr A. Lewis, following the same procedures mentioned in Section 3.2.3. The mineralogy is reported in Lewis *et al*. (2021), and the BET SA was found to be 2.70 ± 0.02 $m^2\ g^{-1}$. Pelletised softwood biochar was sourced from the UK Biochar Research Centre, University of Edinburgh, UK by Dr B. Sarkar. Detailed specifications for their material are reproduced in Figure B.9.

4.2.4 Plant materials

A commercial ryegrass (*Lolium perenne*) variety was chosen for this study, with seeds applied directly to the top surface of the soil columns on day 0, at a rate of 70 g m^{-2}. The day/night temperature in the growth rooms was 20/15 °C and the relative humidity maintained at 75%. Additive CO_2 was used to sustain atmospheric concentrations of 400 ppm in the controlled environment and a photosynthetic photon flux density of 800 µmol photons $m^{-2}\ s^{-1}$ was maintained during the 17-hour days. Shoot biomass was periodically harvested to monitor crop performance, with harvested materials immediately oven-dried at 60 °C for 48 hours. A combined NPKS fertiliser was applied in three doses (on days 13, 48 and 160), with each dose equivalent to 50 kg N ha^{-1} (ammonium nitrate), 9 kg P_2O_5 ha^{-1}, 7 kg K_2O ha^{-1} and 8 kg SO_3 ha^{-1}. For each fertilisation event, sufficient quantities of fertiliser were dissolved in UHP water such that each soil column received 25 ml of fertiliser solution with the following nutrient concentrations: 3.62 g N L^{-1} (ammonium nitrate), 0.651 g P_2O_5 L^{-1}, 0.506 g K_2O L^{-1} and 0.579 g SO_3 L^{-1}. Post-experiment plant tissue handling and analysis was conducted in line with the protocols set out in Section 3.2.6. Unfortunately, plant cation concentration data could not be processed in time in be included in this thesis.

4.2.5 Irrigation regime

A bespoke drip-feed irrigation system was constructed for the trial using commercially available low-density polyethylene (LDPE) drip line (14 mm diameter) and pressure-compensated drippers rated to release water at 50 ml $minute^{-1}$ (Figure 4.4b). The system was then connected to a professionally-fitted, solenoid-driven, fully-automated reverse osmosis water supply, which permitted minute-by-minute control of the flow. Pre-experiment testing indicated low variance (*SD* < 3%) in the drippers flow rates.

Delivery of irrigation water to the columns was staggered over the 5-hour nights, to mitigate excessive leaching of the sandy soils. The irrigation schedule between days 0 and 160 required small daily quantities of water to be supplied to offset evaporation, with a larger quantity applied once-weekly to generate leachate on-demand (Table 4.1).

Table 4.1 – Irrigation schedule in Chapter 4

Timeframe	Daily irrigation volume (ml)	Once-weekly additional over-irrigation volume (ml)
days 1–14	100	300
days 15–21	60	340
days 22–28	60	140
days 29–35	80	220
days 36–49	100	300
days 50–160	100	200

On day 160, the columns' effluent nozzles were sealed and the soil was flooded to a GWC of around 0.55 g g^{-1} to enable measurements of soil-atmosphere GHG fluxes (which could not be integrated into this thesis in time). Soils were then allowed to dry in the growth room between day 199 and 219, when the experiment ended and the final plant and soils materials were harvested.

4.2.6 Leachate, soil and plant sample preparation and cation analysis

With respect to leachate, soil and plant materials, this study used the same procedures and instruments detailed in Section 3.2.3. The only difference in soil handling was a simplified top-/sub-soil arrangement, instead of the 5-layer excavation approach used in Chapter 3.

4.3 Results and discussion

4.3.1 *Lolium perenne* performance

All mesocosms received the same dose of NPKS fertiliser in this study, which ensured that *Lolium* specimens in all treatments were visually healthy and productive. However, the different treatments resulted in divergent plant biomass results (Figure 4.5), with the greatest contrast being that between the acidic and alkaline soil types.

Firstly, total above- and below-ground biomass is compared across all eight treatments in this study (i.e. acidic *vs* alkaline; ±biochar; ±basalt), and initially, each unique treatment is considered as a categorical variable (one-way ANOVA; Figure 4.5), rather than a combination of three soil and additive factors (three-way ANOVA). Total root biomass was generally unaffected by the various combinations of soils and additives;

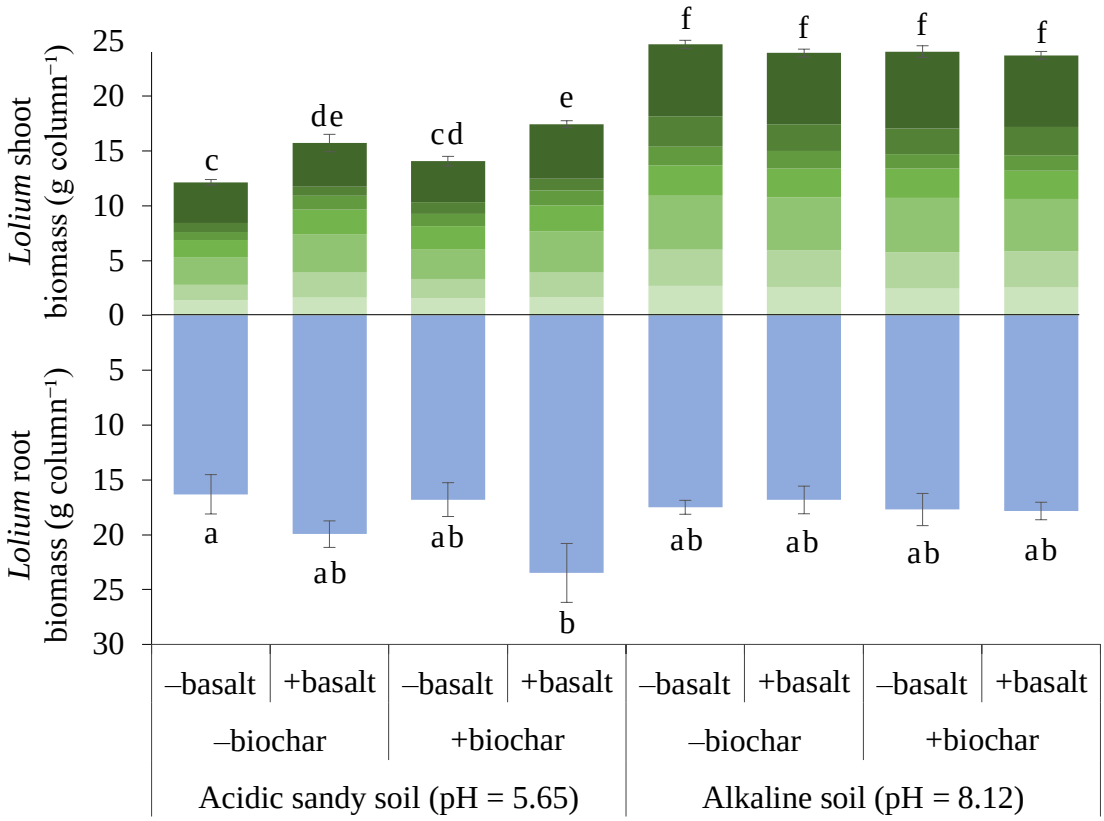

Figure 4.5 – *Lolium perenne* root and shoot (dry) biomass. Shoot data are displayed as a colour gradient, reflecting the seven successive shoot harvests that were conducted during the trial. Root data were collected after the experiment was terminated. Error bars represent *SE* in the mean for total root and shoot (dry) biomass. Total root and shoot biomass bars sharing the same letter are not statistically different ($p > 0.05$; one-way ANOVA with Tukey post hoc test). All statistics were performed in R. $n = 6$.

however, in the acidic sandy soil, the co-application of basalt with biochar did result in a significant ($p < 0.05$) 44.0 ± 22.8% (*SE*) increase in root biomass, with respect to the additive-free control (pH 5.65; –biochar; –basalt), although the same root-related fertilisation effect was not significant in the respective basalt-only and biochar-only treatments. These results for the co-deployment treatment are similar to the those for the manure regime in Chapter 3, where a significant 24.4 ± 9.4% (*SE*) rise in root biomass at 12–24 cm soil depth was observed after basalt amendment (offset, in that case, by a similar reduction at 48–50 cm depth). In this study, it is feasible that the plants in the acidic soil's co-deployment treatment similarly responded by investing more assimilate resources into colonising soils enriched by the basalt and biochar amendments, to extract supplementary nutrients and/or water. Moreover, the strategy appears to have worked, as the fertilisation effect was mirrored aboveground (Figure 4.5). In the alkaline soil, however, no significant changes in root biomass were resolved.

Lolium shoot biomass was strongly affected by soil type in this study, with the biggest treatment-related changes, again, seen in the acidic sandy soil after basalt/biochar amendments (Figure 4.5). Here, in the co-deployment scenario, a significant ($p < 0.05$) increase in total (cumulative) shoot biomass of 43.7 ± 6.3% (*SE*) was measured, with respect to the (unamended) 'native' acidic soil. This was not quite sufficient to place it on par with productivity in the alkaline soil (Figure 4.5), but nonetheless closed the gap. By comparison with this naturally more-productive alkaline soil, total shoot biomass in the 'native' acidic soil was 50.7 ± 7.6% (*SE*) lower, but only 29.1 ± 4.9% (*SE*) lower in the acidic soil's co-deployment treatment. Notably, basalt amendment of the acidic soil's biochar-free treatment was also associated with a significant ($p < 0.05$; 29.5 ± 7.8% *SE*) increase in cumulative aboveground biomass, suggesting that the basalt may have done the 'heavy lifting' in the co-deployment scenario. Statistical analysis probing a possible basalt × biochar interaction (pH 5.65 soil; two-way ANOVA; ±biochar; ±basalt) revealed that the effect was far from significance ($p = 0.85$), but did reveal a significant ($p = 0.003$) positive effect on shoot biomass overall where biochar was added to the acidic soil (across both basalt treatments), and a highly-significant uplift on yield overall where basalt was added ($p = 3\times10^{-6}$; across both biochar treatments). These results are consistent with the 15.6% increase in *Lolium* shoot biomass measured by ten Berge *et al*. (2012) after olivine application, and are similarly consistent with the increased yields reported in Chapter 2. Again, no changes were seen in the alkaline soil.

In this study, the alkaline soil's indifferent biomass response to both soil additives may be linked to its baseline productivity, which was evidently substantial without the basalt/char amendments (Figure 4.5; –biochar; –basalt). In this sense, adding alkaline amendments (e.g. crushed mafic rock or softwood biochar) to this already fairly-high-pH substrate (pH 8.12) only served to further increase the pH of the soil environment and, thus, probably slightly reduced the efficiency of plant N and P uptake (Figure 4.6). This would be consistent with the marginal (i.e. not significant; Figure 4.5) reductions in shoot yield measured in the alkaline soil for the basalt only (–3.2 ± 2.4% *SE*), biochar only (–2.7 ± 2.9% *SE*) and co-deployment (–18.7 ± 11.0% *SE*) treatments. For the acidic soil (pH 5.65), however, baseline uptake efficiency for N, P and K is likely to have been poor in the medium-acidic 'native' soil (Figure 4.6), such that the alkalising effect of the basalt and biochar led to improved nutrient uptake efficiency.

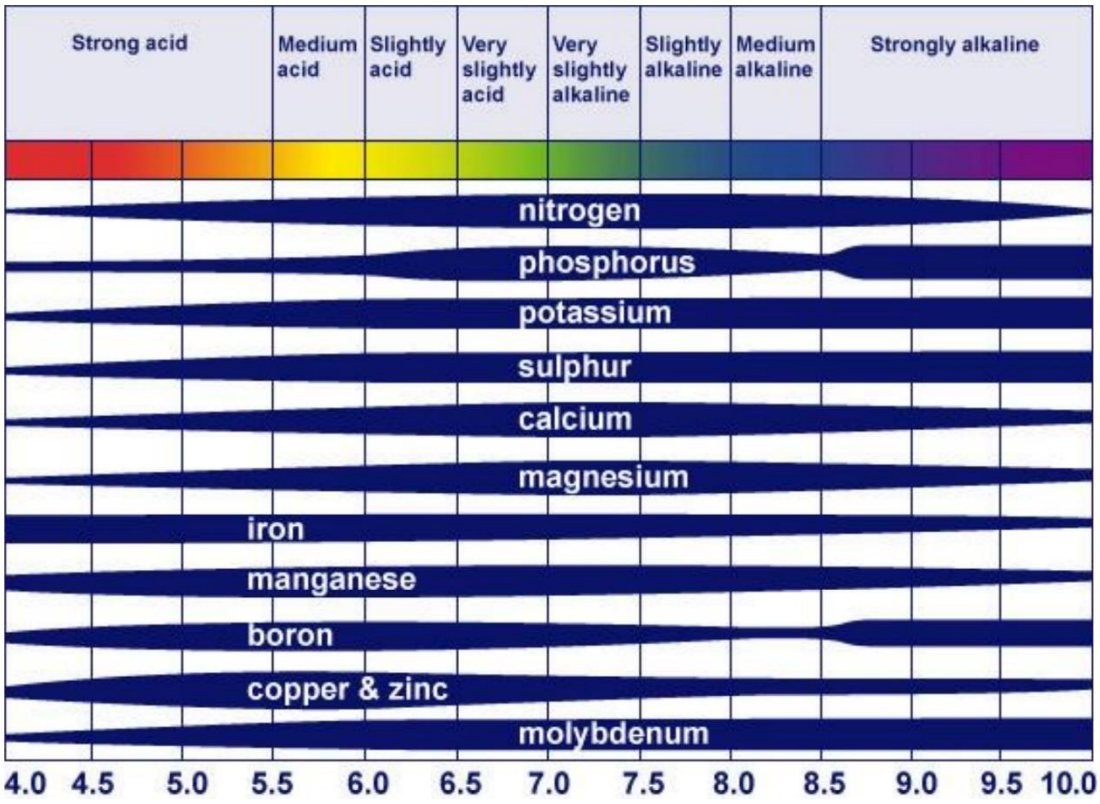

Figure 4.6 – The effect of soil pH on nutrient availability. (Roques *et al.*, 2012).

Further insight into the dynamic fertilisation responses was gained from a time-wise, analysis of the *Lolium* shoot biomass dataset (two-way repeated measures ANOVA), again, considering each unique treatment as a categorical variable, but now considering time as a possible interacting factor (Figure 4.7). On this basis, the effect of basalt in increasing cumulative shoot (dry) biomass develops significance ($p < 0.05$) in the acidic soil –biochar treatment at the second time point (day 43), and further evolves to high significance ($p < 0.01$) on day 92, before then losing significance by the end of the study. These findings echo the results from the *Sorghum* leaf length analysis in Chapter 2, where an early morphological divergence (that later waned during the trial) was determined to be a good indicator of basalt weathering in the NPK treatment (i.e. where no additional organic matter was applied). The results from this study therefore indicate

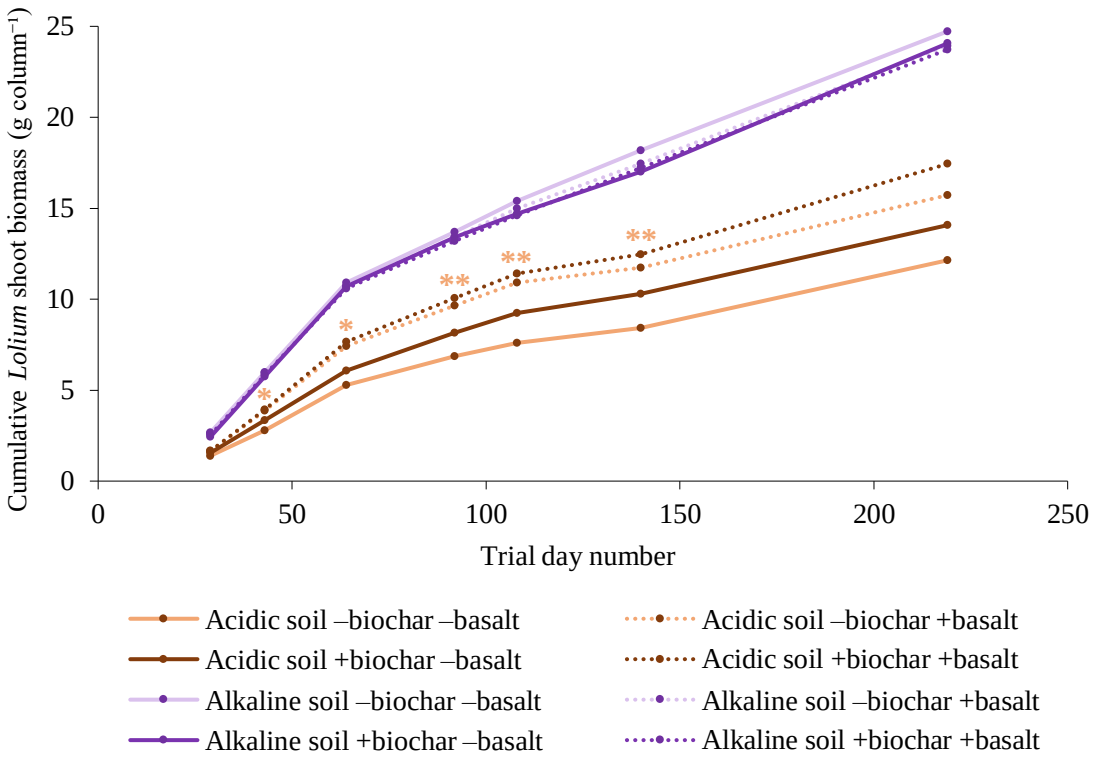

Figure 4.7 – *Lolium perenne* shoot (dry) biomass time-series. Mean biomass values relating to the alkaline sandy soil (pH = 8.12) are displayed in orange/brown, and those relating to the acid sandy soil (pH = 5.65) are shown in purple. The darker hue indicates biochar was added, and as in Chapter 3, dotted lines indicate that basalt was added. Single asterisks indicate a statistically significant change following basalt amendment to soil ($p < 0.05$; two-way repeated measures ANOVA; $n = 6$). Double asterisks indicate that $p < 0.01$. Solid and dotted lines do not indicate data interpolation and are purely for ease of visual reference. Error bars are omitted for clarity. All statistical analyses were performed in R.

comparatively enhanced weathering in the acidic –biochar soils, compared with the acidic +biochar soils (or indeed, either of the alkaline ±basalt treatment pairs), and this is likely due to the high CEC and alkaline nature of the co-applied biochar. As with the manure applied in Chapter 2, the increase in soil pH following biochar application likely led to lower weathering rates, in accordance with the standard Arrhenius equation (Equation 1.5). Moreover, the especially high cation affinity of the biochar material probably means that pore water cation concentrations in this study were supressed, as they were in Chapter 2. This may similarly have curbed a strong early basalt-related fertilisation effect in the present study, such that the effect was only significant for the biochar-free treatment. Together, this evidence suggests that when basalt is co-applied with a high-CEC, C-rich soil additive, the strong early weathering pulse* will be partially adsorbed onto the OM's ion-exchange surfaces, dampening the external manifestation of the weathering signal (i.e. as modified pore water chemistry and improved plant growth characteristics). This was hypothesised to be deleterious for weathering rates in this trial, as it was found to be in the previous.

In summary, the increase in shoot biomass following basalt application was strongest in the acidic soil, implying that the related null hypothesis (*H*11: 0) should be rejected in favour of the alternative (*H*11: 1). And since the biochar did not enhance this basalt-related fertilisation effect in any soil type, the associated null hypothesis (*H*12: 0) is similarly rejected, for the alternative (*H*12: 1).

4.3.2 Leachate geochemistry

Leachate geochemistry showed high intra-treatment variability in this study, such that no significant differences were identified in either soil type, following amendment with basalt and/or biochar (Figure 4.8–9). Errors were generally higher in the acidic soil, but overall the variability was much higher than the previous trials. The source of this variability is unknown, but in general, the low signal to noise ratio for all parameters and analytes may have been affected by the higher irrigation rate in this study and the increased permeability of the sandy soils. The former could easily have diluted any

*Assumed to be a fast-weathering carbonate mineral or ultra-fine particle size

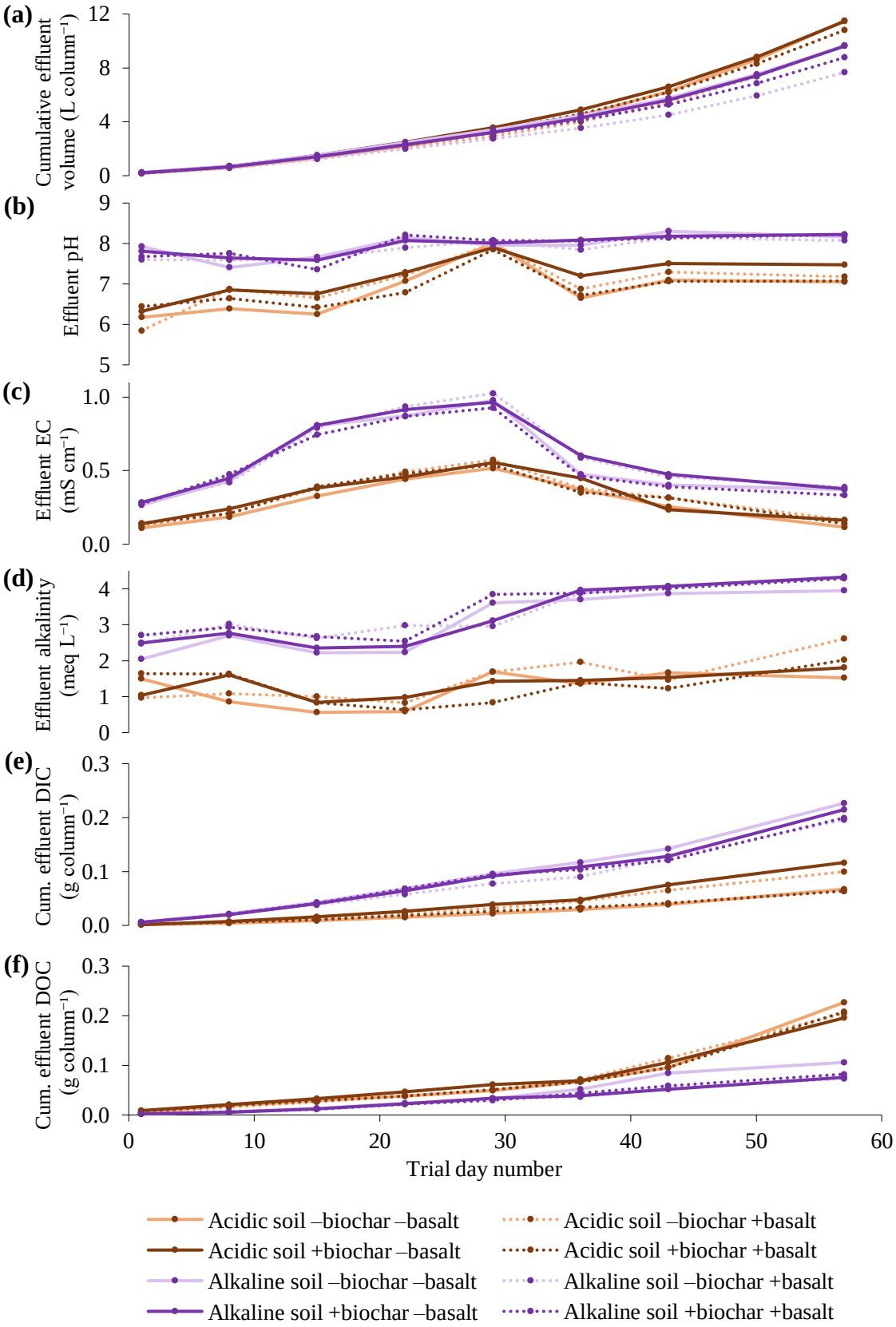

Figure 4.8 – Leachate geochemistry time-series. 57-day time-series for effluent (a) volumes, (b) pH, (c) EC, (d) total alkalinity, and cumulative flux of (e) inorganic and (f) organic carbon. Solid and dotted lines do not indicate data interpolation and are purely for ease of visual reference. Error bars are omitted for clarity. All statistical analyses were performed in R.

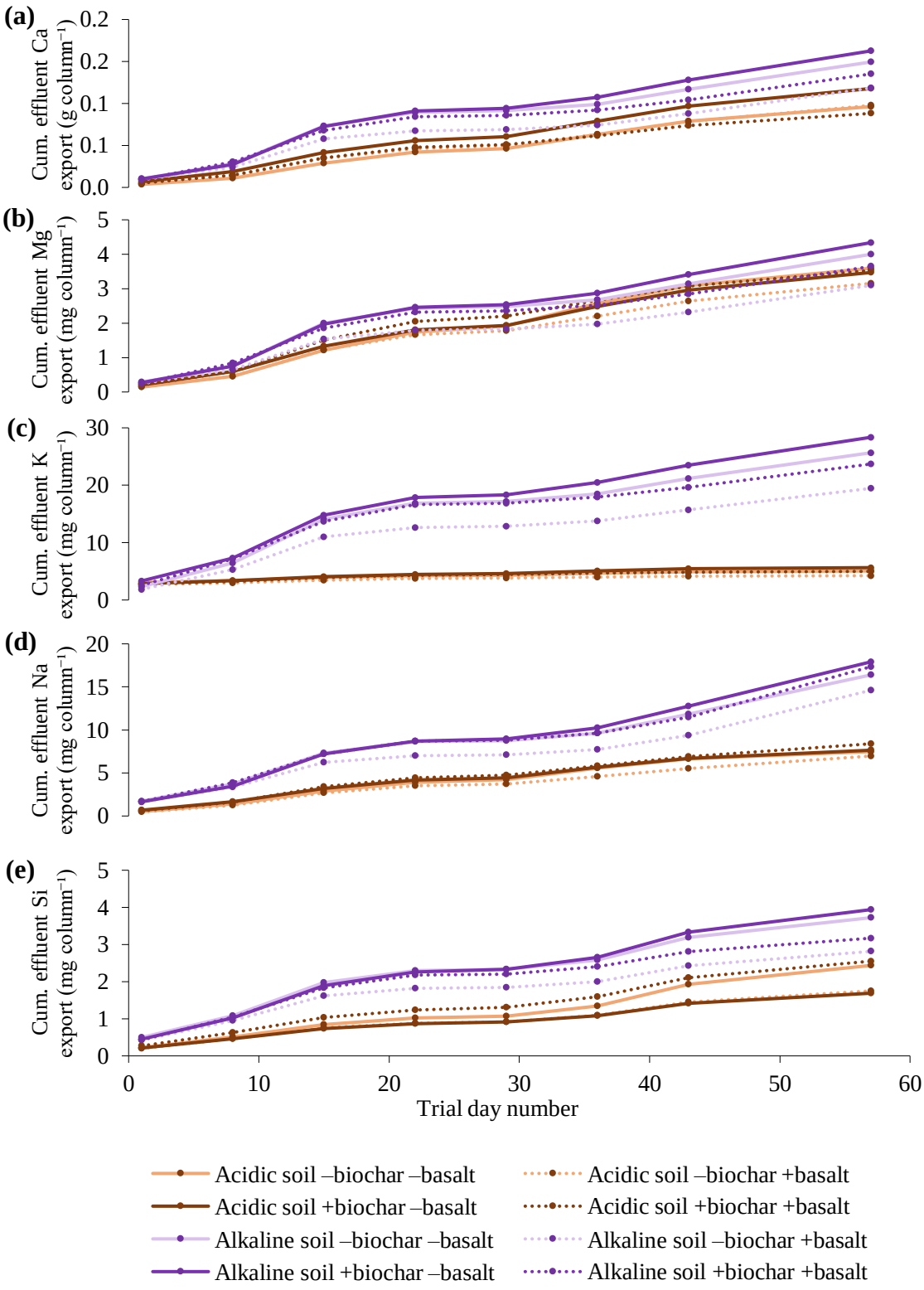

Figure 4.9 – Leachate major cation and Si budgets, time-series results. 57-day effluent time-series for elemental budgets of (a) Ca, (b) Mg, (c) K, (d) Na, and (e) Si. Solid and dotted lines do not indicate data interpolation and are purely for ease of visual reference. Error bars are omitted for clarity. All statistical analyses were performed in R.

weathering signals in the leachate due to the development of preferential flow paths, and the latter may have reduced water residence times (compared to the clay-loam soil in Chapters 2 and 3) to such an extent that the various soils could not impart their characteristics upon the pore waters in time (i.e. before becoming leachate). Whilst the drip-feed irrigation system was well calibrated prior to the experiment, it is possible that some of its components became worn or damaged, such that subtle differences in irrigation rate developed and compounded over the trial. And if much of the excess irrigation solution evaporated, this watering rate error might not register in the leachate volume record at all. Notably, the high variability is in both soil types, which does not imply that any one substrate had markedly high heterogeneity or was affected by significant contamination. Instead, this may simply be a feature of high-irrigation ERW trials with sandy soils. Accordingly, the relevant null hypothesis (*H*13: 0) is rejected, in favour of the alternative (*H*13: 1).

4.3.3 Soil moisture

The large variation in leachate volumes and chemistry (Section 4.3.2) is echoed in the direct measurements of soil moisture taken during the trial (Figure 4.10). The higher productivity in the alkaline soil unsurprisingly led to significantly lower ($p < 0.05$; three-way repeated measures ANOVA) soil moisture from the second timepoint. But in this trial, whilst there is a suggestion that the basalt application led to generally lower soil moisture – possibly indicative of a basalt-related fertilisation effect, as in Chapter 3 – there were no statistically significant differences between any ±basalt or ±biochar pairs of treatments (Figure 4.10; $p > 0.05$; three-way repeated measures ANOVA).

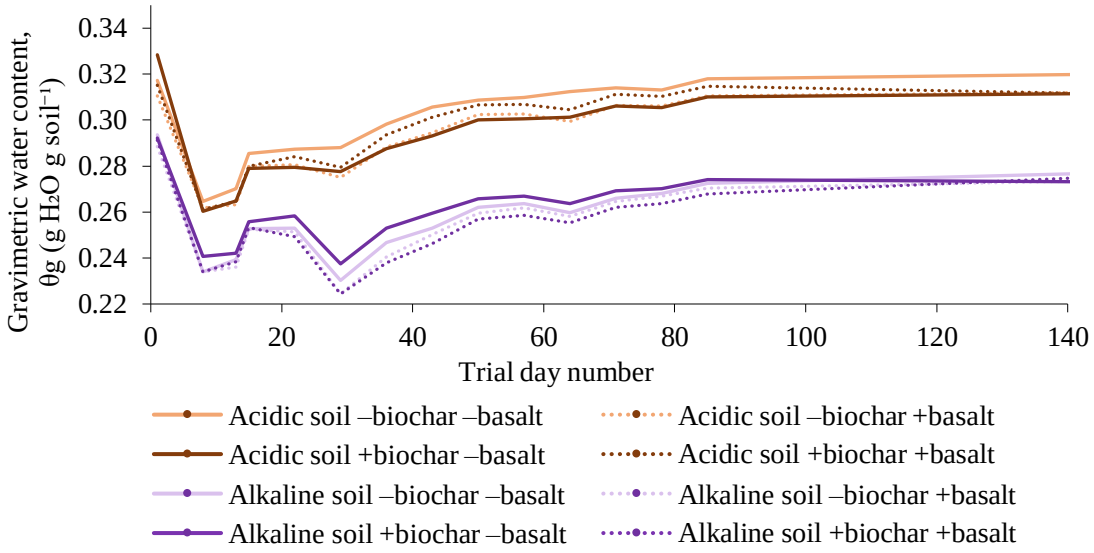

Figure 4.10 – Soil GWC over the first 140 days of the *Lolium* trial.

4.3.4 Soil pH, plant-available Si and exchangeable cation budgets

Every experimental treatment in this study significantly increased the pH of the sandy acidic topsoil (Figure 4.11a; $p < 0.001$; three-way ANOVA; on untransformed [H^+] values), with pH unit increases of 1.41 ± 0.08 (*SE*), 1.29 ± 0.07 (*SE*) and 1.61 ± 0.09 (*SE*) measured for the +basalt, +biochar and co-deployment treatments, respectively, when compared against the respective control soils. These extreme results – which in each case modified the medium-acidic topsoil to circumneutral pH – reflect the extremely low buffer capacity of the native Moss End Farm soil (Section 4.2.2). Perhaps, for this reason, the subsoil pH is also significantly modified, suggesting deep propagation of the weathering signal (Figure 4.11a). No significant changes in pH were detected in the alkaline soil, possibly reflecting its superior buffer capacity, or indicating low weathering rates (Figure 4.11a).

Highly significant ($p < 0.001$) increases in topsoil exchangeable Ca were detected in the acidic soil after basalt application, regardless of biochar application (Figure 4.11b; three-way ANOVA; on untransformed [H^+] values), but the biochar itself also had a significant ($p < 0.05$) effect. It is unclear if the effect on Ca in the biochar treatments is related to cations introduced with the char material, or if some other mechanism is involved; nonetheless, the larger increase in exchangeable Ca after basalt application is more consistent with the weathering of primary basaltic minerals. The soil in the previous chapter had double the amount of Ca in the exchangeable pool (Figure 3.19b), making it difficult to resolve small changes due to weathering. It may have been easier to detect the signal in this sandy acidic soil type due to the low background levels (Figure 4.11b). As above, no significant changes in exchangeable Ca were detected in the alkaline soil. It is conceivable, given the high Ca background in this calcareous soil, that pore waters were saturated for certain Ca-bearing minerals, however this was not verified with geochemical modelling in this study.

Exchangeable Mg was low in both native soils in this study, as in the previous. The change in Mg in the acidic topsoil is highly variable without biochar, and too weak to be significant in the co-deployment treatment (Figure 4.11c). The strong sorptive effect of biochar is resolved here, with a significant ($p < 0.01$) reduction in exchangeable Mg where only biochar was applied. In the alkaline soil, which naturally had a low Mg saturation of just 1%, highly significant ($p < 0.01$) increases in exchangeable Mg are detected in the top- and sub-soil (Figure 4.11c).

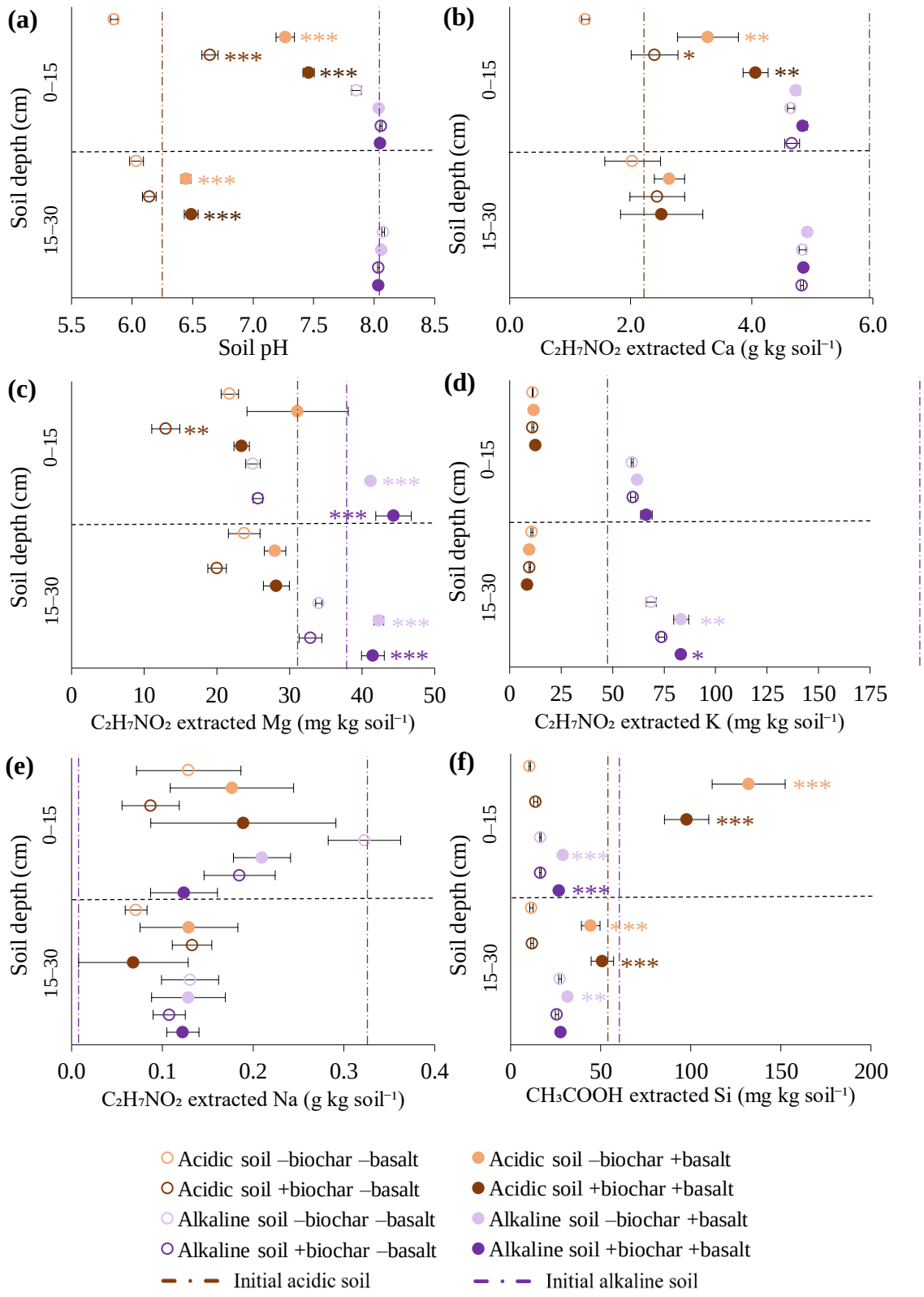

Figure 4.11 – Depth-wise analysis of post-experiment soil pH, soil exchangeable cations and plant-available Si. (a) Soil pH by depth, and the concentration per unit mass of bulk soil for exchangeable (b) Ca, (c) Mg, (d) K, (e) Na, and (f) plant-available Si. Asterisks indicate a statistically significant change following basalt amendment to soil ($p < 0.05$; one-way ANOVA; $n = 7$). Double asterisks indicate that $p < 0.01$. Triple asterisks indicate that $p < 0.001$. Error bars represent the *SE*. All statistical analyses were performed in R.

These results well match the findings in Chapter 3 (Figure 3.19c), and represent strong evidence for weathering of primary Mg-bearing silicate or carbonate minerals, even under high-pH conditions.

In the sandy acidic soil, exchangeable K changed little in response to basalt or biochar, but in the alkaline soil, significant ($p < 0.05$) increases in subsoil K were identified (Figure 3.19d). This additional K in the lowest soil layer may be derived from primary mineral weathering, but could also have accumulated after being displaced from cation exchange surfaces in the soil layer above – through competitive adsorption with the Mg evidently released into the pore waters (Figure 3.19c), as in ten Berge *et al*. (2012).

No significant changes in Na were observed in any treatment or soil. However, plant-available silicon (as determined by an acetic acid soil extraction) increased significantly ($p < 0.01$) at every depth in both soils, and in every treatment where basalt was applied. These results reproduce the findings in both Chapters 2 and 3, where large and often highly statistically significant increases in soil available-Si were measured following basalt application. In this study, both sandy soils had such low Si concentrations that they were likely to be Si deficient (Korndörfer *et al*., 2001; Mahendran *et al*., 2021), and so if this effect were to be replicated in the field, the improvement in plant-available Si is likely to have considerable agronomic benefits. In ryegrass, Si is known to improve structural resistance, and so this strong effect from ultra-fine basalt powder may be of interest to agronomists managing turf that is subjected to intense wear – e.g. sports fields (Pruyne, Schlossberg and Uddin, 2019).

As the basalt-related pH increase was highest in the acidic soil, this implies that the null hypothesis (*H*14: 0) should be rejected for (*H*14: 1). However, the much larger effect in the acidic soil is likely due to its low buffer capacity, and not just the low initial pH.

4.3.5 Basalt weathering and CDR rate estimates

Elemental budgets for key indicators of silicate mineral weathering (Ca, Mg, K, Na and Si) were, again, calculated in accordance with the method in Section 2.3.4 – with the notable absence of plant tissue cation data for this experiment, which could unfortunately not be prepared in time.

As in the *Sorghum* trials, final mass balance tables for this study (Tables 4.2–5) suggest that divalent cations (Ca^{2+} + Mg^{2+}) dominate the weathering budget, with the soil exchange reservoir representing the largest component. Accordingly, the related null hypothesis (*H*15: 0) is confidently rejected in favour of the alternative (*H*15: 1).

Table 4.5 – Changes in whole-system elemental budgets and transfer rates resulting from basalt amendment (40 t basalt ha^{-1}) of an acidic sandy-loam soil (pH 5.65; NPKS fertiliser; 150 kg N ha^{-1}; 27 kg P_2O_5 ha^{-1}; 21 kg K_2O ha^{-1}; 24 kg SO_3 ha^{-1}) planted with *Lolium perenne*, after 219 days. Values are mean differences (±*SE*) between basalt-amended (n = 6) and unamended (control) planted mesocosms (n = 6). Positive values indicate increased element concentrations due to basalt amendment. Soil extraction results are mass-weighted, depth-integrated averages (±*SE*) for the entire column. SA are expressed as SA_L for land surface area, and SA_R for rock SA.

Element	Effect of basalt treatment on rate of elemental release					Measured elemental release from basalt†	Rate of elemental release (BET SSA = 2.70 m^{-2} g^{-1} basalt)‡
	Leachate	Plant (µmol m^{-2} SA_L d^{-1})			Soil extraction* (mmol m^{-2} SA_L d^{-1})		
		Roots	Shoots	Seeds		(mmol m^{-2} SA_L d^{-1})	(mol m^{-2} SA_R s^{-1})
Ca	8.99 ± 280.58	No data	No data	No data	49.4 ± 13.7	49.4 ± 13.8	$9.6\times10^{-11} \pm 2.7\times10^{-11}$
Mg	–5.08 ± 7.16	No data	No data	No data	0.43 ± 0.23	0.43 ± 0.23	$8.3\times10^{-13} \pm 4.4\times10^{-13}$
K	–2.97 ± 4.10	No data	No data	No data	–0.01 ± 0.02	–0.01 ± 0.02	$-1.4\times10^{-14} \pm 4.2\times10^{-14}$
Na	0.96 ± 17.7	No data	No data	No data	0.08 ± 2.37	0.08 ± 2.37	$1.5\times10^{-13} \pm 4.6\times10^{-12}$
Si	–4.26 ± 4.32	No data	No data	No data	4.09 ± 0.52	4.09 ± 0.52	$7.9\times10^{-12} \pm 1.0\times10^{-12}$

*Si data are from an acetic acid extraction (to estimate plant-available Si) and cation data were derived from an ammonium acetate leach. Both extractions were conducted on representative soil samples from two discrete layers (0–15, 15–30 cm depth).

†Measured moles released from basalt and associated uncertainties were calculated following the method in Table 2.1.

‡Calculated by dividing the measured moles released from basalt by BET-determined rock surface area (SSA = 2.70 m^{-2} g^{-1} basalt).

Table 4.6 – Changes in whole-system elemental budgets and transfer rates resulting from basalt amendment (40 t basalt ha^{-1}) and biochar co-amendment (10 t biochar ha^{-1}) of an acidic sandy-loam soil (pH 5.65; NPKS fertiliser; 150 kg N ha^{-1}; 27 kg P_2O_5 ha^{-1}; 21 kg K_2O ha^{-1}; 24 kg SO_3 ha^{-1}) planted with *Lolium perenne*, after 219 days. Values are mean differences (±*SE*) between basalt-amended (n = 6) and unamended (control) planted mesocosms (n = 6). Positive values indicate increased element concentrations due to basalt amendment. Soil extraction results are mass-weighted, depth-integrated averages (±*SE*) for the entire column. SA are expressed as SA_L for land surface area, and SA_R for rock SA.

Element	Effect of basalt treatment on rate of elemental release					Measured elemental release from basalt†	Rate of elemental release (BET SSA = 2.70 m^{-2} g^{-1} basalt) ‡
	Leachate	Plant ($\mu mol\ m^{-2}\ SA_L\ d^{-1}$)			Soil extraction* ($mmol\ m^{-2}\ SA_L\ d^{-1}$)		
		Roots	Shoots	Seeds		($mmol\ m^{-2}\ SA_L\ d^{-1}$)	($mol\ m^{-2}\ SA_R\ s^{-1}$)
Ca	–231 ± 299	No data	No data	No data	24.6 ± 20.2	24.3 ± 20.4	$4.7\times10^{-11} \pm 4.0\times10^{-11}$
Mg	–0.37 ± 7.68	No data	No data	No data	0.44 ± 0.16	0.44 ± 0.16	$8.5\times10^{-13} \pm 3.1\times10^{-13}$
K	–4.90 ± 8.73	No data	No data	No data	0.01 ± 0.04	0.01 ± 0.04	$9.3\times10^{-15} \pm 8.5\times10^{-14}$
Na	16.5 ± 24.2	No data	No data	No data	–2.22 ± 2.03	–2.20 ± 2.02	$-4.3\times10^{-12} \pm 3.9\times10^{-12}$
Si	6.20 ± 4.85	No data	No data	No data	3.26 ± 0.42	3.27 ± 0.42	$6.3\times10^{-12} \pm 8.1\times10^{-13}$

*Si data are from an acetic acid extraction (to estimate plant-available Si) and cation data were derived from an ammonium acetate leach. Both extractions were conducted on representative soil samples from two discrete layers (0–15, 15–30 cm depth).

†Measured moles released from basalt and associated uncertainties were calculated following the method in Table 2.1.

‡Calculated by dividing the measured moles released from basalt by BET-determined rock surface area (SSA = 2.70 m^{-2} g^{-1} basalt).

Table 4.7 – Changes in whole-system elemental budgets and transfer rates resulting from basalt amendment (40 t basalt ha^{-1}) of a calcareous sandy-loam soil (pH 8.12; NPKS fertiliser; 150 kg N ha^{-1}; 27 kg P_2O_5 ha^{-1}; 21 kg K_2O ha^{-1}; 24 kg SO_3 ha^{-1}) planted with *Lolium perenne*, after 219 days. Values are mean differences (±*SE*) between basalt-amended (n = 6) and unamended (control) planted mesocosms (n = 6). Positive values indicate increased element concentrations due to basalt amendment. Soil extraction results are mass-weighted, depth-integrated averages (±*SE*) for the entire column. SA are expressed as SA_L for land surface area, and SA_R for rock surface SA.

Element	Effect of basalt treatment on rate of elemental release						
	Leachate	Plant (µmol m^{-2} SA_L d^{-1})			Soil extraction* (mmol m^{-2} SA_L d^{-1})	Measured elemental release from basalt†	Rate of elemental release (BET SSA = 2.70 m^{-2} g^{-1} basalt)‡
		Roots	Shoots	Seeds		(mmol m^{-2} SA_L d^{-1})	(mol m^{-2} SA_R s^{-1})
Ca	–200 ± 172	No data	No data	No data	–1006 ± 2010	–1206 ± 2002	$-2.3\times10^{-12} \pm 3.9\times10^{-12}$
Mg	–9.19 ± 7.59	No data	No data	No data	764 ± 42.4	755 ± 38.4	$1.5\times10^{-12} \pm 7.4\times10^{-14}$
K	–38.6 ± 27.2	No data	No data	No data	–348 ± 96.3	309 ± 91.4	$6.0\times10^{-13} \pm 1.8\times10^{-13}$
Na	3.23 ± 37.5	No data	No data	No data	–1753 ± 2709	–1750 ± 2698	$-3.4\times10^{-12} \pm 5.2\times10^{-12}$
Si	–6.86 ± 4.82	No data	No data	No data	454 ± 39.5	448 ± 379	$8.7\times10^{-13} \pm 7.4\times10^{-14}$

*Si data are from an acetic acid extraction (to estimate plant-available Si) and cation data were derived from an ammonium acetate leach. Both extractions were conducted on representative soil samples from two discrete layers (0–15, 15–30 cm depth).

†Measured moles released from basalt and associated uncertainties were calculated following the method in Table 2.1.

‡Calculated by dividing the measured moles released from basalt by BET-determined rock surface area (SSA = 2.70 m^{-2} g^{-1} basalt).

Table 4.8 – Changes in whole-system elemental budgets and transfer rates resulting from basalt amendment (40 t basalt ha^{-1}) and biochar co-amendment (10 t biochar ha^{-1}) of a calcareous sandy-loam soil (pH 8.12; NPKS fertiliser; 150 kg N ha^{-1}; 27 kg P_2O_5 ha^{-1}; 21 kg K_2O ha^{-1}; 24 kg SO_3 ha^{-1}) planted with *Lolium perenne*, after 219 days. Values are mean differences (±*SE*) between basalt-amended (n = 6) and unamended (control) planted mesocosms (n = 6). Positive values indicate increased element concentrations due to basalt amendment. Soil extraction results are mass-weighted, depth-integrated averages (±*SE*) for the entire column. SA are expressed as SA_L for land surface area, and SA_R for rock SA.

Element	Effect of basalt treatment on rate of elemental release						
	Leachate	Plant (µmol m^{-2} SA_L d^{-1})			Soil extraction* (mmol m^{-2} SA_L d^{-1})	Measured elemental release from basalt†	Rate of elemental release (BET SSA = 2.70 m^{-2} g^{-1} basalt) ‡
		Roots	Shoots	Seeds		(mmol m^{-2} SA_L d^{-1})	(mol m^{-2} SA_R s^{-1})
Ca	–195 ± 215	No data	No data	No data	–1.78 ± 2.96	–1.97 ± 3.03	$-3.8\times10^{-12} \pm 5.9\times10^{-12}$
Mg	–38.5 ± 9.51	No data	No data	No data	0.85 ± 0.10	0.85 ± 0.11	$1.6\times10^{-12} \pm 2.0\times10^{-13}$
K	–29.7 ± 38.4	No data	No data	No data	0.33 ± 0.10	0.30 ± 0.11	$5.8\times10^{-13} \pm 2.2\times10^{-13}$
Na	11.5 ± 55.9	No data	No data	No data	–0.89 ± 2.14	–0.88 ± 2.13	$-1.7\times10^{-12} \pm 4.1\times10^{-12}$
Si	–4.69 ± 5.93	No data	No data	No data	0.34 ± 0.04	0.34 ± 0.04	$6.5\times10^{-13} \pm 7.9\times10^{-14}$

*Si data are from an acetic acid extraction (to estimate plant-available Si) and cation data were derived from an ammonium acetate leach. Both extractions were conducted on representative soil samples from two discrete layers (0–15, 15–30 cm depth).

†Measured moles released from basalt and associated uncertainties were calculated following the method in Table 2.1.

‡Calculated by dividing the measured moles released from basalt by BET-determined rock surface area (SSA = 2.70 m^{-2} g^{-1} basalt).

Overall, weathering rates for the key elements of interest were much higher in the acidic soil (Tables 4.1–2) than the alkaline soil (Tables 4.3–4), and this is best explained with reference to the Arrhenius equation for acid-catalysed weathering (Equation 1.5), which indicates faster dissolution in lower pH environments. Indeed, the Moss End Farm soil is acidic enough for non-carbonic acids to have had an influence over weathering rates (Dietzen and Rosing, 2023) and so this is corrected for during the later CDR calculation.

As in Section 3.3.6, weathering budgets were converted into units of total equivalents accumulated in the leachate and soil exchange pools (Figure 4.12), excluding Na, as before. The rock application is associated with a statistically significant ($p < 0.05$; one-way ANOVA with Tukey *post hoc* test) increase in accumulated equivalents with and without biochar (compared with respective controls), which implies statistically significant CDR. Measured across all treatments (i.e. ±biochar) in the sandy acidic soil (two-way ANOVA), basalt had a highly significant ($p < 0.01$) effect. This

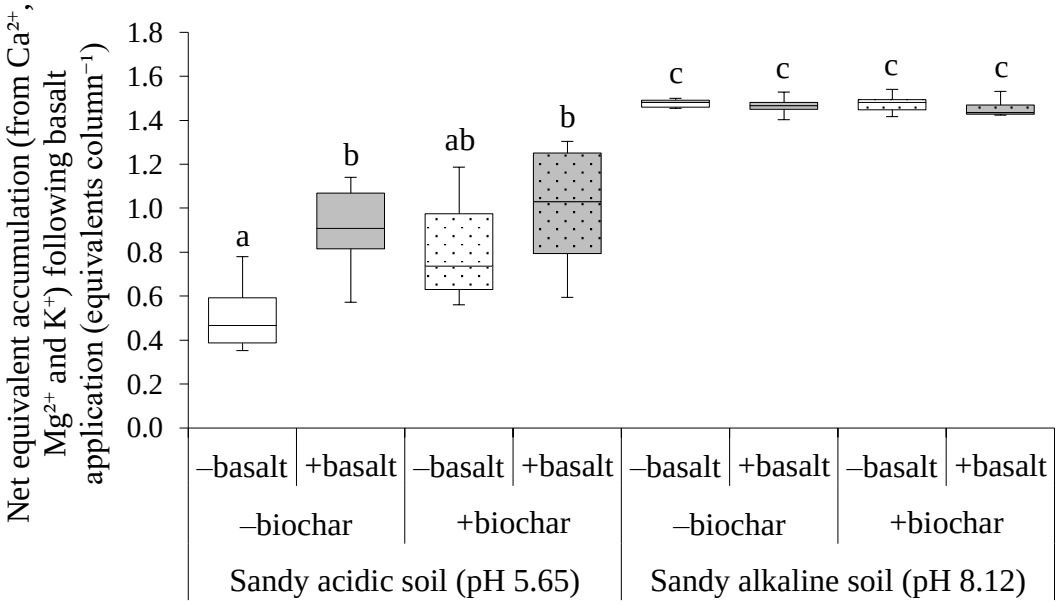

Figure 4.12 – Box plot comparing the accumulation equivalents in the leachate and soil exchange pools of the different treatments in the sandy acidic and alkaline soils. Values represent the total equivalents related to molar quantities of Ca^{2+}, Mg^{2+} and K^{+} measured in the leachate, plant tissues and soil exchange pool. Treatments sharing the same letter are not statistically different ($p > 0.05$; one-way ANOVA with Tukey post hoc test). All statistics were determined in R.

was despite a suppressive effect from the added biochar, which moderated that of the added basalt, yet nonetheless led to significant charge accumulation (Figure 4.12). Neither basalt nor biochar had any significant effect in the alkaline soil, however, which implies very little rock weathering, and is presumably due to the high pH.

As in Chapter 3, CDR estimates for all of the completed experiments are now collated (Figure 4.13), with final values multiplied by a factor of 0.831, to account for ocean losses (Renforth and Henderson, 2017). For the acidic (pH 5.65) soil in this study, a further factor of 0.85 is applied to the CDR value to conservatively account for the action of non-carbonic acids in this low pH environment (Dietzen and Rosing, 2023).

The final results (Figure 4.13) suggest considerable CDR potential in the acidic soil, at around 6.79 ± 1.89 (*SE*) CO_2 ha^{-1} over the duration of the trial (219 days). Normalised on an annual basis this is 11.32 ± 3.14 (*SE*) CO_2 ha^{-1} a^{-1}. Although reported alongside a large uncertainty, this estimate for CDR potential is much higher than the values previously estimated in Chapters 2 and 3, and is presumably due to the low initial pH.

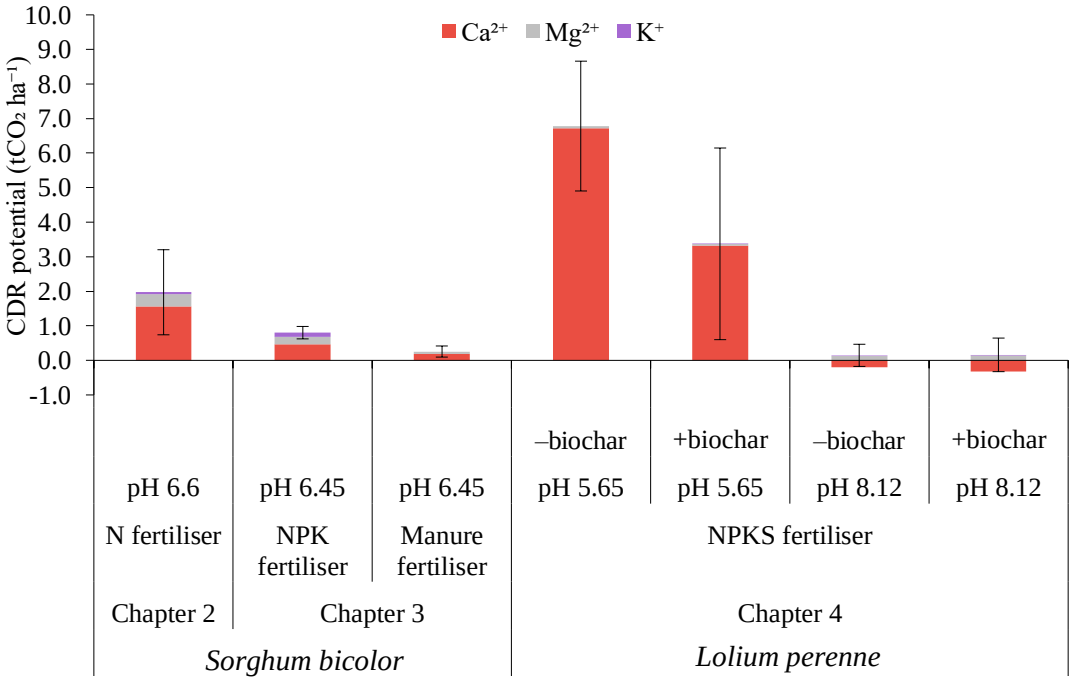

Figure 4.13 – Estimates of potential CDR for the experimental basalt treatments in Chapters 2, 3 and 4. The relative contributions of Ca^{2+}, Mg^{2+} and K^+ towards total surplus charge are shown as different colours within the stacked bar chart. CDR estimates are derived from measurements of additional cationic mass accumulated in the leachate, plant and soil exchange pools following basalt application. Molar quantities of additional Ca^{2+}, Mg^{2+} and K^+ in the pools were converted into equivalents and combined into a single value. Equivalents were then converted to CDR potential according to the 1:1 molar ratio of charge:CO_2 captured. Values are corrected for carbonate buffering (Renforth and Henderson, 2017) and the influence of non-carbonic acids (for the pH 5.65 soil; Dietzen and Rosing, 2023).

The CDR potential due to basalt amendment of the acidic soil was diminished by co-application with biochar, however, at least on these timescales. In Chapter 3, the manure was shown to supress weathering rates, and it is likely for the same reasons that biochar was not a weathering accelerant. As an alkaline material with a high charge affinity, biochar likely lowered dissolution rates by increasing the soil pH, and *via* adsorption of weathered nutrients that otherwise may have been available to trigger biologically-mediated feedback on weathering rates.

Weathering rates in the alkaline soil were effectively zero, which is not unexpected at pH 8.12, given the form of the dissolution rate equation (Equation 1.5). Moreover, the high-abundance of Ca in the soil could supress Ca-bearing mineral dissolution if pore waters become highly saturated. Interestingly, this result is not dissimilar to Buckingham *et al.*'s (2022) mesocosm experiment, which applied Oregon basalt (also used in Chapters 2 and 3) to a calcareous loamy soil (pH ≈ 8.3), which was found to be up to 11% calcium carbonate (calcite) by weight, depending on depth. Very low CDR estimates were determined in that study, which was principally thought to be linked to low soil moisture. But soil moisture was fairly well controlled during this experiment – marginally lower in the more-productive (pH 8.12) soil (Figure 4.10) – yet almost no evidence of the basalt's effects was collected from this alkaline substrate. Other than the significant change in soil available-Si, which might still be of significant agronomic value in this soil type, the clearest evidence of weathering was the exchangeable-Mg signal (Figure 4.11c), and a possible related secondary K signal (Figure 4.11d), but the overall effect on CDR was negligible. The implications of this result are not too severe for the UK, where calcareous soils are generally restricted to relatively narrow high-pH regions in South East England (Figure 4.2b). Indeed, the acidic soil used in this experiment is arguably more representative of the UK's grasslands (Figure 4.2), such that the westernmost counties of the Union may be optimal for ERW deployment.

As CDR was far higher in the sandy acidic soil, the respective null hypothesis ($H16: 0$) is rejected in favour of the alternative ($H16: 1$). Moreover, since the biochar did not accelerate basalt weathering and CDR on the timescale of the experiment, the related null hypothesis ($H17: 0$) is similarly rejected for the alternative ($H17: 0$).

4.4 Conclusions

In this study, the application of an ultra-fine UK basalt powder to sandy acidic and alkaline soils resulted in contrasting CDR estimates and crop performance effects. The pH of the sandy acidic soil was strongly modified (> 1 pH unit) by each experimental treatment (basalt and biochar), which for all soil additives coincided with a yield bonus for the ryegrass cover crop. The highest potential CDR following basalt amendment of this acidic soil (6.79 ± 1.89 CO_2 ha^{-1}) was achieved without co-application with biochar. The interaction between basalt and biochar measurably diminished the basalt-related CDR increase (3.22 ± 2.77 CO_2 ha^{-1}), at least over the timescales of this study, which was run for 219 days. Further research is necessary to better understand the time-lags in the CDR signal associated with the co-application of pulverised basalt with carbon-rich, high-charge-affinity soil additives. Interference from organic agents such as these ostensibly result in lower weathering rates, which could frustrate in-field monitoring, verification and reporting (MRV) in ERW experiments and operations.

Basalt had no discernible effect on CDR in the alkaline soil, which implies low weathering rates under these high-pH conditions. This is unlikely to appreciably limit the range of UK ERW applications, because most British grassland is co-located with acidic, highly-weathered soils in the west of the country. There may still be scope for the use of basalt as a Si fertiliser in alkaline soils, however, as it was highly effective at increasing plant-available Si concentrations at all depths, in all of the soils it was added to. With regards to ryegrass, this significant Si fertilisation effect suggests possible commercial applications for basalt where managed turfs are subjected to high use or intense wear – e.g. stadiums, sports fields etc. (Pruyne, Schlossberg and Uddin, 2019).

In this experiment, soil type was shown to have a strong effect on weathering rates and crop fertilisation, and it is feasible that many other fundamental soil parameters could be important for ERW. Further research is now required to better relate factors such a soil moisture, texture, organic matter content and CEC to mineral weathering rates, and hence, better predict the impact of a deployment location's soil characteristics on CDR.

5

Discussion and conclusions

Contents

5.1 Introduction

The overarching aim of this thesis was to quantify basalt weathering and related CO_2 capture rates in agricultural soils under crop cultivation, and to measure the associated impacts on key soil and plant performance characteristics. Research questions related to these aims were detailed in Section 1.4, but are reiterated here for convenience:

1. Can basalt weathering and CDR rates be determined empirically in a mesocosm-scale experiment with agricultural soil under crop cultivation?
2. Does ERW of basalt confer any co-benefits for crop performance – e.g. yield?
3. Does the addition of basalt modify key soil performance characteristics – e.g. soil pH and plant-available Si concentrations?
4. Does the amendment of soil with basalt result in the accumulation of PTEs in the effluent water, plant tissues or soils?
5. How are mineral weathering and CDR rates affected by co-deployment of basalt with other soil-based CDR approaches (e.g. biochar) or organic-rich fertiliser?

In this chapter, sub-sections related to each research question briefly summarise how this thesis addressed the current gaps in the contemporary understanding the respective issues. Full consideration is then given to the limitations within this research, which doubtless affect the scope of its findings. And lastly, suggestions for future research avenues are outlined, along with potential improvements for further mesocosm-scale ERW experiments in the years to come.

5.2 Can basalt weathering and CDR rates be determined empirically in a mesocosm-scale experiment with agricultural soil under crop cultivation?

The pilot experiment (Chapter 2) was successful in demonstrating that basalt weathering rates could be measured in the laboratory, by using a cation mass balance approach that included contributions from the leachate, plant and soil cation exchange pools. By well characterising the basalt (Section 2.2.6; Appendix B) and analysing the concentrations of cations in the aforementioned mesocosm components, the rates of cation release from the added basalt were estimated (Section 2.3.4; Table 2.1). Unlike an earlier ERW experiment (Renforth, Pogge von Strandmann and Henderson, 2015) – on which the pilot study was broadly modelled – the expected silicate weathering products (notably, Ca and Mg) did not appear in the leachate, and this was reasoned to be due to adsorption onto soil exchange surfaces, cation uptake by the large cover crop and the intermittent irrigation regime, which produced unusual hydrological artefacts (Section 3.1.1).

Sorghum grown on basalt-amended soil became significantly more productive (Section 2.3.1) and accumulated Si and Ca (Section 2.3.2), as well as basalt-derived Sr (Section 2.3.5), in shoot tissues: strong evidence for mass transfer from the basalt's primary minerals into the plant. However, cations released by rock weathering predominantly accumulated in the soil cation exchange reservoir, which in this clay-loam soil was substantial in size compared to the plant and leachate pools (Table 2.1). This was unexpected and, further, implied the existence of a time-lag in the development of a weathering signal. Rather than exiting the column *via* the effluent, weathering products had evidently been scavenged from the pore waters by the soil, and were likely engaged at ion exchange sites within the soil's clay minerals and OM. PHREEQC modelling was used to simulate the dynamic CDR response to the basalt application in this system over longer timeframes and indicated that 3–4 tCO_2 ha^{-1} (Section 2.3.7) would be captured over 2–5 years. The pilot experiment therefore represented a respectable first step towards the empirical quantification of basalt weathering rates and CDR in a planted mesocosm system, under controlled environment conditions.

The mass balance approach used in Chapter 2 was later applied to the two successor experiments detailed in this thesis (Chapters 3 and 4). All potential CDR estimates are compiled in Table 5.1 and compared against published values from prior ERW trials.

Table 5.1 – A compilation of 'potential CDR' estimates calculated in this thesis compared against published values from mesocosm-scale trials

Study	Soil and crop type			Fertiliser application				Rock type	Rock loading	Biochar loading	Trial duration	CDR (tCO_2 ha^{-1})	
	Soil type	Soil pH	Crop	kg N ha^{-1}	kg P_2O_5 ha^{-1}	kg K_2O ha^{-1}	kg SO_3 ha^{-1}		(t ha^{-1})	(t ha^{-1})	(days)	Reported value	Reported Error
ten Berge *et al*. (2012)	Sandy	4.79	*L. perenne*	160	72	292	–	Olivine	1.63 204	– –	224	0.29 2.69	– –
Dietzen *et al*. (2018)	Sandy podzol	3.55	–	–	–	–	–	Olivine	10 50	– –	≈90	3.13 4.16	– –
Haque *et al*. (2019)	–	4.94	*P. vulgaris L.*	–	–	–	–	Wollastonite	221	–	55	39.3	–
Amann *et al.* (2020)	Sandy-loam	6.6	*T. aestivum* and *H. vulgare*	–	–	–	–	Dunite	220	– –	365	0.023 0.049	– –
Buckingham *et al*. (2021)	Loamy, lime-rich	≈8.3	–	–	–	–	–	Basalt (Oregon)	100	–	≈240	0.0068	0.0005
Vienne *et al*. (2022)	Loamy	7.72	*S. tuberosum*	153	280	555	–	Basalt (DURUBAS)	50	–	99	0.77	–
This thesis (Chapter 2)	Clay-loam	6.60	*S. bicolor*	250	–	–	–	Basalt (Oregon)	100	–	121	1.99	1.23
This thesis (Chapter 3)	Clay-loam	6.45	*S. bicolor*	250 250	414 120	490 300	– –	Basalt (Oregon)	50	–	235	0.81 0.28	0.18 0.17
This thesis (Chapter 4)	Sandy-loam Sandy-loam, calcareous	5.65 8.12	*L. perenne*	150	27	21	24	Basalt (Hill House)	40	– 10 – 10	219	6.79 3.22 -0.19 -0.23	1.88 2.78 0.39 0.51

The larger plants in Chapter 3 represented a larger share of the overall cation budgets (Table 3.4–5), but the exchange pool once again dominated the mass balance in a clay-loam substrate (similar to the soil used in Chapter 2) under *Sorghum*. Many of the headline results from the pilot experiment were reproduced here (discussed later in this chapter), but direct measurements of soil moisture indicated even drier soil conditions in this successor study (Section 3.3.1 and 3.3.3). The concept of 'potential CDR' was introduced in Chapter 3, with reference to the assumption that surplus cations reporting in the plant and soil cation exchange pools will, one day, reach the oceans. However, it should be noted that this assumption is untested, and indeed, cations released by rock weathering need not reach the oceans for CDR to occur. The precipitation of secondary carbonate minerals in soils offers an alternative pathway for C sequestration, and whilst mineralisation is around half as effective as ocean sequestration over short timescales, it may be an important process for ERW in alkaline and/or arid environments (Zamanian *et al*., 2016).

Potential CDR was found to be lower in the Chapter 3 study than the pilot (Table 5.1), and unusual hydrological artefacts were once again implicated in the inferior results. Nonetheless, comparisons with an alternative and completely independent basalt weathering quantification method (TiCAT; Section 3.3.7) indicated good agreement on the absolute magnitude of CDR, which adds confidence to the findings in this thesis. As a scientific first, the effect of co-applied manure was examined in this ERW trial (Section 5.5), which did not appear to amplify basalt-related CDR and agronomic effects and, indeed, possibly suppressed them.

In the final experiment (Chapter 4), the effect of contrasting soil types on basalt weathering rates was examined, along with the effect of co-deployed biochar (see Section 5.5). Here, much higher potential CDR rates and related agronomic effects (Section 5.3–4) were calculated for the medium-acidic sandy soil, with negligible weathering detected in the alkaline soil. Biochar was found to have a suppressive effect on basalt weathering (Section 5.5) much like the manure in Chapter 3, but did not reduce the significance of many of the quantified benefits to soils and plants (Section 5.3–4).

Overall, this thesis well-addressed the question of whether basalt weathering could be measured experimentally, by proving the concept through the calculation of cation release and CDR rate estimates for a variety of rock, soil and plant combinations. Taken

together, these results strongly indicate that ERW deployment could be optimised by selecting soils that are naturally acidic – despite the implied penalty from non-carbonic acid weathering (Dietzen and Rosing, 2023) – because soil pH has a strong influence on dissolution rates (Equation 1.5). In a productive soil, with above-average pCO_2, the penalty due to the influence of non-carbonic acids is likely to be <20% of total CDR implied from the cation mass balance (Dietzen and Rosing, 2023) and was evidently worth the trade-off in Chapter 4. The poor CDR results in the calcareous soil are similar to a recent mesocosm-scale study (Buckingham *et al*., 2021), and may reflect the lower weathering potential of this kind of soil environment. The higher pH is likely to supress acid-catalysed weathering processes (Equation 1.5) and so lower mineral dissolution and CDR rates may be expected in alkaline soils, compared to more acidic substrates.

The results presented in Table 5.1 demonstrate the wide range of CDR estimates reported in this thesis and obtained from other mesocosm-scale ERW experiments in the published literature. The underlying reasons for the variation in CDR results are complex, but are likely due to a number of factors, including differences in weathering rate quantification methods, environmental conditions, irrigation regimes, apparatus, soil and crop types, rock mineralogy and particle size. Broadly, studies resulting in the lowest CDR estimates were conducted in alkaline soils and/or relied principally on measurements of cation export in the leachate (Amann *et al.*, 2020; Buckingham *et al.*, 2021; Chapter 4, alkaline soil). Conversely, the trials generating the highest CDR estimates generally selected medium- to high-acidity substrates and/or fast-weathering minerals (e.g. olivine, wollastonite), and notably used a quantification approach that included soil measurements, such as soil inorganic carbon or exchangeable cations (ten Berge *et al.*, 2012; Dietzen *et al.*, 2018; Haque *et al.*, 2019; Chapter 4, acidic soil). The results from these studies indicate that CDR may be strongly influenced by soil pH, and that in short-duration (<1 year) mesocosm-scale experiments, soil biogeochemical interactions are likely to lead to preferential retention of weathering products within the solid phase. The development and successful detection of strong weathering signals in pore and effluent waters might simply require more time, such that low estimates may be expected where CDR is based solely on measurements of aqueous geochemistry.

Mid-range estimates from laboratory-based ERW experiments (Table 5.1) indicate that annual CDR rates in the region of several tonnes of CO_2 per hectare may be feasible. This is supported by evidence from a four-year field trial in the U.S. Corn Belt (Beerling

et al., 2023), where C sequestration rates of just under 4 $tCO_2\ ha^{-1}\ a^{-1}$ were measured. If similar rates could be achieved in the UK, this implies that ERW deployment on just 2% of the 16.8 million hectare Utilised Agricultural Area (UAA; DEFRA, 2022) would enable annual CDR at the megatonne (Mt) scale. Larger-scale deployment across half of the UAA could offset around a tenth of the UK's annual CO_2 emissions of around 330 $MtCO_2\ a^{-1}$ (DESNZ, 2022). Accordingly, ERW has the potential to contribute significantly towards the UK Government's commitment to net zero emissions by 2050.

5.3 Does ERW of basalt confer any co-benefits for crop performance – e.g. yield?

In every experiment in this thesis, and in every treatment of acidic soil that included basalt, significant improvements in the primary measures of crop performance were observed. *Sorghum bicolor* yield in Chapters 2 and 3 – measured as seed (dry) mass – increased by ≈7–21% following basalt application (Sections 2.3.1 and 3.3.1), whereas *Lolium perenne* shoot (dry) mass increased by ≈30–44% (in the acidic soil only; Section 4.3.1). Notably, early plant performance effects (Section 4.3.1) and morphological divergence (Section 3.3.1) were observed in Chapters 3 and 4. This is posited to be largely due to the increase in pH that the alkaline basalt material induced – which, in acidic soils, should lead to improved plant nutrient uptake (Figure 4.6). However, the basalt-related fertilisation effect may also be linked to changes in the availability of plant macro- and micro-nutrients, released from the added basalt or otherwise liberated from the native soil. In the *Sorghum* trials, plants grown on basalt-amended soil accumulated significantly higher total K in seed tissues (Figures 2.5c and 3.7c; but not when basalt was co-applied with manure) and in the alkaline soil, which was generally unresponsive to the basalt application, a significant increase in exchangeable Mg throughout the soil column co-presents with an increase in exchangeable K in the subsoil (Figure 4.11c–d). This may have been caused by preferential adsorption of weathered Mg^{2+} onto ion exchange sites in the topsoil – as in ten Berge *et al*. (2012) – such that K^+ was liberated into pore waters and recaptured by exchange sites further down the soil column. These findings imply that amendment of soil with basalt could beneficially impact crop nutrient use efficiency, and further research into the impact of basalt on soil nutrient dynamics is warranted.

The above findings comprehensively address the research question. Evidence gathered in this thesis suggests that enhanced weathering of basalt can realise significant crop yield bonuses in acidic soils, but may be less effective in calcareous sandy soils.

5.4 Does the addition of basalt modify key soil performance characteristics – e.g. soil pH and plant-available Si concentrations?

In the pilot experiment (Figure 2.6b) and the NPK-treated columns in the following *Sorghum* trial (Figure 3.14a), basalt amendment only marginally (not significantly) increased the pH of the mildly-acidic, clay-loam soils used. However, a statistically significant increase in soil pH following basalt application was detected where basalt was co-applied with manure (Figure 3.14a), which may have been easier to resolve due to the increase in soil buffer capacity provided by the associated OM. In Chapter 4, in the acidic soil, pH increased considerably after basalt was applied, with the particularly strong effect here possibly due to the low buffer capacity of the native 'Moss End' soil (Section 4.2.2). Biochar was also associated with significant increases in soil pH, but did not enhance the neutralising effect of the basalt (Figure 4.11a). No significant pH modification was detected in the alkaline soil in Chapter 4 (Figure 4.11a), which is perhaps due to lower weathering rates in the higher soil pH conditions (Equation 1.5), and possibly also due to the large buffering capacity of the native soil (Section 4.2.2). On balance, this thesis well-addressed the matter of soil pH control, in each of the three experiments. In summary, basalt had a very strong pH neutralising effect in the most acidic soil (Moss End Farm soil; pH 5.65; Section 4.22) – which also had the lowest CEC – was moderately effective in circumneutral clay soils (Loddington soil; pH 6.45–6.6; Sections 2.2.2 and 3.2.2), but had no effect in the calcareous sandy soil (Flitcham Farm soil; pH 8.12; Section 4.22). Accordingly, it is concluded that the weathering rates of basaltic minerals were strongly influenced by the pH of the initial soil material. Moreover, the magnitude of the soil pH increase associated with basalt application may be dependent on the initial buffer capacity and pH of the substrate – with the strongest effects likely to be observed in the most-acidic and most-weakly-buffered soils.

Throughout this thesis, a significant increase in plant-available Si was observed consistently in soils amended with basalt. In every experiment, in every soil (including the sandy alkaline soil) and in combination with every carbon-rich soil amendment used, the application of basalt was associated with large increases in acetic acid extractable-Si (Figure 2.6d; Figure 3.14f; Figure 4.11f). In both *Sorghum* trials, this was shown to significantly increase shoot Si concentrations (Figure 2.5a; Section 3.3.2), and the agronomic importance of these results was highlighted in Chapter 2. Increased plant Si uptake is associated with a wide range of beneficial agronomic effects – e.g. improved durability, and resistance to lodging, drought, predation by pests and fungal pathogens – and could therefore have considerable economic value. Further research is required to quantify this ostensibly dependable co-benefit from ERW with basalt.

On balance, this research question was well addressed, and indeed, provides strong support for the use of crushed basalt for soil pH modification and Si fertilisation.

5.5 Does the amendment of soil with basalt result in the accumulation of PTEs in the effluent water, plant tissues or soils?

Concerns about the potential for Ni or Cr contamination of soils were raised in several of the earliest ERW studies (Schuiling and Krijgsman, 2006; Hartmann *et al.*, 2013; Renforth, Pogge von Strandmann and Henderson, 2015; Taylor *et al.*, 2016), and this is particularly relevant to ultramafic rocks, which contain relatively high concentrations of PTEs (Figure 1.12). However, this is much less of a concern for mafic rocks, like basalt, as the ratio of CDR to Ni/Cr release is likely to be much higher (Figure 1.12). In this study, no evidence was found to suggest Ni or Cr contamination of plant, leachate or soil materials, in any of the experiments and treatments – similarly for As, Cd, Cu and Pb (Appendices D, E and F). Indeed, the increase in pH associated with basalt amendment of soils likely reduced the overall mobility of these relatively high-atomic mass metals, suggesting that crushed basalt may even have utility in remediating contaminated soils. In summary, the matter of PTE contamination was thoroughly addressed in each experiment, but no evidence was found for a basalt-related increase in potentially hazardous metals.

5.6 How are mineral weathering and CDR rates affected by co-deployment of basalt with other soil-based CDR approaches (e.g. biochar) or organic-rich fertiliser?

This research question was well addressed in Chapters 3 and 4, with the inclusion of manure and biochar into the soils selected for those trials. In both experiments, the addition of these alkaline, carbon-rich materials generally did not enhance the effect of the basalt (in terms of comparatively increased CDR rates or soil- and plant-related co-benefits). Accordingly, it is posited that the lower weathering rates implied by the data were principally due to the increased soil pH associated with the application of these organic amendments, but may also be linked to the high cation affinity of the respective materials. Prior to the experiment in Chapter 3, it was expected that the manure might increase the basalt weathering rate, by adsorbing cations released from the basalt, hence, reducing mineral saturation states and encouraging weathering (Equation 1.5). Whilst pore water cation concentrations were evidently suppressed by the manure (Figure 3.12), the overall CDR was lower in the organic regime. Similar results were found in the basalt-biochar co-deployment treatment, in the acidic soils from Chapter 4. Here, again, the inclusion of an alkaline, high-cation-affinity organic material generally supressed weathering rates and associated plant feedbacks. It is conceivable that the reduced pore water cation concentrations induced by the added OM in these trials had deleterious consequences for plant growth, and hence, may have indirectly affected the basalt weathering rate through reduced photosynthesis, lower soil pCO_2 and higher soil pH conditions. Further research is needed elucidate the effect of carbon-rich soil amendments on CDR, and to better understand how plant-mediated feedbacks could be optimised and used to accelerate weathering rates.

5.7 Reflections on the limitations of the experiments

5.7.1 Limitations: estimated basalt weathering and CDR rates

As the principal motivation for this research, limitations in the headline CDR estimates are of paramount importance. Notably, it is acknowledged throughout this thesis that unusual hydrological artefacts developed in the mesocosms (Section 3.3.1). The soils used in this thesis were highly processed (Section 3.2.2), and this was principally carried out to reduce background noise for the key indicators of weathering (soil pH and cation/anion/DIC concentrations). However, this processes necessarily destroys soil structure, and therefore limits the applicability of the results. Intact soil cores – like those used by Renforth, Pogge von Strandmann and Henderson (2015), and Buckingham *et al*. (2021) – are, on reflection, much more realistic analogues for field conditions. The fairly extreme soil moisture fluctuations measured in this thesis (Section 3.3.3) are implicated in the development of preferential flow paths through the columns – perhaps, around the side of the soil columns, after visible shrinkage in low moisture conditions (Section 3.3.1) – and efforts should be made to avoid such effects in future research.

The large plants and evidently insufficient irrigation rates compounded the hydrological impacts in the *Sorghum* trials (and possibly affected the ryegrass experiment also), generating unrealistically low soil moisture levels that poorly simulated field conditions (Section 3.3.1), and could have led to the underestimation of potential CDR rates. Prior to the commencement of this research, it was not fully appreciated that the soils would require such a high level of maintenance to offset effluent and evapotranspirative losses, which were substantial when the plants reached maximum primary productivity. These artefacts were not anticipated in the first experiment (Chapter 2) and were impractical to account for in the second (Chapter 3), but were finally addressed to some degree in Chapter 4 with automation (in the form of drip-feed irrigation). On reflection, what was gained in time by delegating to the irrigation system in Chapter 4, was likely lost from the accuracy and precision of influx volumes, which may have introduced unquantified errors that were easily avoided by manual irrigation of the columns. Unfortunately, there do not appear to be any simple methods to address these hydrological issues in mesocosm experiments.

There are good reasons to suspect that low soil moisture will be deleterious for mineral weathering. Water is *essential* for weathering, as it is the solvent in the chemical equations of silicate and carbonate dissolution (Equations 1.2–3) and is the medium with which the products of mineral weathering are transported away from reactive mineral surfaces (which encourages further weathering). Hence, soil moisture is doubly-represented in the Arrhenius equation for weathering rates (Equation 1.5), as increased soil water content should lower mineral saturations states, but will also increase the *wetted* RSA of minerals in the soil – indeed, the area term in this fundamental rate equation (Equation 1.5) implicitly assumes that SA is in contact with water. Additionally, mineral weathering rates are enhanced under increased soil pCO_2, which is also influenced by soil moisture levels, since root respiration and microbial activity are dependent on water availably (Romero-Mujalli *et al*., 2019).

By removing soils from the ground, researchers tacitly accept responsibility to manage soil moisture from this point forwards, and to ensure that conditions in the mesocosms are representative of the fields from which they were taken. Given the practical challenges involved with simultaneously managing soil moisture in dozens of replicated soil cores, an alternative approach is suggested: instead of bringing the field into the laboratory, it may be preferable to bring the laboratory apparatus to the field. Outdoor mesocosm experiments would represent progress in ERW research, as the limitations of natural precipitation rates on CDR is rightly highlighted in recent work (Buckingham *et al*., 2021). Mesocosm-scale trials are ultimately more realistic when conducted under natural irrigation, but the realism may be further enhanced if experimental soils can remain in the ground. Whole, intact soil monoliths may be partitioned in the soil (e.g. using large PVC dividing panels), possibly several metres in width (or perhaps, simply PVC pipes inserted into the soil but left *in situ*), with rhizon samplers relied upon for measurements of aqueous geochemistry – an adaptation of the approach in Buckingham *et al*. (2021). By partitioning the soil (and preventing lateral water flow), weathering products should concentrate in the partially-closed environment, and a key advantage of the mesocosm approach can still be levered: high-precision control of soil amendments (e.g. mineral RSA) in each replicate. Thus, where experimental treatments lead to reduced water availability, the presence of the water table and the vertical influx of moisture from the field reservoir (e.g. *via* capillary action) might act to mitigate the development of extremely low soil moisture conditions.

In respect of the co-application of basalt with manure or biochar (Chapters 3 and 4), the principal limitation for this thesis is that the experiments were fairly short in duration, so it is unclear how weathering would have evolved in the various treatments over time. It is conceivable that, over longer timescales, the addition of OM could result in higher rates of CDR compared with their respective control soils, but the studies in this thesis were not designed to investigate this. There is a need for geochemical modelling of the time-lags associated with native soil clay-mineral and SOM ion-exchange processes – which appear to prevent cation export in the leachate – as this will likely affect the magnitude and timing of the effective CDR. More-sophisticated geochemical models might include further consideration of the effects of biology (plants, fungi and soil microorganisms) on weathering rates, and enable accurate modelling of the impact of fundamental soil parameters (e.g. soil pH, texture, CEC, OM content etc.) on weathering rates. Ultimately, silicate weathering is an extremely slow process, and so ERW will likely always need geochemical modelling to reliably predict future CDR.

Finally, it is acknowledged that the CDR estimates in this thesis lean heavily on the strength of the soil-exchangeable cation data, and on the assumption that surplus cations reporting in the exchange pool must have been released from the basalt's primary minerals. Whilst this is not an unreasonable assumption to make – indeed, the application of the approach in this thesis is evidently accepted in recent literature (Dietzen and Rosing, 2023) – it has not been rigorously tested in a controlled way. A range of chemicals can be used to extract cations from soil samples, and further research is needed to test the efficiency and accuracy of the various soil cation extraction protocols, as these measurements could be central to ERW weathering budgets.

5.7.2 Limitations: Agronomic benefits of ERW

The research limitations in respect of the perceived soil and plant performance benefits reported in this thesis (Sections 2.3.1, 2.3.3, 3.3.1, 3.3.5, 4.3.1 and 4.3.4) are probably less-restrictive, because the key effects of interest – increased soil pH, yield, plant-available Si *et cetera* – were determined by less complex methods than the CDR calculations and with fewer underlying assumptions. Moreover, the results are far less controversial, as similar effects have been reported in the literature since at least the early-1960's (D'Hotman and de Villiers, 1961). In this thesis, adding basalt to acidic soils significantly increased yield in every experiment, and plant-available Si concentrations were markedly increased in every soil type, in every combination with

manure and biochar. This is strong evidence in support of the use of crushed basalt as a fertiliser, and specifically, to encourage plant Si fertilisation and its related effects. Further research is now required to assess the agronomic value of the added Si, which may be considerable, and particularly useful in some agricultural settings – e.g. where soils are depleted in Si (Figure 4.11f). Si fertilisation may be unwanted in some settings, however, such as when cultivating feedstock for biomass burners, which may require more-regular maintenance when plant silica levels are significantly elevated.

The conclusion that basalt had no impact on PTE concentrations is fairly robust, and consistent with theory. Given that plants have evolved a range of mechanisms to protect their seeds from trace metal contamination, it is unsurprising that no adverse effects on edible *Sorghum* tissues were detected. Moreover, PTEs should be further immobilised by the pH rises associated with basalt weathering in soils, so the overall null result was largely anticipated. This, by no means, implies that PTEs are no longer a concern for this CDR strategy; there are many possible ways in which elements released from basalt could induce harmful changes in managed and natural environments – including downstream watersheds – and further research in this regard is encouraged.

5.8 Conclusion

In summary, the main conclusions of this thesis are as follows:

1. Basalt amendment of agricultural soils under crop production was estimated to result in significant, multi-tonne CDR per hectare over a period of months to several years. Results appear to be optimal in highly acidic soils with low CECs, and were negligible in the alkaline sandy soil used in this trial. Organic, carbon-rich soil amendments tended to supress basalt-related CDR on the short timescales of the studies, but the long-term benefits or disadvantages of co-application with manure or biochar are uncertain.
2. Basalt amendment of agricultural soils was associated with a significant yield increase, and may be linked principally to improved plant nutrient uptake efficiencies induced by the related increase in soil pH.
3. Modest (but not significant) soil pH increases were observed in circumneutral pH soils, but a large and significant pH effect was observed in the acidic sandy soil used, implying that similar soils may benefit greatly from ERW in terms of improved productivity.
4. Basalt amendment markedly increased the availability of soil Si to *Sorghum*, resulting in plants becoming enriched with silica. This should have considerable real-world benefits in terms of improved crop performance.
5. No evidence was found for PTE contamination of leachate, soils and plant tissues by exposure to basalt.

So, in short, ERW was found to be a promising CDR strategy that could also deliver tangible co-benefits for agriculture, potentially offsetting the costs. The technology is ripe for development, but much research is still required to constrain the uncertainties in CDR estimates, and ensure that any potentially harmful consequences are anticipated and mitigated. There is much still to learn about ERW, but the prospects are good.

Appendices

Appendix A – Derivation of Equation 1.6

According to **Equation 1.5**, a change in temperature from T_0 to T_1 will result in a change in the weathering rate from W_0 to W_1:

$$\boldsymbol{W_0 = SA \cdot k e^{\frac{-E_a}{RT_0}} \cdot a_{H^+}(1-\Omega)} \quad \textbf{Equation A.1}$$

$$\boldsymbol{W_1 = SA \cdot k e^{\frac{-E_a}{RT_1}} \cdot a_{H^+}(1-\Omega)} \quad \textbf{Equation A.2}$$

Dividing **Equation A.1** by **Equation A.2** and cancelling the terms yields,

$$\frac{W_0}{W_1} = \frac{e^{\frac{-E_a}{RT_0}}}{e^{\frac{-E_a}{RT_1}}}$$

Since $e^{-x} = \frac{1}{e^x}$ it follows that,

$$\frac{W_0}{W_1} = \frac{1}{e^{\frac{E_a}{RT_0}} \cdot e^{\frac{-E_a}{RT_1}}}$$

Taking the reciprocal of both sides,

$$\frac{W_1}{W_0} = e^{\frac{E_a}{RT_0}} \cdot e^{\frac{-E_a}{RT_1}}$$

And as $e^x \cdot e^y = e^{x+y}$,

$$\frac{W_1}{W_0} = e^{\left(\frac{E_a}{RT_0} - \frac{E_a}{RT_1}\right)}$$

Factorising out $\frac{E_a}{R}$ produces the final form,

$$\frac{W_1}{W_0} = e^{\left[\frac{E_a}{R}\left(\frac{1}{T_0} - \frac{1}{T_1}\right)\right]} \quad \textbf{Equation 1.6}$$

Appendix B – Basaltic rock and biochar characterisation

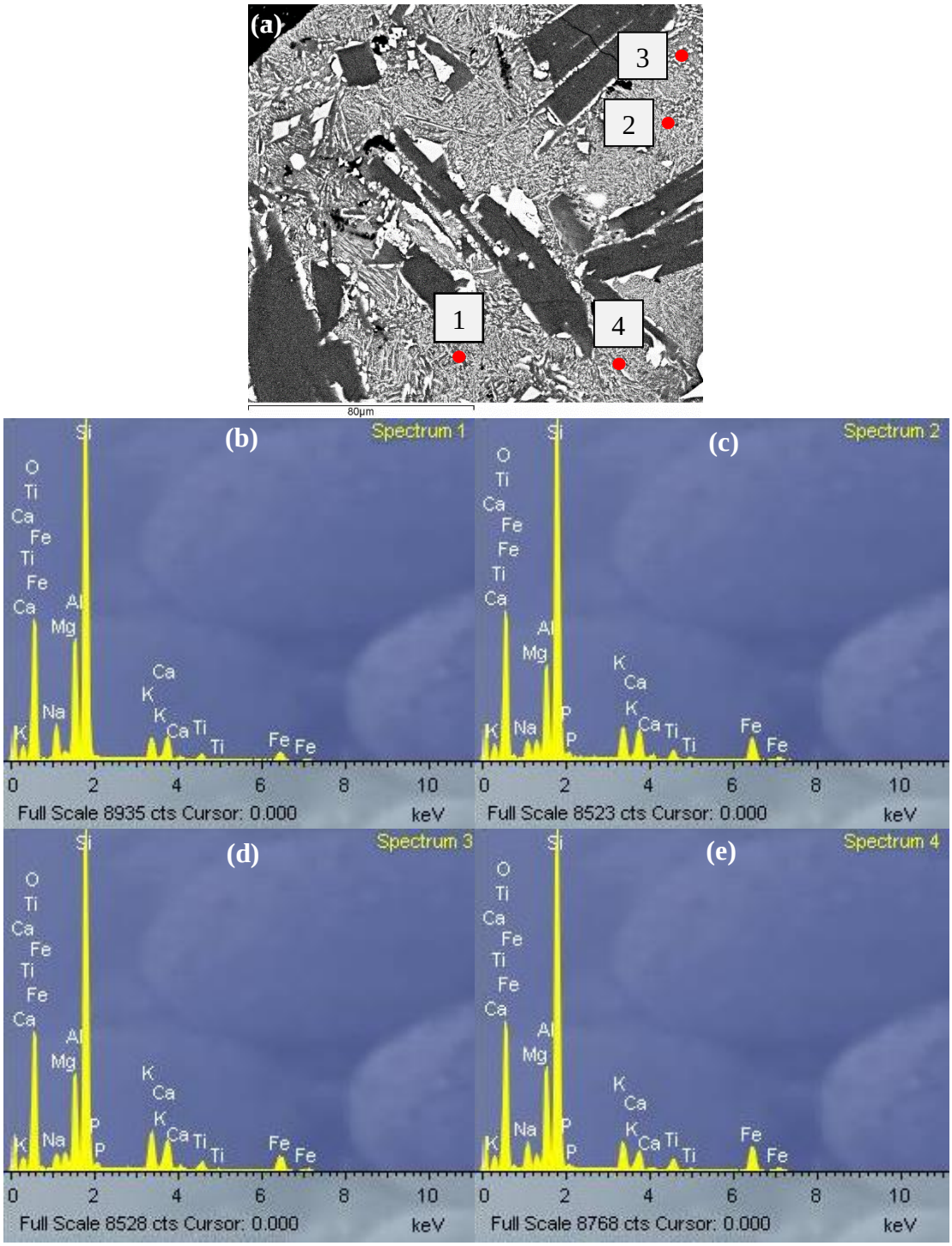

Figure B.1 – Site 1: Scanning Electron Microscopy-Energy Dispersive X-ray Spectroscopy (SEM-EDX) spectra used to estimate the chemical composition of basalt amorphous material. (a) SEM image of basalt grain surface showing target locations within Site 1, (b-e) spectra measured at locations 1-4, respectively.

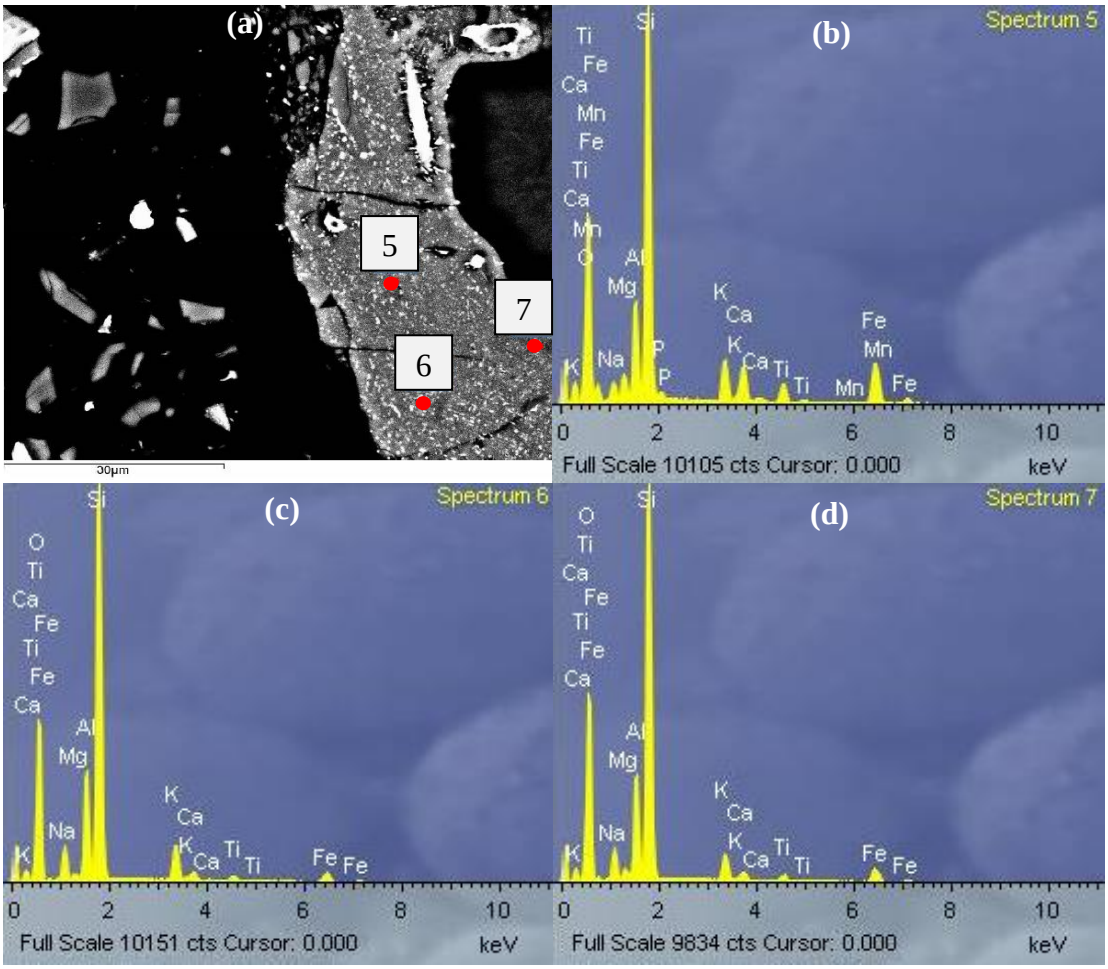

Figure B.2 – Site 2: Scanning Electron Microscopy-Energy Dispersive X-ray Spectroscopy (SEM-EDX) spectra used to estimate the chemical composition of basalt amorphous material. (a) SEM image of basalt grain surface showing target locations within Site 2, (b-d) spectra measured at locations 5-7, respectively.

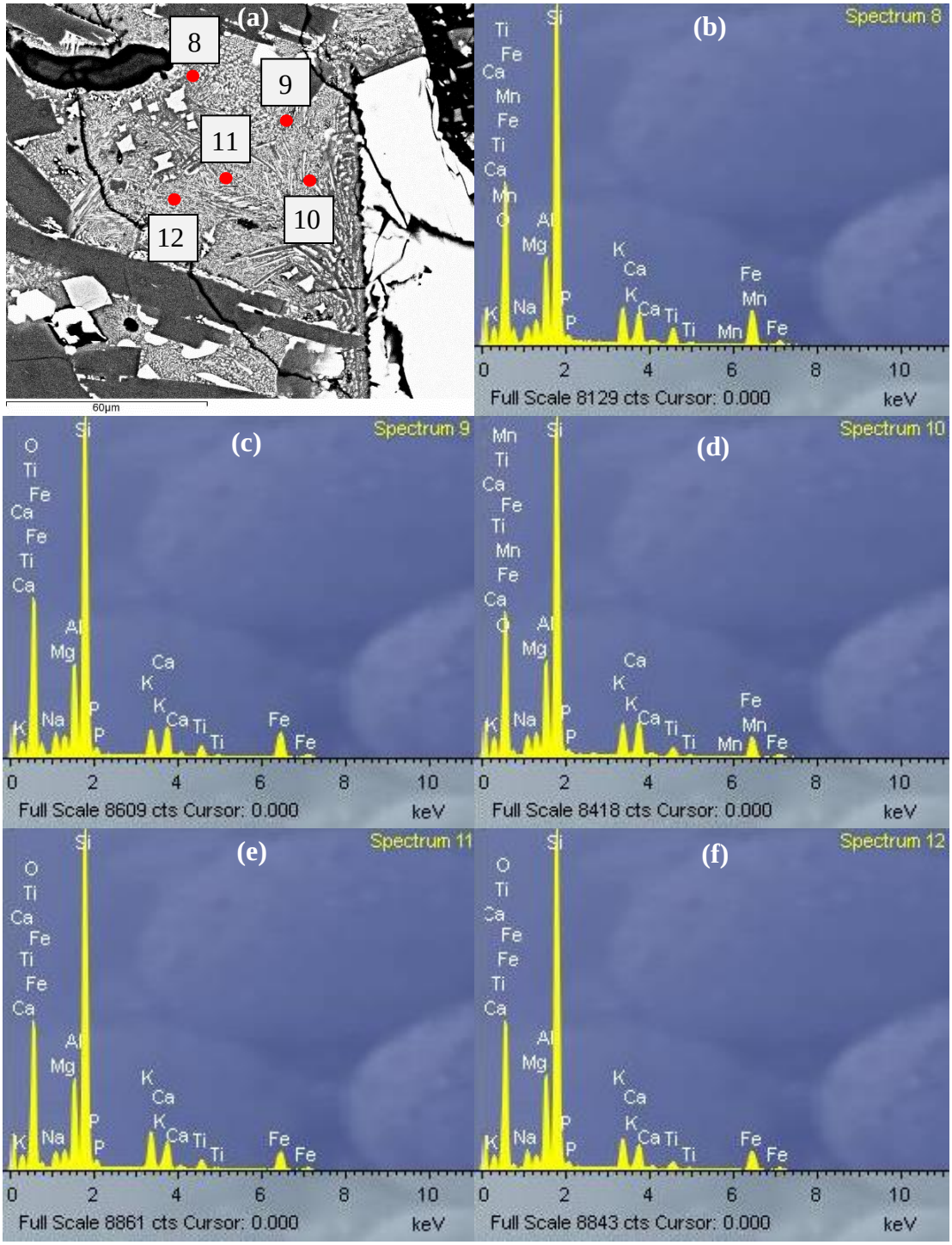

Figure B.3 – Site 3: Scanning Electron Microscopy-Energy Dispersive X-ray Spectroscopy (SEM-EDX) spectra used to estimate the chemical composition of basalt amorphous material. (a) SEM image of basalt grain surface showing target locations within Site 3, (b-f) spectra measured at locations 8-12, respectively.

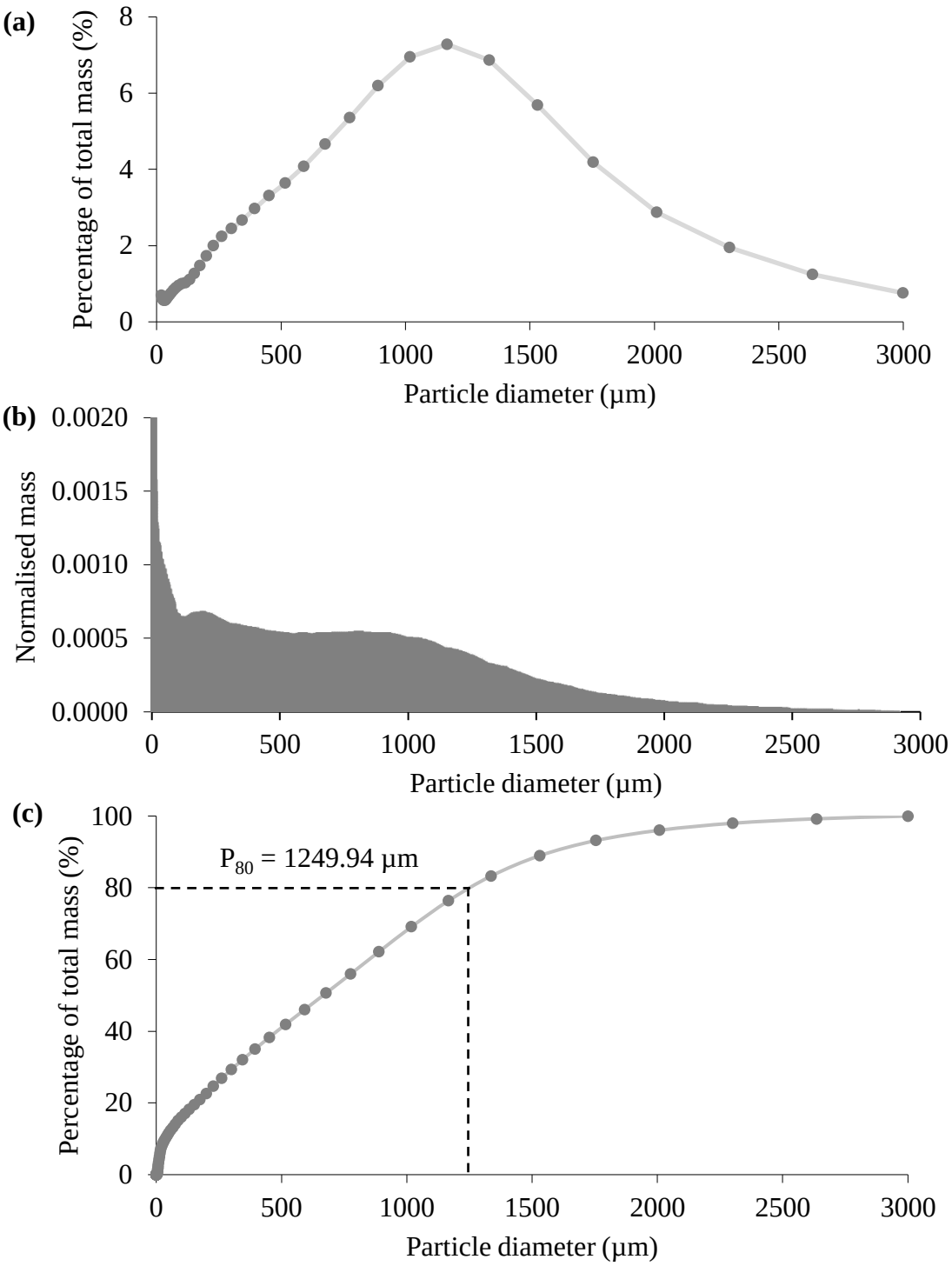

Figure B.4 – Particle size distribution of Central Oregon basalt material used in Chapter 2. (a) measured mass distribution profile of a representative sample of crushed rock, (b) normalised mass distribution as a function of particle diameter, and (c) cumulative percentage of total mass relative to particle size (diameter). 80% of the particles have a diameter less than or equal to the P_{80} value.

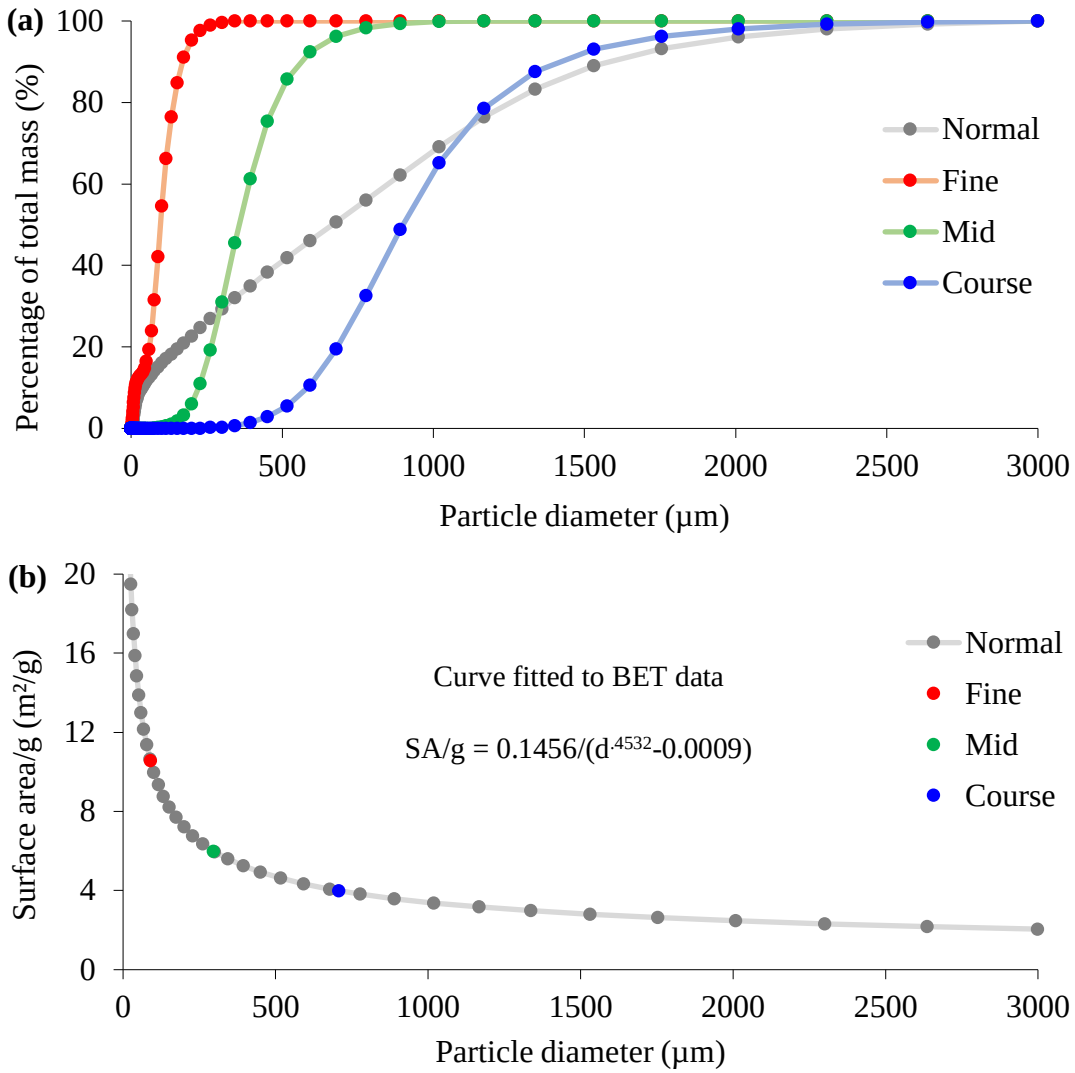

Figure B.5 – Cumulative mass fractions and BET surface area for three classes of sieved particle sizes (Fine ≈ 90 µm, Mid ≈ 297 µm, and Coarse ≈ 707 µm) and unfractionated basalt grains (Normal) used in Chapter 2. (a) cumulative mass fractions for each of the particle size distributions, and (b) BET surface area data for the sieved particle sizes. A curve of the form $a / (d^b + c)$, is fitted to the data; coefficients are reported in the plot. Each coloured marker represents $n = 3$ BET measurements.

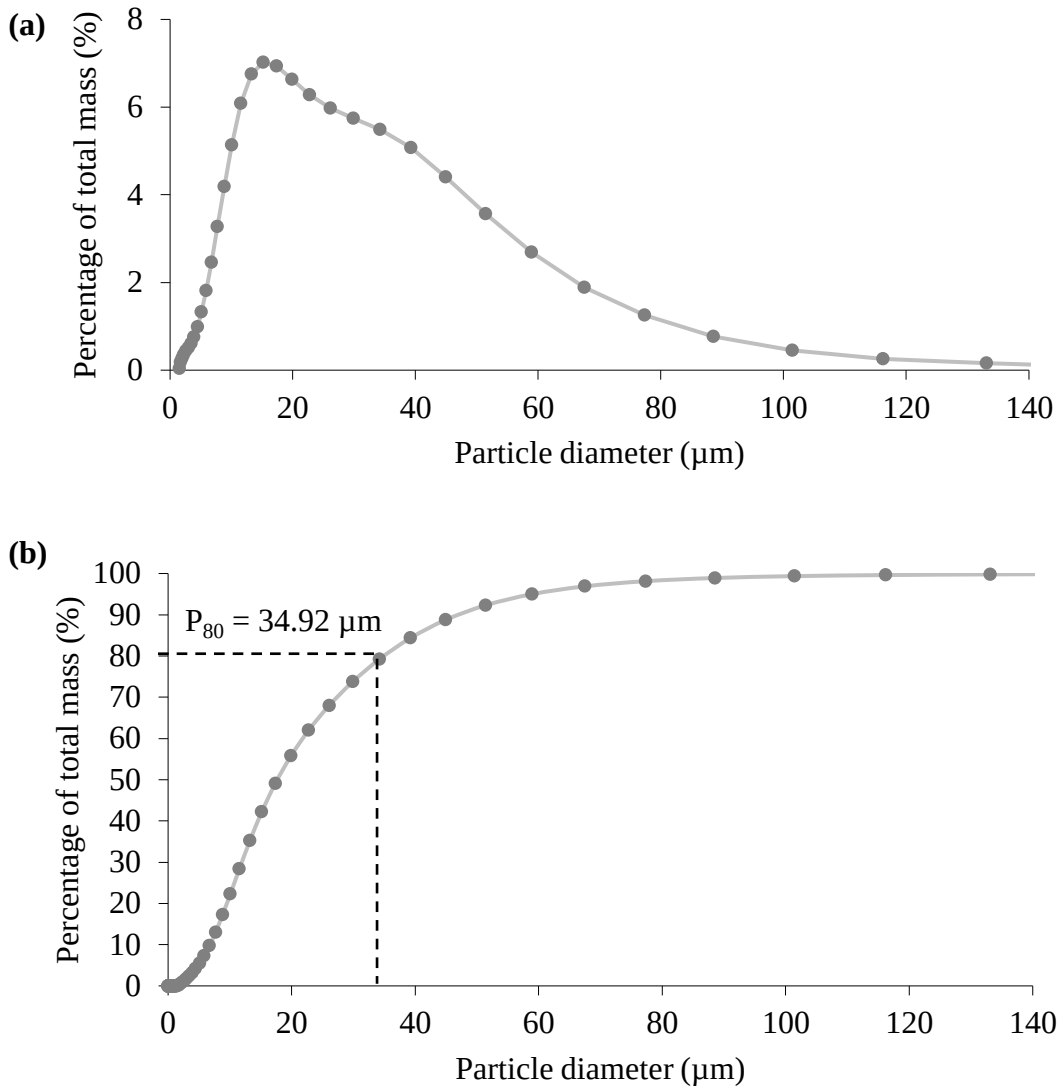

Figure B.6 – Particle size distribution of Central Oregon basalt material used in Chapter 3. (a) measured mass distribution profile of a representative sample of crushed rock, and (b) cumulative percentage of total mass relative to particle size (diameter). 80% of the particles have a diameter less than or equal to the P_{80} value.

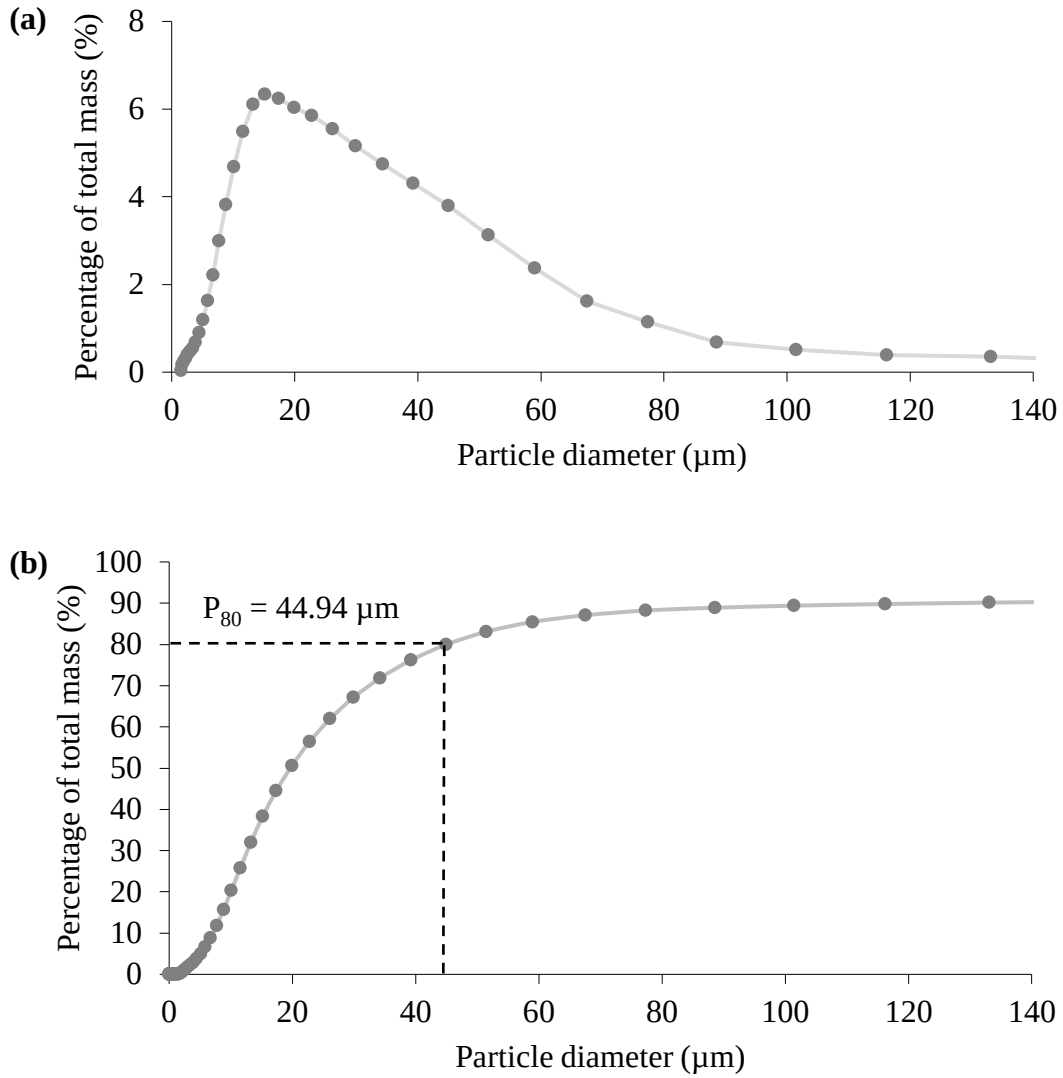

Figure B.7 – Particle size distribution of Hill House basalt material used in Chapter 4. (a) measured mass distribution profile of a representative sample of crushed rock, and (b) cumulative percentage of total mass relative to particle size (diameter). 80% of the particles have a diameter less than or equal to the P_{80} value.

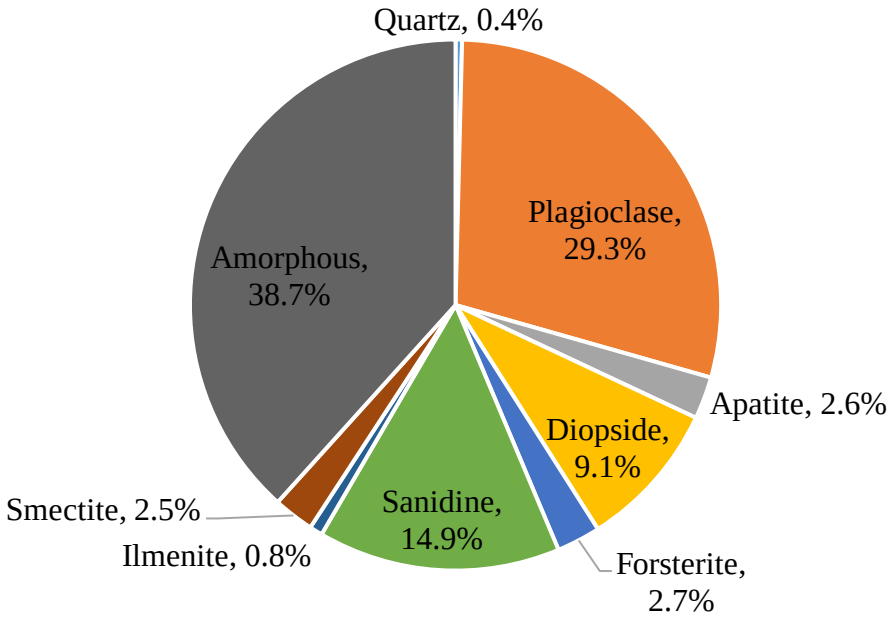

Figure B.8 – Mineralogy of the basalt material in Chapter 3, as determined by X-Ray Diffraction analysis.

UK Biochar Research Centre

reducing and removing CO_2 while improving soils: a significant and sustainable response to climate change

www.biochar.ac.uk | biochar@ed.ac.uk

SWP550 Standard biochar specification sheet – Version 1.1 | January 2019

Feedstock: Soft Wood Pellets | **Production:** Pilot-scale rotary kiln pyrolysis unit, nominal peak temperature 550°C

Key features: • Reproducible • Extensively characterised • Readily available

Biochar C stability compared to a set of 92 biochar

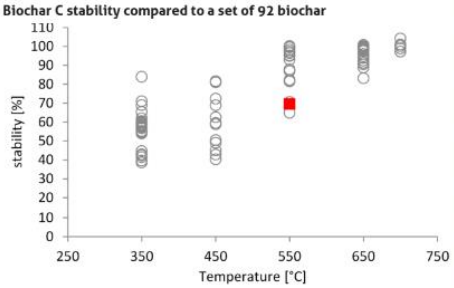

Basic Utility Properties		Mean	Run-to-Run Variation, SD(n)
Moisture[a]	wt% (a.r.)	1.52	0.16 (8)
C_{tot}	wt% (d.b.)	85.52	1.22 (9)
H	wt% (d.b.)	2.77	0.09 (9)
O (by difference)	wt% (d.b.)	10.36	1.19 (9)
$H:C_{tot}$	Molar ratio	0.39	0.01 (9)
$O:C_{tot}$	Molar ratio	0.09	0.01 (9)
C_{org}	wt% (d.b.)	tbd	tbd
$H:C_{org}$	Molar ratio	tbd	tbd
Total ash[a]	wt% (d.b.)	1.25	0.42 (11)
Total N	wt% (d.b.)	<0.10	- (9)
pH	[-]	7.91	0.30 (4)
Electric conductivity	dS/m	0.09	0.03 (4)
Liming (if pH above 7)	% $CaCO_3$	tbd	tbd
Biochar C stability[b]	% C-basis	69.62	0.20 (5)

Production parameters		Mean	Run-to-Run Variation, SD(n)
Nominal HTT	°C	550	- (1)
Reactor wall temp.	°C	550	- (1)
Max. char HTT	°C	543.78	- (1)
Heating rate	°C/min	78	- (1)
Kiln residence time	min	12	- (1)
Mean time at HTT	min	3.9	- (1)
Biochar yield	wt% (d.b.)	21.80	0.79 (6)
Pyrolysis liquid yield	wt% (d.b.)	37.00	- (1)
Pyrolysis gas yield	wt% (d.b.)	39.00	- (1)
Pyrolysis liquid HHV	MJ/kg	13.87	- (1)
Pyrolysis gas HHV	MJ/kg	10.66	- (1)

Advanced Analysis & Soil Enhancement Properties		Mean	Run-to-Run Variation, SD(n)
Mineral N (ammonium & nitrate)	mg/kg (d.b.)	<3	- (4)
Total P[c]	wt% (d.b.)	0.06	0.04 (4)
Total K[c]	wt% (d.b.)	0.25	0.07
Available P	mg/kg (d.b.)	tbd	tbd
Volatile Matter[a]	wt% (d.b.)	14.20	0.81 (8)
Total Surface Area	m^2/g (d.b.)	26.40	- (1)
External Surface Area	m^2/g (d.b.)	tbd	tbd

Toxicant Reporting - Total Content			Mean	Run-to-Run Variation, SD(n)	comparison vs. recommended standard thresholds+	IBI	EBC (premium)	BQM (high grade)
Germination Inhibition Assay		pass/fail	tbd	tbd				
Polycyclic Aromatic Hydrocarbons (EPA16)[d]		mg/kg dry wt	4.39	3.45 (4)		6-20	4	20
Dioxin/ Furan (total PCDD/ Fs)[e]*		ng/kg dry wt	0.02	- (1)		9	20	20
Polychlorinated Biphenyls (PCBs)[f]		ng/kg dry wt	0.17	-(1)		0.2-0.5	0.2	0.50
As	modified dry ashing followed by ICP-OES	mg/kg dry wt	0.90	1.19 (3)		12-100	n/a	10
Cd		mg/kg dry wt	3.48	5.76 (3)		1.4-39	1	3
Cr		mg/kg dry wt	34.57	38.17 (3)		64-1200	80	15
Co		mg/kg dry wt	1.04	0.20 (3)		40-150	n/a	n/a
Cu		mg/kg dry wt	19.41	22.31 (3)		63-1500	100	40
Pb		mg/kg dry wt	bdl	- (3)		70-500	120	60
Hg		mg/kg dry wt	bdl	- (3)		1-17	1	1
Mo		mg/kg dry wt	3.36	1.17 (3)		5-20	n/a	10
Ni		mg/kg dry wt	3.30	2.27 (3)		47-600	30	10
Se		mg/kg dry wt	5.68	5.53 (3)		1-36	n/a	5
Zn		mg/kg dry wt	25.71	5.20 (3)		200-7000	400	150

Notes: HTT=highest treatment temperature, HHV = higher heating value, tbd = to be defined in next version, bdL = below detection limit, SD = standard deviation (refers to run-to-run consistency, not analytical error) + available standards related to biochar (IBI = International Biochar Initiative, EBC = European Biochar Standard, BQM = Biochar Quality Mandate), * as TEQ (toxic equivalent) values were bdl, total (tetra to octa chlorinated) dioxin/furan content is reported instead.

(a) TGA, (b) Cross A, Sohi SP (2013), (c) Aqua Regia digestion followed by ICP, (d) Soxhlet extraction (toluene, 6h) determination by GCMS, (e) US EPA 1613, (f) AES 084 (based on US EPA 1668)

For full details please go to: http://www.charchive.org/record.php?record_id=94

Figure B.9 – Detailed specifications for the softwood biochar used in Chapter 4.

Table B.1 – Major oxide concentrations of the Central Oregon basalt used in Chapter 2. Primary XRF data are compared with typical mean values for basalts from Large Igneous Provinces using data from the GEOROC database (Max Planck Institute for Chemistry, 2015). NAIP = North Atlantic Igneous Province, CAMP = Central Atlantic Magmatic Province.

Element	Unit	Central Oregon	Deccan Traps	NAIP	CAMP	Paraná & Etendeka	Siberian Traps
SiO_2	%	44.3	50.5	48.6	50.8	51.2	49.1
FeO	%	9.7	9.2	8.0	8.7	7.8	6.8
Al_2O_3	%	13.0	13.9	14.6	14.5	14.1	15.1
CaO	%	7.6	10.4	10.3	10.1	9.2	9.7
K_2O	%	3.4	0.6	0.3	0.6	1.2	0.9
TiO_2	%	3.5	2.3	1.6	1.1	2.0	1.7
Na_2O	%	2.3	2.4	2.3	2.5	2.7	2.5
MgO	%	2.0	6.1	8.5	7.5	5.2	6.8
P_2O_5	%	2.3	0.2	0.2	0.1	0.3	0.3
Ba	$\mu g\ g^{-1}$	3840	161	148	157	397	334
Mn	$\mu g\ g^{-1}$	2783	1480	1509	1422	1505	1463
Sr	$\mu g\ g^{-1}$	679	244	223	181	323	383
Zr	$\mu g\ g^{-1}$	359	157	102	92	172	160
Zn	$\mu g\ g^{-1}$	249	110	90	87	99	102
Cu	$\mu g\ g^{-1}$	141	190	134	97	144	91
Cr	$\mu g\ g^{-1}$	128	165	366	241	124	155
Rb	$\mu g\ g^{-1}$	100	17	5	20	34	20
Ni	$\mu g\ g^{-1}$	69	87	166	115	60	109
Co	$\mu g\ g^{-1}$	28	45	53	52	44	46

Table B.2 – Basalt mineralogy (from XRD) and kinetic rate parameters (Palandri and Kharaka, 2004) used for the PHREEQC model in Chapter 2.

			Acid kinetic parameters			Neutral kinetic parameters		Base kinetic parameters		
Mineral name	Molecular formula	Weight	logK	Eapp	n	logK	Eapp	logK	Eapp	n
Plagioclase[a]	$Ca_{0.5}Na_{0.5}Al_{1.5}Si_{2.5}O_8$	35.1%	-7.87	42.1	0.626	-10.91	45.2	0	0	0
Alkali-feldspar[b]	$K_{0.41}Na_{0.56}Ca_{0.03}Al_{1.03}\ Si_{2.97}O_8$	23.0%	-10.06	51.7	0.5	-12.41	38	-21.2	94.1	-0.82
Diopside (Mang)	$Ca_{0.87}Mg_{0.94}Mn_{0.19}Si_2O_6$	6.2%	-6.36	96.1	0.71	-11.11	40.6	0	0	0
Diopside	$CaMg_{0.7}Al_{0.6}Si_{1.7}O_6$	4.4%	-6.36	96.1	0.71	-11.11	40.6	0	0	0
Apatite	$Ca_5(PO_4)_3(OH)$	2.8%	-4.29	250	0.171	-6	250	0	0	0
Montmorillonite	$Ca_{0.6}Al_2Si_4O_{10}(OH)_2.H_2O$	1.2%	-12.71	48	0.22	-14.41	48	-14.41	48	-0.13
Olivine[c]	$Fe_{0.96}Mg_{1.04}SiO_4$	1.0%	-6.85	67.2	0.47	-10.64	79	0	0	0
Ilmenite	$Fe_{1.4}Ti_{0.6}O_3$	0.6%	-8.35	37.9	0.421	-11.16	37.9	0	0	0
Quartz	SiO_2	<0.5%	-9.98	87.7	0.31	-13.99	87.7	-14.96	87.7	-0.41
Basaltic glass[d]	$Na_{0.13}Ca_{0.08}Mg_{0.05}\ K_{0.10}Fe_{0.12}Al_{0.26}SiO_{2.86}$	24.9%								
Calcium carbonate[e]	$CaCO_3$	0.34 ± 0.07 %								

Weathering rates for each mineral were modelled using the following equation (Palandri and Kharaka, 2004):

$$\frac{dm}{dt} = -SA\left[k_{acid}^{298.15K} e^{\frac{-E_{acid}}{R}\left(\frac{1}{T}-\frac{1}{298.15}\right)} a_{H^+}^{n_1}(1-\Omega^{p_1})^{q_1} + k_{neut}^{298.15K} e^{\frac{-E_{neut}}{R}\left(\frac{1}{T}-\frac{1}{298.15}\right)}(1-\Omega^{p_2})^{q_2} + k_{base}^{298.15K} e^{\frac{-E_{base}}{R}\left(\frac{1}{T}-\frac{1}{298.15}\right)} a_{H^+}^{n_3}(1-\Omega^{p_3})^{q_3}\right]$$

where $\frac{dm}{dt}$ is the weathering rate, SA is the mineral surface area, $k_i^{298.15K}$ is the dissolution rate constant for the respective mechanisms at 298.15 K, E_i is the apparent activation energy, R is the gas constant, T is the temperature in K, $a_{H^+}^i$ is the hydrogen ion activity, n_i is the order of the reaction, Ω is the mineral saturation index, and p_i and q_i are dimensionless empirical constants for the particular mineral.

[a]rate constant is for labradorite (the plagioclase mineral closest to the XRD-derived stoichiometry).

[b]rate constant taken for albite and for K-feldspar (substituting for sanidine).

[c]modelled as iron-rich forsterite.

[d]stoichiometry derived from SEM/EDX analysis of basalt amorphous material (Table B.3). Basaltic glass dissolution rates modelled using this equation (Gislason and Oelkers, 2003):

$$r_{+,\ geo} = A_A exp^{-\left(\frac{E_A}{RT}\right)}\left(\frac{a_{H^+}^3}{a_{Al^{3+}}}\right)^{1/3}$$

where $r_{+,\ geo}$ is the geometric surface area-normalised steady-state basaltic glass dissolution rate, A_A is a constant equivalent to $10^{-5.6}$ (mol of Si)/cm^2/s, E_A is a pH independent activation energy of 25.5 kJ mol^{-1}, R is the gas constant, T is the temperature in K, and a_i is the activity of the respective aqueous species.

[e]weight derived from carbon analysis of unweathered basalt samples using a CN Analyser, before and after treatment with 6 M HCl. Calcium carbonate in the basalt was modelled as an equilibrium phase.

Table B.3 – Chemical composition of basalt amorphous material used in Chapter 2, measured by SEM/EDX as determined on three discrete basalt grain surface locations.

	Spectra	Na	Mg	Al	Si	P	K	Ca	Ti	Mn	Fe	O	Total
Site 1	Spectrum 1	4.418	0.476	9.225	28.990	0.000	2.867	3.112	1.017	0.000	3.346	46.549	100
	Spectrum 2	2.354	1.476	6.589	26.823	0.594	3.883	4.123	1.687	0.000	7.716	44.755	100
	Spectrum 3	2.100	1.244	7.015	27.328	0.661	4.961	4.233	1.504	0.000	5.807	45.149	100
	Spectrum 4	3.446	0.985	7.204	26.533	0.449	3.493	2.426	1.980	0.000	8.875	44.610	100
Site 2	Spectrum 5	3.526	0.384	7.289	30.755	0.000	4.500	0.977	1.593	0.000	4.354	46.623	100
	Spectrum 6	4.051	0.263	7.626	31.248	0.000	4.521	0.910	1.074	0.000	3.372	46.936	100
	Spectrum 7	3.877	0.677	7.383	30.852	0.000	3.308	1.085	1.134	0.000	4.901	46.782	100
Site 3	Spectrum 8	1.977	1.818	5.789	24.412	0.672	3.985	3.569	2.746	0.239	11.610	43.183	100
	Spectrum 9	2.878	1.619	6.441	25.914	0.780	3.001	3.779	2.085	0.000	9.064	44.439	100
	Spectrum 10	2.403	1.709	6.689	26.209	0.641	3.744	4.501	1.774	0.260	7.499	44.570	100
	Spectrum 11	2.176	1.410	6.499	26.980	0.828	4.563	3.655	1.746	0.000	7.240	44.904	100
	Spectrum 12	2.431	1.045	6.906	27.449	0.754	3.867	3.326	1.500	0.000	7.524	45.198	100
Mean		2.970	1.092	7.055	27.791	0.448	3.891	2.975	1.653	0.042	6.776	45.308	100
SD		0.853	0.540	0.847	2.185	0.344	0.656	1.313	0.483	0.097	2.502	1.164	-
Mean / A_r		0.129	0.045	0.261	0.990	0.014	0.100	0.074	0.035	0.001	0.121	2.832	4.602
Stoichiometric coefficient		0.131	0.045	0.264	1.000	0.015	0.101	0.075	0.035	0.001	0.123	2.862	-
Composition (%)		2.807	0.976	5.682	21.503	0.314	2.163	1.613	0.751	0.016	2.637	61.538	100

Table B.4 – Geometric vs BET surface area calculations for the basalt material in Chapter 2. Estimates for surface roughness (λ) of basalt material (the ratio of BET-measured to geometric surface area).

Basalt	Particle size (μm)	SA (geo)[1] (m^2g^{-1})	BET[2] (m^2g^{-1})	Roughness ratio (λ)
Bulk		0.0234	7.35	322.6
Fine	53-150	0.0542	10.6 ± 0.9	195.6
Mid	212-415	0.0061	6.4 ± 0.3	1049.2
Coarse	500-1000	0.0024	4.9 ± 0.7	2041.7

[1]Geometric surface area, SA(geo), was calculated by first calculating the surface area per mass for a profile as follows. For each bin, centred at δ_i and of width δ_d, let $m_p(d_i)$ equal the mass of a single particle,

$$m_p(d_i) = \frac{1}{6}\pi d_i^3 \rho$$

And, $sa_p(d)$ equal the surface area of a single particle,

$$sa_p(d_i) = \pi d_i^2$$

Then denoting the mass fraction depicted in Figure B.4a as $m_f(d)$,the number of particles is given by,

$$no(d_i) = \frac{m_f(d_i)\delta_d}{m_p(d_i)}$$

So that the total surface area of all particles of diameter d_i is given by,

$$sa_t(d_i) = no(d_i)\, sa_p(d_i) = \frac{6\, m_f(d_i)\delta_d}{\rho\, d_i}$$

And, the total surface area of all particles of all diameters, per unit mass is then given by,

$$SA = \frac{6}{\rho}\sum_{i=1}^{n}\frac{m_f(d_i)\,\delta_d}{d_i}$$

This method was used to calculate the surface area per unit mass with the 3 basalt size fractions shown in Figure B.4a.

[2]BET surface area was calculated using the function fitted to the BET data (in conjunction with the mass profile (Figure B.4a)) to obtain an estimate of surface area per gram for the particle size distribution given in Figure B.4b, calculated as,

$$SA = \sum_{d=1}^{n}\frac{m_f(d)\,0.1456}{d^{0.4532} - 0.0009} = 7.3453$$

Appendix C – Reactive transport model

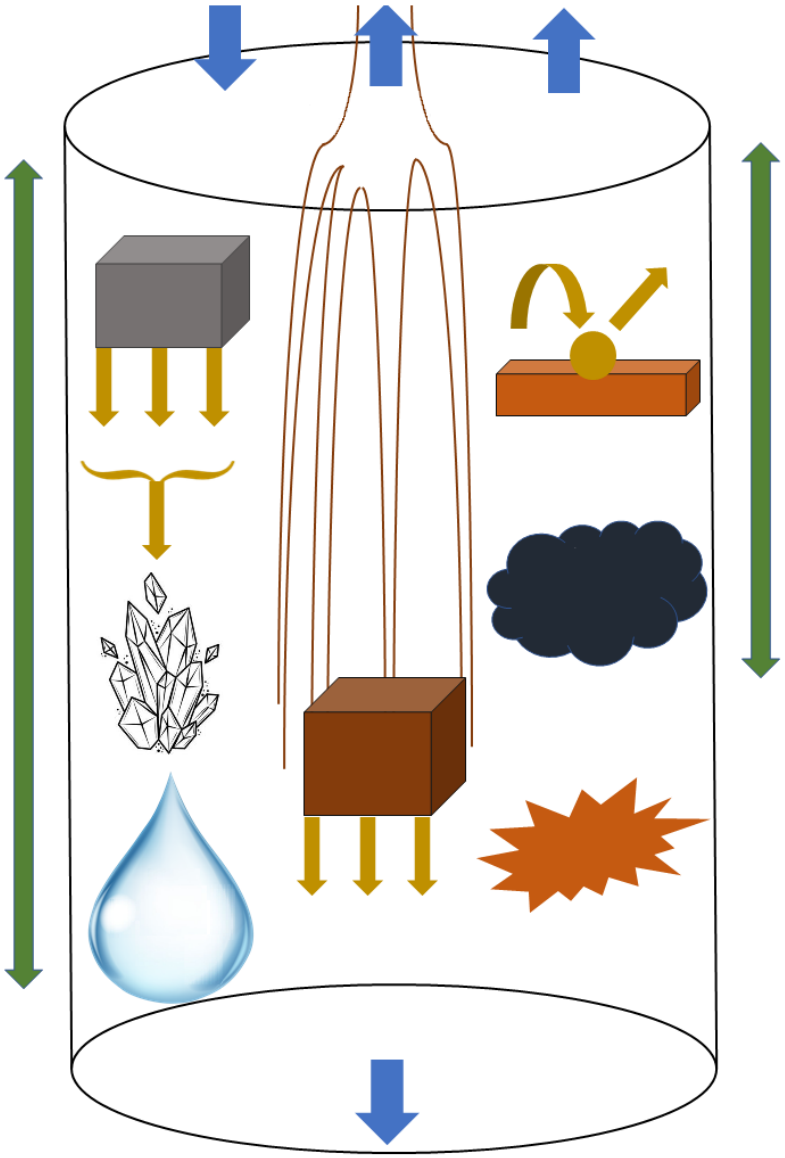

Figure C.1 – Schematic diagram of key components of the reactive transport model representing the experimental soil columns. Not to scale. The diagram illustrates water flows regulating soil moisture. It shows dissolution of basaltic minerals and native soil minerals releasing metal ions (M+), silicon (Si) and generating hydroxide ions (OH-). Released elements can form precipitates or interact with ion exchange surfaces on clay minerals and particulate organic matter. Iron oxyhydroxide (FeOOH) represents the sink for iron.

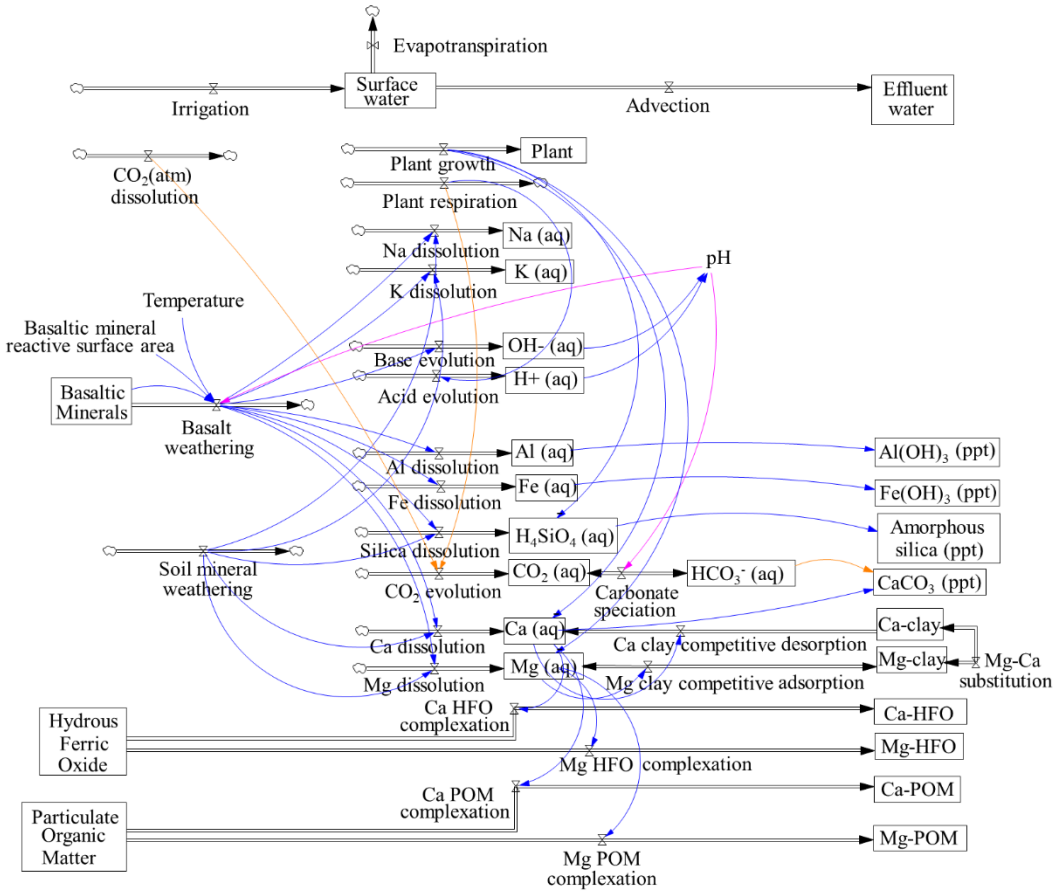

Figure C.2 – Systems diagram of processes and interactions represented in the reactive transport model in Chapter 2. The system dynamics diagram encapsulates all the most important aspects of the basalt-soil-plant-atmosphere system as modelled by Reactive Transport Model. Components of the system such as soil, basalt, plant and atmosphere are transformed in processes such as weathering and dissolution of ions into pore waters to yield secondary precipitates – crystalline and amorphous. These precipitates act as sinks for generated iron, silicon and aluminium ions in the soil pore waters. Clays, hydrous ferric oxides and particulate organic carbon adsorb and exchange ions, regulating precipitation of secondary minerals such as silica, hydrated alumina and iron solids, and calcium containing solids. Atmospheric carbon dioxide is introduced into the system by direct dissolution in pore waters, and via plant respiration, transforming into aqueous bicarbonate and precipitating as calcite (orange arrows). Acidity and alkalinity modify pH, which influences weathering rates and the rate of direct capture of carbon dioxide in the soil pore waters (pink arrows).

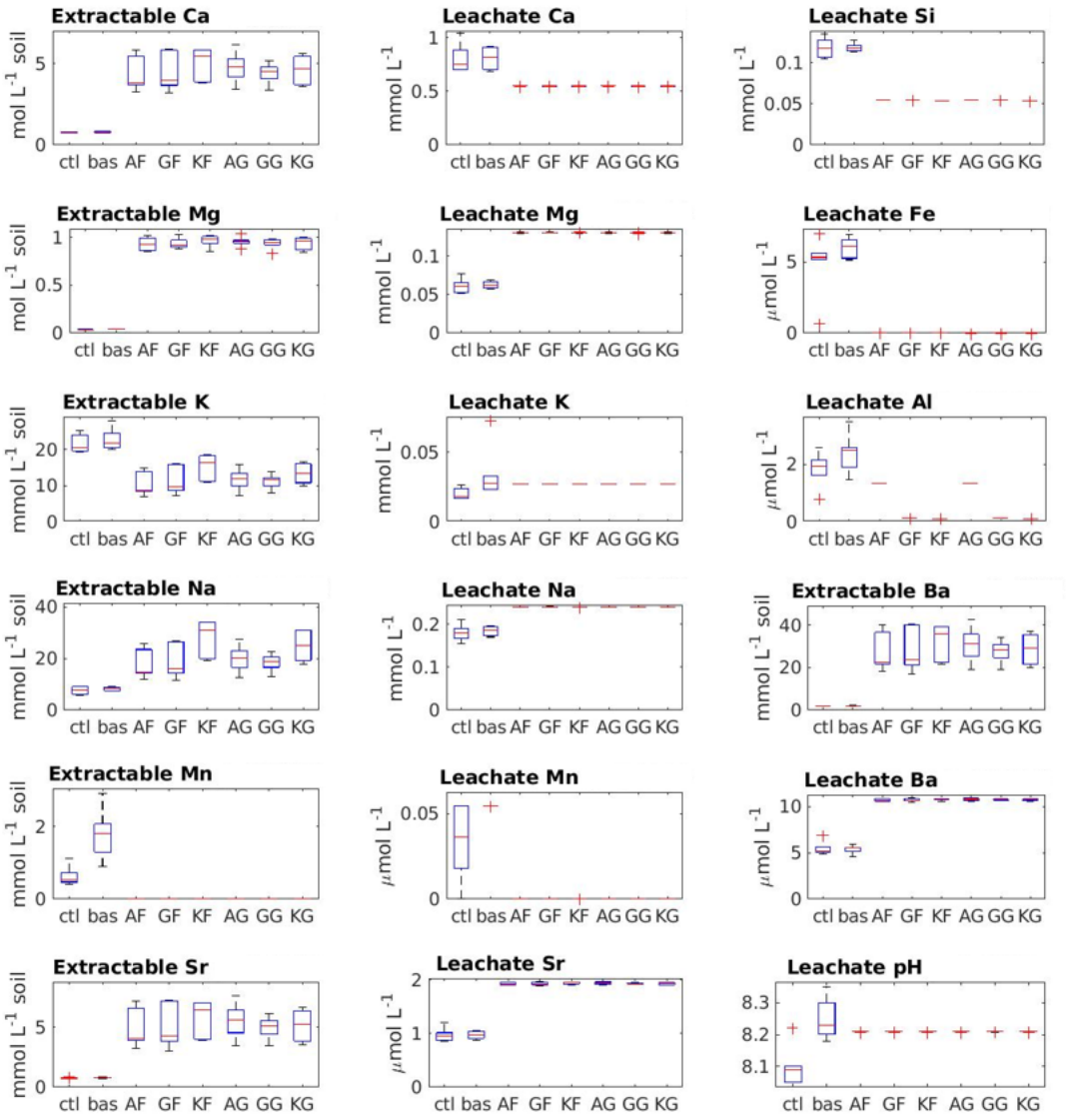

Figure C.3 – Results of optimisations using six combinations of Al and Fe equilibrium sinks. The *p*-values (determined by one-way ANOVA using "anova1" and "multcompare" in MATLAB) compare control (ctl) and treated (bas) observations, not observations vs any of the models. These 18 parameters were chosen because they were measured and related to elements released from basalt. Modelled conditions are: AF (amorphous $Al(OH)_3$ and $Fe(OH)_3$), GF (Gibbsite and $Fe(OH)_3$), KF (Kaolinite and $Fe(OH)_3$), AG ($Al(OH)_3$ and Goethite), GG (Gibbsite and Goethite), and KG (Kaolinite and Goethite). Each treated column was modelled individually resulting in six replications for both observed and modelled conditions, resulting in a total of 36 optimisation tests. Note that for leachate Al (righthand column, third from top), there is a clear improvement when amorphous $Al(OH)_3$ is the Al sink. Extractable and leachate Mn are both poorly modelled and, although nonzero, are several orders of magnitude too small.

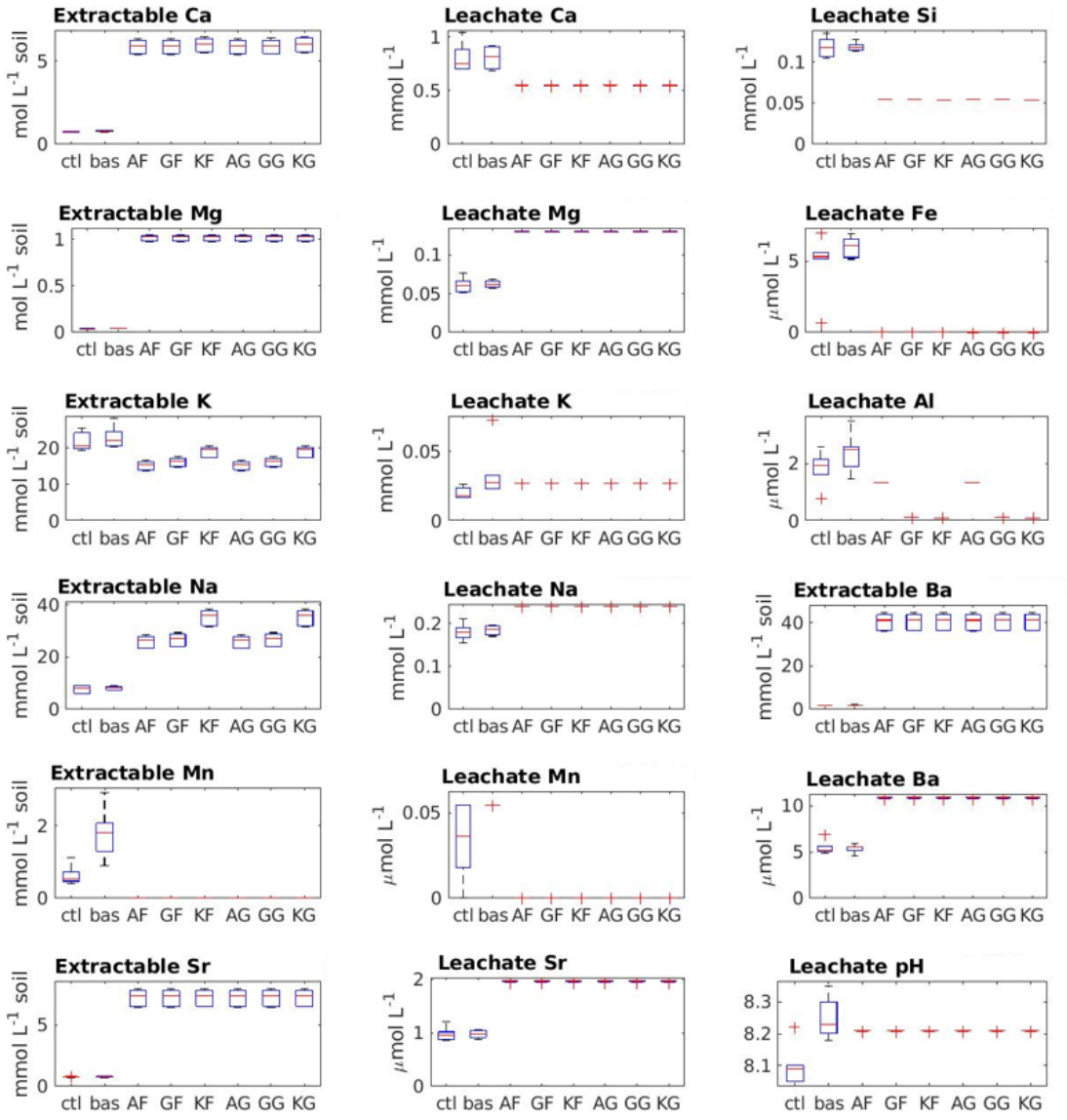

Figure C.4 – Considering the effect of using BET-derived RSA and net measured charge without optimising RSA and CEC for comparison with Figure C.3.

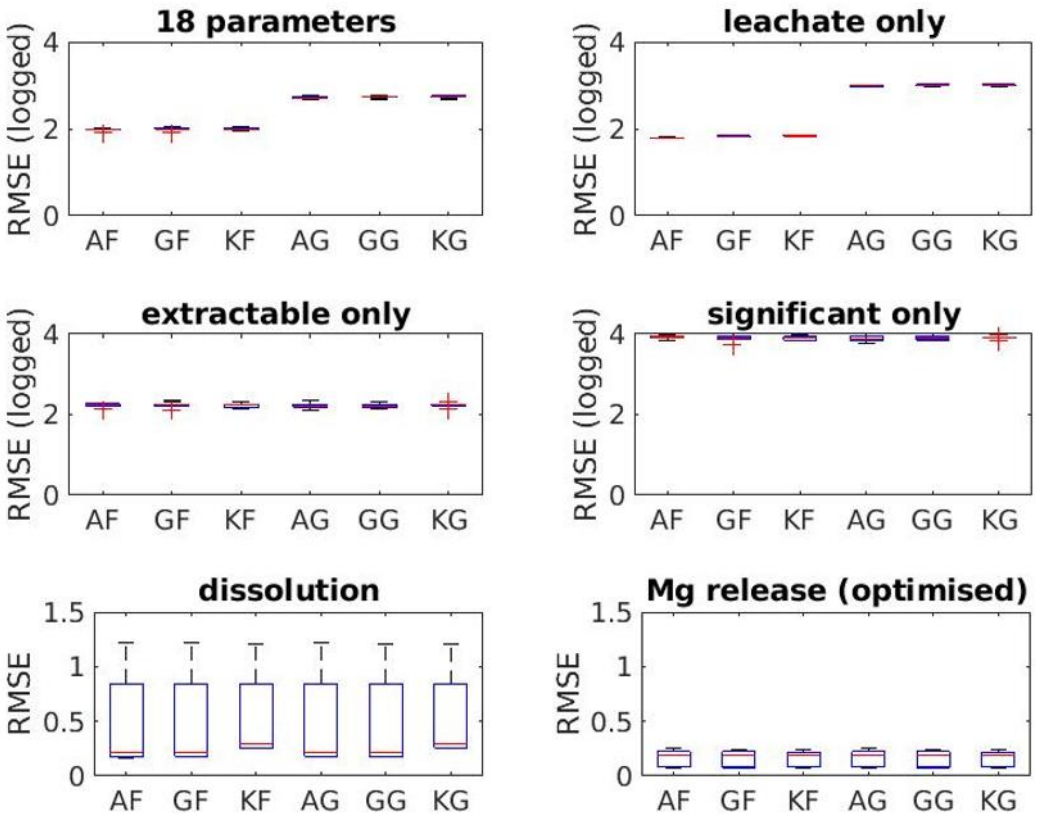

Figure C.5 – Results of optimisations shown in Figure C.3, with the same codes for combinations of equilibrium Al and Fe sinks. Model goodness-of-fit was calculated from Mg release from basalt dissolution (bottom right panel) as described in the main text, but root-mean-square errors (RMSE) were calculated from several combinations of model-observed parameters. Where RMSE (logged) is shown, RMSE was calculated using the sum of $\log_{10}$(model)-$\log_{10}$(observed) for the designated parameters. In the top left corner, all 18 parameters shown in Figure C.3 are included. These results, along with those for leachate parameters only, suggest that goethite is an inappropriate sink for Fe in this model.

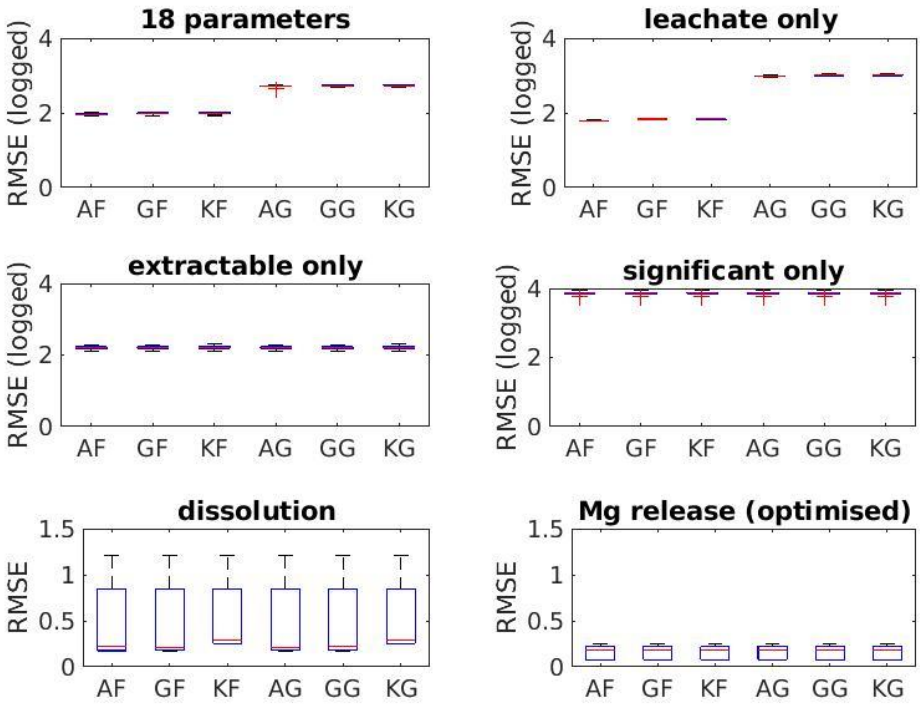

Figure C.6 – Considering the effect of using BET-derived RSA and net measured charge without optimising RSA and CEC for comparison with Figure C.5.

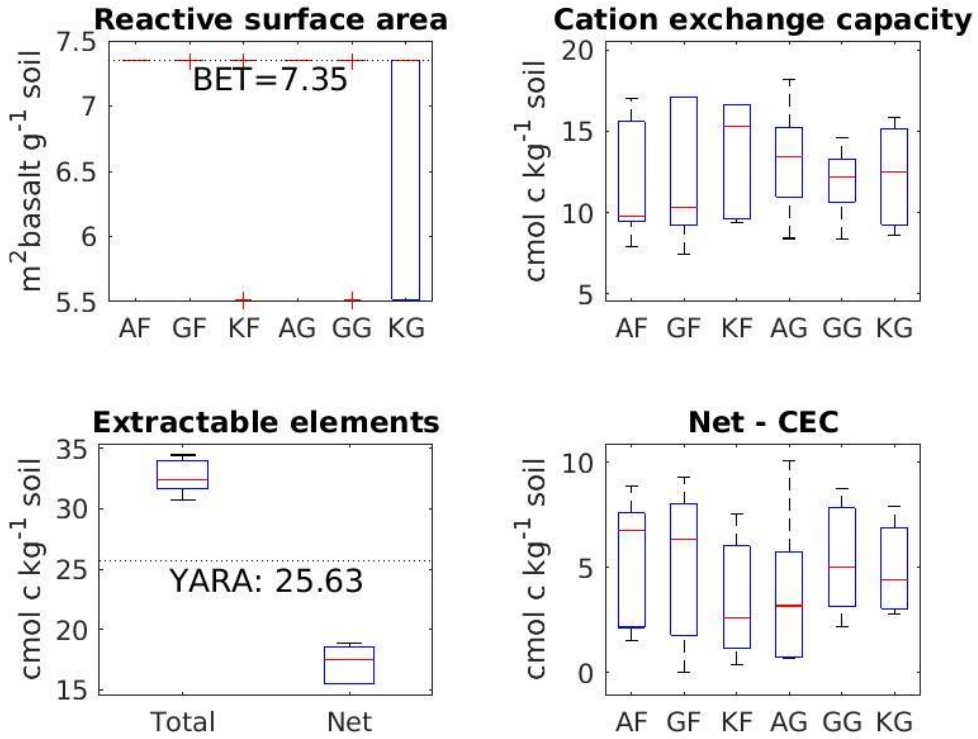

Figure C.7 – Results of optimisations for RSA and CEC. Modelled CEC is that which appears in the PHREEQC "EXCHANGE" datablock represented as the pseudospecies "X". Total charge accounted for was calculated following the chemical extractions ("Total", bottom left panel) and subtracted from that the charge assigned to surface complexation with organic phases to get our net charge ("Net", bottom left panel). In four out of 26 optimisations, the MATLAB solver "fmincon" failed to perform an optimisation away from the starting points which were 75% of BET RSA and our net measured extractable charge (bottom left panel), likely because the response curve was too flat. All other simulations converged toward BET RSA (top left panel) and lower CEC (top right panel). The difference between optimised CEC and measured net charge is under 10 cmolc kg^{-1} soil for nearly all optimisations (bottom right panel).

Appendix D – Plant biomass and tissue elemental composition

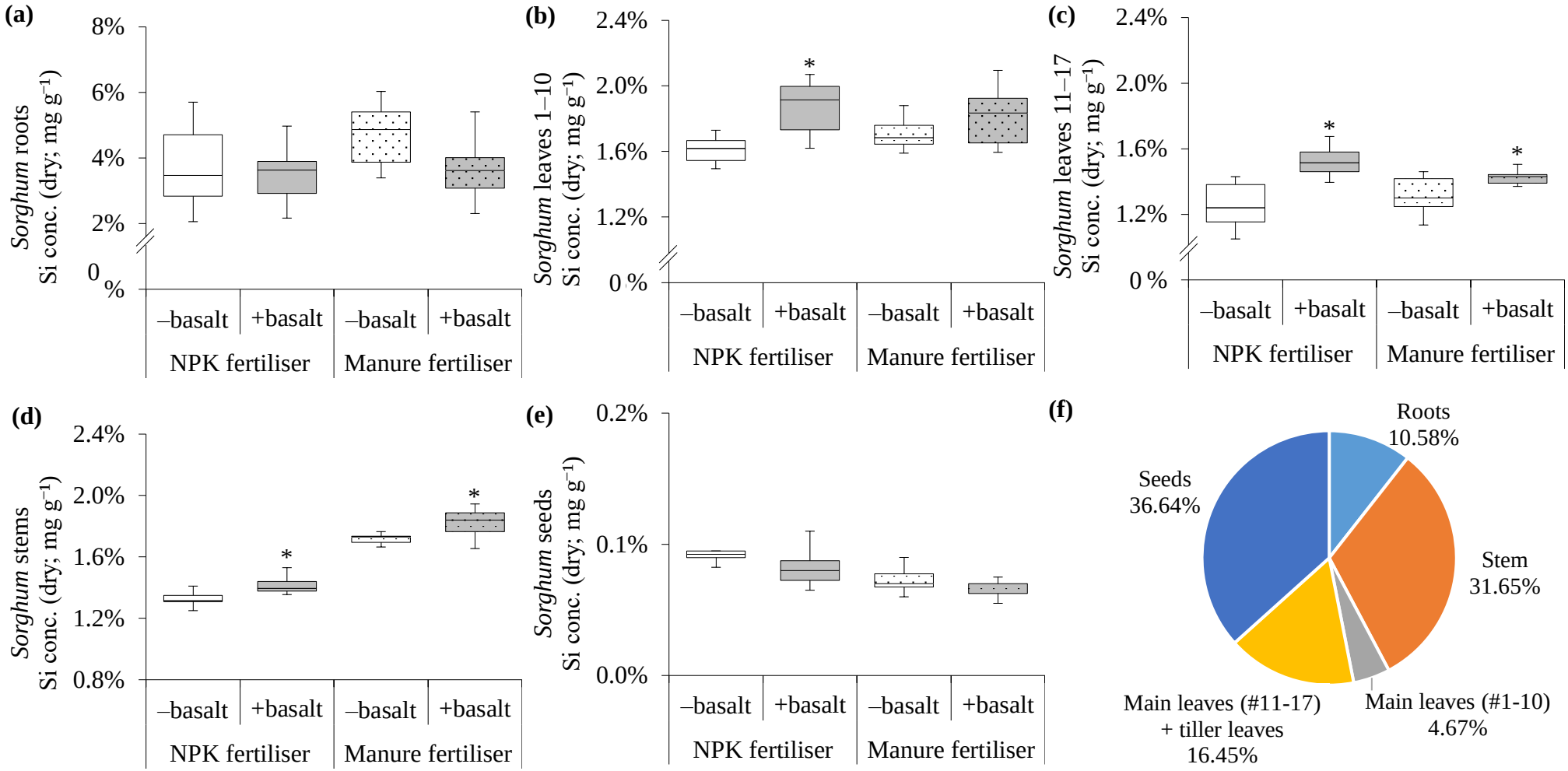

Figure D.1 – *Sorghum* silicon concentrations for tissues harvested in Chapter 3. *Sorghum* tissue Si concentrations (n = 7) for (a) roots, (b) leaf numbers 1–10, (c) leaf numbers 11–17, (d) stems, (e) seeds, and (f) experiment-wide average mass proportions of *Sorghum* tissues. Si data were obtained *via* X-ray fluorescence spectroscopy following the protocol in (Reidinger, Ramsey and Hartley, 2012). Asterisks indicate a statistically significant difference ($p < 0.05$) compared with respective basalt-free control, determined in R *via* a one-way ANOVA.

Table D.1 – *Sorghum* total plant biomass, leaf length and leaf number

Units: biomass, kg length, m	Treatment	Chapter 2 Acidic (pH = 6.6), clay-loam soil N fertiliser (*n* = 6) Mean	*SE*	Chapter 3 Acidic (pH = 6.45), clay-loam soil NPK fertiliser (*n* = 7) Mean	*SE*	Manure fertiliser (*n* = 7) Mean	*SE*
Total plant (dry) biomass	–basalt	0.052	0.002	0.133	0.005	0.124	0.001
	+basalt	0.056	0.001	0.143	0.001	0.123	0.005
Total above-ground (dry) biomass	–basalt	0.044	0.002	0.118	0.006	0.109	0.001
	+basalt	0.048	0.001	0.129	0.001	0.109	0.005
Total leaf length	–basalt	14.6	0.330	17.7	0.761	14.5	0.183
	+basalt	15.5	0.441	16.6	0.584	15.6	0.479
Total length of main culm leaves	–basalt	8.52	0.153	7.98	0.118	7.88	0.075
	+basalt	8.69	0.162	7.98	0.052	7.61	0.053
Total length of tiller leaves	–basalt	6.06	0.309	9.68	0.778	6.65	0.197
	+basalt	6.77	0.352	8.57	0.626	7.99	0.461
Total leaf number	–basalt	35.7	0.615	36.0	2.01	30.4	0.202
	+basalt	36.3	0.558	33.1	1.34	33.0	1.450
Main culm leaf number	–basalt	19.0	0.000	15.0	0.00	15.0	0.000
	+basalt	19.0	0.000	15.0	0.00	14.9	0.143
Tiller leaf number	–basalt	16.7	0.615	21.0	2.01	15.4	0.202
	+basalt	17.3	0.558	18.1	1.34	18.1	1.400

Leaf length time-series data from Chapters 2 and 3 were analysed with time as a factor (*via* a two-way repeated measures ANOVA) to test for significant basalt-related effects at each timepoint. Hence, leaf length values in red indicate a statistically significant ($p < 0.05$) interaction effect between basalt and time for the respective fertiliser, soil and analyte (i.e. the addition of basalt resulted in a statistically significant difference at one or more timepoints). All other values in red indicate a statistically significant effect (one-way ANOVA; $p < 0.05$) due to addition of basalt, for the respective fertiliser, tissue and analyte.

Table D.2 – *Sorghum* root, shoot and seed (dry) biomass and elemental composition (Al to Mg)

Units: Biomass, g plant⁻¹ Conc., mg kg⁻¹		Chapter 2 Acidic (pH = 6.6), clay-loam soil N fertiliser (*n* = 6)						Chapter 3 Acidic (pH = 6.45), clay-loam soil NPK fertiliser (*n* = 7)						Acidic (pH = 6.45), clay-loam soil Manure fertiliser (*n* = 7)					
		Roots		Shoots		Seeds		Roots		Shoots		Seeds		Roots		Shoots		Seeds	
	Treatment	Mean	*SE*	Mean	*SE*	Mean	*SE*	Mean	*SE*	Mean	*SE*	Mean	*SE*	Mean	*SE*	Mean	*SE*	Mean	*SE*
Bio-mass	–basalt	0.008	0.000	0.032	0.001	0.012	0.001	0.014	0.002	0.075	0.003	**0.051**	**0.001**	0.015	0.001	0.063	0.001	**0.046**	**0.001**
	+basalt	0.008	0.000	0.033	0.001	0.015	0.000	0.014	0.001	0.071	0.001	**0.058**	**0.001**	0.015	0.001	0.066	0.003	**0.049**	**0.001**
Al	–basalt	1139	136	15	6.0	24	20	4.8	0.57	**2972**	**582**	2.8	0.23	7.6	1.5	**3843**	**480**	3.5	0.58
	+basalt	1043	79	16	3.5	12	5.7	4.4	1.00	**2329**	**359**	2.8	0.22	4.5	0.64	**2414**	**517**	3.7	0.34
B	–basalt	8.5	0.61	14	1.0	6.6	0.74	6.1	0.53	2.8	0.91	11	0.48	6.6	0.57	1.8	0.57	12	1.1
	+basalt	12	0.42	18	1.5	6.1	0.76	5.8	0.68	2.2	0.57	12	0.50	5.7	0.52	1.6	0.54	14	1.4
Ba	–basalt	12	0.78	34	2.0	0.20	0.019	6.0	0.59	24	4.9	0.33	0.25	6.3	0.076	24	3.6	0.039	0.011
	+basalt	12	0.60	36	1.5	0.17	0.027	6.4	0.23	20	2.9	0.17	0.13	5.6	0.44	16	2.4	0.18	0.12
Ca	–basalt	3273	246	7810	223	86	13	6995	181	7229	68	208	17	6357	120	6520	260	282	14
	+basalt	3452	208	8383	103	82	10	6887	189	7731	457	203	12	5948	186	6685	118	278	16
Cd	–basalt	0.49	0.045	0.42	0.050	0.023	0.0023	0.85	0.088	1.0	0.150	0.03	0.004	0.61	0.017	0.87	0.039	0.02	0.0011
	+basalt	0.40	0.059	0.43	0.032	0.023	0.0027	0.80	0.02	0.86	0.025	0.036	0.003	0.61	0.054	0.96	0.094	0.019	0.0013
Cr	–basalt	47	8.8	22	1.9	1.8	0.037	2.3	0.29	59	10	0.17	0.0150	2	0.18	84	7.4	0.13	0.017
	+basalt	45	3.3	32	15	1.8	0.074	2.0	0.13	60	6.0	0.12	0.0095	2	0.096	82	7.9	0.14	0.017
Cu	–basalt	30	5.1	3.2	0.16	4.1	0.270	4.5	0.14	**42**	**8.7**	3.3	0.13	4.2	0.093	**79**	**9.8**	4.0	0.13
	+basalt	34	9.3	3.3	0.23	3.8	0.086	4.4	0.10	**35**	**6.5**	3.4	0.37	4.1	0.25	**41**	**12**	3.9	0.14
Fe	–basalt	1627	173	101	7.8	32	2.5	**70**	**6.4**	16063	4870	35	0.89	**48**	**2.4**	16020	4688	30	0.71
	+basalt	1562	109	140	54	33	5.5	**52**	**3.0**	11930	3279	35	0.75	**41**	**1.5**	8903	1976	31	0.89
K	–basalt	8903	453	11850	184	2958	38	8583	408	8084	715	5030	92	7985	217	14162	1246	5363	111
	+basalt	9705	402	12100	320	3000	182	9098	176	10592	622	5085	122	7505	281	13095	1050	5390	129
Mg	–basalt	652	27	1808	57	1490	40	2938	89	938	76	1930	65	2070	63	1131	80	1945	43
	+basalt	664	26	1885	24	1455	127	2987	101	911	58	2043	69	2077	51	951	91	1983	66

Values in red indicate a statistically significant effect (one-way ANOVA; $p < 0.05$) due to addition of basalt, for the respective fertiliser, tissue and analyte. Paired emboldened values indicate a significant change (two-way ANOVA; $p < 0.05$) due to addition of basalt, across the entire experiment (i.e., ignoring the fertilisation factor), for the respective tissue and analyte. Paired blocks with peach backgrounds indicate a significant interaction effect between basalt and fertiliser (two-way ANOVA; $p < 0.05$). All statistics were determined in R.

Table D.3 – *Sorghum* root, shoot and seed (dry) elemental composition (Mn to Zn) and shoot $^{87}Sr/^{86}Sr$ ratio

Units: Conc., mg kg^{-1}		Chapter 2						Chapter 3											
		Acidic (pH = 6.6), clay-loam soil						Acidic (pH = 6.45), clay-loam soil						Acidic (pH = 6.45), clay-loam soil					
		N fertiliser (n = 6)						NPK fertiliser (n = 7)						Manure fertiliser (n = 7)					
		Roots		Shoots		Seeds		Roots		Shoots		Seeds		Roots		Shoots		Seeds	
	Treatment	Mean	*SE*	Mean	*SE*	Mean	*SE*	Mean	*SE*	Mean	*SE*	Mean	*SE*	Mean	*SE*	Mean	*SE*	Mean	*SE*
Mn	–basalt	20	1.7	13	0.42	9.5	0.43	**45**	**1.5**	223	54	20	0.39	**23**	**0.66**	226	52	18	0.47
	+basalt	19	1.3	16	1.6	8.4	0.81	**41**	**1.4**	174	35	19	0.69	**20**	**0.82**	131	25	17	0.5
Mo	–basalt	2.8	1.3	2.1	0.12	1.4	0.18	0.37	0.0150	1.1	0.18	0.22	0.0069	0.53	0.02	1.7	0.13	0.25	0.01
	+basalt	1.7	0.07	4.6	1.9	1.3	0.23	0.41	0.0058	1.1	0.12	0.22	0.0052	0.58	0.038	1.4	0.15	0.29	0.014
Na	–basalt	245	23	24	4	18	1.2	2.8	0.69	252	32	8.7	0.37	1.8	0.57	270	22	10	1.6
	+basalt	237	20	29	6.5	16	4.3	2.4	0.71	281	21	7.8	0.48	1.3	0.33	301	13	10	1.0
Ni	–basalt	20	2.8	8.9	0.96	2.4	0.110	0.86	0.071	32	5.2	**1.7**	**0.110**	0.80	0.099	43	4.0	**0.96**	**0.020**
	+basalt	20	1.7	18	9.4	2.2	0.075	0.82	0.074	32	3.0	**1.2**	**0.049**	0.81	0.068	39	3.8	**1.00**	**0.032**
P	–basalt	1169	73	1712	258	3455	79	2398	162	2247	179	4450	101	2347	90	1759	155	4267	75
	+basalt	1099	42	1457	44	3372	266	2271	60	2097	86	4642	147	2446	189	1609	181	4364	104
Si	–basalt	11842	786	10508	389	24	3.9	37607	5024	**13318**	**277**	908	24	46943	3881	**16031**	**111**	729	38
	+basalt	10375	389	13275	290	22	5.3	34886	3491	**14910**	**230**	843	75	38371	5398	**17012**	**274**	667	31
Sr	–basalt	6.7	0.52	14	0.37	0.13	0.0088	15	0.51	35	8.1	0.2	0.022	14	0.24	27	6.7	0.3	0.013
	+basalt	7.0	0.26	15	0.14	0.13	0.0088	15	0.42	31	5.4	0.2	0.02	13	0.49	19	1.4	0.28	0.017
$^{87}Sr/^{86}Sr$	–basalt	–	–	0.71154	0.00003	–	–	–	–	–	–	–	–	–	–	–	–	–	–
	+basalt	–	–	0.71148	–	–	–	–	–	–	–	–	–	–	–	–	–	–	–
Ti	–basalt	32	4.1	30	1.8	34	1.6	1.7	0.036	50	6.2	24	1.1	1.6	0.034	57	7.5	21	0.59
	+basalt	34	2.6	33	0.71	32	2.6	1.7	0.056	44	5.0	24	1.0	1.5	0.043	46	4.2	24	1.4
Zn	–basalt	60	3.2	30	1.8	34	1.6	**30**	**1.6**	50	6.2	24	1.1	**27**	**1.6**	57	7.5	21	0.59
	+basalt	59	3.5	33	0.71	32	2.6	**27**	**2.3**	44	5.0	24	1.0	**23**	**1.0**	46	4.2	24	1.4

Values in red indicate a statistically significant effect (one-way ANOVA; $p < 0.05$) due to addition of basalt, for the respective fertiliser, tissue and analyte. Emboldened values indicate a significant change (two-way ANOVA; $p < 0.05$) due to addition of basalt, across the entire experiment (i.e., ignoring the fertilisation factor), for the respective tissue and analyte. Blocks with peach backgrounds indicate a significant interaction effect between basalt and fertiliser (two-way ANOVA; $p < 0.05$). All statistics were determined in R.

Appendix E – Aqueous geochemistry

Table E.1 – Leachate volumes, mean pH, EC, M alkalinity, dissolved total (TC), inorganic (DIC) and organic (DOC) carbon concentrations

Units: Vol., L column^{-1} EC, mS cm^{-1} Alk., meq L^{-1} Carbon, mg L^{-1}		Chapter 2 N fertiliser (n = 6) Acidic (pH = 6.6), clay-loam soil		Chapter 3 NPK fertiliser (n = 7) Acidic (pH = 6.45), clay-loam soil		Chapter 3 Manure fertiliser (n = 7) Acidic (pH = 6.45), clay-loam soil		Chapter 4 NPKS fertiliser (n = 6) Alkaline (pH = 8.12), sandy soil				Chapter 4 NPKS fertiliser (n = 6) Acidic (pH = 5.65), sandy soil			
								–biochar		+biochar		–biochar		+biochar	
	Treatment	Mean	SE	Mean	SE	Mean	SE	Mean	SE	Mean	SE	Mean	SE	Mean	SE
Vol.	–basalt	4.71	0.189	1.7	0.083	1.6	0.086	3.5	0.33	3.7	0.41	4.7	0.42	4.2	0.56
	+basalt	4.58	0.133	1.6	0.067	1.4	0.058	3.0	0.26	3.2	0.39	3.6	0.44	3.9	0.5
pH	–basalt	8.1	0.0257	6.3	0.078	6.4	0.053	7.9	0.057	7.9	0.11	6.4	0.26	7.0	0.31
	+basalt	8.25	0.0274	6.2	0.070	6.4	0.11	7.9	0.074	7.8	0.13	6.6	0.44	6.7	0.33
EC	–basalt	0.35	0.0175	1.7	0.14	1.3	0.022	0.49	0.01	0.52	0.013	0.22	0.043	0.26	0.042
	+basalt	0.375	0.0159	2.0	0.17	1.4	0.015	0.53	0.016	0.49	0.016	0.27	0.044	0.25	0.047
Alk.	–basalt	–	–	0.34	0.060	0.23	0.018	3.3	0.21	3.6	0.14	1.2	0.35	1.4	0.43
	+basalt	–	–	0.33	0.047	0.42	0.034	3.7	0.21	3.7	0.15	1.5	0.4	1.3	0.41
TC	–basalt	–	–	18	1.4	19	1.0	49	2.2	50	2.3	43	3.0	44	3.1
	+basalt	–	–	25	1.5	22	1.2	54	2.2	54	1.4	50	2.8	48	3.6
DIC	–basalt	–	–	2.2	0.34	1.7	0.17	37	2.3	39	1.6	9.4	4.7	14	5.2
	+basalt	–	–	3.1	0.28	3.9	0.38	41	2.0	41	2.2	13	5.5	10	5.4
DOC	–basalt	–	–	16	1.2	18	0.94	12	0.72	11	1.1	34	4.2	30	2.6
	+basalt	–	–	22	1.4	18	1.20	12	0.82	13	1.0	36	5.7	37	2.7

Quoted concentrations are volume-corrected averages for all leachate samples collected during the experiment and do not necessarily represent the data included in related statistical analyses (which for Chapters 3 and 4 included time-series results). Statistical results for Chapter 2 data relate to one-way ANOVA tests. Time-series data from Chapters 3 and 4 were analysed with time as a factor (*via* a two-way repeated measures ANOVA) to test for significant basalt-related effects at each timepoint. Hence, Chapter 3 and 4 values in red indicate a statistically significant ($p < 0.05$) interaction effect between basalt and time for the respective fertiliser, soil and analyte (i.e. the addition of basalt resulted in a statistically significant difference at one or more timepoints). Reported statistics for pH relate to an analysis of untransformed [H^+] data, converted into pH units *post hoc*. All statistics were determined in R.

Table E.2 – Leachate mean dissolved cation concentrations (Al to Mg)

Units: Conc., mg L^{-1} $^{87}Sr/^{86}Sr$, no units		Chapter 2 N fertiliser (n = 6) Acidic (pH = 6.6), clay-loam soil		Chapter 3 NPK fertiliser (n = 7) Acidic (pH = 6.45), clay-loam soil		Chapter 3 Manure fertiliser (n = 7) Acidic (pH = 6.45), clay-loam soil		Chapter 4 NPKS fertiliser (n = 6) Alkaline (pH = 8.12), sandy soil				Chapter 4 NPKS fertiliser (n = 6) Acidic (pH = 5.65), sandy soil			
								–biochar		+biochar		–biochar		+biochar	
	Treatment	Mean	SE	Mean	SE	Mean	SE	Mean	SE	Mean	SE	Mean	SE	Mean	SE
Al	–basalt	0.0499	0.00694	0.53	0.12	0.59	0.061	6.0	1.1	4.8	0.44	332	89	308	101
	+basalt	0.0654	0.00748	0.17	0.044	0.38	0.062	5.3	0.57	4.7	0.45	286	84	359	105
As	–basalt	0.00071	0.00003	0.0012	0.00012	0.0013	0.00006	0.18	0.0062	0.17	0.005	0.56	0.088	0.57	0.099
	+basalt	0.00076	0.00002	0.0009	0.00003	0.0012	0.00005	0.18	0.0078	0.19	0.015	0.52	0.091	0.57	0.12
B	–basalt	0.0566	0.00389	0.079	0.0046	0.075	0.0028	0.048	0.0017	0.051	0.0032	0.018	0.0014	0.019	0.00072
	+basalt	0.0649	0.0015	0.079	0.0036	0.083	0.0025	0.052	0.0042	0.047	0.0018	0.019	0.0022	0.022	0.0021
Ba	–basalt	0.752	0.0425	0.07	0.0037	0.058	0.0022	1.4	0.024	1.6	0.046	3	0.18	3.0	0.23
	+basalt	0.738	0.0259	0.075	0.0047	0.06	0.0011	1.6	0.094	1.6	0.15	3	0.2	3.7	0.21
Ca	–basalt	32.2	2.20	304	15	246	5.7	82	2.3	89	2.5	41	8.9	50	9.2
	+basalt	32.4	1.71	337	17	255	3.4	86	3.3	82	2.6	48	9.7	45	11
Cd	–basalt	0.00006	0.00001	0.00014	0.00001	0.00014	0.00001	0.0036	0.00015	0.0033	0.00007	0.016	0.0035	0.014	0.0043
	+basalt	0.00004	0.00001	0.00015	0	0.00017	0.00002	0.0044	0.001	0.0032	0.00017	0.013	0.0038	0.015	0.0041
Co	–basalt	0.0002	0.00001	0.00026	0.00003	0.00028	0.00002	0.045	0.0066	0.03	0.0012	0.051	0.013	0.038	0.0023
	+basalt	0.00022	0.00001	0.00021	0.00001	0.00027	0.00002	0.05	0.012	0.035	0.003	0.04	0.0049	0.037	0.003
Cu	–basalt	0.00362	0.00016	0.0023	0.00032	0.0033	0.0003	0.64	0.038	0.65	0.047	0.58	0.096	0.59	0.063
	+basalt	0.00366	0.00012	0.0016	0.00005	0.0035	0.00023	0.86	0.11	0.64	0.06	0.81	0.28	0.52	0.089
Fe	–basalt	0.27	0.0489	0.56	0.12	0.66	0.065	4.5	1.2	2.9	0.29	730	209	705	247
	+basalt	0.325	0.0166	0.2	0.053	0.51	0.065	3.4	0.36	3.2	0.47	610	194	797	255
K	–basalt	0.787	0.0676	18	0.52	20	0.34	15	0.34	15	0.43	1	0.16	1.3	0.31
	+basalt	1.35	0.304	20	1.1	20	0.25	15	0.38	15	0.32	0.99	0.095	1.3	0.32
Mg	–basalt	1.49	0.095	18	0.88	15	0.34	2.2	0.071	2.4	0.076	1.6	0.039	1.6	0.079
	+basalt	1.52	0.0454	20	1	15	0.26	2.3	0.12	2.2	0.057	1.7	0.057	1.7	0.035

Quoted concentrations are volume-corrected averages for all leachate samples collected during the experiment and do not necessarily represent the data included in related statistical analyses (which for Chapters 3 and 4 included time-series results). Statistical results for Chapter 2 data relate to one-way ANOVA tests. Time-series data from Chapters 3 and 4 were analysed with time as a factor (*via* a two-way repeated measures ANOVA) to test for significant basalt-related effects at each timepoint. Hence, Chapter 3 and 4 values in red indicate a statistically significant ($p < 0.05$) interaction effect between basalt and time for the respective fertiliser, soil and analyte (i.e. the addition of basalt resulted in a statistically significant difference at one or more timepoints). All statistics were determined in R.

Table E.3 – Leachate mean dissolved cation concentrations (Mn to Sr) and $^{87}Sr/^{86}Sr$ ratio

Units: Conc., mg L^{-1} $^{87}Sr/^{86}Sr$, no units		Chapter 2 N fertiliser (n = 6) Acidic (pH = 6.6), clay-loam soil		Chapter 3 NPK fertiliser (n = 7) Acidic (pH = 6.45), clay-loam soil		Chapter 3 Manure fertiliser (n = 7) Acidic (pH = 6.45), clay-loam soil		Chapter 4 NPKS fertiliser (n = 6) Alkaline (pH = 8.12), sandy soil				Chapter 4 NPKS fertiliser (n = 6) Acidic (pH = 5.65), sandy soil			
								–biochar		+biochar		–biochar		+biochar	
	Treatment	Mean	SE	Mean	SE	Mean	SE	Mean	SE	Mean	SE	Mean	SE	Mean	SE
Mn	–basalt	0.00276	0.00037	0.014	0.0023	0.019	0.00087	0.14	0.013	0.099	0.0091	2.4	0.74	2.2	0.79
	+basalt	0.00355	0.00013	0.017	0.0015	0.016	0.0027	0.11	0.012	0.11	0.02	1.9	0.66	2.5	0.81
Mo	–basalt	0.00006	0	0.00008	0.00001	0.00017	0.00002	0.12	0.0052	0.1	0.0042	0.056	0.026	0.08	0.031
	+basalt	0.00006	0.00001	0.00006	0	0.00017	0.00001	0.11	0.0067	0.13	0.012	0.065	0.025	0.05	0.023
Na	–basalt	4.13	0.188	5.0	0.2	4	0.075	8.9	0.073	9.6	0.25	3.3	0.088	3.4	0.2
	+basalt	4.24	0.109	5.6	0.12	4.3	0.054	10	0.28	11	0.45	3.7	0.17	4.1	0.08
Ni	–basalt	0.00286	0.00015	0.007	0.00025	0.007	0.00028	0.15	0.0082	0.14	0.0071	0.17	0.027	0.15	0.027
	+basalt	0.00304	0.00007	0.0071	0.00031	0.0076	0.00038	0.16	0.01	0.16	0.013	0.16	0.029	0.15	0.027
Pb	–basalt	0.00014	0.00001	0.00065	0.00011	0.00067	0.00008	0.038	0.0021	0.021	0.0013	1.6	0.41	1.4	0.48
	+basalt	0.00014	0.00001	0.00028	0.00005	0.0005	0.00006	0.027	0.0051	0.025	0.0018	1.2	0.36	1.5	0.47
Rb	–basalt	0.00093	0.00008	0.0021	0.0001	0.002	0.00007	0.13	0.0053	0.13	0.0017	0.11	0.0075	0.11	0.0076
	+basalt	0.00167	0.00023	0.0018	0.00002	0.0018	0.00009	0.13	0.0083	0.14	0.011	0.13	0.018	0.12	0.0049
S	–basalt	1.89	0.106	25	1.5	23	0.49	5.3	0.16	6.1	0.18	3.6	0.27	4.3	0.36
	+basalt	2.18	0.066	29	1.9	24	0.6	6.0	0.35	5.6	0.36	4.3	0.34	4.7	0.36
Se	–basalt	0.00069	0.00004	0.00015	0.00001	0.00016	0.00001	0.026	0.001	0.025	0.0012	0.061	0.0032	0.057	0.003
	+basalt	0.00078	0.00005	0.00014	0	0.00017	0.00001	0.029	0.0015	0.03	0.0026	0.059	0.0045	0.054	0.0055
Si	–basalt	3.33	0.136	8.3	0.26	7.8	0.13	2.3	0.084	2.4	0.059	1.1	0.23	0.85	0.18
	+basalt	3.34	0.0592	8	0.23	8	0.1	2.4	0.079	2.3	0.082	1.1	0.25	1.2	0.22
Sr	–basalt	0.086	0.00461	0.73	0.038	0.6	0.016	7.1	0.14	7.9	0.19	3	0.79	4.2	1.1
	+basalt	0.0857	0.00268	0.81	0.042	0.63	0.011	7.8	0.41	7.9	0.8	3.8	0.93	4.3	1.3
$^{87}Sr/^{86}Sr$	–basalt	0.71157	0.00002	–	–	–	–	–	–	–	–	–	–	–	–
	+basalt	0.71128	0.00001	–	–	–	–	–	–	–	–	–	–	–	–

Quoted concentrations are volume-corrected averages for all leachate samples collected during the experiment and do not necessarily represent the data included in related statistical analyses (which for Chapters 3 and 4 included time-series results). Statistical results for Chapter 2 data relate to one-way ANOVA tests. Time-series data from Chapters 3 and 4 were analysed with time as a factor (*via* a two-way repeated measures ANOVA) to test for significant basalt-related effects at each timepoint. Hence, Chapter 3 and 4 values in red indicate a statistically significant ($p < 0.05$) interaction effect between basalt and time for the respective fertiliser, soil and analyte (i.e. the addition of basalt resulted in a statistically significant difference at one or more timepoints). All statistics were determined in R.

Table E.4 – Leachate mean dissolved cation concentrations (Ti to Zn) and mean dissolved major anions

Units: Conc., mg L^{-1} $^{87}Sr/^{86}Sr$, no units		Chapter 2 N fertiliser (n = 6) Acidic (pH = 6.6), clay-loam soil		Chapter 3 NPK fertiliser (n = 7) Acidic (pH = 6.45), clay-loam soil		Chapter 3 Manure fertiliser (n = 7) Acidic (pH = 6.45), clay-loam soil		Chapter 4 NPKS fertiliser (n = 6) Alkaline (pH = 8.12), sandy soil				Chapter 4 NPKS fertiliser (n = 6) Acidic (pH = 5.65), sandy soil			
								–biochar		+biochar		–biochar		+biochar	
	Treatment	Mean	SE	Mean	SE	Mean	SE	Mean	SE	Mean	SE	Mean	SE	Mean	SE
Ti	–basalt	0.00276	0.00037	0.014	0.0023	0.019	0.00087	0.14	0.013	0.099	0.0091	2.4	0.74	2.2	0.79
	+basalt	0.00355	0.00013	0.017	0.0015	0.016	0.0027	0.11	0.012	0.11	0.02	1.9	0.66	2.5	0.81
Zn	–basalt	0.00006	0	0.00008	0.00001	0.00017	0.00002	0.12	0.0052	0.1	0.0042	0.056	0.026	0.08	0.031
	+basalt	0.00006	0.00001	0.00006	0	0.00017	0.00001	0.11	0.0067	0.13	0.012	0.065	0.025	0.05	0.023
Br	–basalt	4.13	0.188	5	0.2	4	0.075	8.9	0.073	9.6	0.25	3.3	0.088	3.4	0.2
	+basalt	4.24	0.109	5.6	0.12	4.3	0.054	10	0.28	11	0.45	3.7	0.17	4.1	0.08
Cl	–basalt	0.00286	0.00015	0.007	0.00025	0.007	0.00028	0.15	0.0082	0.14	0.0071	0.17	0.027	0.15	0.027
	+basalt	0.00304	0.00007	0.0071	0.00031	0.0076	0.00038	0.16	0.01	0.16	0.013	0.16	0.029	0.15	0.027
F	–basalt	0.00014	0.00001	0.00065	0.00011	0.00067	0.00008	0.038	0.0021	0.021	0.0013	1.6	0.41	1.4	0.48
	+basalt	0.00014	0.00001	0.00028	0.00005	0.0005	0.00006	0.027	0.0051	0.025	0.0018	1.2	0.36	1.5	0.47
N-NO^{2-}	–basalt	0.00093	0.00008	0.0021	0.0001	0.002	0.00007	0.13	0.0053	0.13	0.0017	0.11	0.0075	0.11	0.0076
	+basalt	0.00167	0.00023	0.0018	0.00002	0.0018	0.00009	0.13	0.0083	0.14	0.011	0.13	0.018	0.12	0.0049
N-NO^{3-}	–basalt	1.89	0.106	25	1.5	23	0.49	5.3	0.16	6.1	0.18	3.6	0.27	4.3	0.36
	+basalt	2.18	0.066	29	1.9	24	0.6	6.0	0.35	5.6	0.36	4.3	0.34	4.7	0.36
P-PO_4^{3-}	–basalt	0.00069	0.00004	0.00015	0.00001	0.00016	0.00001	0.026	0.001	0.025	0.0012	0.061	0.0032	0.057	0.003
	+basalt	0.00078	0.00005	0.00014	0	0.00017	0.00001	0.029	0.0015	0.03	0.0026	0.059	0.0045	0.054	0.0055
S-SO_4^{2-}	–basalt	3.33	0.136	8.3	0.26	7.8	0.13	2.3	0.084	2.4	0.059	1.1	0.23	0.85	0.18
	+basalt	3.34	0.0592	8	0.23	8	0.1	2.4	0.079	2.3	0.082	1.1	0.25	1.2	0.22

Quoted concentrations are volume-corrected averages for all leachate samples collected during the experiment and do not necessarily represent the data included in related statistical analyses (which for Chapters 3 and 4 included time-series results). Statistical results for Chapter 2 data relate to one-way ANOVA tests. Time-series data from Chapters 3 and 4 were analysed with time as a factor (*via* a two-way repeated measures ANOVA) to test for significant basalt-related effects at each timepoint. Hence, Chapter 3 and 4 values in red indicate a statistically significant ($p < 0.05$) interaction effect between basalt and time for the respective fertiliser, soil and analyte (i.e. the addition of basalt resulted in a statistically significant difference at one or more timepoints). All statistics were determined in R.

Table E.5 – Pore water mean pH, EC, DIC, DOC, dissolved cation and major anion concentrations

Units: Vol., L column⁻¹ EC, mS cm⁻¹ Conc., mg L⁻¹		Chapter 3 Acidic (pH = 6.45), clay-loam soil			
		NPK fertiliser (*n* = 7)		Manure fertiliser (*n* = 7)	
	Treatment	Mean	SE	Mean	SE
pH	–basalt	5.4	0.02	6.6	0.04
	+basalt	5.4	0.03	6.5	0.02
EC	–basalt	2.4	0.20	0.56	0.27
	+basalt	2.7	0.38	0.79	0.05
TC	–basalt	16	0.28	33	0.9
	+basalt	17	0.72	30	1.2
DIC	–basalt	1.1	0.085	6.4	0.59
	+basalt	1.9	0.170	9.9	0.59
DOC	–basalt	15	0.34	27	0.84
	+basalt	15	0.59	21	0.89
Al	–basalt	2.1	0.38	1.2	0.38
	+basalt	1.9	0.38	1.4	0.24
As	–basalt	0.028	0.005	0.036	0.010
	+basalt	0.030	0.006	0.032	0.007
B	–basalt	<LOD	<LOD	<LOD	<LOD
	+basalt	<LOD	<LOD	<LOD	<LOD
Ba	–basalt	4.8	0.96	0.18	0.054
	+basalt	5.8	1.20	0.29	0.075
Ca	–basalt	176	11	50	26
	+basalt	228	28	67	4.9

Units: Vol., L column⁻¹ EC, mS cm⁻¹ Conc., mg L⁻¹		Chapter 3 Acidic (pH = 6.45), clay-loam soil			
		NPK fertiliser (*n* = 7)		Manure fertiliser (*n* = 7)	
	Treatment	Mean	SE	Mean	SE
Cd	–basalt	0.001	0.001	0.001	0.001
	+basalt	0.002	0.001	0.001	0.001
Co	–basalt	0.040	0.008	0.008	0.002
	+basalt	0.038	0.008	0.007	0.002
Cu	–basalt	0.16	0.027	0.31	0.065
	+basalt	0.17	0.033	0.27	0.050
Fe	–basalt	2.0	0.7	3.6	3.1
	+basalt	2.0	1.1	3.0	1.4
K	–basalt	31	0.85	6.7	3.8
	+basalt	33	3.8	5.6	0.24
Mg	–basalt	197	18	22	7.2
	+basalt	245	27	61	7.6
Mn	–basalt	28	6.7	0.068	0.032
	+basalt	27	5.7	0.034	0.011
Mo	–basalt	0.026	0.005	0.033	0.009
	+basalt	0.028	0.005	0.033	0.006
Na	–basalt	113	12	4.1	1.4
	+basalt	153	17	11	0.74
Ni	–basalt	0.85	0.16	0.17	0.046
	+basalt	0.92	0.19	0.15	0.036

Units: Vol., L column⁻¹ EC, mS cm⁻¹ Conc., mg L⁻¹		Chapter 3 Acidic (pH = 6.45), clay-loam soil			
		NPK fertiliser (*n* = 7)		Manure fertiliser (*n* = 7)	
	Treatment	Mean	SE	Mean	SE
Pb	–basalt	0.021	0.004	0.012	0.003
	+basalt	0.02	0.004	0.014	0.002
Rb	–basalt	0.079	0.014	0.014	0.004
	+basalt	0.099	0.018	0.016	0.004
S	–basalt	7.8	0.59	5.9	1.6
	+basalt	10	0.92	9.3	0.53
Se	–basalt	0.006	0.001	0.006	0.001
	+basalt	0.007	0.001	0.006	0.001
Sr	–basalt	26	5.1	1.5	0.46
	+basalt	32	6.6	2.5	0.73
Ti	–basalt	0.016	0.001	0.005	0.002
	+basalt	0.021	0.002	0.007	0.001
Zn	–basalt	1.4	0.24	0.66	0.18
	+basalt	1.5	0.28	0.75	0.13
Cl^-	–basalt	114	12	4.1	1.40
	+basalt	153	17	11	0.82
NO^{3-}	–basalt	195	17	22	7.2
	+basalt	246	27	61	7.4
SO_4^{2-}	–basalt	7.9	0.60	5.9	1.50
	+basalt	10	0.94	9.2	0.51

Quoted concentrations are averages for all pore water samples collected during the experiment and do not represent the data included in related statistical analyses (which were time-series measurements). Time-series data were analysed with time as a factor (*via* a two-way repeated measures ANOVA) to test for significant basalt-related effects at each timepoint. Hence, values in red indicate a statistically significant ($p < 0.05$) interaction effect between basalt and time for the respective fertiliser, soil and analyte (i.e. the addition of basalt resulted in a statistically significant difference at one or more timepoints). Reported statistics for pH relate to an analysis of untransformed [H^+] data, converted into pH units *post hoc*. All statistics were determined in R.

Appendix F – Soil characterisation

Table F.1 – Soil (dry) mass, pH and mass of exchangeable cations per unit (dry) mass of soil (Al to Cr)

Soil mass, kg column^{-1}; Soil exchange-able cations conc., mg kg^{-1}		Chapter 2 N fertiliser (n = 6) Acidic (pH = 6.6), clay-loam soil		Chapter 3 NPK fertiliser (n = 7) Acidic (pH = 6.45), clay-loam soil		Chapter 3 Manure fertiliser (n = 7) Acidic (pH = 6.45), clay-loam soil		Chapter 4 NPKS fertiliser (n = 6) Alkaline (pH = 8.12), sandy soil				Chapter 4 NPKS fertiliser (n = 6) Acidic (pH = 5.65), sandy soil			
								–biochar		+biochar		–biochar		+biochar	
	Treatment	Mean	SE	Mean	SE	Mean	SE	Mean	SE	Mean	SE	Mean	SE	Mean	SE
Soil mass	–basalt	9.300	0.001	8.252	0.001	8.270	0.001	5.792	0.001	5.810	0.001	5.792	0.001	5.810	0.001
	+basalt	9.481	0.001	8.343	0.001	8.361	0.001	5.865	0.001	5.883	0.001	5.865	0.001	5.883	0.001
pH	–basalt	6.57	0.035	6.08	0.035	6.2	0.010	**7.96**	**0.016**	**8.05**	**0.006**	**5.94**	**0.028**	**6.8**	**0.02**
	+basalt	6.66	0.025	6.12	0.032	6.2	0.017	**8.05**	**0.005**	**8.04**	**0.008**	**6.86**	**0.050**	**7.0**	**0.04**
Al	–basalt	–	–	0.24	0.0072	0.21	0.0039	–	–	–	–	**4.4**	**0.19**	**5.2**	**0.2**
	+basalt	–	–	0.22	0.0071	0.2	0.005	–	–	–	–	**5.5**	**0.24**	**5.1**	**0.19**
As	–basalt	–	–	0.15	0.0021	0.15	0.0013	0.047	0.00087	0.048	0.00072	0.062	0.0026	0.063	0.0015
	+basalt	–	–	0.15	0.0012	0.15	0.0013	0.049	0.0012	0.049	0.00099	0.066	0.0019	0.061	0.0057
Ba	–basalt	51.1	0.778	**3.7**	**0.027**	**3.8**	**0.035**	7.6	0.25	8	0.34	7.6	0.36	7.1	0.12
	+basalt	51.1	0.964	**4.0**	**0.025**	**3.9**	**0.042**	7.1	0.14	7.5	0.24	7.4	0.15	6.8	0.55
Ca	–basalt	5860	48.9	2772	17	2778	14	4829	19	4855	47	**1642**	**223**	**2667**	**358**
	+basalt	6023	121	2800	10	2774	14	4742	51	4747	65	**2962**	**301**	**3299**	**416**
Cd	–basalt	–	–	0.012	0.00022	0.012	0.00018	0.022	0.00056	0.023	0.00063	0.016	0.00057	0.013	0.00041
	+basalt	–	–	0.013	0.00027	0.012	0.00029	0.024	0.00069	0.023	0.00079	0.014	0.00054	0.013	0.0013
Co	–basalt	–	–	0.0021	0.00056	0.0019	0.00033	0.0029	0.00013	0.0033	0.00033	0.0031	0.00014	0.0026	0.00012
	+basalt	–	–	0.00099	0.0001	0.0017	0.00026	0.0028	0.00013	0.003	0.00018	0.0032	0.00009	0.0028	0.00025
Cr	–basalt	–	–	0.002	0.00023	0.0027	0.0012	0.0056	0.00043	0.0057	0.00026	0.0098	0.00055	0.011	0.00049
	+basalt	–	–	0.0015	0.00035	0.0036	0.00066	0.0065	0.00073	0.0067	0.0004	0.012	0.00078	0.011	0.0011

Values in red indicate a statistically significant effect (one-way ANOVA; $p < 0.05$) due to addition of basalt for the respective analyte, fertiliser and soil type. Paired emboldened values indicate a significant change (two-way ANOVA; $p < 0.05$) due to addition of basalt, across all replicates of the same soil type (i.e., ignoring the fertiliser or biochar factor), for the respective analyte. Reported statistics for pH relate to an analysis of untransformed [H^+] data, converted into pH units post hoc. All statistics were determined in R.

Table F.2 – Mass of exchangeable cations per unit (dry) mass of soil (Cs to Ni)

Soil mass, kg column^{-1}; Soil exchange-able cations conc., mg kg^{-1}		Chapter 2 N fertiliser (n = 6) Acidic (pH = 6.6), clay-loam soil		Chapter 3 NPK fertiliser (n = 7) Acidic (pH = 6.45), clay-loam soil		Chapter 3 Manure fertiliser (n = 7) Acidic (pH = 6.45), clay-loam soil		Chapter 4 NPKS fertiliser (n = 6) Alkaline (pH = 8.12), sandy soil –biochar		Chapter 4 NPKS fertiliser (n = 6) Alkaline (pH = 8.12), sandy soil +biochar		Chapter 4 NPKS fertiliser (n = 6) Acidic (pH = 5.65), sandy soil –biochar		Chapter 4 NPKS fertiliser (n = 6) Acidic (pH = 5.65), sandy soil +biochar	
	Treatment	Mean	SE	Mean	SE	Mean	SE	Mean	SE	Mean	SE	Mean	SE	Mean	SE
Cs	–basalt	–	–	0.013	0.00037	0.013	0.00017	0.006	0.00018	0.0059	0.0002	**0.018**	**0.0014**	**0.014**	**0.00073**
	+basalt	–	–	0.014	0.00034	0.013	0.00033	0.0059	0.0001	0.0059	0.00016	**0.015**	**0.00066**	**0.012**	**0.0011**
Cu	–basalt	–	–	**0.31**	**0.0064**	**0.29**	**0.0041**	0.11	0.027	0.22	0.12	**0.025**	**0.0026**	**0.03**	**0.0014**
	+basalt	–	–	**0.29**	**0.003**	**0.28**	**0.0039**	0.095	0.0039	0.1	0.0027	**0.038**	**0.0014**	**0.046**	**0.0068**
Fe	–basalt	–	–	0.99	0.028	0.92	0.017	0.19	0.0067	0.19	0.0047	1.4	0.09	1.2	0.025
	+basalt	–	–	0.92	0.013	0.93	0.013	0.19	0.0081	0.19	0.0046	1.3	0.029	1.1	0.10
K	–basalt	164	7.71	195	4.3	191	1.8	**64**	**1.2**	**67**	**1.9**	11	0.24	10	0.26
	+basalt	171	9.18	193	1.8	194	2.3	**73**	**2.3**	**75**	**1.9**	11	0.54	11	1.1
Li	–basalt	–	–	0.21	0.0096	0.21	0.0070	**0.030**	**0.00087**	**0.029**	**0.00081**	–	–	–	–
	+basalt	–	–	0.22	0.0065	0.19	0.0047	**0.028**	**0.0012**	**0.027**	**0.00072**	–	–	–	–
Mg	–basalt	170	3.88	**101**	**0.66**	**117**	**0.5**	**30**	**0.61**	**29**	**0.38**	**23**	**1.4**	**16**	**1.2**
	+basalt	193	3.52	**112**	**0.73**	**124**	**0.84**	**42**	**0.35**	**43**	**1.6**	**30**	**3.5**	**23**	**2.4**
Mn	–basalt	6.77	1.16	2.2	0.31	1.4	0.2	1.3	0.12	1.3	0.12	0.33	0.049	0.25	0.038
	+basalt	18.9	3.02	1.3	0.13	1.5	0.12	1.5	0.17	1.4	0.14	0.33	0.054	0.4	0.065
Mo	–basalt	–	–	0.038	0.0069	0.034	0.0014	0.0077	0.00028	0.0078	0.00028	0.0098	0.00028	0.0082	0.00025
	+basalt	–	–	0.037	0.0029	0.06	0.017	0.008	0.0003	0.008	0.00035	0.0087	0.00044	0.0075	0.0008
Na	–basalt	34.3	2.57	**18**	**0.59**	**18**	**0.25**	189	30	129	27	66	22	84	20
	+basalt	36.1	1.25	**19**	**0.42**	**21**	**1.3**	159	30	113	19	132	8.9	73	30
Ni	–basalt	–	–	**0.19**	**0.0018**	**0.16**	**0.0018**	**0.035**	**0.001**	**0.037**	**0.0018**	**0.015**	**0.00048**	**0.014**	**0.0011**
	+basalt	–	–	**0.18**	**0.0019**	**0.16**	**0.0014**	**0.04**	**0.00083**	**0.042**	**0.002**	**0.025**	**0.0017**	**0.021**	**0.0016**

Values in red indicate a statistically significant effect (one-way ANOVA; $p < 0.05$) due to addition of basalt for the respective analyte, fertiliser and soil type. Paired emboldened values indicate a significant change (two-way ANOVA; $p < 0.05$) due to addition of basalt, across all replicates of the same soil type (i.e., ignoring the fertiliser or biochar factor), for the respective analyte. All statistics were determined in R.

Table F.3 – Mass of exchangeable cations per unit (dry) mass of soil (P to Zn) and $^{87}Sr/^{86}Sr$ ratio

Soil mass, kg column^{-1}; Soil exchange-able cations conc., mg kg^{-1}		Chapter 2 N fertiliser (n = 6) Acidic (pH = 6.6), clay-loam soil		Chapter 3 NPK fertiliser (n = 7) Acidic (pH = 6.45), clay-loam soil		Chapter 3 Manure fertiliser (n = 7) Acidic (pH = 6.45), clay-loam soil		Chapter 4 NPKS fertiliser (n = 6) Alkaline (pH = 8.12), sandy soil –biochar		Chapter 4 NPKS fertiliser (n = 6) Alkaline (pH = 8.12), sandy soil +biochar		Chapter 4 NPKS fertiliser (n = 6) Acidic (pH = 5.65), sandy soil –biochar		Chapter 4 NPKS fertiliser (n = 6) Acidic (pH = 5.65), sandy soil +biochar	
	Treatment	Mean	SE	Mean	SE	Mean	SE	Mean	SE	Mean	SE	Mean	SE	Mean	SE
P	–basalt	–	–	23	0.36	23	0.27	8.3	0.32	8.3	0.19	1.6	0.061	1.8	0.078
	+basalt	–	–	23	0.28	22	0.22	8.2	0.33	8.4	0.33	1.9	0.18	1.9	0.19
Pb	–basalt	–	–	0.0041	0.00038	0.0027	0.00025	0.0063	0.0004	0.014	0.0077	**0.2**	**0.019**	**0.12**	**0.016**
	+basalt	–	–	0.0035	0.00023	0.0026	0.0004	0.0049	0.00024	0.0059	0.00044	**0.11**	**0.0094**	**0.087**	**0.014**
Rb	–basalt	–	–	0.58	0.016	0.59	0.0069	**0.2**	**0.004**	**0.21**	**0.0065**	0.16	0.01	0.14	0.0051
	+basalt	–	–	0.6	0.0093	0.58	0.014	**0.23**	**0.0025**	**0.24**	**0.0067**	0.16	0.0062	0.14	0.013
S	–basalt	10.8	0.28	**8.9**	**1.8**	**17**	**2.6**	7.0	0.79	6.2	1.70	4.1	0.67	1.4	0.37
	+basalt	11.8	0.561	**17**	**1.5**	**17**	**1.8**	5.4	0.80	6.4	0.76	2.5	1.1	3.4	0.83
Se	–basalt	–	–	0.018	0.00049	0.018	0.00031	0.014	0.00033	0.014	0.00029	0.013	0.00046	0.014	0.00047
	+basalt	–	–	0.017	0.00025	0.017	0.00022	0.014	0.00047	0.014	0.00042	0.015	0.00054	0.014	0.0012
Si	–basalt	10.2	0.624	**343**	**4.7**	**395**	**2.6**	**22**	**0.4**	**21**	**0.61**	**11**	**0.44**	**13**	**0.52**
	+basalt	12.6	0.242	**377**	**2.8**	**404**	**2**	**30**	**0.64**	**27**	**0.48**	**89**	**9.9**	**75**	**7.9**
Sr	–basalt	12.8	0.302	**7**	**0.063**	**7.2**	**0.036**	**6.5**	**0.056**	**6.7**	**0.072**	**2.4**	**0.24**	**3.4**	**0.44**
	+basalt	13	0.271	**7.3**	**0.028**	**7.3**	**0.035**	**6.8**	**0.061**	**6.8**	**0.071**	**4**	**0.35**	**4.4**	**0.55**
$^{87}Sr/^{86}Sr$	–basalt	0.71168	0.00001	–	–	–	–	–	–	–	–	–	–	–	–
	+basalt	0.71139	0.00007	–	–	–	–	–	–	–	–	–	–	–	–
Ti	–basalt	–	–	**269**	**2.1**	**273**	**1.6**	0.61	0.0073	0.61	0.0064	**0.23**	**0.026**	**0.35**	**0.042**
	+basalt	–	–	**274**	**1.2**	**275**	**0.82**	0.59	0.0069	0.6	0.0078	**0.37**	**0.034**	**0.42**	**0.053**
Zn	–basalt	–	–	–	–	–	–	0.20	0.0044	0.21	0.0120	**0.23**	**0.029**	**0.094**	**0.028**
	+basalt	–	–	–	–	–	–	0.20	0.0060	0.20	0.0048	**0.1**	**0.017**	**0.100**	**0.024**

Values in red indicate a statistically significant effect (one-way ANOVA; $p < 0.05$) due to addition of basalt for the respective analyte, fertiliser and soil type. Paired emboldened values indicate a significant change (two-way ANOVA; $p < 0.05$) due to addition of basalt, across all replicates of the same soil type (i.e., ignoring the fertiliser or biochar factor), for the respective analyte. All statistics were determined in R.

Appendix G – ICP-MS limits of detection: Chapter 3 analyses

Table G.1 – Limits of detection for the Thermo Fisher iCAP Q ICP-MS instrument used for aqueous, plant and soil extract analyses in Chapter 3

Element	LOD
Li (ppb)	0.08788
Be (ppb)	0.04151
B (ppm)	0.00196
Na (ppm)	0.00038
Mg (ppm)	0.00006
Al (ppb)	0.50966
P (ppm)	0.00027
S (ppm)	0.39952
K (ppm)	0.00162
Ca (ppm)	0.00360
V (ppb)	0.00171
Cr (ppb)	0.00475
Mn (ppb)	0.01174
Fe (ppb)	0.01204
Co (ppb)	0.00044
Ni (ppb)	0.01502
Cu (ppb)	0.00502
Zn (ppb)	0.07573
As (ppb)	0.00481
Se (ppb)	0.00118
Rb (ppb)	0.00148
Sr (ppb)	0.00702
Mo (ppb)	0.00118
Ag (ppb)	0.00108
Cd (ppb)	0.00204
Cs (ppb)	0.00000
Ba (ppb)	0.01066
Tl (ppb)	0.00006
Pb (ppb)	0.00147
U (ppb)	0.00007

Appendix G – C++ code for Arduino-based dataloggers

```
/*
  5-PROBE SOIL MOISTURE DATALOGGER CODE FOR ARDUINO NANO

  Code adapted from an article in Electronic Wings (2017), available
  at: https://www.electronicwings.com/arduino/soil-moisture-sensor-
  interfacing-with-arduino-uno

  By Mike E. Kelland, 18 February 2018
  Released into the public domain.

  ARDUINO MODUL AND SENSOR WIRING GUIDE--->

  SD MODULE "GND"  -> ARDUINO "GND"
  SD MODULE "VCC"  -> ARDUINO "+5V"
  SD MODULE "MISO" -> ARDUINO "D12"
  SD MODULE "MOSI" -> ARDUINO "D11"
  SD MODULE "SCK"  -> ARDUINO "D13"
  SD MODULE "CS"   -> ARDUINO "D10"

  RTC MODULE "SCL" -> ARDUINO "A5"
  RTC MODULE "SDA" -> ARDUINO "A4"
  RTC MODULE "VCC" -> ARDUINO "+5V"
  RTC MODULE "GND" -> ARDUINO "GND"

  SENSOR1 "VCC"    -> ARDUINO "D2"
  SENSOR1 "GND"    -> ARDUINO "GND"
  SENSOR1 "A0"     -> ARDUINO "A0"

  SENSOR2 "VCC"    -> ARDUINO "D3"
  SENSOR2 "GND"    -> ARDUINO "GND"
  SENSOR2 "A0"     -> ARDUINO "A1"

  SENSOR3 "VCC"    -> ARDUINO "D4"
  SENSOR3 "GND"    -> ARDUINO "GND"
  SENSOR3 "A0"     -> ARDUINO "A2"

  SENSOR4 "VCC"    -> ARDUINO "D5"
  SENSOR4 "GND"    -> ARDUINO "GND"
  SENSOR4 "A0"     -> ARDUINO "A3"

  SENSOR5 "VCC"    -> ARDUINO "D6"
  SENSOR5 "GND"    -> ARDUINO "GND"
  SENSOR5 "A0"     -> ARDUINO "A6"
*/
```

```
//  MAIN CODE

#include <DS3231.h>           // Load library for real-time clock (RTC)
#include <SPI.h>              // Load libraries for SD module
#include <SD.h>

DS3231 rtc(SDA, SCL);         // Initiate RTC using hardware interface
const int chipSelect = 10;    // Set SD module CS to pin 10

int powerPin1 = 2;            // Assign sensor1 power pin
int inputPin1 = A0;           // Assign sensor1 input pin
int reading1;                 // Assign variable for sensor1 reading

int powerPin2 = 3;            // Assign sensor2 power pin
int inputPin2 = A1;           // Assign sensor2 input pin
int reading2;                 // Assign variable for sensor2 reading

int powerPin3 = 4;            // Assign sensor3 power pin
int inputPin3 = A2;           // Assign sensor3 input pin
int reading3;                 // Assign variable for sensor3 reading

int powerPin4 = 5;            // Assign sensor4 power pin
int inputPin4 = A3;           // Assign sensor4 input pin
int reading4;                 // Assign variable for sensor4 reading

int powerPin5 = 6;            // Assign sensor5 power pin
int inputPin5 = A6;           // Assign sensor5 input pin
int reading5;                 // Assign variable for sensor5 reading

void setup() {                // "void setup" runs only once

  Serial.begin(9600);         // Initiate communication between
                              // Arduino and PC serial port

  rtc.begin();                // Initiate the RTC object

// The following lines can be uncommented to set the date and time

//rtc.setDOW(WEDNESDAY);      // Set Day-of-Week to FRIDAY
//rtc.setTime(11, 42, 13);    // Set time to 21:15:00 (24hr format)
//rtc.setDate(25, 07, 2018);  // Set date to 6th April 2018

  Serial.print("Initializing SD card...");  // Check SD card is ready

    if (!SD.begin(chipSelect)) {

// Print to serial port if SD card cannot be initialised
     Serial.println("Card failed, or not present");
```

```
    return;             // Stop program if SD card initialisation fails
   }

// Print "SD card initialised" to the serial port
     Serial.println("card initialised.");

// Set digital pin 1 as an output to power sensor1
  pinMode(powerPin1,OUTPUT);

// Set digital pin 2 as an output to power sensor 2
  pinMode(powerPin2,OUTPUT);

// Set digital pin 3 as an output to power sensor 3
  pinMode(powerPin3,OUTPUT);

// Set digital pin 4 as an output to power sensor4
  pinMode(powerPin4,OUTPUT);

// Set digital pin 5 as an output to power sensor 5
  pinMode(powerPin5,OUTPUT);

  String headerString = "";      // Make a string for the data header
  headerString += "Date";        // Add date to headerString
  headerString += "\t";          // Add a tab to headerString
  headerString += "Time";        // Add time to headerString
  headerString += "\t";          // Add a tab to headerString
  headerString += "Sensor1";     // Add "Sensor1" to headerString
  headerString += "\t";          // Add a tab to headerString
  headerString += "Sensor2";     // Add "Sensor2" to headerString
  headerString += "\t";          // Add a tab to headerString
  headerString += "Sensor3";     // Add "Sensor3" to headerString
  headerString += "\t";          // Add a tab to headerString
  headerString += "Sensor4";     // Add "Sensor4" to headerString
  headerString += "\t";          // Add a tab to headerString
  headerString += "Sensor5";     // Add "Sensor5" to headerString
  headerString += "\t";          // Add a tab to headerString
  headerString += "Column1";     // Add "Column1" to headerString


// Open the data file from the SD card
  File dataFile = SD.open("datalog.txt", FILE_WRITE);

// If the file is available, write headerString to it
  if (dataFile) {
    dataFile.println(headerString);

// Close the data file
    dataFile.close();
```

```
// Print headerString to the serial port
   Serial.println(headerString);
   }

// Else, if the file isn't open, display error
  else {
    Serial.println("error opening datalog.txt");
   }
  }

// This function loops indefinitely

void loop() {

// Set powerPin1 as HIGH, outputting current through pin 2
  digitalWrite (powerPin1, HIGH);
  delay (25);

// Update soil moisture variable (reading1) with reading from sensor1
  reading1 = analogRead(inputPin1);
  delay (25);

// Set powerPin1 to LOW turning off sensor 1
  digitalWrite (powerPin1, LOW);
  delay (500);

// This measuring sequence for probe 1 is then repeated for all probes

  digitalWrite (powerPin2, HIGH);
  delay (25);
  reading2 = analogRead(inputPin2);
  delay (25);
  digitalWrite (powerPin2, LOW);
  delay (500);

  digitalWrite (powerPin3, HIGH);
  delay (25);
  reading3 = analogRead(inputPin3);
  delay (25);
  digitalWrite (powerPin3, LOW);
  delay (500);

  digitalWrite (powerPin4, HIGH);
  delay (25);
  reading4 = analogRead(inputPin4);
  delay (25);
  digitalWrite (powerPin4, LOW);
  delay (500);
```

```
  digitalWrite (powerPin5, HIGH);
  delay (25);
  reading5 = analogRead(inputPin5);
  delay (25);
  digitalWrite (powerPin5, LOW);

// Make a string for assembling the data to log
  String dataString = "";
  dataString += String(rtc.getDateStr());    // Add date to dataString
  dataString += "\t";                        // Add a tab
  dataString += String(rtc.getTimeStr());    // Add time
  dataString += "\t";                        // Add a tab
  dataString += String(reading1);            // Add reading1
  dataString += "\t";                        // Add a tab
  dataString += String(reading2);            // Add reading2
  dataString += "\t";                        // Add a tab
  dataString += String(reading3);            // Add reading3
  dataString += "\t";                        // Add a tab
  dataString += String(reading4);            // Add reading4
  dataString += "\t";                        // Add a tab
  dataString += String(reading5);            // Add reading5

// Open the data file from the SD card
  File dataFile = SD.open("datalog.txt", FILE_WRITE);

// If the file is available, write dataString to it
  if (dataFile) {
    dataFile.println(dataString);
    dataFile.close();                       // Close the data file
    Serial.println(dataString);             // Print to serial port
   }

// Else, if the file isn't open, display error
  else {
    Serial.println("error opening datalog.txt");
   }
  delay(60000);                             // Delay for 60 seconds
  }
```

References

Abreha, K.B. *et al.* (2022) '*Sorghum* in dryland: morphological, physiological, and molecular responses of sorghum under drought stress', *Planta*. Springer Science and Business Media Deutschland GmbH. Available at: https://doi.org/10.1007/s00425-021-03799-7.

Amann, T. *et al.* (2020) 'Enhanced weathering and related element fluxes – a cropland mesocosm approach', *Biogeosciences*, 17(1), pp. 103–119. Available at: https://doi.org/10.5194/bg-17-103-2020.

Amann, T. and Hartmann, J. (2019) 'Ideas and perspectives: synergies from co-deployment of negative emission technologies', *Biogeosciences*, 16(15), pp. 2949–2960. Available at: https://doi.org/10.5194/bg-16-2949-2019.

Anda, M., Shamshuddin, J. and Fauziah, C.I. (2013) 'Increasing negative charge and nutrient contents of a highly weathered soil using basalt and rice husk to promote cocoa growth under field conditions', *Soil and Tillage Research*, 132, pp. 1–11. Available at: https://doi.org/10.1016/j.still.2013.04.005.

Anda, M., Shamshuddin, J. and Fauziah, C.I. (2015) 'Improving chemical properties of a highly weathered soil using finely ground basalt rocks', *Catena*, 124, pp. 147–161. Available at: https://doi.org/10.1016/j.catena.2014.09.012.

Andrews, M.G. *et al.* (2016) 'Radiogenic and stable Sr isotope ratios (87Sr/86Sr, δ88/86Sr) as tracers of riverine cation sources and biogeochemical cycling in the Milford Sound region of Fiordland, New Zealand', *Geochimica et Cosmochimica Acta*, 173, pp. 284–303. Available at: https://doi.org/10.1016/j.gca.2015.10.005.

Appelo, C.A.J. and Postma, D (2005) *Geochemistry, groundwater and pollution*. 2nd edn. Edited by C.A.J. Appelo and Dieke Postma. London, UK: CRC Press, Taylor & Francis Group.

Aradóttir, E.S.P., Sonnenthal, E.L. and Jónsson, H. (2012) 'Development and evaluation of a thermodynamic dataset for phases of interest in CO_2 mineral sequestration in basaltic rocks', *Chemical Geology*, 304–305, pp. 26–38. Available at: https://doi.org/10.1016/j.chemgeo.2012.01.031.

Archer, D. (2005) ‘Fate of fossil fuel CO_2 in geologic time’, *Journal of Geophysical Research*, 110(C9), p. C09S05. Available at: https://doi.org/10.1029/2004JC002625.

Artyszak, A. (2018) ‘Effect of silicon fertilization on crop yield quantity and quality—A literature review in Europe’, *Plants*. MDPI AG. Available at: https://doi.org/10.3390/plants7030054.

Augé, R.M. (2001) ‘Water relations, drought and vesicular-arbuscular mycorrhizal symbiosis’, *Mycorrhiza*, 11(1), pp. 3–42. Available at: https://doi.org/10.1007/s005720100097.

Azarbad, H. (2022) ‘Conventional vs. Organic Agriculture–Which One Promotes Better Yields and Microbial Resilience in Rapidly Changing Climates?’, *Frontiers in Microbiology*. Frontiers Media S.A. Available at: https://doi.org/10.3389/fmicb.2022.903500.

Banwart, S.A., Berg, A. and Beerling, D.J. (2009) ‘Process-based modeling of silicate mineral weathering responses to increasing atmospheric CO_2 and climate change’, *Global Biogeochemical Cycles*, 23(4), p. n/a-n/a. Available at: https://doi.org/10.1029/2008GB003243.

Bartram, A.K. *et al.* (2014) ‘Exploring links between pH and bacterial community composition in soils from the Craibstone Experimental Farm’, *FEMS Microbiology Ecology*, 87(2), pp. 403–415. Available at: https://doi.org/10.1111/1574-6941.12231.

Beerling, D.J. *et al.* (2018) ‘Farming with crops and rocks to address global climate, food and soil security’, *Nature Plants*, 4(3), pp. 138–147. Available at: https://doi.org/10.1038/s41477-018-0108-y.

Beerling, D.J. *et al.* (2023) ‘Enhanced weathering in the U.S. Corn Belt delivers carbon removal with agronomic benefits’, [Preprint]. Available at: https://arxiv.org/pdf/2307.05343v1.

ten Berge, H.F.M. *et al.* (2012) ‘Olivine weathering in soil, and its effects on growth and nutrient uptake in ryegrass (Lolium perenne L.): a pot experiment’, *PLoS ONE*, 7(8). Available at: https://doi.org/10.1371/journal.pone.0042098.

Berner, E.K., Berner, R.A. and Moulton, K.L. (2003) ‘Plants and Mineral Weathering: Present and Past’, in *Treatise on Geochemistry*. Elsevier, pp. 169–188. Available at: https://doi.org/10.1016/B0-08-043751-6/05175-6.

Berner, R.A., Lasaga, A.C. and Garrels, R.M. (1983) ‘The carbonate-silicate geochemical cycle and its effect on atmospheric carbon dioxide over the past 100 million years’, *American Journal of Science*, 283(7), pp. 641–683. Available at: https://doi.org/10.2475/ajs.283.7.641.

Bide, T.P., Styles, M.T. and Naden, J. (2014) ‘An assessment of global resources of rocks as suitable raw materials for carbon capture and storage by mineralisation’, *Applied Earth Science*, 123(3), pp. 179–195. Available at: https://doi.org/10.1179/1743275814Y.0000000057.

Blanc, P. *et al.* (2012) ‘Thermoddem: A geochemical database focused on low temperature water/rock interactions and waste materials’, *Applied Geochemistry*, 27(10), pp. 2107–2116. Available at: https://doi.org/10.1016/j.apgeochem.2012.06.002.

van Bockhaven, J., de Vleesschauwer, D. and Höfte, M. (2013) ‘Towards establishing broad-spectrum disease resistance in plants: silicon leads the way’, *Journal of Experimental Botany*, 64(5), pp. 1281–1293. Available at: https://doi.org/10.1093/jxb/ers329.

Bolan, N.S., Hedley, M.J. and White, R.E. (1991) ‘Processes of soil acidification during nitrogen cycling with emphasis on legume based pastures’, *Plant and Soil*, 134(1), pp. 53–63. Available at: https://doi.org/10.1007/BF00010717.

Bonfante, P. and Genre, A. (2010) ‘Mechanisms underlying beneficial plant–fungus interactions in mycorrhizal symbiosis’, *Nature Communications*, 1(1), p. 48. Available at: https://doi.org/10.1038/ncomms1046.

Brantley, S.L. and Mellott, N.P. (2000) ‘Surface area and porosity of primary silicate minerals’, *American Mineralogist*, 85(11–12), pp. 1767–1783. Available at: https://doi.org/10.2138/am-2000-11-1220.

Brunauer, S., Emmett, P.H. and Teller, E. (1938) ‘Adsorption of gases in multimolecular layers’, *Journal of the American Chemical Society*, 60(2), pp. 309–319. Available at: https://pubs.acs.org/sharingguidelines.

Bryan, S.E. *et al.* (2002) ‘Silicic volcanism: An undervalued component of large igneous provinces and volcanic rifted margins’, in M.A. Menzies et al. (eds) *Volcanic Rifted Margins*. Boulder, CO: Geological Society of America.

Buckingham, F.L. *et al.* (2022) ‘Soil core study indicates limited CO2 removal by enhanced weathering in dry croplands in the UK’, *Applied Geochemistry*, 147, p. 105482. Available at: https://doi.org/10.1016/j.apgeochem.2022.105482.

Burghelea, C. *et al.* (2015) ‘Mineral nutrient mobilization by plants from rock: influence of rock type and arbuscular mycorrhiza’, *Biogeochemistry*, 124(1–3), pp. 187–203. Available at: https://doi.org/10.1007/s10533-015-0092-5.

Burghelea, C.I. *et al.* (2018) ‘Trace element mobilization during incipient bioweathering of four rock types’, *Geochimica et Cosmochimica Acta*, 234, pp. 98–114. Available at: https://doi.org/10.1016/j.gca.2018.05.011.

Canadell, J.G. *et al.* (2021) ‘2021: Global Carbon and other Biogeochemical Cycles and Feedbacks’, in V., P. Masson-Delmotte et al. (eds) *Climate Change 2021: The Physical Science Basis. Contribution of Working Group I to the Sixth Assessment Report of the Intergovernmental Panel on Climate Change*. Cambridge, UK and New York, NY: Cambridge University Press, pp. 1–144. Available at: https://doi.org/10.1017/9781009157896.007.

Caporaso, J.G. *et al.* (2010) ‘QIIME allows analysis of high-throughput community sequencing data’, *Nature Methods*, pp. 335–336. Available at: https://doi.org/10.1038/nmeth.f.303.

Cempel, M. and Nikel, G. (2006) ‘Nickel: A Review of Its Sources and Environmental Toxicology’, *Polish Journal of Environmental Studies*, 15(3), pp. 375–382.

Chapman, H.D. (1965) ‘Cation-Exchange Capacity’, in A.G. Norman (ed.) *Methods of soil analysis*. Madison, WI: American Society of Agronomy, pp. 891–901. Available at: https://doi.org/10.2134/agronmonogr9.2.c6.

Chen, D. *et al.* (2016) 'Silicon-moderated K-deficiency-induced leaf chlorosis by decreasing putrescine accumulation in sorghum', *Annals of Botany*, 118(2), pp. 305–315. Available at: https://doi.org/10.1093/aob/mcw111.

Churchman G. J. and Lowe, D.J. (2012) 'Alteration, formation, and occurrence of minerals in soils', in P.M. Huang, Y. Li, and M.E. Sumner (eds) *Handbook of Soil Sciences*. 2nd Edition. Boca Raton, FL: CRC Press.

Clarke, L.J. and Jenkyns, H.C. (1999) 'New oxygen isotope evidence for long-term Cretaceous climatic change in the Southern Hemisphere', *Geology*, 27(8), p. 699. Available at: https://doi.org/10.1130/0091-7613(1999)027<0699:NOIEFL>2.3.CO;2.

Colbourn, G., Ridgwell, A. and Lenton, T.M. (2015) 'The time scale of the silicate weathering negative feedback on atmospheric CO2', *Global Biogeochemical Cycles*, 29(5), pp. 583–596. Available at: https://doi.org/10.1002/2014GB005054.

Cordell, D., Drangert, J.-O. and White, S. (2009) 'The story of phosphorus: Global food security and food for thought', *Global Environmental Change*, 19(2), pp. 292–305. Available at: https://doi.org/10.1016/j.gloenvcha.2008.10.009.

Crooks, R. and Prentice, P. (2017) 'Extensive investigation into field based responses to a silica fertiliser', *Silicon*, 9(2), pp. 301–304. Available at: https://doi.org/10.1007/s12633-015-9379-3.

Cuong, T.X. *et al.* (2017) 'Effects of silicon-based fertilizer on growth, yield and nutrient uptake of rice in tropical zone of Vietnam', *Rice Science*, 24(5), pp. 283–290. Available at: https://doi.org/10.1016/j.rsci.2017.06.002.

Das, S. *et al.* (2019) 'Cropping with slag to address soil, environment, and food security', *Frontiers in Microbiology*, 10(1320). Available at: https://doi.org/10.3389/fmicb.2019.01320.

Daval, D. *et al.* (2011) 'Influence of amorphous silica layer formation on the dissolution rate of olivine at 90°C and elevated pCO2', *Chemical Geology*, 284(1–2), pp. 193–209. Available at: https://doi.org/10.1016/j.chemgeo.2011.02.021.

Davidson, E.A. and Janssens, I.A. (2006) 'Temperature sensitivity of soil carbon decomposition and feedbacks to climate change', *Nature*, 440(7081), pp. 165–173. Available at: https://doi.org/10.1038/nature04514.

Debona, D., Rodrigues, F.A. and Datnoff, L.E. (2017) 'Silicon's role in abiotic and biotic plant stresses', *Annual Review of Phytopathology*, 55(1), pp. 85–107. Available at: https://doi.org/10.1146/annurev-phyto-080516.

Department for Energy Security and Net Zero (2023) *2022 UK greenhouse gas emissions, provisional figures*. Available at: https://assets.publishing.service.gov.uk/government/uploads/system/uploads/attachment_data/file/1147372/2022_Provisional_emissions_statistics_report.pdf (Accessed: 31 August 2023).

Department for Environment, Food and Rural Affairs (2022) *Agricultural land use in the United Kingdom*. Available at: https://www.gov.uk/government/statistics/agricultural-land-use-in-the-united-kingdom/agricultural-land-use-in-united-kingdom-at-1-june-2022 (Accessed: 31 August 2023).

Dey, S., Zeeshan Ali, S. and Padhi, E. (2019) 'Terminal fall velocity: the legacy of Stokes from the perspective of fluvial hydraulics', *Proceedings of the Royal Society A: Mathematical, Physical and Engineering Sciences*, 475(2228), p. 20190277. Available at: https://doi.org/10.1098/rspa.2019.0277.

D'Hotman, D. and de Villiers, O. (1961) 'Soil rejuvenation with crushed basalt in Mauritius. Part I – consistent results of world-wide interest', *International Sugar Journal*, 63, pp. 363–364.

Dietzen, C., Harrison, R. and Michelsen-Correa, S. (2018) 'Effectiveness of enhanced mineral weathering as a carbon sequestration tool and alternative to agricultural lime: an incubation experiment', *International Journal of Greenhouse Gas Control*, 74, pp. 251–258. Available at: https://doi.org/10.1016/j.ijggc.2018.05.007.

Dietzen, C. and Rosing, M.T. (2023) 'Quantification of CO2 uptake by enhanced weathering of silicate minerals applied to acidic soils', *International Journal of Greenhouse Gas Control*, 125, p. 103872. Available at: https://doi.org/10.1016/j.ijggc.2023.103872.

Drever, J.L. (1997) *The Geochemistry of Natural Waters: Surface and Groundwater Environments*. 3rd edition. Upper Saddle River, NJ: Prentice Hall.

EASAC (2018) *Negative emission technologies: what role in meeting Paris Agreement targets?* Halle, Germany: European Academies Science Advisory Council. Available at: https://easac.eu/publications/details/easac_net.

Edgar, R.C. (2010) 'Search and clustering orders of magnitude faster than BLAST', *Bioinformatics*, 26(19), pp. 2460–2461. Available at: https://doi.org/10.1093/bioinformatics/btq461.

Edgar, R.C. *et al.* (2011) 'UCHIME improves sensitivity and speed of chimera detection', *Bioinformatics*, 27(16), pp. 2194–2200. Available at: https://doi.org/10.1093/bioinformatics/btr381.

Edwards, D.P. *et al.* (2017) 'Climate change mitigation: potential benefits and pitfalls of enhanced rock weathering in tropical agriculture', *Biology Letters*, 13, 20160715. Available at: https://doi.org/10.1098/rsbl.2016.0715.

ElectronicWings (2017) *Soil moisture sensor interfacing with Arduino UNO*. Available at: https://www.electronicwings.com/arduino/soil-moisture-sensor-interfacing-with-arduino-uno (Accessed: 26 March 2023).

Fajardy, M. *et al.* (2021) 'The economics of bioenergy with carbon capture and storage (BECCS) deployment in a 1.5 °C or 2 °C world', *Global Environmental Change*, 68, p. 102262. Available at: https://doi.org/10.1016/j.gloenvcha.2021.102262.

FAO (2015a) *Acid soils*, *Food and Agriculture Organisation*.

FAO (2015b) *FAOSTAT, Food and Agriculture Organization of the United Nations*. Available at: https://www.fao.org/faostat/en/#home.

FAO (2020) *The state of world fisheries and aquaculture 2020. Sustainability in action*. Rome, Italy: Food and Agriculture Organisation. Available at: https://doi.org/10.4060/ca9229en.

FAO (2022) *Soils for nutrition: state of the art*, *Soils for nutrition: state of the art*. Rome, Italy: Food and Agriculture Organization of the United Nations. Available at: https://doi.org/10.4060/cc0900en.

Flaathen, T.K., Gislason, S.R. and Oelkers, E.H. (2010) ‘The effect of aqueous sulphate on basaltic glass dissolution rates’, *Chemical Geology*, 277(3–4), pp. 345–354. Available at: https://doi.org/10.1016/j.chemgeo.2010.08.018.

Fondriest (2014) *Solar Radiation and Photosynthetically Active Radiation, Fondriest Environmental Learning Centre* . Available at: www.fondriest.com/environmental-measurements/parameters/weather/photosynthetically-active-radiation/.

Fortner, S.K. *et al.* (2012) ‘Silicate weathering and CO_2 consumption within agricultural landscapes, the Ohio-Tennessee River Basin, USA’, *Biogeosciences*, 9(3), pp. 941–955. Available at: https://doi.org/10.5194/bg-9-941-2012.

Friedlingstein, P. *et al.* (2022) ‘Global carbon budget 2022’, *Earth System Science Data*, 14(11), pp. 4811–4900. Available at: https://doi.org/10.5194/essd-14-4811-2022.

Giammar, D.E., Bruant, R.G. and Peters, C.A. (2005) ‘Forsterite dissolution and magnesite precipitation at conditions relevant for deep saline aquifer storage and sequestration of carbon dioxide’, *Chemical Geology*, 217(3–4), pp. 257–276. Available at: https://doi.org/10.1016/j.chemgeo.2004.12.013.

Gillman, G.P. (1980) ‘The Effect of Crushed Basalt Scoria on the Cation Exchange Properties of a Highly Weathered Soil’, *Soil Science Society of America Journal*, 44(3), pp. 465–468. Available at: https://doi.org/10.2136/sssaj1980.03615995004400030005x.

Gislason, S.R. and Oelkers, E.H. (2003) ‘Mechanism, rates, and consequences of basaltic glass dissolution: II. An experimental study of the dissolution rates of basaltic glass as a function of pH and temperature’, *Geochimica et Cosmochimica Acta*, 67(20), pp. 3817–3832. Available at: https://doi.org/10.1016/S0016-7037(00)00176-5.

Gransee, A. and Führs, H. (2013) ‘Magnesium mobility in soils as a challenge for soil and plant analysis, magnesium fertilization and root uptake under adverse growth conditions’, *Plant and Soil*, 368(1–2), pp. 5–21. Available at: https://doi.org/10.1007/s11104-012-1567-y.

Gruber, N. *et al.* (2019) 'The oceanic sink for anthropogenic CO2 from 1994 to 2007', *Science*, 363(6432), pp. 1193–1199. Available at: https://doi.org/10.1126/science.aau5153.

Guntzer, F., Keller, C. and Meunier, J.D. (2012) 'Benefits of plant silicon for crops: a review', *Agronomy for Sustainable Development*, 32(1), pp. 201–213. Available at: https://doi.org/10.1007/s13593-011-0039-8.

Hancock, P.L. and Skinner, B.J. (eds) (2000) *The Oxford Companion to the Earth*. Oxford University Press. Available at: https://doi.org/10.1093/acref/9780198540397.001.0001.

Hao, X. and Chang, C. (2002) 'Effect of 25 annual cattle manure applications on soluble and exchangeable cations in soil', *Soil Science*, 167(2), pp. 126–134. Available at: https://doi.org/10.1097/00010694-200202000-00005.

Haque, F. *et al.* (2019) 'Co-benefits of wollastonite weathering in agriculture: CO_2 sequestration and promoted plant growth', *ACS Omega*, 4(1), pp. 1425–1433. Available at: https://doi.org/10.1021/acsomega.8b02477.

Hartmann, J. *et al.* (2009) 'Global CO2-consumption by chemical weathering: What is the contribution of highly active weathering regions?', *Global and Planetary Change*, 69(4), pp. 185–194. Available at: https://doi.org/10.1016/j.gloplacha.2009.07.007.

Hartmann, J. *et al.* (2013) 'Enhanced chemical weathering as a geoengineering strategy to reduce atmospheric carbon dioxide, supply nutrients, and mitigate ocean acidification', *Reviews of Geophysics*, 51(2), pp. 113–149. Available at: https://doi.org/10.1002/rog.20004.

Harvey, L.D.D. (2008) 'Mitigating the atmospheric CO2 increase and ocean acidification by adding limestone powder to upwelling regions', *Journal of Geophysical Research*, 113(C4), p. C04028. Available at: https://doi.org/10.1029/2007JC004373.

Hata, S., Kobae, Y. and Banba, M. (2010) 'Interactions Between Plants and Arbuscular Mycorrhizal Fungi', in, pp. 1–48. Available at: https://doi.org/10.1016/S1937-6448(10)81001-9.

Hausfather, Z. and Peters, G.P. (2020) ‘Emissions – the “business as usual” story is misleading’, *Nature*, 577(7792), pp. 618–620. Available at: https://doi.org/10.1038/d41586-020-00177-3.

Hayashi, M. (2004) ‘Temperature-Electrical Conductivity Relation of Water for Environmental Monitoring and Geophysical Data Inversion’, *Environmental Monitoring and Assessment*, 96(1–3), pp. 119–128. Available at: https://doi.org/10.1023/B:EMAS.0000031719.83065.68.

Haynes, R.J. (2017) ‘Significance and role of Si in crop production’, *Advances in Agronomy*, 146, pp. 83–166. Available at: https://doi.org/10.1016/bs.agron.2017.06.001.

Hellenbrandt, M. (2004) ‘The inorganic crystal structure database (ICSD) - Present and future’, in *Crystallography Reviews*, pp. 17–22. Available at: https://doi.org/10.1080/08893110410001664882.

Hénault, C. *et al.* (2019) ‘Management of soil pH promotes nitrous oxide reduction and thus mitigates soil emissions of this greenhouse gas’, *Scientific Reports*, 9(1), p. 20182. Available at: https://doi.org/10.1038/s41598-019-56694-3.

Hindumathi, A. and Reddy, B.N. (2011) ‘Dependency of Sorghum on arbuscular mycorrhizal colonization for growth and development’, *Journal of Mycology and Plant Pathology*, 41(4), pp. 537–542. Available at: https://www.researchgate.net/publication/308320439.

Hoffland, E. *et al.* (2004) ‘The role of fungi in weathering’, *Frontiers in Ecology and the Environment*, 2(5), pp. 258–264. Available at: https://doi.org/10.1890/1540-9295(2004)002[0258:TROFIW]2.0.CO;2.

Högberg, M.N. and Högberg, P. (2002) ‘Extramatrical ectomycorrhizal mycelium contributes one-third of microbial biomass and produces, together with associated roots, half the dissolved organic carbon in a forest soil’, *New Phytologist*, 154(3), pp. 791–795. Available at: https://doi.org/10.1046/j.1469-8137.2002.00417.

ICL (2015) *Glossary: Basalt*, *Imperial College Rock Library*. Available at: https://www.imperial.ac.uk/earth-science/current-student-staff-info/rl/.

IEA (2022) ‘Direct Air Capture’, in. Paris, France: International Energy Agency. Available at: https://www.iea.org/reports/direct-air-capture.

Ihrmark, K. *et al.* (2012) ‘New primers to amplify the fungal ITS2 region - evaluation by 454-sequencing of artificial and natural communities’, *FEMS Microbiology Ecology*, 82(3), pp. 666–677. Available at: https://doi.org/10.1111/j.1574-6941.2012.01437.x.

IPCC (1990) *Scientific assessment of climate change*. Geneva, Switzerland. Available at: https://www.ipcc.ch/site/assets/uploads/2018/05/ipcc_90_92_assessments_far_full_report.pdf.

IPCC (2007) *Climate Change 2007: The Physical Science Basis. Contribution of Working Group I to the Fourth Assessment Report of the Intergovernmental Panel on Climate Change*. Edited by S. Solomon et al. Cambridge, United Kingdom: . Cambridge University Press.

IPCC (2021) *Climate Change 2021: The Physical Science Basis. Contribution of Working Group to the Sixth Assessment Report of the Intergovernmental Panel on Climate Change*. Edited by V. Masson-Delmotte et al. Cambridge, UK and New York, NY: Cambridge University Press. Available at: https://doi.org/10.1017/9781009157896.

IPCC (2022) *Climate Change 2022: Impacts, Adaptation and Vulnerability. Contribution of Working Group II to the Sixth Assessment Report of the Intergovernmental Panel on Climate Change*. Edited by H.-O. Pörtner et al. Cambridge, UK and New York, NY: Cambridge University Press.

Jagadamma, S. *et al.* (2014) ‘Sorption of organic carbon compounds to the fine fraction of surface and subsurface soils’, *Geoderma*, 213, pp. 79–86. Available at: https://doi.org/10.1016/j.geoderma.2013.07.030.

Jin, X., Cao, L. and Zhang, J. (2022) ‘Effects of solar radiation modification on the ocean carbon cycle: An earth system modeling study’, *Atmospheric and Oceanic Science Letters*, 15(3), p. 100187. Available at: https://doi.org/10.1016/j.aosl.2022.100187.

Kaiser, K. and Zech, W. (2000) ‘Dissolved organic matter sorption by mineral constituents of subsoil clay fractions’, *Journal of Plant Nutrition and Soil Science*, 163(5), pp. 531–535. Available at: https://doi.org/10.1002/1522-2624(200010)163:5<531::AID-JPLN531>3.0.CO;2-N.

Kantola, I.B. *et al.* (2017) ‘Potential of global croplands and bioenergy crops for climate change mitigation through deployment for enhanced weathering’, *Biology Letters*, 13, 20160714. Available at: https://doi.org/10.1098/rsbl.2016.0714.

Keenan, T.F. and Williams, C.A. (2018) ‘The Terrestrial Carbon Sink’, *Annual Review of Environment and Resources*, 43(1), pp. 219–243. Available at: https://doi.org/10.1146/annurev-environ-102017-030204.

Kelemen, P.B. and Matter, J. (2008) ‘In situ carbonation of peridotite for CO2 storage’, *Proceedings of the National Academy of Sciences*, 105(45), pp. 17295–17300. Available at: https://doi.org/10.1073/pnas.0805794105.

Kelland, M.E. (2015) *The importance of bio-geoengineering in avoiding dangerous climate change and less-desirable climate intervention measures*. Master’s thesis [Unpublished]. Open University.

Kelland, M.E. *et al.* (2020) ‘Increased yield and CO_2 sequestration potential with the C_4 cereal Sorghum bicolor cultivated in basaltic rock dust-amended agricultural soil’, *Global Change Biology*, 26(6), pp. 3658–3676. Available at: https://doi.org/10.1111/gcb.15089.

Kelly, S.P. (2003) ‘Biogeochemical cycles’, in P.W. Skelton (ed.) *The Cretaceous World*. New York. NY: Cambridge University Press, pp. 185–207.

Kemp, S.J. *et al.* (2016) *An Improved Approach to Characterize Potash-Bearing Evaporite Deposits, Evidenced in North Yorkshire, United Kingdom*, *Economic Geology*. Available at: http://pubs.geoscienceworld.org/segweb/economicgeology/article-pdf/111/3/719/3474002/719-742.pdf.

Kennett, J.P. and Stott, L.D. (1991) ‘Abrupt deep-sea warming, palaeoceanographic changes and benthic extinctions at the end of the Palaeocene’, *Nature*, 353(6341), pp. 225–229. Available at: https://doi.org/10.1038/353225a0.

Kiehl, J.T. and Trenberth, K.E. (1997) ‘Earth’s Annual Global Mean Energy Budget’, *Bulletin of the American Meteorological Society*, 78, pp. 197–208. Available at: https://doi.org/10.1175/1520-0477(1997)078<0197:EAGMEB>2.0.CO;2.

Kim, H.K. *et al.* (2010) ‘Regulation of tillering in sorghum: Environmental effects’, *Annals of Botany*, 106(1), pp. 57–67. Available at: https://doi.org/10.1093/aob/mcq079.

Kirchner, J. (2001) *Data Analysis Toolkit #5: Uncertainty Analysis and Error Propagation*. Berkeley CA. Available at: http://seismo.berkeley.edu/~kirchner/eps_120/Toolkits/Toolkit_05.pdf.

Kleczewski, N.M., Lewandowski, D. and Bonello, P. (2008) *Mycorrhizae in Urban Landscapes*. Columbus, OH. Available at: https://ohioline.osu.edu/factsheet/plpath-tree-01.

Knapp, W.J. and Tipper, E.T. (2022) ‘The efficacy of enhancing carbonate weathering for carbon dioxide sequestration’, *Frontiers in Climate*, 4. Available at: https://doi.org/10.3389/fclim.2022.928215.

Koch, P.L., Zachos, J.C. and Gingerich, P.D. (1992) ‘Correlation between isotope records in marine and continental carbon reservoirs near the Palaeocene/Eocene boundary’, *Nature*, 358(6384), pp. 319–322. Available at: https://doi.org/10.1038/358319a0.

Kochian, L. (2014) *Science enlists nature and collaboration to ‘neutralise’ acidic soils* . Available at: http://blog.generationcp.org/2014/07/23/science-enlists-nature-and-collaboration-to-neutralise-acidic-soils/.

Koele, N. *et al.* (2014) ‘Ecological significance of mineral weathering in ectomycorrhizal and arbuscular mycorrhizal ecosystems from a field-based comparison’, *Soil Biology and Biochemistry*, 69, pp. 63–70. Available at: https://doi.org/10.1016/j.soilbio.2013.10.041.

Köhler, P., Hartmann, J. and Wolf-Gladrow, D.A. (2010) ‘Geoengineering potential of artificially enhanced silicate weathering of olivine’, *Proceedings of the National Academy of Sciences*, 107(47), pp. 20228–20233. Available at: https://doi.org/10.1073/pnas.1000545107.

Köhler, P., Hartmann, J. and Wolf-Gladrow, Dieter A (2010) ‘Geoengineering potential of artificially enhanced silicate weathering of olivine’, *Proceedings of the National Academy of Sciences of the United States of America*, 107(47), pp. 20228–20233. Available at: https://doi.org/10.1073/pnas.1000545107.

Korchagin, J., Caner, L. and Bortoluzzi, E.C. (2019) ‘Variability of amethyst mining waste: A mineralogical and geochemical approach to evaluate the potential use in agriculture’, *Journal of Cleaner Production*, 210, pp. 749–758. Available at: https://doi.org/10.1016/j.jclepro.2018.11.039.

Korndörfer, G.H. *et al.* (2001) ‘Calibration of soil and plant silicon analysis for rice production’, *Journal of Plant Nutrition*, 24(7), pp. 1071–1084. Available at: https://doi.org/10.1081/PLN-100103804.

Lafarge, T.A. and Hammer, G.L. (2002) ‘Tillering in grain sorghum over a wide range of population densities: Modelling dynamics of tiller fertility’, *Annals of Botany*, 90(1), pp. 99–110. Available at: https://doi.org/10.1093/aob/mcf153.

Landeweert, R. *et al.* (2001) ‘Linking plants to rocks: ectomycorrhizal fungi mobilize nutrients from minerals’, *Trends in Ecology & Evolution*, 16(5), pp. 248–254. Available at: https://doi.org/10.1016/S0169-5347(01)02122-X.

Leake, J. *et al.* (2004) ‘Networks of power and influence: the role of mycorrhizal mycelium in controlling plant communities and agroecosystem functioning’, *Canadian Journal of Botany*, 82(8), pp. 1016–1045. Available at: https://doi.org/10.1139/b04-060.

Leake, J.R. *et al.* (2008) ‘Biological weathering in soil: the role of symbiotic root-associated fungi biosensing minerals and directing photosynthate-energy into grain-scale mineral weathering’, *Mineralogical Magazine*, 72(1), pp. 85–89. Available at: https://doi.org/10.1180/minmag.2008.072.1.85.

Lean, J.L. (2018) ‘Estimating Solar Irradiance Since 850 CE’, *Earth and Space Science*, 5(4), pp. 133–149. Available at: https://doi.org/10.1002/2017EA000357.

Lenton, T.M. and Vaughan, N.E. (2009) ‘The radiative forcing potential of different climate geoengineering options’, *Atmospheric Chemistry and Physics*, 9(15), pp. 5539–5561. Available at: https://doi.org/10.5194/acp-9-5539-2009.

Lewis, A.L. *et al.* (2021) 'Effects of mineralogy, chemistry and physical properties of basalts on carbon capture potential and plant-nutrient element release via enhanced weathering', *Applied Geochemistry*, 132. Available at: https://doi.org/10.1016/j.apgeochem.2021.105023.

Li, Z. *et al.* (2018) 'Silicon enhancement of estimated plant biomass carbon accumulation under abiotic and biotic stresses. A meta-analysis', *Agronomy for Sustainable Development*. Springer-Verlag France. Available at: https://doi.org/10.1007/s13593-018-0496-4.

Lienhard, J.H. (2000) *No. 1776: CARBON DIOXIDE, Engines of Our Ingenuity*. Available at: https://uh.edu/engines/epi1776.htm.

De Lima, D.T. *et al.* (2019) 'Silicon accumulation and its effect on agricultural traits and anthracnose incidence in lignocellulosic sorghum', *Pesquisa Agropecuaria Tropical*, 49. Available at: https://doi.org/10.1590/1983-40632019v4954201.

Lithos (2023) *About*. Available at: https://www.lithoscarbon.com/about (Accessed: 25 March 2023).

Liu, J. *et al.* (2017) 'Silicon supplementation alters the composition of herbivore induced plant volatiles and enhances attraction of parasitoids to infested rice plants', *Frontiers in Plant Science*, 8. Available at: https://doi.org/10.3389/fpls.2017.01265.

Ma, J.F. (2004) 'Role of silicon in enhancing the resistance of plants to biotic and abiotic stresses', *Soil Science and Plant Nutrition*, 50(1), pp. 11–18. Available at: https://doi.org/10.1080/00380768.2004.10408447.

Ma, J.F. and Yamaji, N. (2006) 'Silicon uptake and accumulation in higher plants', *Trends in Plant Science*, pp. 392–397. Available at: https://doi.org/10.1016/j.tplants.2006.06.007.

Maggio, A. *et al.* (2012) *NPK: Will there be enough plant nutrients to feed a world of 9 billion in 2050*. Brussels, Belgium: European Commission.

Mahendran, P.P. *et al.* (2021) 'Identifying critical limit in soil and plant for determining response of rice (*Oryza Sativa* L.) to silicon application in Periyar Vaigai command area of Tamil Nadu, India', *Phosphorus, Sulfur, and Silicon and the*

Related Elements, 196(2), pp. 146–154. Available at: https://doi.org/10.1080/10426507.2020.1818240.

Majaneva, M. *et al.* (2015) 'Bioinformatic amplicon read processing strategies strongly affect eukaryotic diversity and the taxonomic composition of communities', *PLoS ONE*, 10(6). Available at: https://doi.org/10.1371/journal.pone.0130035.

Malik, A.A. *et al.* (2018) 'Land use driven change in soil pH affects microbial carbon cycling processes', *Nature Communications*, 9(1). Available at: https://doi.org/10.1038/s41467-018-05980-1.

Manning, D.A.C. *et al.* (2013) 'Carbonate precipitation in artificial soils produced from basaltic quarry fines and composts: an opportunity for passive carbon sequestration', *International Journal of Greenhouse Gas Control*, 17, pp. 309–317. Available at: https://doi.org/10.1016/j.ijggc.2013.05.012.

Max Planck Institute for Chemistry (2015) *Geochemistry of Rocks of the Oceans and Continents, Geochemistry of Rocks of the Oceans and Continents*. Available at: http://georoc.mpch-mainz.gwdg.de/georoc/Start.asp.

McQueen, N. *et al.* (2021) 'A review of direct air capture (DAC): Scaling up commercial technologies and innovating for the future', *Progress in Energy*. Institute of Physics. Available at: https://doi.org/10.1088/2516-1083/abf1ce.

Meena, V.D. *et al.* (2014) 'A case for silicon fertilization to improve crop yields in tropical soils', *Proceedings of the National Academy of Sciences India Section B - Biological Sciences*. Springer India, pp. 505–518. Available at: https://doi.org/10.1007/s40011-013-0270-y.

Meharg, C. and Meharg, A.A. (2015) 'Silicon, the silver bullet for mitigating biotic and abiotic stress, and improving grain quality, in rice?', *Environmental and Experimental Botany*. Elsevier, pp. 8–17. Available at: https://doi.org/10.1016/j.envexpbot.2015.07.001.

Mitchell, M.J. *et al.* (2010) 'A model of carbon dioxide dissolution and mineral carbonation kinetics', *Proceedings of the Royal Society A: Mathematical, Physical and Engineering Sciences*, 466(2117), pp. 1265–1290. Available at: https://doi.org/10.1098/rspa.2009.0349.

Montgomery, D.R. and Biklé, A. (2021) ‘Soil Health and Nutrient Density: Beyond Organic vs. Conventional Farming’, *Frontiers in Sustainable Food Systems*. Frontiers Media S.A. Available at: https://doi.org/10.3389/fsufs.2021.699147.

Moosdorf, N., Renforth, P. and Hartmann, J. (2014) ‘Carbon dioxide efficiency of terrestrial enhanced weathering’, *Environmental Science and Technology*, 48(9), pp. 4809–4816. Available at: https://doi.org/10.1021/es4052022.

Muller, A. *et al.* (2017) ‘Strategies for feeding the world more sustainably with organic agriculture’, *Nature Communications*, 8(1), p. 1290. Available at: https://doi.org/10.1038/s41467-017-01410-w.

Myhre, G., *et al.* (2013) ‘Anthropogenic and natural radiative forcing’, in T.F. Stocker et al. (eds) *Climate Change 2013: The Physical Science Basis. Contribution of Working Group I to the Fifth Assessment Report of the Intergovernmental Panel on Climate Change*. Cambridge, UK: Cambridge University Press, pp. 659–740.

Mylonas, I. *et al.* (2020) ‘Better farming practices to combat climate change’, in *Climate Change and Food Security with Emphasis on Wheat*. Elsevier, pp. 1–29. Available at: https://doi.org/10.1016/B978-0-12-819527-7.00001-7.

Nan, W. *et al.* (2016) ‘The factors related to carbon dioxide effluxes and production in the soil profiles of rain-fed maize fields’, *Agriculture, Ecosystems and Environment*, 216, pp. 177–187. Available at: https://doi.org/10.1016/j.agee.2015.09.032.

Navarre-Sitchler, A. and Brantley, S. (2007) ‘Basalt weathering across scales’, *Earth and Planetary Science Letters*, 261(1–2), pp. 321–334. Available at: https://doi.org/10.1016/j.epsl.2007.07.010.

Neina, D. (2019) ‘The Role of Soil pH in Plant Nutrition and Soil Remediation’, *Applied and Environmental Soil Science*, 2019, pp. 1–9. Available at: https://doi.org/10.1155/2019/5794869.

Nesbitt, H.W. and Young, G.M. (1982) ‘Early Proterozoic climates and plate motions inferred from major element chemistry of lutites’, *Nature*, 299(5885), pp. 715–717. Available at: https://doi.org/10.1038/299715a0.

Nilsson, R.H. *et al.* (2019) 'The UNITE database for molecular identification of fungi: Handling dark taxa and parallel taxonomic classifications', *Nucleic Acids Research*, 47(D1), pp. D259–D264. Available at: https://doi.org/10.1093/nar/gky1022.

NOAA (2023) *Trends in Atmospheric Carbon Dioxide, Global Monitoring Laboratory*. Available at: https://gml.noaa.gov/ccgg/trends/ (Accessed: 28 March 2023).

NRC (2015) *Climate intervention: carbon dioxide removal and reliable sequestration*. Washington, DC: The National Academies Press. Available at: https://doi.org/10.17226/18805.

O'Mara, F.P. (2012) 'The role of grasslands in food security and climate change', *Annals of Botany*, 110(6), pp. 1263–1270. Available at: https://doi.org/10.1093/aob/mcs209.

Organics International (2018) *The World of Organic Agriculture Statistics and Trends 2018*. 18th edn. Edited by H. Willer and J. Lernoud. Bonn, Germany: Research Institute of Organic Agriculture, Organic International.

Palandri, J.L. and Kharaka, Y.K. (2004) *A compilation of rate parameters of water-mineral interaction kinetics for application to geochemical modeling*. Menlo Park, CA: US Geological Survey.

Panhwar, Q.A. *et al.* (2019) 'Fertilizer Management Strategies for Enhancing Nutrient Use Efficiency and Sustainable Wheat Production', in *Organic Farming*. Elsevier, pp. 17–39. Available at: https://doi.org/10.1016/B978-0-12-813272-2.00002-1.

Parkhurst, D. and Appelo, C. (2013) 'Description of Input and Examples for PHREEQC Version 3-A Computer Program for Speciation, Batch-Reaction, One-Dimensional Transport, and Inverse Geochemical Calculations', in *US Geological Survey Techniques and Methods*. Denver, CO : US Geological Survey, pp. 1–497. Available at: http://www.hydrochemistry.eu.

Paustian, K. *et al.* (2016) 'Climate-smart soils', *Nature*. Nature Publishing Group, pp. 49–57. Available at: https://doi.org/10.1038/nature17174.

Paye, W. *et al.* (2018) 'Determination of Critical Soil Silicon Levels for Rice Production in Louisiana Using Different Extraction Procedures', *Communications in Soil Science and Plant Analysis*, 49(17), pp. 2091–2102. Available at: https://doi.org/10.1080/00103624.2018.1495731.

Penman, D.E. *et al.* (2020) 'Silicate weathering as a feedback and forcing in Earth's climate and carbon cycle', *Earth-Science Reviews*, 209, p. 103298. Available at: https://doi.org/10.1016/j.earscirev.2020.103298.

Pétriacq, P. *et al.* (2017) 'Metabolite profiling of non-sterile rhizosphere soil', *Plant Journal*, 92(1), pp. 147–162. Available at: https://doi.org/10.1111/tpj.13639.

Potter, P. *et al.* (2010) 'Characterizing the spatial patterns of global fertilizer application and manure production', *Earth Interactions*, 14(2), pp. 1–22. Available at: https://doi.org/10.1175/2009EI288.1.

Poux, X. and Aubert, P.-M. (2018) *An agroecological Europe in 2050: multifunctional agriculture for healthy eating*. Paris, France: Institute for Sustainable Development and International Relations. Available at: www.iddri.org.

Pruyne, D.T., Schlossberg, M.J. and Uddin, W. (2019) 'Perennial Ryegrass Wear Resistance and Soil Amendment by Ca- and Mg-Silicates', *Agronomy*, 9(10), p. 578. Available at: https://doi.org/10.3390/agronomy9100578.

Quirk, J. *et al.* (2012) 'Evolution of trees and mycorrhizal fungi intensifies silicate mineral weathering', *Biology Letters*, 8(6), pp. 1006–1011. Available at: https://doi.org/10.1098/rsbl.2012.0503.

Quirk, J. *et al.* (2014) 'Ectomycorrhizal fungi and past high CO2 atmospheres enhance mineral weathering through increased below-ground carbon-energy fluxes', *Biology Letters*, 10(7). Available at: https://doi.org/10.1098/rsbl.2014.0375.

Reershemius, T. *et al.* (2023) 'Initial validation of a soil-based mass-balance approach for empirical monitoring of enhanced rock weathering rates', [Preprint]. Available at: https://doi.org/10.48550/arXiv.2302.05004.

Reidinger, S., Ramsey, M.H. and Hartley, S.E. (2012) 'Rapid and accurate analyses of silicon and phosphorus in plants using a portable X-ray fluorescence spectrometer',

New Phytologist, 195(3), pp. 699–706. Available at: https://doi.org/10.1111/j.1469-8137.2012.04179.x.

Renforth, P. (2012) 'The potential of enhanced weathering in the UK', *International Journal of Greenhouse Gas Control*, 10, pp. 229–243. Available at: https://doi.org/10.1016/j.ijggc.2012.06.011.

Renforth, P. (2019) 'The negative emission potential of alkaline materials', *Nature Communications*, 10, 1401. Available at: https://doi.org/10.1038/s41467-019-09475-5.

Renforth, P. and Henderson, G. (2017) 'Assessing ocean alkalinity for carbon sequestration', *Reviews of Geophysics*, 55(3), pp. 636–674. Available at: https://doi.org/10.1002/2016RG000533.

Renforth, P., Pogge von Strandmann, P.A.E. and Henderson, G.M. (2015) 'The dissolution of olivine added to soil: implications for enhanced weathering', *Applied Geochemistry*, 61, pp. 109–118. Available at: https://doi.org/10.1016/j.apgeochem.2015.05.016.

Rice, J.R. (1973) *A physiological study of the flag leaf and developing grain of four grain sorghum lines*. Texas Tech University.

Rimstidt, J.D. (2014) *Geochemical rate models: an introduction to geochemical kinetics*. New York, NY: Cambridge University Press.

Romero-Mujalli, G. *et al*. (2019) 'Ecosystem controlled soil-rock pCO_2 and carbonate weathering – Constraints by temperature and soil water content', *Chemical Geology*, 527, 118634. Available at: https://doi.org/10.1016/j.chemgeo.2018.01.030.

Roques, S. *et al.* (2012) *A review of the non-NPKS nutrient requirements of UK cereals and oilseed rape*. Kenilworth, UK. Available at: https://ahdb.org.uk/a-review-of-the-non-npks-nutrient-requirements-of-uk-cereals-and-oilseed-rape.

Roques, S. *et al.* (2013) *Review of the non-NPKS nutrient requirements of UK cereals and oilseed rape*. Kenilworth, UK: Agricultural and Horticultural Development Board. Available at: https://www.researchgate.net/publication/277669269.

Rosling, A., Lindahl, B.D. and Finlay, R.D. (2004) 'Carbon allocation to ectomycorrhizal roots and mycelium colonising different mineral substrates', *New*

Phytologist, 162(3), pp. 795–802. Available at: https://doi.org/10.1111/j.1469-8137.2004.01080.x.

Sanna, A. *et al.* (2014) 'A review of mineral carbonation technologies to sequester CO2', *Chem. Soc. Rev.*, 43(23), pp. 8049–8080. Available at: https://doi.org/10.1039/C4CS00035H.

van Schöll, L. *et al.* (2008) 'Rock-eating mycorrhizas: their role in plant nutrition and biogeochemical cycles', *Plant and Soil*, 303(1–2), pp. 35–47. Available at: https://doi.org/10.1007/s11104-007-9513-0.

Schuiling, R.D. and De Boer, P.L. (2011) 'Fast weathering of olivine in shallow seas Earth System Dynamics Discussions Rolling stones; fast weathering of olivine in shallow seas for cost-effective CO 2 capture and mitigation of global warming and ocean acidification Fast weathering of olivine in shallow seas', *Earth Syst. Dynam. Discuss*, 2, pp. 551–568. Available at: https://doi.org/10.5194/esdd-2-551-2011.

Schuiling, R.D. and Krijgsman, P. (2006) 'Enhanced Weathering: An Effective and Cheap Tool to Sequester Co2', *Climatic Change*, 74(1–3), pp. 349–354. Available at: https://doi.org/10.1007/s10584-005-3485-y.

Schuiling, R.D. and Tickell, O. (2010) 'Enhanced weathering of olivine to capture CO2', *Journal of Applied Geochemistry*, 12(4), pp. 510–519.

Seufert, V., Ramankutty, N. and Foley, J.A. (2012) 'Comparing the yields of organic and conventional agriculture', *Nature*, 485(7397), pp. 229–232. Available at: https://doi.org/10.1038/nature11069.

Shackley, S. *et al.* (2011) 'The feasibility and costs of biochar deployment in the UK', *Carbon Management*, pp. 335–356. Available at: https://doi.org/10.4155/cmt.11.22.

Shanker, A. *et al.* (2005) 'Chromium toxicity in plants', *Environment International*, 31(5), pp. 739–753. Available at: https://doi.org/10.1016/j.envint.2005.02.003.

Shepherd, J. *et al.* (2009) *Geoengineering the climate: science, governance & uncertainty*. London, UK. Available at: https://royalsociety.org/-/media/Royal_Society_Content/policy/publications/2009/8693.pdf.

Sintorini *et al.* (2021) ‘Effect of pH on metal mobility in the soil’, *IOP Conference Series: Earth and Environmental Science*, 737(1), p. 012071. Available at: https://doi.org/10.1088/1755-1315/737/1/012071.

Sintorini, M.M. *et al.* (2021) ‘Effect of pH on metal mobility in the soil’, in *IOP Conference Series: Earth and Environmental Science*. Institute of Physics. Available at: https://doi.org/10.1088/1755-1315/737/1/012071.

Smith, G.A. and Hayman, G.A. (1987) *Geologic map of the Eagle Butte and Gateway quadrangles, Jefferson and Wasco Counties, Oregon. 1:24,000. Geological Map Series 43.*

Smith, P. *et al.* (2019) ‘Land-management options for greenhouse gas removal and their impacts on ecosystem services and the sustainable development goals’, *Annual Review of Environment and Resources*, 44(1), pp. 255–287. Available at: https://doi.org/10.1146/annurev-environ-101718-033129.

Smith, S.E. and Read, D.J. (2008) *Mycorrhizal Symbiosis*. 3rd edition. New York, NY: Elsevier Ltd.

Smits, M.M. *et al.* (2012) ‘Plant-driven weathering of apatite - the role of an ectomycorrhizal fungus’, *Geobiology*, 10(5), pp. 445–456. Available at: https://doi.org/10.1111/j.1472-4669.2012.00331.x.

Soil Association (2021) *Soil Association Standards Farming and growing*. Bristol, UK: The Soil Association.

Stamboliadis, E., Pantelaki, O. and Petrakis, E. (2009) ‘Surface area production during grinding’, *Minerals Engineering*, 22(7–8), pp. 587–592. Available at: https://doi.org/10.1016/j.mineng.2008.12.001.

van Straaten, P. (2006) ‘Farming with rocks and minerals: challenges and opportunities’, *Annals of the Brazilian Academy of Sciences*, 78(4), pp. 731–747. Available at: https://doi.org/10.1590/S0001-37652006000400009.

Strefler, J. *et al.* (2018) ‘Potential and costs of carbon dioxide removal by enhanced weathering of rocks’, *Environmental Research Letters*, 13, 034010. Available at: https://doi.org/10.1088/1748-9326/aaa9c4.

Tavakkoli, E., Rengasamy, P. and McDonald, G.K. (2010) 'High concentrations of Na+ and Cl– ions in soil solution have simultaneous detrimental effects on growth of faba bean under salinity stress', *Journal of Experimental Botany*, 61(15), pp. 4449–4459. Available at: https://doi.org/10.1093/jxb/erq251.

Taylor, L.L. *et al.* (2016) 'Enhanced weathering strategies for stabilizing climate and averting ocean acidification', *Nature Climate Change*, 6(4), pp. 402–406. Available at: https://doi.org/10.1038/nclimate2882.

Taylor, L.L. *et al.* (2021) 'Increased carbon capture by a silicate-treated forested watershed affected by acid deposition', *Biogeosciences*, 18(1), pp. 169–188. Available at: https://doi.org/10.5194/bg-18-169-2021.

Theimer, T.C. and Gehring, C.A. (2007) 'Mycorrhizal plants and vertebrate seed and spore dispersal: incorporating mycorrhizas into the seed dispersal paradigm', in A.J. Dennis et al. (eds) *Seed dispersal: theory and its application in a changing world*. UK: CABI. Available at: https://doi.org/10.1079/9781845931650.0000.

Thorley, R.M.S. *et al.* (2015) 'The role of forest trees and their mycorrhizal fungi in carbonate rock weathering and its significance for global carbon cycling', *Plant, Cell & Environment*, 38(9), pp. 1947–1961. Available at: https://doi.org/10.1111/pce.12444.

Tipping, E. (1998) 'Humic ion-binding model VI: an improved description of the interactions of protons and metal ions with humic substances', *Aquatic Geochemistry*, 4, pp. 3–48.

Tipping, E. and Hurley, M.A. (1992) 'A unifying model of cation binding by humic substances', *Geochimica et Cosmochimica Acta*, 56(10), pp. 3627–3641.

Le Treut, H. *et al.* (2007) 'Historical Overview of Climate Change', in S. Solomon et al. (eds) *Climate Change 2007: The Physical Science Basis. Contribution of Working Group I to the Fourth Assessment Report of the Intergovernmental Panel on Climate Change*. Cambridge, UK: Cambridge University Press.

Tubana, B.S., Babu, T. and Datnoff, L.E. (2016) 'A review of silicon in soils and plants and its role in US agriculture', *Soil Science*, 181(9/10), pp. 393–411. Available at: https://doi.org/10.1097/SS.0000000000000179.

Turhollow, A.F., Webb, E.G. and Downing, M.P. (2010) *Review of sorghum production practices: applications for bioenergy*. Oak Ridge, TN: US Department of Energy. Available at: http://www.osti.gov/contact.html.

UKCEH (2021) *UKCEH Land Cover Maps*. Available at: https://www.ceh.ac.uk/data/ukceh-land-cover-maps.

UKSO (2007) *UKSO Map Viewer*. Available at: https://mapapps2.bgs.ac.uk/ukso/home.html?layer=CEHTSPH.

UNDO (2023) *Our Story*. Available at: https://un-do.com/our-story (Accessed: 25 March 2023).

UNEP (2018) *The emissions gap report 2018*. Nairobi, Kenya: United Nations Environment Programme. Available at: https://www.unep.org/resources/emissions-gap-report-2018.

UNFCCC (2015) *The Paris Agreement*. Paris, France: United Nations Framework Convention on Climate Change. Available at: https://unfccc.int/process/conferences/pastconferences/paris-climate-change-conference-november-2015/paris-agreement.

USDA-NRCS (1999) *Soil Taxonomy*. 2nd Edition. Washington, DC: USDA-NRCS.

Vengadaramana, A., Jashothan, J. and Thairiyanathan, P. (2019) *Effect of organic fertilizers on the water holding capacity of soil in different terrains of Jaffna peninsula in Sri Lanka*. Available at: https://www.researchgate.net/publication/259900746.

Verbruggen, E. *et al.* (2010) 'Positive effects of organic farming on below-ground mutualists: Large-scale comparison of mycorrhizal fungal communities in agricultural soils', *New Phytologist*, 186(4), pp. 968–979. Available at: https://doi.org/10.1111/j.1469-8137.2010.03230.x.

Vienne, A. *et al.* (2022) 'Enhanced Weathering Using Basalt Rock Powder: Carbon Sequestration, Co-benefits and Risks in a Mesocosm Study With Solanum tuberosum', *Frontiers in Climate*, 4. Available at: https://doi.org/10.3389/fclim.2022.869456.

West, L.J. *et al.* (2023) ‘Making mistakes in estimating the CO_2 sequestration potential of UK croplands with enhanced weathering’, *Applied Geochemistry*, 151, p. 105591. Available at: https://doi.org/10.1016/j.apgeochem.2023.105591.

West, T.O. and McBride, A.C. (2005) ‘The contribution of agricultural lime to carbon dioxide emissions in the United States: Dissolution, transport, and net emissions’, *Agriculture, Ecosystems and Environment,* 108(2), pp. 145–154. Available at: https://doi.org/10.1016/j.agee.2005.01.002.

White, T.J. *et al.* (1990) ‘Amplification and direct sequencing of fungal ribosomal RNA genes for phylogenetics’, in M.A. Innis et al. (eds) *PCR protocols: A guide to methods and applications*. New York, NY: Academic Press Inc., pp. 315–322. Available at: https://www.researchgate.net/publication/262687766.

Willer, H., Schlatter, B. and Trávníček, J. (2023) ‘The World of Organic Agriculture Statistics and Emerging Trends 2023 Edited by’. Available at: https://doi.org/10.5281/zenodo.7572890.

Withers, P.J.A. *et al.* (2014) ‘Agriculture and eutrophication: Where do we go from here?’, *Sustainability (Switzerland)*. MDPI, pp. 5853–5875. Available at: https://doi.org/10.3390/su6095853.

World Bank (2015) *World Development Indicators*. Available at: http://data.worldbank.org/data-catalog/world-development-indicators.

Wundernest (2012) *Giusto Giovannetti: il rivoluzionario del fungo. Quando il biofertilizzante purifica*. Available at: http://www.wundernest.com/2012/03/giusto-giovannetti-il-rivoluzionario-del-fungo-quando-il-biofertilizzante-purifica/ (Accessed: 3 December 2015).

Yu, D. (2008) *Chromium Toxicity, Case Studies in Environmental Medicine, Agency for Toxic Substances and Disease Registry*. Available at: http://www.atsdr.cdc.gov/csem/chromium/docs/chromium.pdf.

Zabinski, C.A. and Bunn, R.A. (2014) ‘Function of Mycorrhizae in Extreme Environments’, in Z.M. Solaiman, L.K. Abbott, and A. Varma (eds) *Mycorrhizal Fungi: Use in Sustainable Agriculture and Land Restoration*. Berlin, Germany: Springer.

Zak, D.R. *et al.* (2000) ‘Elevated atmospheric CO2, fine roots and the response of soil microorganisms: a review and hypothesis’, *New Phytologist*, 147(1), pp. 201–222. Available at: https://doi.org/10.1046/j.1469-8137.2000.00687.x.

Zamanian, K., Pustovoytov, K. and Kuzyakov, Y. (2016) ‘Pedogenic carbonates: Forms and formation processes’, *Earth-Science Reviews*. Elsevier B.V., pp. 1–17. Available at: https://doi.org/10.1016/j.earscirev.2016.03.003.

Zhang, G. *et al.* (2018) ‘Review and outlook for agromineral research in agriculture and climate mitigation’, *Soil Research*, 56(2), pp. 113–122. Available at: https://doi.org/10.1071/SR17157.

Zhang, Y.G. *et al.* (2013) ‘A 40-million-year history of atmospheric CO2’, *Philosophical Transactions of the Royal Society A: Mathematical, Physical and Engineering Sciences*, 371(2001), p. 20130096. Available at: https://doi.org/10.1098/rsta.2013.0096.

Zhou, C. *et al.* (2021) ‘Greater committed warming after accounting for the pattern effect’, *Nature Climate Change*, 11(2), pp. 132–136. Available at: https://doi.org/10.1038/s41558-020-00955-x.